Ultrasonic Measurements of the Piston Ring Lubricant Film Thickness in Three Different Sized Engines

Jack Rooke

A thesis submitted in partial fulfilment of the requirements for the degree of

Doctor of Philosophy

The University of Sheffield

Faculty of Engineering

Department of Mechanical Engineering

Submission Date

Winter 2021

Acknowledgements

The timely completion of this thesis would not have been possible without the guidance and incite of many people, to whom I owe my sincerest thanks.

Firstly, I would like to thank my supervisors, Rob Dwyer-Joyce and Tom Slatter for their advice and seemingly unwavering optimism throughout my PhD.

Thanks to Bryn Littlefair for his technical expertise and support during the project. I would like to thank Oliver Cooper and Dave Butcher for teaching me some of their expertise in rig design and manufacturing.

Thank you to Winterthur Gas & Diesel and the College of Power and Energy Engineering at Harbin Engineering University for enabling testing upon their engines that provided a wealth of data that I would have struggled without.

A sincere thank you to Andy Hunter and Henry Brunskill for enlightening me with their limitless ultrasound knowledge. A special thanks to Xiangwei Li, whose data processing software and suggestions saved me an unfathomable amount of time.

My time at the University of Sheffield would not have been the same without everyone in the iT-CDT. Especially the fourth cohort: Scott, Sam, Ben, Dave, Tom, Rasmus, Will, John and Royce. What a ride it has been, lost in the depths of our research.

Lastly, and most importantly, I would like to dedicate this work to my Mum and Dad for their endless support, belief and sacrifice throughout my education. A special thanks to my partner Clarissa for her encouragement and patience in my times of need. I could not have completed this without them.

Abstract

Internal combustion engines are undisputedly one of the most impactful engineering achievements and are the predominant power source for a range of industries. Modern developments focus on producing cleaner and greener engines in part to meet emission legislation and growing customer demand for more environmentally friendly options. Large sections of engine research focus on raising the mechanical efficiency by reducing frictional losses. The greatest contributing factor to frictional losses is the contact between the piston and piston ring pack with the cylinder liner. This is due to the reciprocating motion of the piston in which the piston rings form a seal between the high temperature/pressure combustion chamber and the engine crankcase. Optimisation of the interaction between the piston and liner, therefore, has the potential to reduce engine emissions whilst simultaneously reducing frictional losses, raising the efficiency of the engine.

This thesis developed novel ways to use ultrasound to monitor the lubricating oil film between the piston/piston rings and the cylinder liner in engines from various sectors (passenger, marine and agricultural). The ultrasonic method is based on studying the portion of an ultrasonic wave that is reflected from a boundary which can be correlated to oil film thickness. A new data processing technique has been created to define the reflection coefficient from the Hilbert envelope, this novel technique simultaneously removed several undesired factors in the results, and revealed trends hidden by the previous data processing technique. The novel data processing technique calculated oil films typically 20% greater than those from the previous technique as it was subject to ultrasonic reflections from an unaligned piston ring leading to an underestimation of the lubricant film thickness. In addition to this, spectrograms and B-scans have been applied to ultrasonic piston ring reflections for the first time and were able to identify a series of trends, such as the detection of a piston ring outside of the alignment zone.

The ultrasonic sensors have successfully been used to quantify the piston ring lubricant film thickness in a series of engine conditions not previously studied. These include: during start-up and shut-down of an engine, residual oil films on the cylinder liner, live variation in the film thickness with varying engine loading/lubricant feed rate etc. and the detection of metal-metal contact between the piston ring and liner. The sensors have also been used for the first time in the design phase of an engine. In the marine diesel engine, ultrasonic sensors were used to evaluate a series of lubricant injector configurations and led to the identification of a configuration that consistently produced thicker lubricant films.

Contents

List of Figures

List of Tables

Nomenclature

Symbol	**Unit**	**Description**
A	m^2	Area
A_o, A_d	bits	Amplitude
B	$N.m^{-2}$	Bulk modulus
C	F	Capacitance
D_t	m	Diameter of transducer
E	-	Youngs modulus
F	m^2	Force
K_{dc}	-	Dieletric constant
K	$N.m^{-1}$	Interfacial stiffness
L	mm	Stroke length
N	m	Near field length
N_c	rpm	Crank rotational speed
P	Pa	Pressure
R	-	Reflection coefficient
R_{rc}	-	Connecting rod length to crank radius ratio
$\bar{S_p}$	m/s	Mean piston velocity
S_p	m/s	Instantaneous piston velocity
a	mm	Crank radius
c	$m.s^{-1}$	Wave velocity
d	m	Distance
f	Hz	Frequency
h	μm	Thickness

Symbol	**Unit**	**Description**
l	mm	Connecting rod length
r	m	Radius
s	mm	Piston displacement
t	s	Time
u	$m.s^{-1}$	Velocity
z	$Pa.s.m^{-2}$	Acoustic impedance
α	-	Attenuation coefficient
α_η	$m^2.N^{-1}$	Pressure-viscosity coefficient
δ	m	Penetration depth
ε	$s^4.A^2.m^{-3}.kg^{-1}$	Permittivity of free space
η	$Pa.s$	Dynamic viscosity
θ	$^\circ$	Angle
λ	m	Wavelength
λ	-	Lambda ratio
ρ	$kg.m^{-3}$	Density
ν	-	Poisson's ratio
σ	μm	Composite surface roughness
ω	$rad.s^{-1}$	Angular velocity

Acronyms

aTDC	After top dead centre
BDC	Bottom dead centre
CA	Crank angle
CI	Compression ignition
COV	Coefficient of variance
FFT	Fast fourier transform
ICE	Internal combustion engine
IMO	International maritime organization
JLR	Jaguar land rover
LIF	Laser induced fluorescence
MOFT	Minimum oil film thickness
NDT	Non-destructive testing
NLT	Needle lift type
OFR	Oil feed rate
OFT	Oil film thickness
PJ	Pulse jet
PZT	Lead zirconate titante
SI	Spark ignition
TDC	Top dead centre
UPR	Ultrasonic pulser receiver
VI	Viscosity index
WinGD	Winterthur Gas and Diesel

Chapter 1

Introduction

The first chapter provides the reader with a brief introduction to the project and covers the development of internal combustion engines alongside the current research directions. The legislative motivation behind the research is detailed and the chapter closes by introducing the aim and objectives of the project as well as a summary of each chapter.

1.1 The internal combustion engine

Internal combustion engines (ICEs) have been the driving force behind transportation since the late 1800s. The first successful variant of the modern internal combustion engine is attributed to Nikolaus Otto in 1867. Starting from this first ICE, engine manufacturers have developed countless engine variants each with its progressive line of technological advancements. Twenty-first century ICE research is focused around improving engine efficiency whilst reducing engine emissions. A limited number of engine research fields include:

1. Engine downsizing - obtaining the same power output from an engine of a smaller size.
2. Reducing weight - a lighter engine requires less power output to run the vehicle.
3. Greener fuels - burning a greener fuel that produces fewer emissions per unit of burnt fuel.

The main components of a typical four-stroke spark-ignition engine and a two-stroke large diesel marine engine are identified in Figure 1.1.

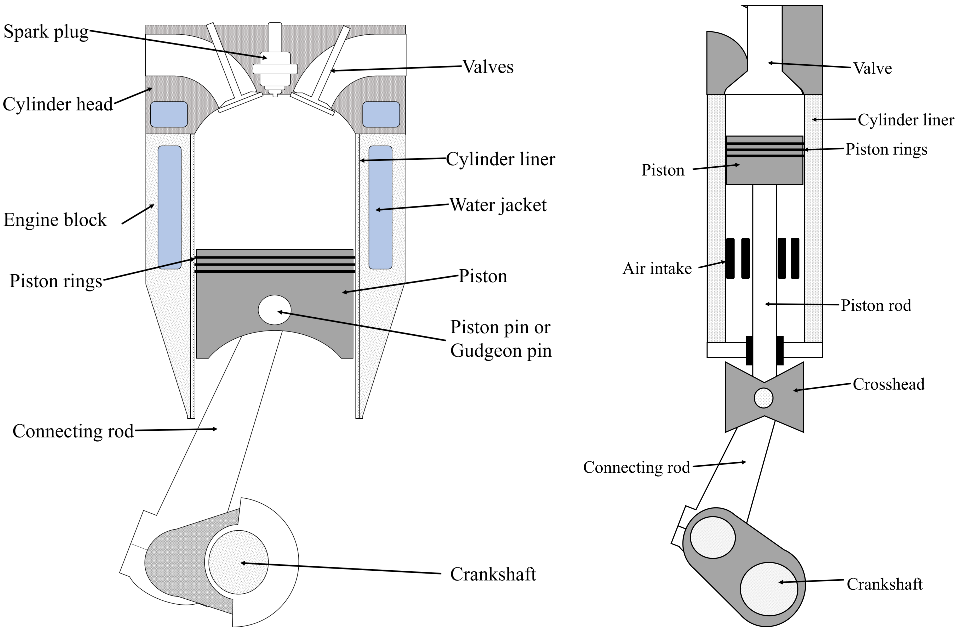

(a) Four-stroke spark-ignition engine (b) Two-stroke large marine diesel

Figure 1.1: Main components of a typical four-stroke spark-ignition engine and a two-stroke large diesel marine engine.

The overall efficiency of an ICE is subject to a series of inefficiencies attributable to different aspects of the engine, such as those covered in Figure 1.2. Typical efficiency levels have not been provided due to the efficiency levels varying significantly between engines and engine operating conditions. To limit mechanical friction and reduce wear, a lubricant is supplied between mating surfaces to prevent solid contact. Even with a lubricant, the parasitic losses that occur consume up to 9.5-20% of the energy content in the fuel in a passenger engine [1, 2, 3]. Research to minimise the parasitic losses provides a route to raise the overall engine efficiency whilst improving the interaction between components reducing the likelihood of wear and raising the required engine maintenance interval.

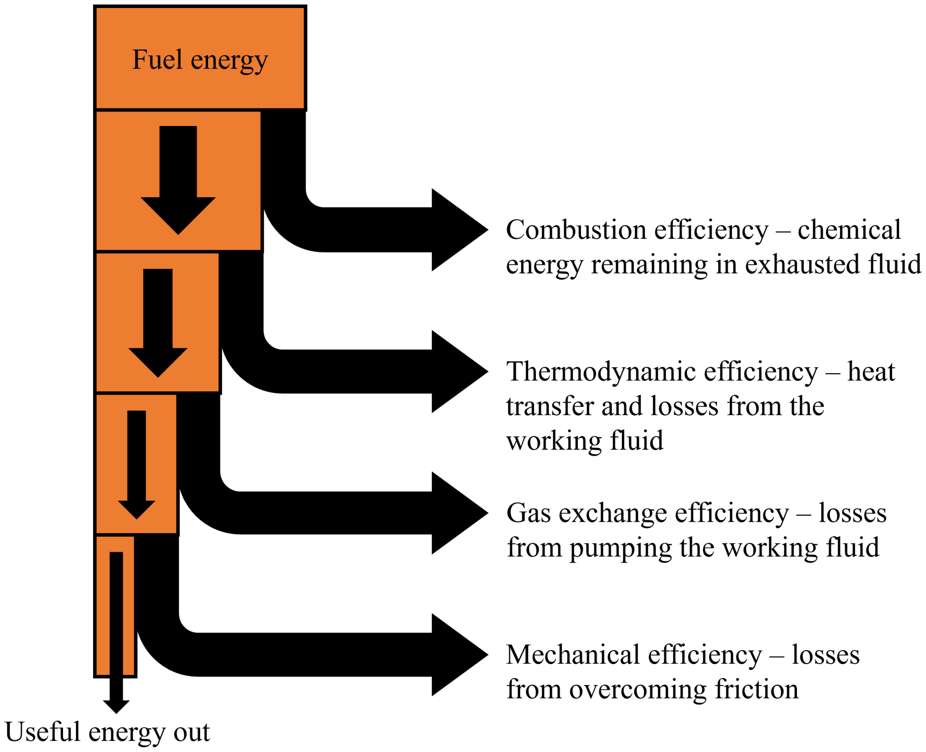

Figure 1.2: Inefficiencies in an ICE.

The passenger vehicle industry in the UK alone is worth an estimated £82 billion [4], therefore even minor mechanical frictional improvements by ensuring all mating surfaces in an engine are sufficiently lubricated to prevent metal-metal contact may provide sizeable benefits. Studying the lubricating oil film between two mating components without compromising the tribological properties of the surfaces is a desirable route for technological advancements but is inherently difficult. Research into this field is commonly invasive leading to the findings of the study often not being a true representation of the real-life application. This work studied potential mechanical frictional improvements by examining three ICEs of varying sizes and applications, as shown in Figures 1.3 and 1.4. The defining features of each engine are as follows:

- Figure 1.3a, AJ200 - A Jaguar Land Rover petrol Ingenium engine, a 4 cylinder four-stroke, 2 litre.
- Figure 1.3b, YTRC2110D - A YTO engine, typically used in tractors, a 2 cylinder four-stroke, 2 litre.
- Figure 1.4, RTX-6 - A Winterthur Gas & Diesel engine, a 6 cylinder two-stroke, 16000 litre.

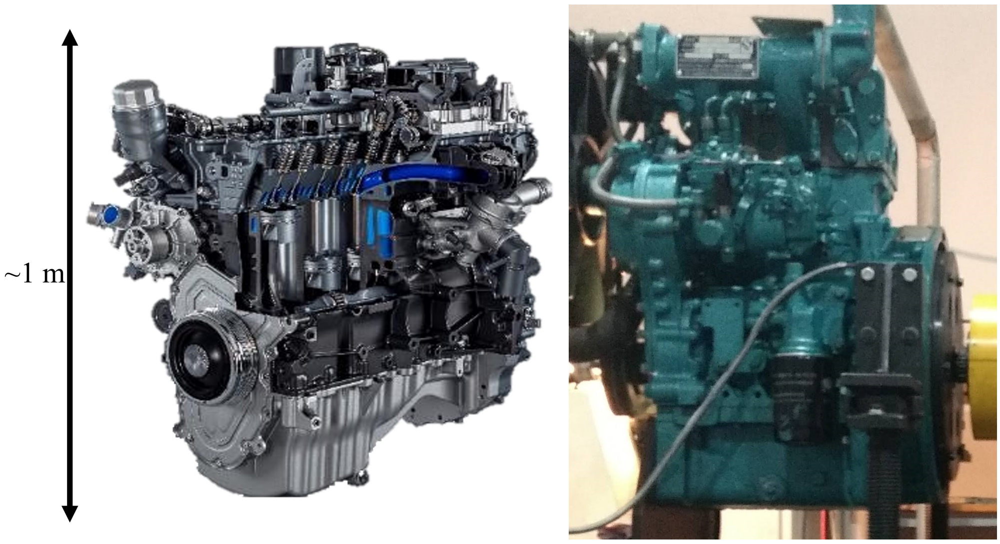

(a) AJ200 engine [5]. (b) YTRC2110D engine.

Figure 1.3: The AJ200 and YTRC2110D engines.

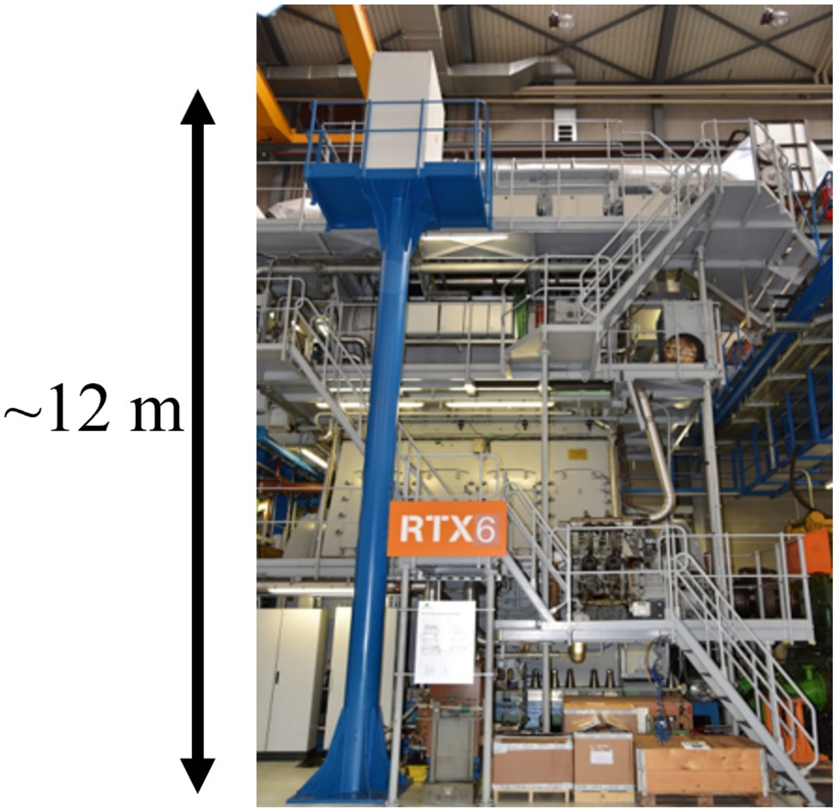

Figure 1.4: RTX-6 engine [6] © SAE International.

1.2 Powertrain frictional improvement

There are many lubricated contacts in an engine, each contributing to frictional losses. Although it is difficult to deduce the amount each contact contributes to the frictional losses. Research into ICE frictional losses typically categorises the cause of the losses into three groups; valve train, piston assembly and engine bearings. With the relative contribution of each group varying with oil temperature/classification and engine load. Detailed models have been developed to replicate the frictional losses of major engine components in gasoline engines, the reader is referred to Sandoval and Heywood [7] for a model on the three main groups.

These frictional losses have been measured experimentally in a single-cylinder four-valve Ricardo Hydra gasoline engine [8]. This research ultimately found that at low speeds and oil temperature (similar to cold start) the engine bearings contributed the greatest amount to mechanical friction (52%). Whilst after cold start, with increased oil temperature, the frictional loss from the piston assembly contributed the greatest factor and increased further with greater engine speed, peaking at 44%. With the peak friction contribution from the piston assembly arising at the start of the power stroke due to a combination of boundary lubrication and peak combustion pressure [3]. Over steady-state operation, the piston assembly was the greatest contributing factor in the system to frictional losses in this engine. Interestingly, as [8] was performed on a single-cylinder engine, this gave a cylinder to main bearing ratio of 1:2, whilst, in multi-cylinder engines, like those considered in this work, this ratio reduces. Therefore, the engine bearing contribution is likely overstated in this work when considering multi-cylinder engines. Alternative works have found the piston assembly frictional losses to range between 40-65% in engines of varying size [2, 9, 10].

Of the 9.5-20% [1, 2, 3] of energy contained in the fuel that is wasted due to friction, 25% of that is directly attributable to the ring pack [11]. Indicating that the ring pack wastes roughly 3-4% of energy in the fuel with the rest of the piston contributing a further 2% [2]. With current prices of petrol and diesel being £1.27 and £1.30 per litre (2021) respectively, the friction from the piston and ring pack wastes 7p per litre of fuel. In 2019 an estimated 46.9 bn litres of fuel was consumed in the UK [12] providing a rough value of £3.2 bn spent on fuel that was wasted overcoming friction due to the piston assembly. Through optimisation of the piston ring oil film thickness this amount has the potential to be significantly reduced.

1.3 Engine development and legislation

Over the past few decades the mechanical friction in ICEs is believed to have decreased by $15-20\%$ [7, 10]. Even with these sizeable improvements, further research is required to achieve the legislative criteria of future engines. For example, light commercial vehicles in the EU are responsible for 14.5% [13] of CO_2 emissions in the EU. This has led to the implementation of Euro Standard Regulation (EU) 2019/631 which aims to reach a net reduction of CO_2 by 55% by 2030 through a series of increasingly stringent targets for engine manufacturers which the UK largely continues to follow [14]. The legislative targets are:

- 2020-2024: Average fleet-wide CO_2 emissions of 95 g CO_2/km and 147 g CO_2/km for cars and vans respectively.
- 2025-2030: A CO_2 reduction relative to 2021 levels of 15% from 2025 and 37.5%/31% for cars/vans by 2030.

Although these targets only refer to CO_2 levels, the Euro Standards also set acceptable levels of NO_x, hydrocarbons and particulate matter in engine emissions. From Euro 1 (1992) to Euro 6 (2015) acceptable levels of NO_x and hydrocarbons have reduced by 83%. Whereas particulate emission standards were introduced in Euro 5 (2009). In [15, 16] a locomotive engine was studied and found 40-60% of particulate emissions were due to piston ring lubricating oil being thrown off into the combustion chamber and exhausted from the engine. This lubricated contact evidently has a major impact on both engine emissions and mechanical friction.

The legislation also contains an incentive mechanism for manufactures to produce zero- and low-emission vehicles through an enhanced contribution towards their fleet CO_2 levels and a penalty per newly registered vehicle of €95 per g/km for exceeding their targets. Further premiums are applied in the UK through the addition of road tax, which is an annual rate which the vehicle owner pays, the size of which is dependent on CO_2 emission levels. For example, a petrol car that produces 100 g CO_2/km costs £140 [17] annually leading to emissions levels being a consideration for the customer.

Marine engines are subject to a similar emission approach as international shipping contributes 2.2% of anthropogenic CO_2 emissions [18]. This field is regulated by the International Maritime Organization (IMO), whose strategy aims to reduce greenhouse gas emissions from this sector by 40% by 2030 relative to 2008 levels [18].

1.4 Motivation

The emission legislation that engine manufacturers are required to meet is becoming ever more stringent. To meet these regulations novel technologies are required to refine engine design. The piston is the largest contributing factor to an engines mechanical friction and in some engines lubricant throw off causes the majority of particulate emissions. Therefore, a greater understanding of this lubricated contact has the potential to raise engine efficiency by reducing powertrain friction, (via a reduction in boundary lubrication) whilst also reducing emissions to meet emission targets.

1.5 Aim and objectives

The project aimed to develop an ultrasonic transducer system to quantify and evaluate the oil film thickness between piston rings and cylinder liner, at a range of engine operating conditions in engines of varying sizes. To achieve this the objectives were thus:

1. Design and production of a motored AJ200 test rig.
2. Refinement of ultrasonic instrumentation capable of withstanding the harsh operational environments close to ICE combustion chambers.
3. Instrument ultrasonic transducers on the three engines selected for the project.
4. Refine data processing techniques to improve the oil film thickness calculation.
5. Study the relative similarities and differences in oil film thickness data between the various engines to evaluate the applicability of the technique in each engine.

1.6 Expected novelty

The expected novelty to be produced from this thesis can be summarised as follows:

1. Refine the ultrasonic instrumentation technique such that it is specialised for piston ring oil film thickness measurements.
2. Increase the resolution of piston ring lubricant film thickness measurements beyond those hitherto seen, to enable a closer examination of anomalies in previous research.
3. Use ultrasonic sensors to study a series of engine phases currently not studied in other works (start-up and shut-down, engine slow-down, piston ring scuffing).

4. To move away from purely using ultrasound as a research tool to study the operation of a fired engine and use the technology to aid in the design phase of an engine by evaluating how novel designs affect the piston ring oil film thickness.

1.7 Thesis layout

Chapter 1: Introduction
Chapter One provides the reader with a generic background to the research field stating the motivation behind the project, introducing key regions for thought and the greater picture of this research in respect to modern ICE development.

Chapter 2: Internal combustion engines
The second chapter introduces the reader to the operation of internal combustion engines, this develops to show lubricant formulation and classification. This is followed by a literature review of previous works performed to study oil films in engines using a whole range of methodologies. Attention is given to the ultrasonic approach due to its ability to provide non-invasive measurements of the oil films, therefore, leading to its selection for the appropriate route for further study.

Chapter 3: Ultrasound
The third chapter starts from the definition of ultrasound and leads the reader through to different methodologies currently used in the field to study oil films. This chapter also introduces piezoelectric transducers that are used to generate and receive sound waves. The chapter includes a review of previous ultrasonic transducer test rigs developed to study the oil films between pistons and cylinder liners. The closing section of the chapter provides an overview to k-Wave, a MATLAB toolbox to model ultrasonic wave propagation and highlights key features of the toolbox.

Chapter 4: Motored rig design
Chapter four is an overview of the design methodology of the motored AJ200 test rig developed and it explains the process behind the main sections of the test rig. Key troubleshooting regions are identified to aid the future design of a similar test rig. The chapter concludes by showing the reader the test rig produced to study the piston ring oil films in the AJ200 engine.

Chapter 5: Motored gasoline automotive engine

The fifth chapter covers the instrumentation and motored engine testing on the AJ200 engine. The reader is led through the data processing required to replicate such results.

Chapters 6: Lubricant injector comparison in a fired marine diesel engine

Chapter sixth is the first chapter on the fired diesel marine engine and compares the oil film thickness from two different lubricant injector designs at a range of engine loadings levels and oil feed rates.

Chapters 7 and 8: Fired marine engine advanced analysis and shear analysis

Chapters 7 and 8 develop additional data processing steps to the longitudinal and shear sensor results from the fired marine engine to provide a more in-depth view of the piston ring oil film thickness.

Chapter 9: Fired diesel tractor engine

The ninth chapter uses the advancements in data processing found in Chapter 7 and applies them to a fired diesel tractor engine. The engine features a wet removable liner enabling more complex instrumentation than seen on the AJ200 with minimal modifications. The chapter covers the instrumentation and testing of the fired tractor engine at a range of engine loadings and engine speeds as well as start-up and shut-down testing.

Chapter 10: Conclusions

The final chapter concludes the refinement of the data processing and key findings from the work. The closing remarks cover potential future directions of ultrasonic measurements of piston ring oil film thickness.

Chapter 2

Internal combustion engines

This chapter leads the reader from the basic operation of two-stroke and four-stroke engines through to the design and operation of the piston ring pack. The closing portion provides a review of a broad range of research on piston ring oil film thickness measurements.

2.1 Basic concepts

A internal combustion engine can be described as a device that converts energy from one form to another. In this case, chemical energy in the fuel into useful work in the form of a mechanical force leading to vehicular motion. This operation is achieved by the combustion of the hydrocarbon fuel in the presence of oxygen located in a combustion chamber.

The two main types of internal combustion engines are spark-ignition and compression-ignition. In spark-ignition (SI) engines, combustion is initiated via a spark that ignites the fuel/air mixture. Whereas in compression-ignition (CI) engines the compression of the mixture of fuel/air raises the temperature and pressure in the combustion chamber and causes the mixture to spontaneously ignite.

There are variants within both SI and CI engines such as depending on the number of strokes for one complete cycle of the engine. Of the three engines considered in this project the smaller engines (AJ200 (SI) and YTRC2110D (CI)) are four-stroke engines whilst the RTX-6 (CI) is a two-stroke engine. Therefore, the engines have distinct differences in their design and operation, the basics of which are covered here.

2.1.1 Automotive four-stroke engine

The four-stroke ICE was first prototyped by Nikolaus Otto in 1876 and is the predominant engine type in the automotive industry. As the name implies, there are four stages in a four-stroke engine that occurs over two distinct engine cycles. The four strokes are shown in Figure 2.1 and are detailed below:

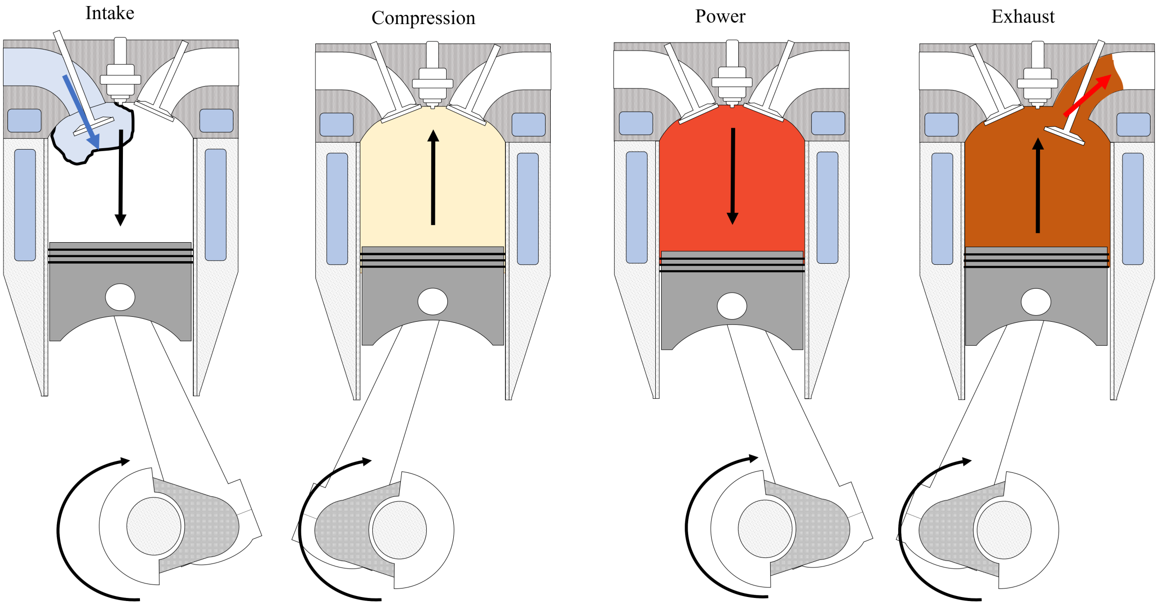

Figure 2.1: The four strokes in a four-stroke reciprocating piston engine.

1. Intake stroke: Fluid is drawn into the combustion chamber by the opening of the inlet valves. In SI engines fuel/air mixture is drawn in whereas in CI engines only air is drawn in.
2. Compression stroke: The valves close and the piston runs up the cylinder compressing the mixture. The compression of the fluid raises the temperature and pressure.
3. Power stroke: Combustion of the fluid occurs further raising the temperature and pressure of the mixture forcing the piston down and turning the crankshaft. In SI engines a spark ignites the fluid, in CI engines fuel is injected which auto-ignites in the high temperature/pressure.
4. Exhaust stroke: The combusted mixture is removed from the combustion chamber by the opening of the exhaust valves.

2.1.2 Marine two-stroke engine

Following the development of the four-stroke, two-stroke engines were established with the primary advantages over a four-stroke being greater thermal efficiency and greater power density due to combustion occurring every engine cycle. The first two-stroke engines were attributed to Dugald Clerk, James Robson and Karl Benz in the 1880s with common modern applications being in motorcycles and large marine engines. The two stages in marine diesel two-stroke engines cycle are shown in Figure 2.2 and detailed below.

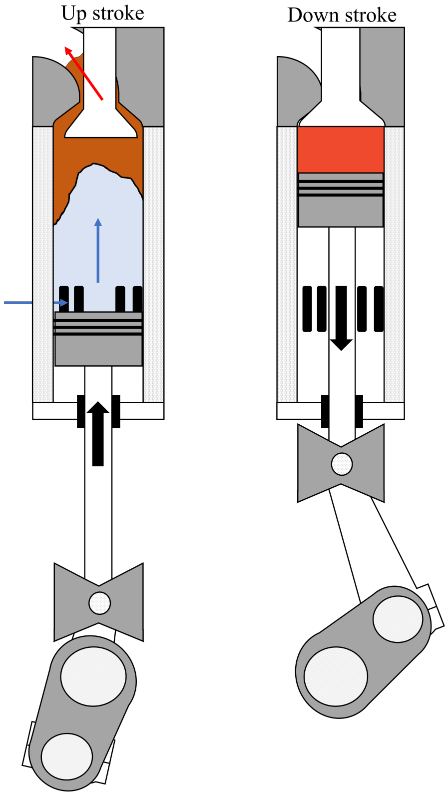

Figure 2.2: The two strokes in a two-stroke marine diesel engine.

1. First stroke: Piston moves up the liner. Cross flow scavenging allows air to be drawn into the cylinder whilst expelling combustion products. After the piston moves past the air intake the valve closes and then compresses the fluid in the cylinder.
2. Second stroke: The fluid combusts pushing the piston down the liner. After the piston moves past the air intake the valve opens are cross-flow scavenging begins.

2.2 Piston assembly

The piston is arguably the most challenging part of an ICE to design as its primary function is a moving wall of the combustion chamber. Therefore, it is exposed to severe pressures and temperatures the magnitude of which depends on the stroke of the engine. The piston is also the component that transfers energy from the combustion products to the mechanical movement of the engines drivetrain. This is achieved whilst the piston assembly provides a seal between the combustion chamber and crankcase to enable an efficient energy transfer. The four key areas of the piston assembly are: crown, pin, skirt and ring pack and are highlighted in Figure 2.3. Each of the four key areas is discussed in the following section.

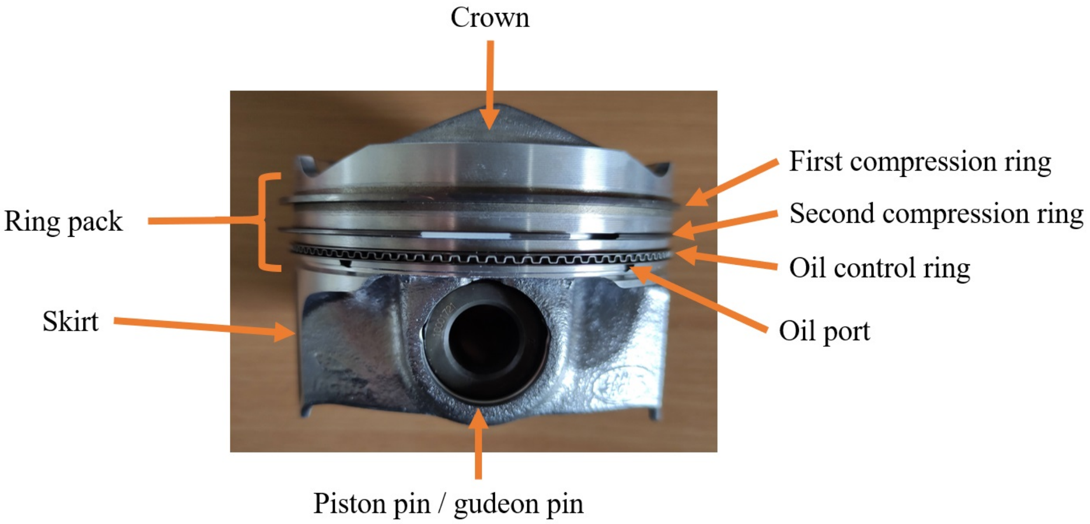

Figure 2.3: Labelled areas of an automotive piston.

2.2.1 Piston

Small automotive pistons are commonly produced from an aluminium alloy that is cast or forged whilst larger automotive pistons are commonly made from cast iron. A coating is often applied to improve the sliding of the piston and to reduce friction, typical coatings include tin, lead or phenolic resin graphite coatings. The key areas of an automotive piston are described below:

- Crown: The piston crown is the moving wall of the combustion chamber and is typically either a bowl (diesel) or flat design (gasoline). Automotive engines also often have the addition of reliefs for the valves. The crown is commonly has a coating (e.g. zinc) to raise high-temperature performance as an automotive piston crowns may reach temperatures of 325 $°C$ with variations across the face of the crown up to $\pm$ 50$°C$ [19].

- Pin: The piston pin/gudgeon pin connects the piston assembly to the connecting rod and enables rotation of the piston through the course of an engine stroke. The centreline of the pin can be offset from the centreline of the crankshaft to counteract the piston tilt in the power stroke.
- Skirt: The asymmetric loading of the piston assembly and connecting rod leads to a lateral force between the cylinder and piston. The skirt provides a large surface area for this force to act over whilst also preventing excessive tilt of the piston.
- Ring grooves: The ring grooves locate the piston rings. The groove for the oil control ring contains a series of ports to route excessive lubricant on the liner down into the crankcase.

The temperature gradient down the piston leads to the majority of the mass being centred around the piston crown, see Figure 2.4. This mass distribution causes the skirt to be less stiff and is subject to a greater thermal distortion than that of the crown. To minimise the effect of the distortion on blow-by the radius of the piston varies down its length. Therefore, as the engine runs, raising the temperature of the piston, the thermal expansion leads to the piston having a more desirable shape at working conditions. The piston is prevented from reaching undesired temperatures by forced cooling in which lubricant jets are directed at the piston undercrown to cool the piston from underneath.

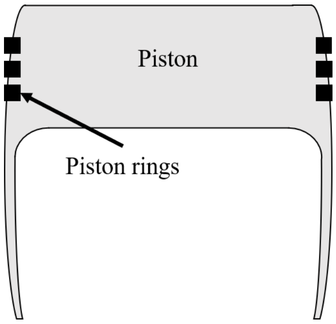

Figure 2.4: Cross-section of an automotive piston.

Marine diesel engine pistons are largely similar to automotive pistons as their primary purposes remain the same; although there are minor differences in the piston design, due to the significantly increased engine size. The piston crown is often flat and it does not have a pin, instead the piston is rigidly connected to the piston rod preventing relative motion between the two.

2.2.2 Ring pack

The ring pack consists of a series of piston rings that form a seal between the combustion chamber and crankcase to prevent blow-by of combustion products. The rings also control the quantity of lubricating oil film left on the liner and a compromise is achieved between forming a sufficient oil film to prevent friction and wear. Whilst not establishing an excessively thick film that leads to greater oil thrown off in the combustion chamber and, therefore, raises engine emissions.

Conventional rings are manufactured from cast iron or steel/stainless steel and with coatings such as chromium-ceramic. High-performance automotive engines may have piston rings widths of less than 0.9 mm whilst in marine engines their widths may be in the order of 15 mm.

There are three types of piston rings: first compression ring, secondary compression ring/scraper ring and oil control ring. The number of piston rings depends upon a multitude of factors such as bore shape, ring stiffness, ring tension, surface textures, oil control/management through the rings. A typical ring pack usually consist of two to five rings with at least one first compression ring and one oil control ring.

Each piston ring contains a gap to locate the ring in its groove. The tolerance of the cylinder liner tensions the piston ring to conform to the shape of the liner and reduce the size of the ring gap.

2.2.2.1 First compression ring

The first compression ring forms the primary seal to prevent combustion products from escaping from the combustion chamber into the crankcase which would significantly limit the efficiency of an engine. The combustion pressure in the power stroke acts on the top and back face of the piston ring and forces the ring to conform to the cylinder bore providing a greater seal and preventing lateral movement of the ring in its groove (ring flutter). A schematic of the combustion pressure acting upon a piston ring is shown in Figure 2.5. The common profile types for first compression rings are barrel, rectangular, bevelled rectangular, and tapered. The cross-section of each is shown in Figure 2.6.

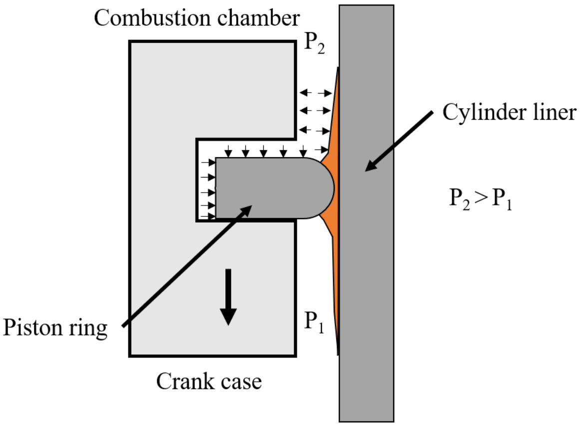

Figure 2.5: Combustion pressure acting upon the first ring.

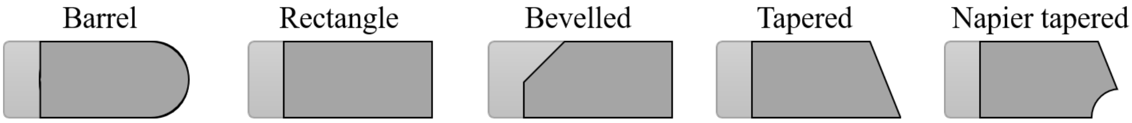

Figure 2.6: Cross-section of common compression ring designs.

1. Barrel - The barrel profile helps to aid the formation of a hydrodynamic lubricant film whilst providing an effective seal. The radius of ring curvature is a compromise between; how quickly the ring picks up oil, the formation of hydrodynamic oil film and how quickly the film collapses near the ends of the piston stroke.

2. Rectangular - The simplest and low-cost compression ring design. The large face causes a greater contact to the liner than any other ring profile leading to greater frictional losses. An advantage of this design is the greater contact aids in heat transfer to the cylinder thus limiting the maximum temperature reached by the piston ring and the thermal expansion.

3. Bevelled rectangular - An advancement on the rectangular design by being notched on the inner edge of the ring. The notch enables ring twist during low-pressure strokes, therefore, reducing liner contact and friction. The angled ring enables oil to be scraped down the liner more effectively. Whereas in high-pressure strokes, the notch provides a greater resultant force outwards on the ring leading to a greater sealing force. The bevelled ring provides a route to prevent ring flutter.

4. Tapered - The profile is tapered, this controls the thickness of the lubricating film by forming a line contact around the circumference of the liner. The narrow point of

contact enables greater conformability between the ring and the cylinder and reduces the running in interval. The taper provides a surface for the combustion pressure to act over reducing ring friction and loading.

2.2.2.2 Secondary compression rings

The second compression ring (scraper ring) further helps to seal the combustion chamber and prevents excessive amounts of oil from reaching the first compression ring. The second ring is seen to provide a buffer between the high pressure (combustion chamber) and low pressure (crankcase) regions. The common types of second rings are tapered and napier tapered (a cross-section is shown in Figure 2.6).

- Tapered - The same function as defined above.
- Napier taper - Similar to the tapered design with the addition of a hook-shaped notch on the lower edge of the ring. This improves the rings ability to scrape away excessive amounts of oil.

2.2.2.3 Control ring

The oil control ring is designed to control the quantity of oil that is in the ring pack. Without this ring, large amounts of oil would be entrained through the ring pack and into the combustion chamber by the high velocities of the piston raising particulate emissions. The control ring is combined with ports in the piston to enable excess oil to be directed back down into the crankcase. This ring often operates in starved lubricated conditions as oil in this area is directed away leading to this ring being a large contributor to ring pack friction. Automotive oil control rings usually contain two rails (< 0.4 mm each) and are either a single piece, two-piece or a three-piece set-up, see Figure 2.7 and summarised below:

- Single piece - A single piece of cast iron that has two distinct rails and is held against the cylinder liner under its natural tension.
- Two-piece - A similar design to a single piece with the addition of a spring on the inner edge forcing the rail against the cylinder. Therefore, the two-piece has a greater scraping capability than the single piece.
- Three-piece - A development on the two-piece, that the two rails are separate rings that are separated by a flexible spacer. The spacer maintains a standard separation between the two rings and aids in sealing the ring against the cylinder.

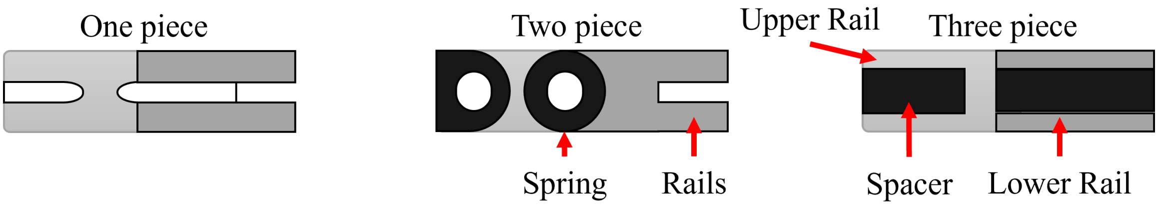

Figure 2.7: Cross-section of oil control ring designs.

The piston rings studied across the three engines in this work are summarised in Table 2.1.

Table 2.1: Piston rings studied.

Ring	**AJ200**	**RTX-6**	**YTRC2110D**
First	Barrel	Barrel	Barrel
Second	Tapered	Barrel	Barrel
Third	Three piece	Barrel	One piece

2.3 Piston dynamics

A piston undergoes linear motion that contains a reversal point at the end of every stroke. Standard automotive engines run at several thousand revolutions per minute leading to the piston being subject to high velocities and accelerations. Under the assumption that the piston assembly is rigid, a piston is capable of two distinct types of motion, see Figure 2.8. The primary motion of the piston is the desired motion, in which the piston is moving parallel to the cylinder wall. Secondary motion is the motion that is perpendicular to the liner, this occurs due to the geometry of the system and causes a rotation about the piston pin. This may potentially cause metal-metal contact between the piston and liner.

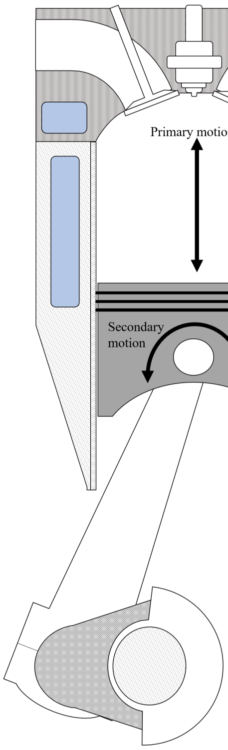

Figure 2.8: Primary and secondary motions of a piston.

2.3.1 Primary motion

The primary motion is defined by the cylinder liner walls and the rotation of the crankshaft as shown in Figure 2.9. The constraints of the system allow the displacement, velocity and acceleration of the piston assembly to be defined parametrically. The top of the stroke is termed the top dead centre (TDC) and the bottom is the bottom dead centre (BDC).

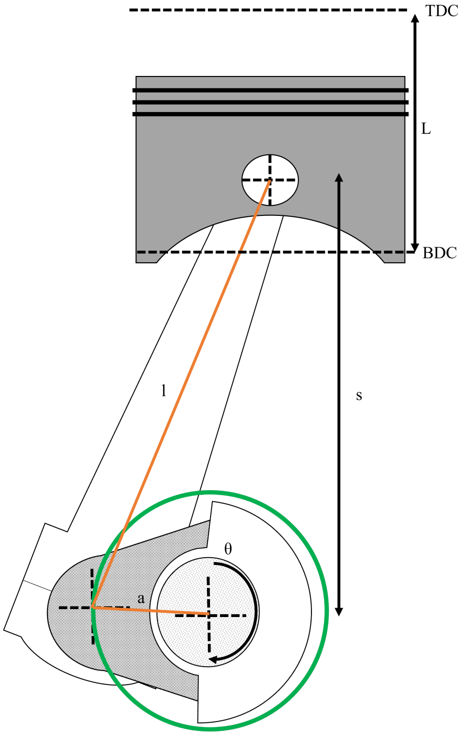

Figure 2.9: Geometry of the cylinder, piston, connecting rod and crankshaft.

R_{rc} is the ratio of the connecting rod length, l, to crank radius, a (Equation 2.1).

$$R_{rc} = \frac{l}{a} \tag{2.1}$$

The movement of the piston can be defined by its position relative to the TDC. The displacement of the piston, s, is summarised in Equation 2.2.

$$s = acos(\theta) + (l^2 - a^2 sin^2(\theta))^{0.5} \tag{2.2}$$

The mean piston velocity, $\bar{S_p}$ is defined in Equation 2.3, in which L, is the stroke length (twice the crank radius) and N_c, is the rotational speed of the crank.

$$\bar{S_p} = 2LN_c \tag{2.3}$$

The instantaneous piston velocity, S_p, is zero at the TDC and BDC and reaches a maximum near the middle of the stroke. The piston velocity is defined by differentiating Equation 2.2 and through several stages of rearrangements Equation 2.4 is defined. See Figure 2.10 for an example of piston velocity at three engine speeds.

$$S_p = \frac{\pi}{2}\bar{S_p} sin(\theta)\left[1 + \frac{cos(\theta)}{(R_{rc}^2 - sin^2(\theta))^{0.5}}\right] \tag{2.4}$$

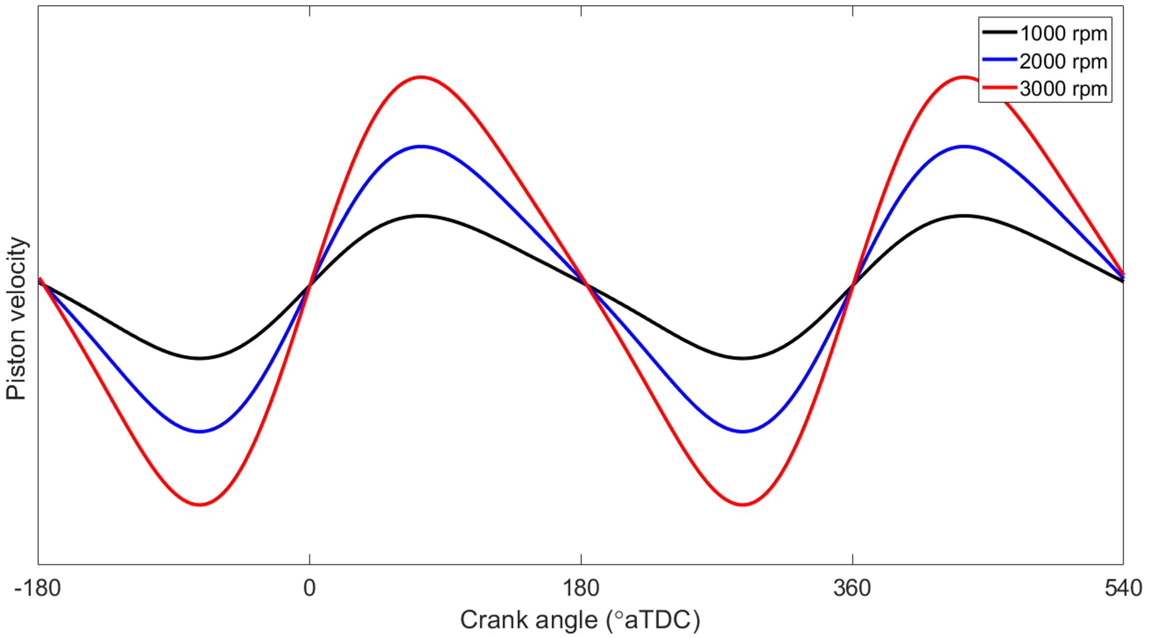

Figure 2.10: Piston velocities for a range of crankshaft rotational speeds using Equation 2.4.

Differentiating Equation 2.4, provides Equation 2.5 for the acceleration of the piston. An example of piston accelerations for three engines speeds are shown in Figure 2.11.

$$\frac{d^2s}{dt^2} = \pi^2 N_c \bar{S_p} \left[cos(\theta) + \frac{R_{rc}^2 cos(2\theta) + sin^4(\theta)}{(R_{rc}^2 - sin^2(\theta))^{1.5}} \right] \tag{2.5}$$

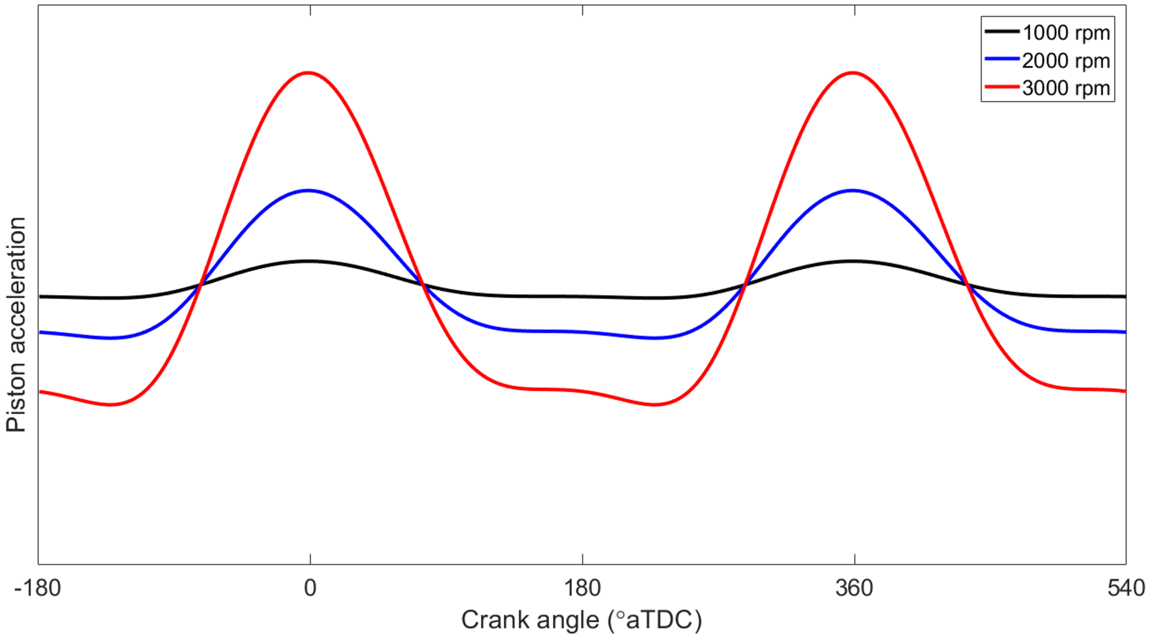

Figure 2.11: Piston accelerations for a range of crankshaft rotational speeds using Equation 2.5.

Equations 2.4 and 2.5 should not be seen as a complete representation of the linear motion of the piston assembly. Factors such as combustion pressure or dynamic effects from other components interacting with the piston assembly in the form of component deformation or clearances will affect these profiles.

2.3.2 Secondary motion

The secondary motion relates to the piston rotation about the piston pin by the side force that is generated through the motion of the piston. This rotation may cause the piston to impact the liner. The magnitude of this motion varies through each stroke with the greatest secondary motion often in the early stages of the power stroke. An example of piston secondary motion in a four-stroke engine is shown in Figure 2.12. This motion primarily affects the lubricating film between the two and affects the blow-by of combustion gases. The portion of the skirt exposed to the greater force is the major thrust side and the opposite side is the minor thrust side. The secondary motion of the piston can be reduced by offsetting the piston pin centre relative to the crankshaft centreline to create a torque that counteracts the piston tilt or offsetting the centreline of the crankshaft from the cylinder.

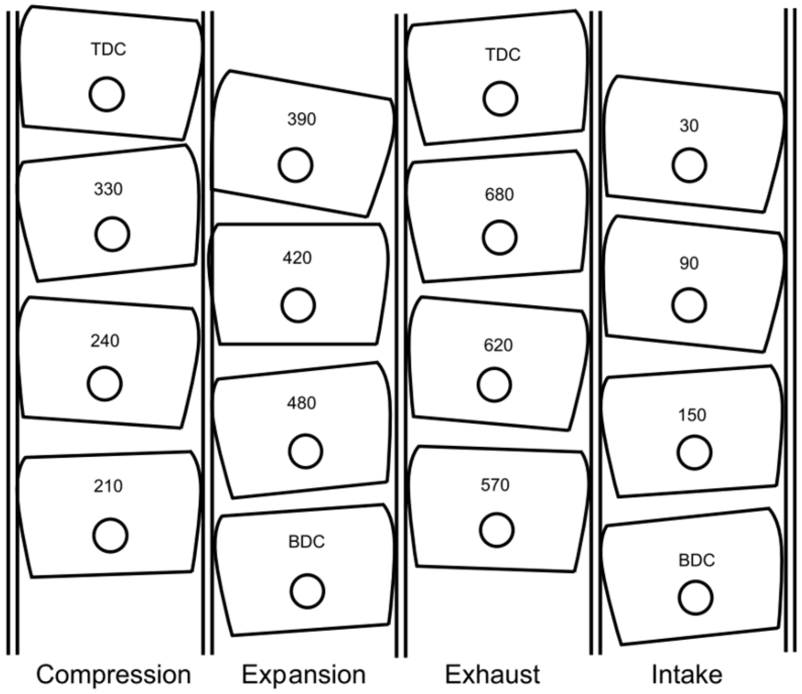

Figure 2.12: Secondary motion in a four-stroke engine, reproduced from [19].

2.4 Piston loading

The asymmetric loading of the piston leads to a differential loading on the piston depending on whether it is rising or falling in the cylinder. A third force is required to balance the system which is applied by the liner resisting the rotation of the piston about the piston pin. A free-body diagram of the forces is shown in Figure 2.13 for the two types of loading. In the compression stroke, one side of the cylinder is loaded, termed the anti-thrust side. Whereas in the power stroke the opposite side of the cylinder is loaded and to a much greater extent, termed the thrust side. Piston loading occurs in all four engine strokes although it is significantly larger in the power stroke due to the combustion process. Factors such as the inertia of the piston itself also add to the lateral loading in each stroke.

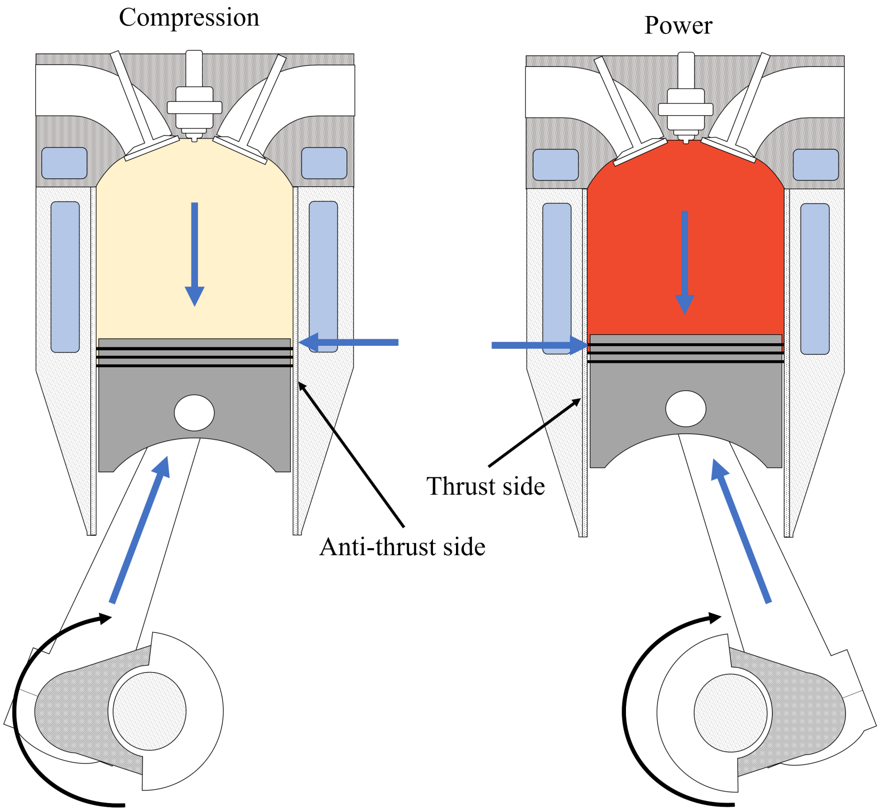

Figure 2.13: The thrust and anti-thrust side of an engine.

The piston loading in Figure 2.13 relies on the cylinder pressure acting upon the piston. In a motored engine, such as the AJ200 rig covered in Chapter 5, there is no compression or combustion as the cylinder head is removed from the engine. Instead of the piston driving the crankshaft the crankshaft is now driving the piston. This, therefore, reverses a force in the free body diagram so that the lateral force always acts on the same side of the piston, as shown in Figure 2.14.

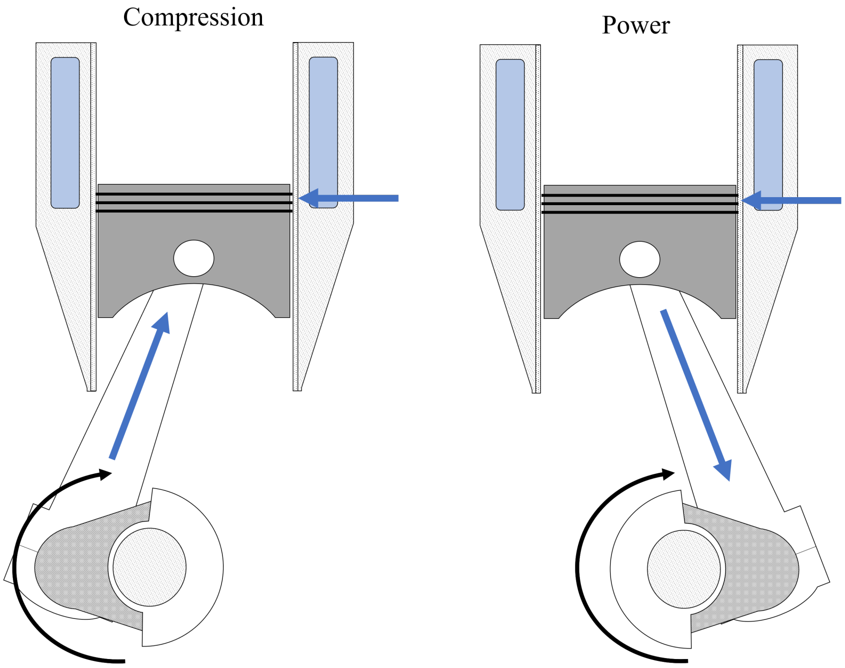

Figure 2.14: Forces acting upon a motored piston.

2.5 Cylinder liner design

Upon initial consideration, the reader may think the ideal cylinder liner design may be perfectly smooth, although this would not necessarily reduce the friction as it may cause greater contact (as well as being unfeasible to manufacture). This would also lead to issues with oil retention between strokes and wear transportation. In the compression and exhaust strokes, the only oil present to form a lubricating film is that which was left during the previous downward stroke. Therefore, the oil must be able to sufficiently adhere to the liner surface and not run down towards the sump. To retain oil, grooves are machined in the liner which vary in depth from 1.5 μm to 8 μm with the spread of the groove depths related to the wear expected in different portions of the engines lifetime. For example, the shallowest grooves (1.5 μm) provide additional lubrication during the running-in of the engine limiting the excessive wear during this period.

The cylinder liners considered in this work are cast iron, however, this is not always the case. A range of materials may be used for the liners, some engines use aluminium liners to save weight which has a spray coating to provide the desired surface properties. Similar to the oval machining of the piston, the liner may be angled down the length of its profile leading to the bottom of the liner having a marginally greater radius. This machining is performed as when the engine is at normal operating conditions the top section of liner is exposed to greater temperatures and, therefore, thermally distorts greater than the lower section of the liner. This angled honing, therefore, allows for a greater cylindricity of the liner at elevated temperatures. In addition, an angled profile of the liner aids in routing oil and debris down into the crankcase.

The liner grooves are frequently cross-hatched (see Figure 2.15a) commonly 15°-35° from the horizontal. The honing operation consists of two sub-operations, an initial hone to produce the grooves of desired depth followed by a finer hone to remove the peaks of the asperities. This creates a smooth operating surface whilst leaving the valleys on the surface which allows for oil retention, named a plateau honed surface, see Figure 2.15b. This dual honing process increases machining costs but significantly reduces the wear during running-in of the engine and enables for more rapid ring seating.

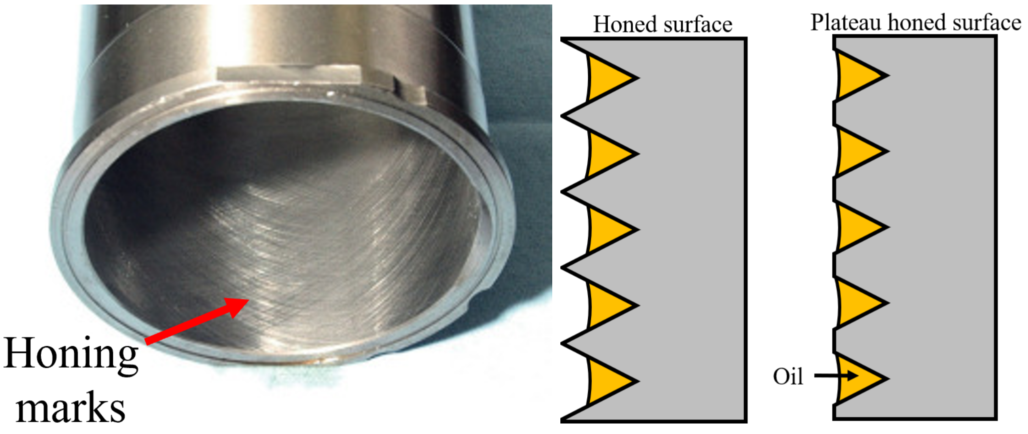

(a) A honed cylinder liner [20].

(b) Profile of a honed liner versus a plateau honed liner.

Figure 2.15: Honed cylinder liners.

2.6 Engine oil composition

Automotive oil consists of a mixture of base oil and added components (such as viscosity modifiers and additives). The lubricant mixture is typically $75-85\%$ base oil and $15-25\%$ additive package. This helps the oil to achieve its desired properties, primarily to reduce friction although it provides secondary benefits of; component cooling and sealing, protection against corrosion, cleaning surfaces from debris and carrying this debris to the oil filter. Modern automotive oil provides these benefits whilst the price is low enough to be commercially viable and with extended periods between oil changes.

The base oil consists of hydrocarbon chains which provide the starting point for the properties of the oil and can be made either directly from crude oil or synthetic hydrocarbons. There are variations in the composition of hydrocarbons in base oils but the major variations in automotive lubrications arise from the additives. There is a range of additives added to base oils with the most common additives and their functions shown in Table 2.2.

Table 2.2: Lubricant additives.

Additive	**Function**	**Example**
Dispersants	To hold debris in suspension	Alkaline-earth soaps
Detergents	Aids removing dirt and deposits from component surfaces	Calcium / Sulfonic acid
Overbase additives	Neutralises acidic combustion products	Modified alkaline-earth soaps
Anitwear and Anticorrosion additives	Adsorb onto the surface to prevent surface damage	Zinc dialkyl-dithio- -phosphates / ZDTPs
Viscosity Index improvers	Reduces change in viscosity with temperature	Polymethacrylate esters
Antioxidants	Prevents surface oxidisation	Aromatic amines

2.7 Viscosity

Viscosity is defined as a fluid's resistance to deformation by a shear stress and can be described as either a dynamic or kinematic viscosity. The dynamic viscosity is defined in Equation 2.6, this equation is based on two infinitely long parallel plates separated by a fluid film. The force required, F, to shear a fluid is proportional to the wetted area, A, the fluid velocity, u and separation of the plates, h. The proportional factor linking these parameters together is the dynamic viscosity, η, and is measured in Pascal-Second, $Pa.s$.

$$\eta = \frac{F/A}{u/h} \tag{2.6}$$

The viscosity of a fluid is highly dependent on the temperature of the fluid, in some cases, the viscosity of an oil falls by 80% with a temperature increase of only $25°C$. Throughout engine operation (cold start to full load) the oil temperature may vary by over $100°C$, leading to significant changes in the oil properties. Therefore, knowledge of the oil properties over this whole range is required for efficient operation. Viscosity also varies with the pressure of the fluid, with an increased pressure leading to a rise in viscosity. This effect can be described by the Barus Equation (Equation 2.7) in which η_p and η_0 is the viscosity and pressure and atmospheric respectively. α_η, is the pressure-viscosity coefficient and p, is the pressure. This equation is often applied to contacts in the elast-hydrodynamic regime. Additional factors such as fuel dilution in the engine lubricant and water content (significantly higher during cold start) may have a significant impact on the oil viscosity.

$$\eta_p = \eta_0 e^{\alpha_\eta p} \tag{2.7}$$

The selection and quantity of the lubricating oil is key to engine operation. An oil of low viscosity requires less energy to shear, this causes less heat generation but the oil has a lower load-carrying capacity, increasing friction. Conversely, a high viscosity oil can support greater loads and reduces wear but requires a greater force to shear, limiting the efficiency. Overall, a greater viscosity decreases the likelihood of boundary lubrication but with increased shear losses [19, 21]. Automotive oil viscosity is categorised by the SAE J300 standard [22] which separates oils based on their shear rate viscosity and low-temperature viscosity. The engine oils defined in this standard are shown in Table 2.7.

Table 2.3: Standard engine oils as outlined in the J300, 2021 [22].

SAE Viscosity Grade	**Low Temperature** $(°C)$ **Cranking Viscosity** $(mPas)$	**Low Temperature** $(°C)$ **Pumping Viscosity** $(mPas)$	**Low Shear Rate Kinematic Viscosity** (mm^2/s) **at 100**$°C$	**Low Shear Rate Kinematic Viscosity** (mm^2/s) **at 100**$°C$ **Max**	**High Shear Rate Viscosity** $(mPas)$ **at 150**$°C$ **Min**
0W	6200 at -35$°C$	60000 at -40$°C$	3.8	-	-
5W	6600 at -30$°C$	60000 at -35$°C$	3.8	-	-
10W	7000 at -25$°C$	60000 at -30$°C$	4.1	-	-
15W	7000 at -20$°C$	60000 at -25$°C$	5.6	-	-
20W	9500 at -15$°C$	60000 at -20$°C$	5.6	-	-
25W	13000 at -10$°C$	60000 at -15$°C$	9.3	-	-
8	-	-	4.0	<6.1	1.7
12	-	-	5.0	<7.1	2.0
16	-	-	6.1	<8.2	2.3
20	-	-	6.9	<9.3	2.6
30	-	-	9.3	<12.5	2.9
40	-	-	12.5	<16.3	3.5
40	-	-	12.5	<16.3	3.7
50	-	-	16.3	<21.9	3.7
60	-	-	21.9	<26.1	3.7

Table 2.7 consists of two types of oil grades, multigrade and monograde oils. Multigrade oils contain 'W' (typically denotes "winter") following the numerical value, these oils are desirable for their cold start properties. For example, SAE 0W30 is a multigrade oil whereas SAE 30 is a monograde oil.

The SAE J300 [22] standard is revised sporadically every few years with the latest being April 2021. The later J300 standards have seen additional monograde oils added that operate with more desirable properties over a greater range of temperatures. The variation in dynamic viscosity for a selection of these oils is shown in Figure 2.16. In the engines covered in this work the AJ200 uses Castrol GTX 0W-20 [23], whilst the RTX-6 used a standard marine engine oil and YTRC2110D used CF-4 15W40.

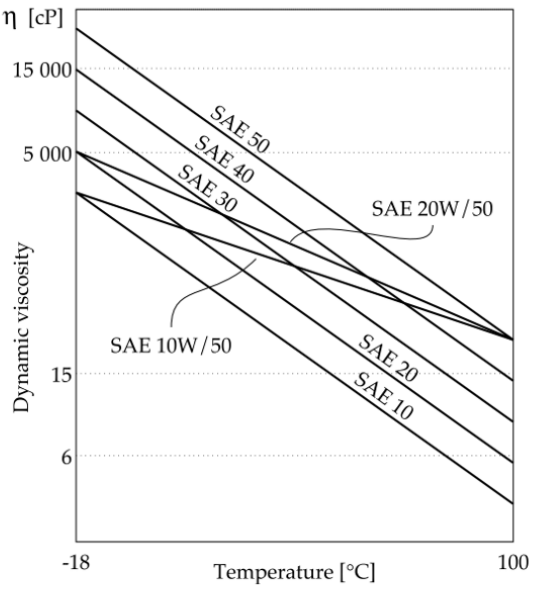

Figure 2.16: Viscosity temperature graph for monograde and multigrade engine oils reproduced from [24].

The requirements of diesel marine engine lubricants are largely the same as in automotive engines as the oil provides the same function. The current focus of the marine sector is a reduction in sulphur content in both the fuel oil and lubricant used to 0.5% [25] from the start of 2020.

2.8 Lubrication regimes

2.8.1 Stribeck curve

The Stribeck Curve provides a measure of a systems coefficient of friction depending on the parameters of the system (such as viscosity, surface sliding velocity and load on the contact). A Stribeck Curve is shown in Figure 2.17 with the addition of the regions applicable to various automotive contacts. There are three regions of this curve each corresponding to a different type of interaction; surface contact, a mix of asperities touching and pockets of lubricant and an excessively thick oil film. Each case leads to a different lubrication regime named; boundary, mixed and hydrodynamic lubrication respectively. These regions can be characterised by their friction coefficient as shown in the Stribeck Curve.

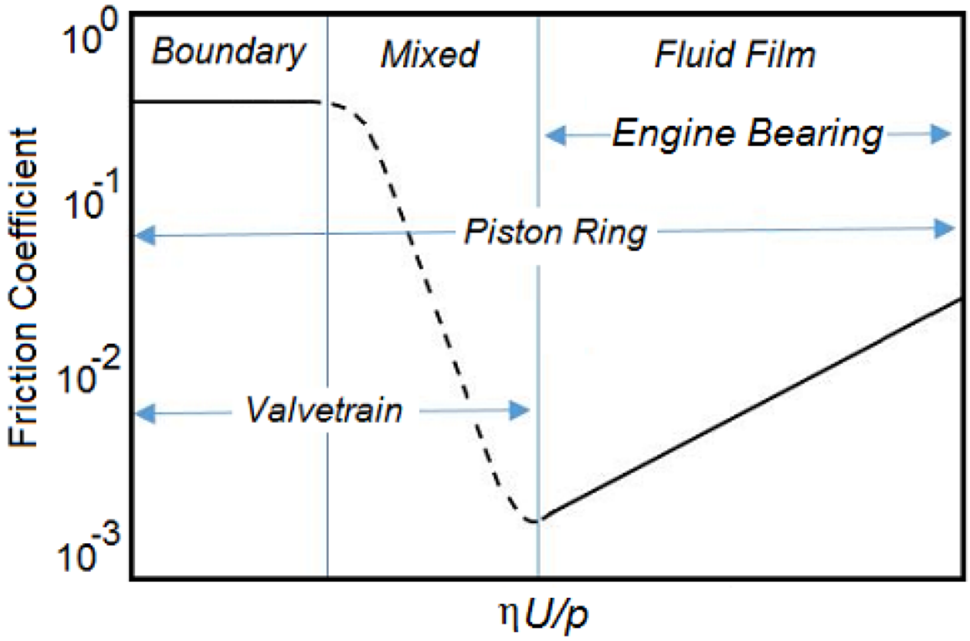

Figure 2.17: The Stribeck Curve reproduced from [26].

The boundary lubrication regime has the greatest friction coefficient. This is because a lubricating layer is not formed and the surface asperities are in contact. The load is transmitted by the solid asperities instead of a lubricating layer. This is therefore, linked to the cold start conditions of engines as this occurs before a fully formed lubricating film has been able to form and is the time in which the greatest wear occurs.

The next regime is mixed lubrication, a combination of boundary lubrication and hydrodynamic lubrication. In this region, there is partial contact between asperities and pockets of a lubricant film partially separates the two surfaces. Thus, greatly reducing the friction coefficient as the load is supported by both the asperities and the lubricant.

The final zone of the Stribeck Curve is the hydrodynamic lubrication region in which a complete oil film is formed between the two surfaces and the asperities are not in contact. The friction coefficient increases in this region due to excessive shearing of the lubricating oil.

The lambda ratio (λ_r) is the ratio of the lubricant film thickness, h, to the composite surface roughness, σ. This ratio, as seen in Equation 2.8, can be used to suggest which region of the Stribeck Curve a contact operating in. According to [27], boundary lubrication is defined by $\lambda_r < 1$, mixed by $1 < \lambda_r < 5$ and hydrodynamic by $5 < \lambda_r$.

$$\lambda_r = \frac{h}{\sigma} = \frac{h}{\sqrt{Ra_1^2 + Ra_2^2}} \tag{2.8}$$

2.9 Piston ring and liner lubrication

Most piston rings covered in this work have a barrel profile, leading to the contact between the ring and liner being that of a flat and a converging-diverging section. A lubricated piston ring and pressure profile is shown in Figure 2.18. This ring is a buffer between higher (combustion chamber) and lower (crankcase) pressure regions so there is a complex pressure profile across the contact.

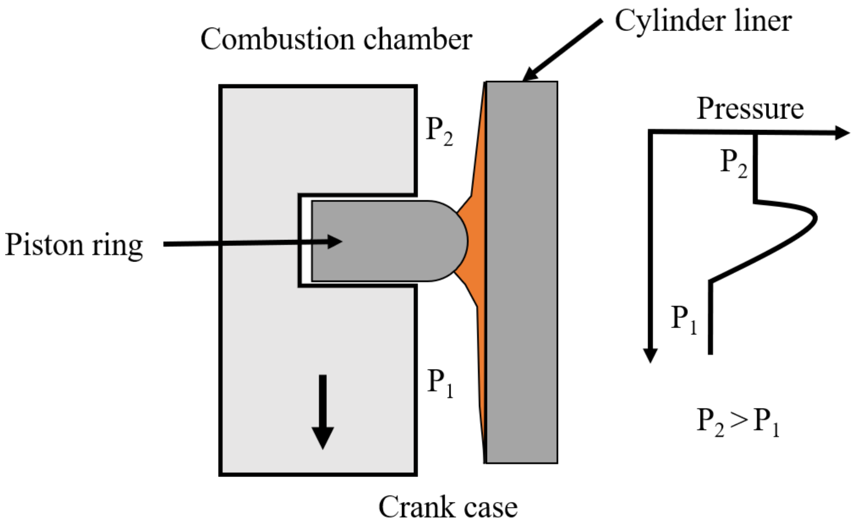

Figure 2.18: Piston ring pressure profile.

The high relative velocity mid-stroke between the piston ring and cylinder liner entrains oil between the two generating a hydrodynamic pressure that maintains separation of the two. Although through the course of each engine stroke the piston velocity varies, with low ring velocity regions at the start and end of each stroke and an instant of zero velocity at the TDC and BDC. A lack of relative velocity between the two leads to there being no ability to form a fluid pressure that can support the ring tension forcing the ring outwards. At this point, the lubricant is forced out of the contact leading to the breakdown of the hydrodynamic regime, changing to either mixed or boundary lubrication. In both mixed and boundary, there are asperities in contact between the two media leading to greater friction and wear of both components. The lubricating film also varies depending on the engine stroke with the power stroke having an elevated combustion chamber pressure, this causes the lubricant film between the ring and liner to be thinner during this stroke than others.

The greatest frictional regime is that of boundary lubrication, this has led to most previous piston ring lubricant film thickness works studying the film at or close to the TDC [28, 29, 30, 31, 32, 33, 34, 35, 36]. It is believed that boundary lubrication only occurs near the ends of strokes, due to the lower piston velocities although this may not be the case.

The amount of lubricant present has a major impact on the formation of the lubricant film. A combination of factors affects the quantity of lubricant present: the oil control ring directs excess oil on the liner down to the oil sump and the lubricant to form an oil film on an up-stroke is that which was left by the previous down-stroke. This causes oil rings to often operate under starved conditions [37].

Cavitation can occur in the lubricant at or around contact points between the ring and liner. This may occur if the lubricant pressure is below saturated pressure as it passes through the ring-liner contact which can initiate a phase change process producing lubricant vapour. In addition, cavitation can occur when dissolved gases are released from the lubricant after a reduction in pressure [38]. Cavitation is aimed to be avoided where possible as the process can damage components exposed to it.

2.10 Oil film thickness measurement techniques

In recent years numerous techniques have been developed to study the oil film thickness (OFT) of a lubricated contact, with many of those applicable to the interaction between piston/piston rings and cylinder liners. In the following section, the techniques for quantifying the oil film thickness between pistons and cylinder liners have been evaluated and reviewed.

2.10.1 Capacitance

Capacitance probes are based upon the principle, that when two electrodes of different electric potentials are separated by an insulator, a charge is stored on the surface of both electrodes which forms a capacitance. The capacitance, C, between two plates follows Equation 2.9.

$$C = \frac{K_{dc}\varepsilon A}{d} \tag{2.9}$$

In which ε, is the permittivity of free space, A, is the area of the plates, d, is the separation between the ring and liner and K_{dc}, is the dielectric constant. A capacitance can be formed between a piston ring and an electrode that is mounted flush with the liner. This has been achieve in numerous works [35, 36, 39, 40, 41, 42, 43] a schematic is shown in Figure 2.19. This technique has provided film thicknesses ranging from 0.2 to 9 μm. Although the methodology is prone to breakdown from excessively thin films (< 1 μm) as shorting of the circuit may occur (metal-metal contact).

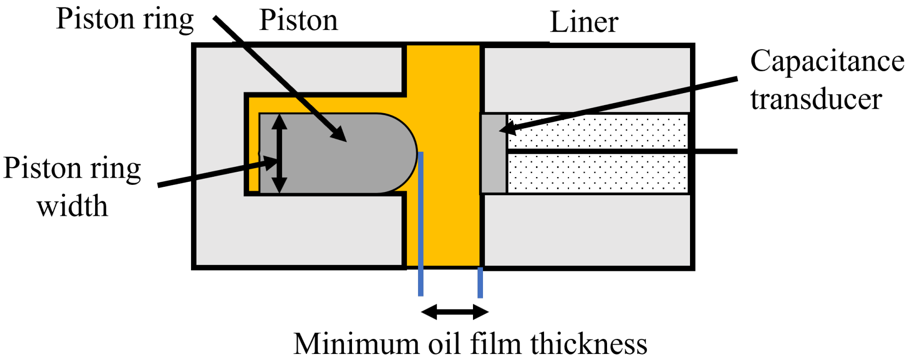

Figure 2.19: Schematic of capacitance probes mounted flush in the liner.

A key assumption with this method is that the region between the two plates is fully flooded with oil, if there is any cavitation then the dielectric constant of the intermediate region (lubricant in this case) varies. This can affect the calculated value of the oil film thickness by up to a factor of two [44]. This assumption causes the technique to often not be suitable for the oil film thickness over the whole ring but for the point of minimum film thickness (in which it can be assumed fully flooded at this point). The presence of metallic wear particles in the lubricant also has an impact on the recorded capacitance. Another limitation of this technique is the size of the capacitance probes. The probes are often several millimetres wide, significantly wider than piston rings (ring width defined in Figure 2.19) that are typically less than 1 mm in automotive engines, this therefore, may provide a poor spatial resolution.

To form the capacitor, it requires the transducer to be mounted flush with the inner surface of the liner by honing the liner post sensor installation. The electrode material often has a greater wear rate than that of cast iron liners, therefore, the electrode is worn away through the course of testing affecting the calibration of the probe as the separation distance increases over time. The value for the dielectric constant also varies with temperature so this approach is only suitable for steady-state testing. Although capacitance probes themselves are seen to have good thermal stability and robustness.

A noteworthy instrumentation was performed by Takiguchi et al. [39] on a six-cylinder diesel engine. Capacitance transducers were instrumented behind the first compression ring (barrel-faced) and the scraper ring (napier tapered). The fired testing at a range of engine speeds (1200-2400 rpm) measured oil films ranging from 1.5-9 μm over the full stroke of the piston. Their results showed minimal cyclic variation with the film thickness increasing with greater engine speed. The novelty arose from the instrumentation behind the piston rings, greatly increasing the complexity of routing the cables out of the engine.

A more standard capacitance instrumentation is shown in Dhar et al. [36] in which transducers were instrumented flush on the internal surface of the liner in an adapted motored diesel CVR-5 at 1400 rpm. The testing provided oil films ranging from 0.2-8 μm with their being relatively small differences between the up and down strokes of the engine, thought to be due to the motored operation of the engine. The work is expanded on in [35] studying the same single-cylinder engine at the TDC, mid-stroke and BDC to provide a greater picture of the oil film through the stroke.

Capacitance transducers have also been implemented for in-situ measurements of oil deterioration such as to indicate oil viscosity in [45, 46] or to show when an oil change was required in [47]. For an in-depth study into the design of capacitance probes, the reader is recommended to read Ducu et al. [40].

2.10.2 Laser induced fluorescence

Laser induced fluorescence (LIF) is the most common type of optical measurement technique used for measuring oil film thickness between piston rings and cylinder liners. Other optical techniques include replacing the liner with Perspex glass, glass or using ultraviolet fluorescence. The LIF approach uses the natural fluorescence of an oil, or has an additive to enable such measurements. A wavelength of light (typically blue lasers of wavelength $400-500$ *nm*) is shone on the oil film which excites specific bonds on the fluorescent components causing electrons to move to a higher energy state. Upon their return to their original state, radiation of a smaller wavelength is emitted. The emitted light is filtered and processed to quantify the oil film thickness. The technique is calibrated by performing measurements on a series of known gap sizes and applying a scaling function to the measurement signals. A schematic of the LIF system is shown in Figure 2.20.

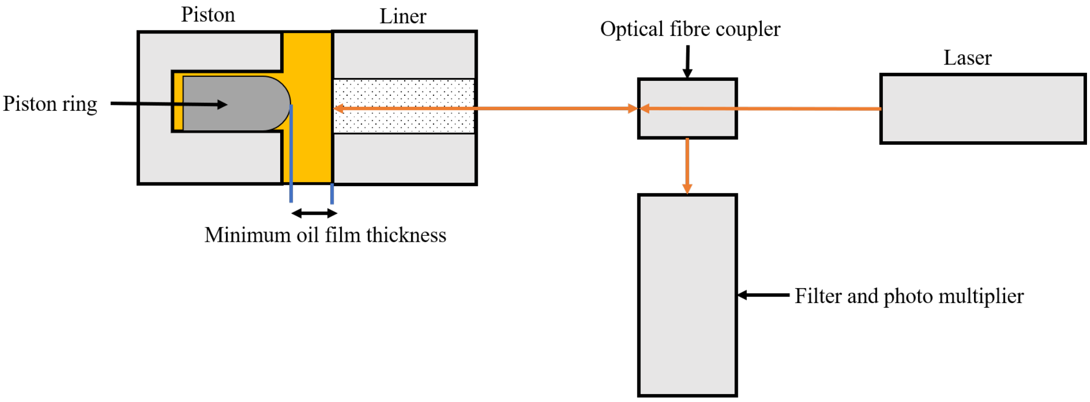

Figure 2.20: Schematic of laser induced fluorescence with optical path through to the oil film.

The technique originates from Ting [48] and has led to numerous works capable of measuring oil films ranging between 0.4 μm to 24 μm [33, 34, 49, 50, 51] for the first piston ring. A key advantage of this technique is the spatial resolution, with it being an order of magnitude less than the width of piston rings. This technique can be used for measurements over the full stroke of the piston as it does not require the piston to be aligned with the laser to record meaningful results. This can, therefore, be used to show the oil film retained by the liner and the bow wave of oil ahead of the piston. This overcomes a limitation of the capacitance technique as data can be recorded during the whole piston stroke. LIF is also not limited to oil film thickness measurements in [52, 53] the degradation state of the oil was studied using this technology.

In [50] LIF was applied to a single-cylinder Ricardo Hydra gasoline engine to study the ring pack film thickness at a series of degradation states of the oil. Three states of oil were tested in motored and fired conditions at a range of engine speeds (1000-4000 rpm). It was shown that as the lubricant degrades, it leads to thicker oil films for the complete ring pack. The minimum oil film thickness for the first compression ring using fresh oil ranged from 0.5-10.5 μm whilst degraded oil under the same conditions ranged from 0.5-24 μm. The work found a greater lubricant throw-oil and engine emissions were associated with degraded oil.

LIF was applied at four locations down the liner in [34] on the thrust side of a single-cylinder diesel engine at 1500 and 2000 rpm, 75% load. The piston had three piston rings (barrel-faced, napier and two-piece control ring), in the testing three different types of oil control rings were used. A reduction in engine load was found to produce negligible differences in the control ring oil film thickness. However, as LIF is capable of measuring residual oil film levels, this load reduction showed a significant increase in residual oil levels with a reduction in engine load and thus provided a greater amount of lubricant available for the compression ring.

The oil distribution and film thickness has been studied at a range of starvation conditions in [54] using a tribometer. The work used LIF and was capable of measuring film thicknesses down to 0.05 μm. This indicates the sensitivity of the method although it is not necessarily applicable to engine testing as plateau honed grooves on a cylinder liner may be up to two orders of magnitude greater than this.

There are unavoidable drawbacks related to LIF, as the technique is hindered by the visible light produced from the combustion process. Along with the requirement of a pathway for the laser to enter the oil film producing discontinuities on the internal surface of the liner and changing the one of the boundaries of the lubricating film. There is also an extensive calibration and data processing requirement. The build up of wear particles or combustion products in the oil film will also affect the lubricants fluorescence thus limiting the applicability of the calibration.

2.10.3 Inductance

The inductance approach is based upon the electromagnetic coupling between a wire coil and a target material. The wire is exposed to a high-frequency alternating current, this creates an oscillating magnetic field in neighbouring conductive material. The eddy current formed generates an electromagnetic field, the strength of which depends on the separation between the two. The spatial resolution of this approach makes it is more commonly used for piston skirt clearance measurements or piston secondary motion than for oil film thickness measurements.

Inductance has been applied in several ways to measure piston ring film thickness. In [55] a motored test rig was developed and an inductance probe was mounted in the end of a piston ring to measure the ring gap. A schematic of this instrumentation is shown in Figure 2.21. The size of the gap was then used to infer an average film thickness around the circumference of the liner. The test rig ran up to 1000 rpm providing films ranging from 2-8 μm.

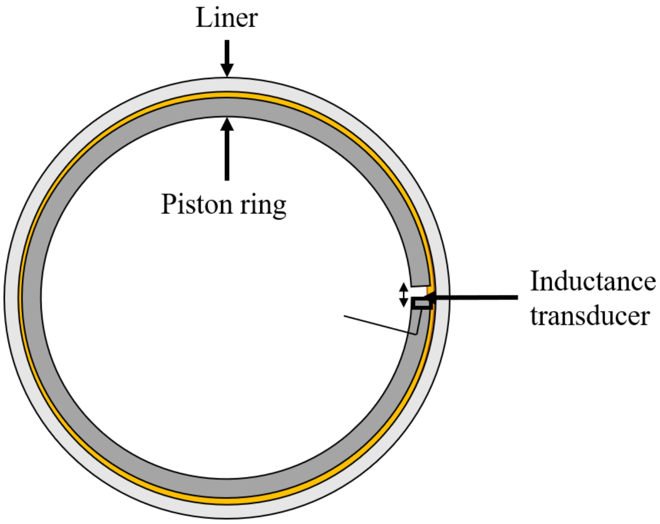

Figure 2.21: Schematic of the inductance approach to measure the ring gap.

In [56] four eddy current sensors covering the TDC, the BDC on the thrust/anti-thrust side were tested. The engine was a six-cylinder diesel engine fired at 900 rpm. The results for the first compression ring show the film thickness to increase with engine load for each engine stroke with either the compression or expansion stroke providing the thickest films. Whilst the thinnest film was during the exhaust stroke when a large quantity of the oil that remained on the liner was thought to have evaporated or been expelled into the combustion chamber. The oil film thickness values provided were all relative to the thinnest point instead of the absolute value of film thickness.

In [51] eddy current transducers were mounted in the top and bottom of the piston skirt in a single-cylinder CAT 1Y73 diesel engine. These sensors were used to study piston tilt and clearance of the piston skirt. The tilt of the piston peaked at 200 μm at the start of the power stroke and varied significantly in each engine stroke, see Figure 2.22.

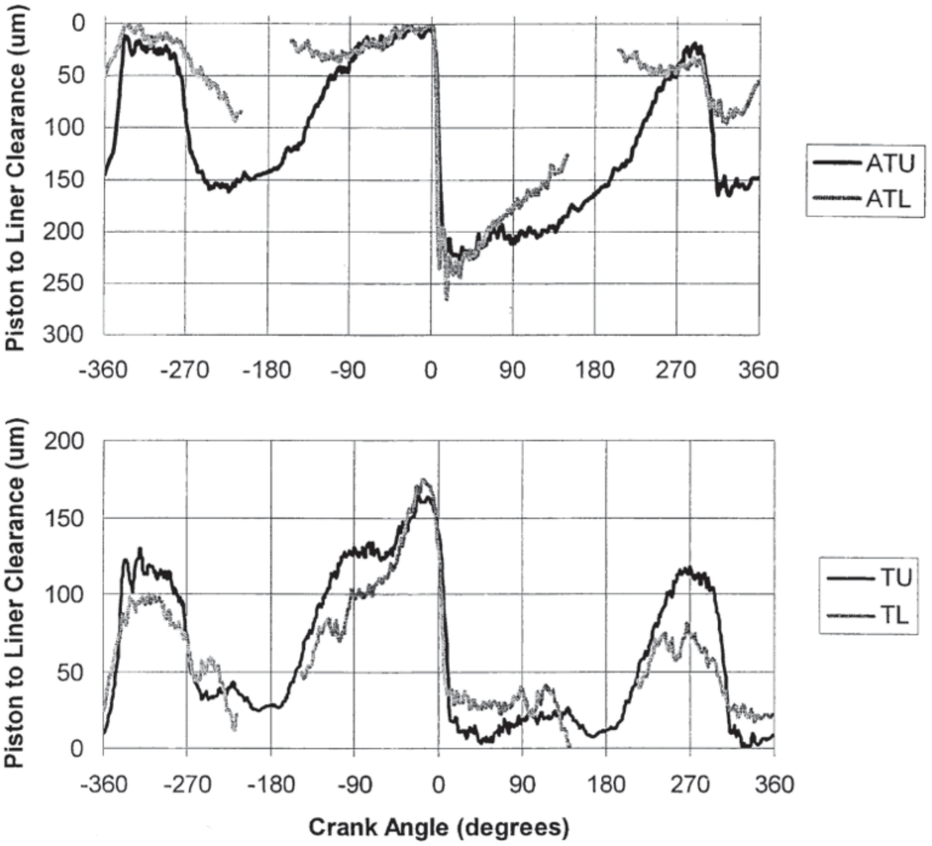

Figure 2.22: Piston clearance reproduced from [51] ATU/ATL refers to anti-thrust upper/lower respectively and TU/TL is thrust upper/lower respectively.

There are evidently many routes to apply the inductance method each with varying levels of complexity to study lubricant film thickness. Inductance has even been used to study bore distortion from either the liner or piston side in [57, 58, 59, 60, 61]. An overall summary of inductance can be stated as having extensive data processing requirements and the presence of ferromagnetic material add to the difficulty by its impact on the magnetic field. The transducers themselves are also prone to a non-linear response and are difficult to calibrate as temperature drift has a large impact on the measurements.

2.10.4 Resistance

Provided that the ring and liner are conductive, they can form part of an electric circuit. The circuit utilises the dielectric nature of the engine oil to deduce the lubricant film thickness. By measuring the resistance across the oil film its magnitude can be correlated to lubricant film thickness. If the ring and liner are in close proximity there is greater asperity contact causing greater conductivity, versus the opposite trend for a sufficiently thick lubricant film. A schematic of this method is shown in Figure 2.23.

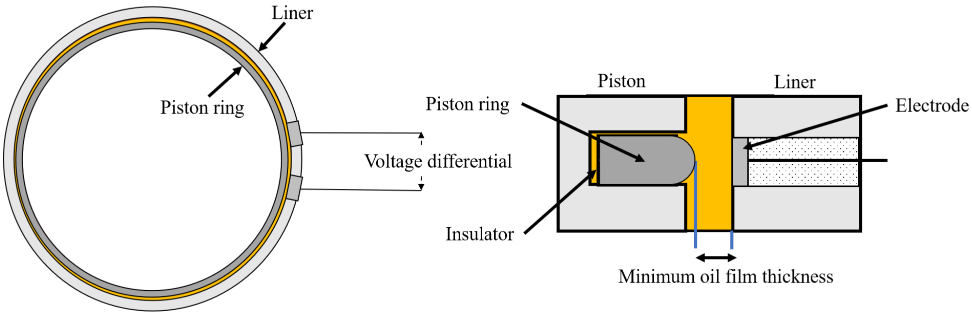

Figure 2.23: Schematic of the resistance technique that has two electrodes mounted flush in the liner.

The resistance approach is another invasive technique that has electrodes mounted flush with the inner surface of the liner. In [62] a single-cylinder AVL diesel engine was modified with two insulated grooves down the liner surface to enable 5 pairs of electrodes covering the TDC to the BDC. The fired testing covered a range of loads and engine speeds up to 2200 rpm. The thickest films were found mid-stroke when the piston velocity was greatest aiding to form a hydrodynamic film although the instrumentation was only able to provide a single discrete measurement from a ring passage.

The resistance method requires a high degree of modification to the engine to electrically isolate the piston rings which is difficult to achieve over the complete stroke to avoid shorting the circuit. The state of the oil also limits the technique as the presence of third body particles from either component wear or soot can have an impact on the conductivity of the oil film, affecting the measured lubricant film thickness.

2.10.5 Strain gauge

A less explored route to quantify the oil film thickness is to use a strain gauge mounted behind the rings, as shown in Figure 2.24. The oil film thickness is determined by the difference in the strain values from running the piston in lubricated and unlubricated conditions. Although the use of strain gauges in this way is only suitable for unfired testing. In [63] a motored single-cylinder engine was spun up to 1500 rpm to provide oil film thickness measurements up to 5 μm. A series of bore diameter measurements were required to offset any cylindricity in the bore to remove its impact on the film thickness. The requirement of a reference bore measurement at each location and temperature studied provides a practical flaw in this method due to the quantity of calibration needed.

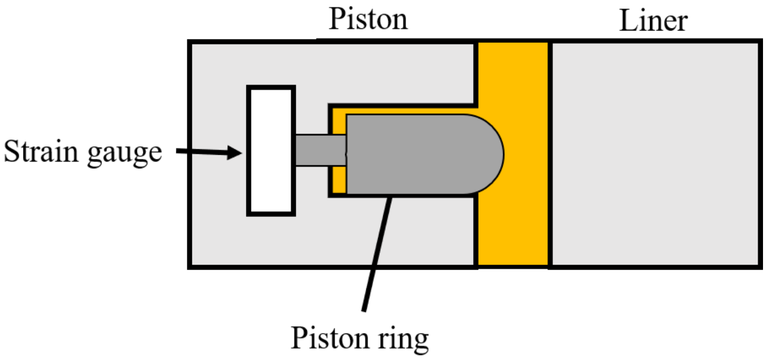

Figure 2.24: Schematic of a strain gauge mounted in the piston to monitor ring deflection.

2.10.6 Ultrasound

A final approach is to use ultrasonic transducers placed on the outside of the cylinder liner to pulse sound waves through the liner to quantify the oil film, shown schematically in Figure 2.25. This has a key advantage over the previously mentioned routes as this is non-invasive and can provide results in real-time.

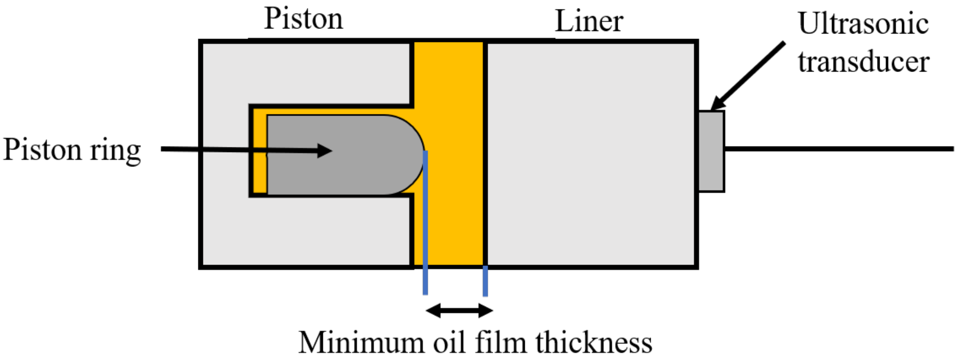

Figure 2.25: Schematic of an ultrasonic transducer mounted on the outer surface of the liner.

In [28] a single-cylinder engine was ran under motored and fired conditions at a series of speeds (850, 1800 and 6000 rpm). A 7 mm diameter transducer was instrumented onto the external surface of the liner to quantity the piston skirt film thickness. The motored tests provided a film thickness ranging from 9-21 μm whilst the fired tests gave measurements down to 2 μm.

The method has since been developed in [32] in which motored tests were performed on a four-cylinder Perkins 1100 series engine at 600, 720 and 840 rpm. An increased sensitivity enabled the method to detect piston ring passage over the transducer with the film thickness ranging from 5-10 μm from a single transducer on the neutral side of an end cylinder. A non-permanently bonded sensor was used on this engine which enabled one sensor to study the piston rings at a series of locations.

Ultrasonic transducers have also been applied to fired engines, in [30, 64] a single-cylinder Briggs and Stratton Quantum engine was used and in [29, 31, 64, 65] a single-cylinder Honda CRF450R. The single-cylinder engines enabled complex instrumentation of a series of ultrasonic transducers on the thrust, anti-thrust and neutral sides of the engine, as shown in Figure 2.26. The instrumentation used transducers with a width of 1 mm, a similar size to the width of the first compression ring in the engine. The reduction in transducer size provided an increased resolution on the film thickness measurements for both the piston skirt and rings. Ultrasonic transducers provide an average measurement over the complete sensing surface, therefore, the measurements in this engine will have a closer representation to the true film thickness than those in [32] where an overestimation of the film thickness will have been measured. This is shown in the film thickness measurements in the Briggs and Stratton Quantum and Honda CRF450R engines with oil films as thin as 0.5 μm. An interesting result was found in [31] where the applied model indicated oil films of -0.1 μm in the early stages of the power stroke, this implies the ring has penetrated the liner which is obviously not practically possible. In the method applied it was assumed that a fully formed hydrodynamic film was maintained for the whole piston stroke inferring no asperity contact. This negative film thickness, therefore, suggests potential asperity contact between the ring and liner and that the Spring Model may no longer be appropriate for that sensor as the model is for a solid-oil-solid system.

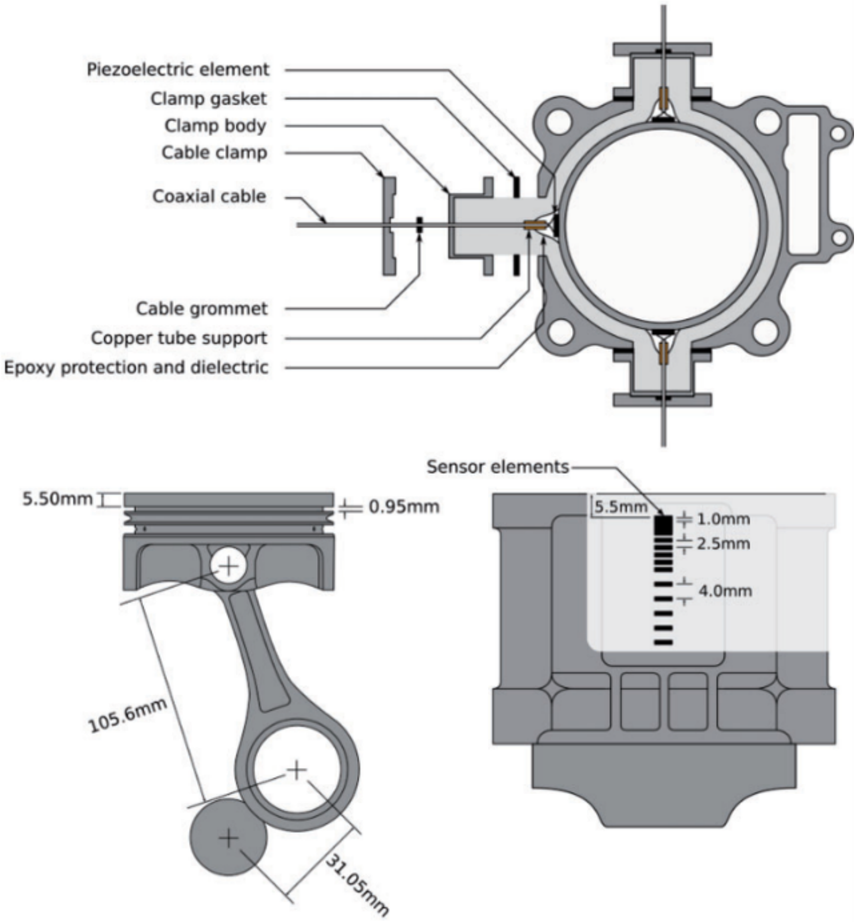

Figure 2.26: Ultrasonic instrumentation on a Honda CRF450R reproduced from [31].

2.10.7 Method comparison

In review of the previous sections on alternative routes to quantify piston ring film thickness, the measured oil films from the articles reviewed (including other key factors from the testing such as the engine rpm, whether the test was motored or fired) are summarised in Table 2.4. The ultrasonic measurement articles are highlighted in red. Similarly, the relative advantages and disadvantages of each technique is detailed in Table 2.5.

Table 2.4: Summary of the outlined techniques to measure oil film thickness for ring-liner contacts. The ultrasonic measurement articles are highlighted in red. *film thickness relative to thinnest point.

Method	**Oil Film Thickness (μm)**	**Engine Speed (rpm)**	**Diesel / Gasoline**	**Motored / Fired**	**Reference**
Capacitance	0.2 - 8	1300-1400	Diesel	M	[35]
	0.2 - 8	1400	Diesel	M	[36]
	1.5 - 9	1600-2800	Diesel	F	[39]
	2 - 4	1300	Diesel	F	[40]
	5 - 25	2000 & 3000	Gasoline	F	[42]
	5 - 23	2000	Diesel	F	[43]
Inductance	1.4 - 5	1000	Diesel	F	[51]
	1 - 8	200-800	Diesel	M	[55]
	up to 10*	900	Diesel	F	[56]
LIF	0.6 - 3.5	1000-2000	Diesel	F	[33]
	0.4 - 5	1500 & 2000	Diesel	F	[34]
	5 - 18	1200	Gasoline	M	[49]
	2 - 24	1000-4000	Gasoline	F	[50]
	1.5 - 15	1000-1800	Diesel	F	[51]
Resistance	0.5 - 15	1400 & 2200	Diesel	F	[62]
Strain Gauge	Up to 5	500	Diesel	M	[63]
Ultrasound	2 - 21	850-6000	-	M + F	[28]
	3 - 15	4000	Gasoline	M + F	[29]
	3.2 - >15	2230	Gasoline	F	[30]
	0.5 - 15	3200	Diesel	F	[31]
	5 - 10	600-840	Diesel	M	[32]
	2.3 - 17	3200	Gasoline	F	[65]
	6 - 22	114	Diesel	F	[66]

Table 2.5: A summary of the advantages and disadvantages of the various piston ring oil film thickness techniques.

Method	**Advantages**	**Disadvantages**
Capacitance	• Can perform complex instrumentation • Can study oil deterioration • Sensors can be instrumented at a range of locations	• Metallic wear particles affects the oils capacitance • Assumes liner is fully flooded Temperature affects dielectric constant • Spatial resolution issues • Invasive
Inductance	• Can study bore distortion • Can study piston secondary tilt • A number of potential instrumentation routes	• Extensive data process requirements • Difficult to calibrate and sensors are prone to non-linear response • Presence of ferromagnetic material affects sensor response • Invasive
LIF	• Can study residual oil films and bow waves of oil • Good spatial resolution • Can study oil deterioration	• Hindered by radiation produced from combustion process • Invasive • Extensive data processing requirements • Built up of wear particles/combustion products in the oil affects the lubricants fluorescence • Extensive data process requirements
Resistance		• Difficult to insulate sensors to avoid shorting the circuit • Invasive • Wear particles/soot impacts the lubricants conductivity
Strain gauge		• Only suitable for motored testing • Extensive referencing requirements • Invasive

Method	**Advantages**	**Disadvantages**
Ultrasound	• Non-invasive • Can provide results in real time • Relative simple data processing and calibration requirements • Can instrument complex sensor arrays	• Spatial resolution issues • Assumes region is fully flooded with lubricant • Provides an average measurement over complete sensing area

Study of Table 2.4 displays that there are numerous techniques available to measure the oil films formed between piston rings and liners in motored and fired engines each of which find a similar film thickness at a range of engine speeds. Arguably, the key difference in the methods (Table 2.5) is the amount of modification to the engine required, with most techniques requiring transducers to be mounted flush with the inner surface of the liner. The invasive nature of this undoubtedly affects the oil films formed. The literature survey performed shows ultrasound to be the clear approach to monitor the contact due to its non-invasive capabilities enabling the closest representation of the real-world lubricant film. Combined with the robust nature of piezoelectric transducers this allows the potential for motored and fired testing. From the reviewed literature ultrasound has been selected as the route for further analysis into all areas required for this work and is the technique discussed from this point.

2.11 Conclusions

Internal combustion engines are a prime example of engineering achievement in which each aspect of the engine is under constant review for minuscule refinements of its operation. This chapter has provided a brief introduction to ICEs and the research into piston ring oil film thickness measurements. The main points from this chapter are summarised as follows:

- The piston assembly is a moving wall of the combustion chamber that is subject to a complex velocity trace that leads to the piston rings moving through all regimes of the Stribeck curve in each engine stroke.

- The lubricant film thickness between the piston rings and cylinder liner has been measured using a series of techniques, each with relative merits and flaws. The most common methodologies are based around capacitance, LIF and ultrasound.
- The most distinguishable difference in capacitance, LIF and ultrasound is the level of modification required to the engine to perform the testing. Both capacitance and LIF require replacing a portion of the liner with either a transducer or optical window whilst for the ultrasonic method, transducers are positioned on the external surface of the liner. In addition, the ultrasonic method arguably requires less calibration and data processing than the two other approaches.

Chapter 3

Ultrasound

The third chapter begins with the definition of ultrasound and leads the reader through to methodologies applied in the field of tribology to study the thickness of lubricant films. This chapter also introduces piezoelectric transducers used to pulse and receive the ultrasonic signals and previously developed test rigs to study the piston ring oil film thickness.

3.1 Definition

Sound waves propagate through solid, liquid and gaseous media by the elastic deformations of particles due to an initial external mechanical displacement. These sound waves are audible for humans up to 20 kHz, after which they surpass the limit of human hearing and are defined as ultrasonic.

Ultrasound is used in various fields such as; sonar systems, non-destructive testing, seismology or medical imaging. These waves even occur naturally in nature, bats and frogs use ultrasound to aid in communication and foraging for food. These applications work on the base principle that after an ultrasonic wave is emitted from a source the wave propagates through a media until a boundary is reached. Depending on the contact formed between the two media a portion of the wave is reflected and a portion is transmitted, this occurs at each boundary.

The propagation of ultrasonic waves follows the one-dimensional wave equation. In cartesian coordinates this is defined as Equation 3.1, in which u, is the wave displacement, c, the wave velocity and t, is time.

$$\frac{d^2u}{dx^2} = \frac{1}{c^2}\frac{d^2u}{dt^2} \tag{3.1}$$

Ultrasonic waves propagate through media due to a pressure being exerted on a particle and as each particle is interlinked to adjacent particles by electrostatic forces, this enables wave propagation. One possible analogy is to assume the media is a series of masses held together by springs that are not deformed beyond their elastic limit, see Figure 3.1. Therefore, the displacement of a mass and spring leads to the adjacent masses displacing accordingly. This process repeats to allow the wave to propagate through. The stiffness of the springs, therefore, dictates the rate at which the wave propagates through the body and the efficiency of the energy transfer between masses.

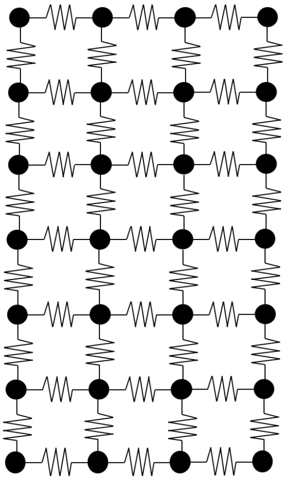

Figure 3.1: A series of particles connected via springs.

There are several modes of vibration that can be experienced in solid media. This work considers pressure and shear waves which are both plane waves meaning that the wave has a constant frequency and whose wavefront acts as a parallel wave.

3.2 Ultrasonic wave properties

3.2.1 Longitudinal and transverse waves

The propagation of longitudinal and transverse waves can be explained by the expansion of the wave equation into three dimensions, see Equation 3.2 in which x, y and z refer to three perpendicular axes.

$$c_x^2\frac{d^2u}{dx^2}+c_y^2\frac{d^2u}{dy^2}+c_z^2\frac{d^2u}{dz^2}=\frac{1}{c^2}\frac{d^2u}{dt^2} \tag{3.2}$$

Consider a wave that is propagating in the x-direction, whose particles are also oscillating in the same direction, a longitudinal/pressure wave. A cross-section of this type of propagation is shown in Figure 3.2a. This wave experiences a series of compressions (series of particle planes in close proximity) and rarefactions (series of particles planes spread apart).

Alternatively, a wave propagating in the x-direction with particles oscillating in either the y- or z-direction is termed a transverse/shear wave. A cross-section for this type of wave is shown in Figure 3.2b. This wave type produces a cross-section that has an overall sinusoidal shape. Two sub-types of transverse waves are possible, with the oscillations in either the y or z directions that are independent of each other.

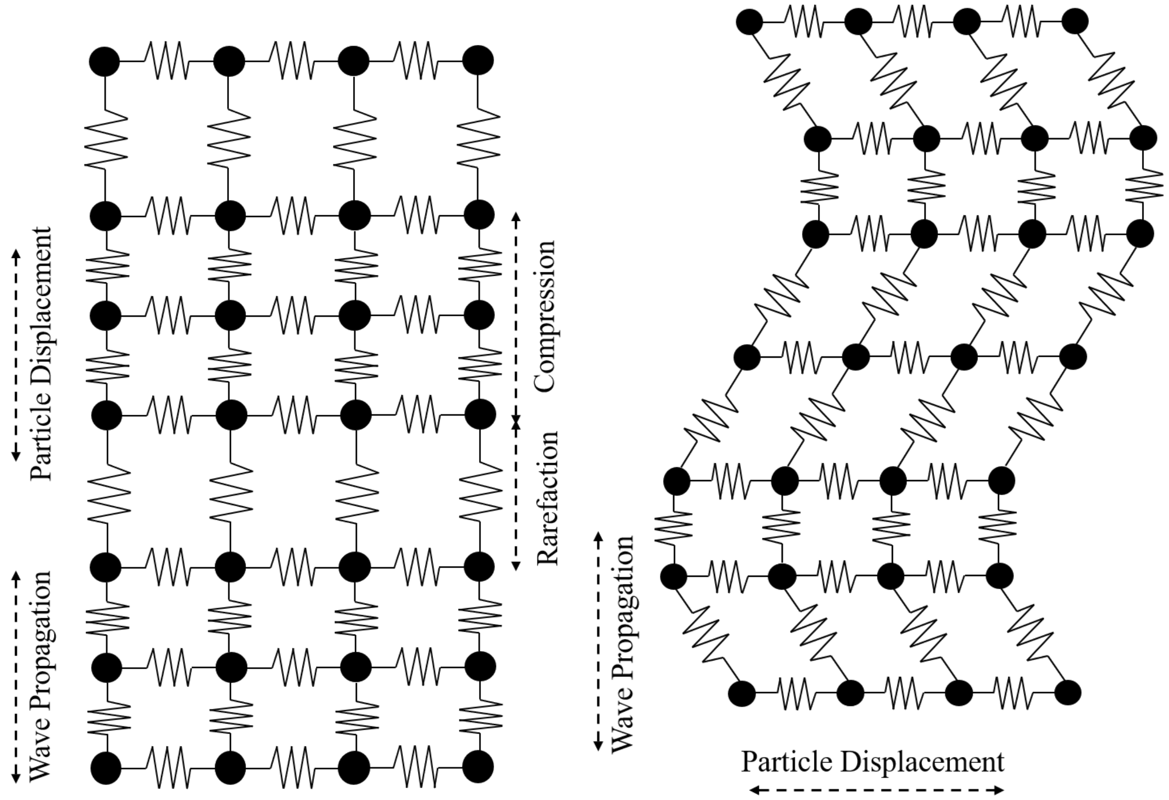

(a) Longitudinal wave propagation.

(b) Transverse wave propagation.

Figure 3.2: Wave propagation for longitudinal and transverse waves.

Both longitudinal and transverse waves can be supported in solids, however, as fluids have negligible shear strength they do not support transverse waves. For greater detail, the reader is referred to Pain [67].

3.2.2 Ultrasonic wave velocity

The rate of transmission of a wave through a media depends upon the stiffness of the interparticle bonds. In relation to the mass-spring analogy (Figure 3.1), the stiffness of the springs. A stiffer spring increases the transmission speed of the wave. It is also worth noting that the frequency of an ultrasonic wave is unchanged from that of the source (non-dispersive wave).

The wave velocity, c, or the 'speed of sound' through a media depends on the density, ρ, the elastic modulus, E of the medium and the Poisson's ratio, ν. Longitudinal and transverse waves have differing wave velocities as shown in Equations 3.3 and 3.4 in which c_l is the longitudinal wave velocity and c_s the shear wave velocity. The speed of sound through a medium is also dependent on the temperature, pressure and stress acting upon it. The temperature has a significant impact on the wave velocity, with an increase in temperature reducing the wave velocity. Whereas the pressure and stress only have a significant impact on the wave velocity when each factor is in the order of giga pascals and, therefore, a minor concern in the piston ring and cylinder liner interaction.

$$c_l = \sqrt{\frac{E}{\rho}\frac{1-\nu}{(1+\nu)(1-2\nu)}} \tag{3.3}$$

$$c_s = \sqrt{\frac{E}{\rho}\frac{1}{2(1+\nu)}} \tag{3.4}$$

The wave velocity relates to the wavelength, λ and the vibrational frequency, f, as defined in Equation 3.5.

$$c = f\lambda \tag{3.5}$$

Knowledge of the longitudinal wave velocity through a media combined with the time taken for the wave to travel from an ultrasonic pulser to an ultrasonic receiver can be used to determine the distance travelled or often the thickness of a component and is the basis for non-destructive testing (NDT). Commonly, the ultrasonic wave is pulsed and received from the same transducer, therefore, the distance travelled is twice the thickness of the component. This analysis is referred to as time-of-flight analysis in which d, is the component thickness and t, is the time of flight as shown in Equation 3.6.

$$d = \frac{ct}{2} \tag{3.6}$$

3.2.3 Acoustic impedance

The acoustic impedance, Z, is a measure of the acoustic pressure generated as a wave propagates through a media. The equation for this is shown in Equation 3.7, which displays that it is purely dependant on the density of the medium, ρ, and the wave velocity, c. An alternative definition uses P, the acoustic pressure and the longitudinal wave velocity. The acoustic impedance is commonly measured in $Pa.s/m^3$.

$$z = \rho c = \frac{P}{c} \tag{3.7}$$

The acoustic impedance also indicates how an ultrasonic wave interacts at a boundary between two media of different material by defining the proportion of energy that is transmitted and reflected at the boundary. Two materials with a similar acoustic impedance will cause less of a hindrance to the wave and, therefore, a greater amount is transmitted. Whilst for two acoustically dissimilar materials a greater portion of the wave is reflected. The acoustic impedance for a series of typical engineering materials is shown in Table 3.1.

Table 3.1: Acoustic impedance of various media [68].

Media	**Acoustic Impedance** ($MRayls$)
Steel	46.00
Aluminium	17.33
Lead	7.83
SAE 20	1.51
Water (20°C)	1.48
Acetone	1.07
Gasoline	1.00

It can be seen in Table 3.1 that the acoustic impedance of solids is much greater than those for fluids. Referring to the mass-spring analogy used to describe wave propagation (Figure 3.1), in solids the masses are more compact than those in fluids this allows smaller energy losses between individual masses and, therefore, in solids the acoustic pressure is much greater than that in fluids.

3.2.4 Attenuation

Attenuation is a measure of the rate at which the amplitude of an ultrasonic wave is lost as the wave propagates through a media. The major causes of attenuation are radiation, scattering and absorption.

- Radiation - Related to the energy density, as a wave propagates further from its source the energy distribution is reduced resulting in a reduction in amplitude. Radiation attenuation is therefore mainly concerned with beam spreading.
- Scattering - Occurs due to inhomogeneities in a media, such as foreign inclusions, gaseous pores or an anisotropic material. Any of these causes micro-variations in the acoustic impedance and acts the same as a boundary between two media leading to a portion of the ultrasonic wave being reflected at each imperfection. Scattering becomes a significant factor when the size of an imperfection/discontinuity is similar to (or greater than) the wavelength of the sound wave. This is often a significant factor in cylinder liners due to them typically being made from cast iron.
- Absorption - Absorption is concerned with particle vibration, this causes friction that converts the sound energy into thermal energy. This factor is frequency dependent, a greater frequency causes greater particle velocity which leads to more frictional heating taking place.

A combined measure of these phenomena can be quantified in Equation 3.8.

$$A_d = A_o e^{(-\alpha d)} \tag{3.8}$$

In which d is the distance from the source of the ultrasonic wavefront, α is the attenuation coefficient and A_o/A_d are the amplitudes of the wave at the origin and wavefront distance respectively. This equation can therefore be used to quantify the attenuation after any distance through a medium. The attenuation in a medium can be shown experimentally via the use of an A-scan. This is a time-domain plot that displays the magnitude of a series of ultrasonic reflections. An A-scan can be used to display attenuation if the back surface of the medium is free (air is used as it is considered a perfect reflection of the ultrasonic wave). Therefore, if there is no attenuation in a body, successive peaks would have the same amplitude. An example A-scan is shown in Figure 3.3 in which three consecutive reflections are shown, each successive reflection has a reduced amplitude due to wave attenuation.

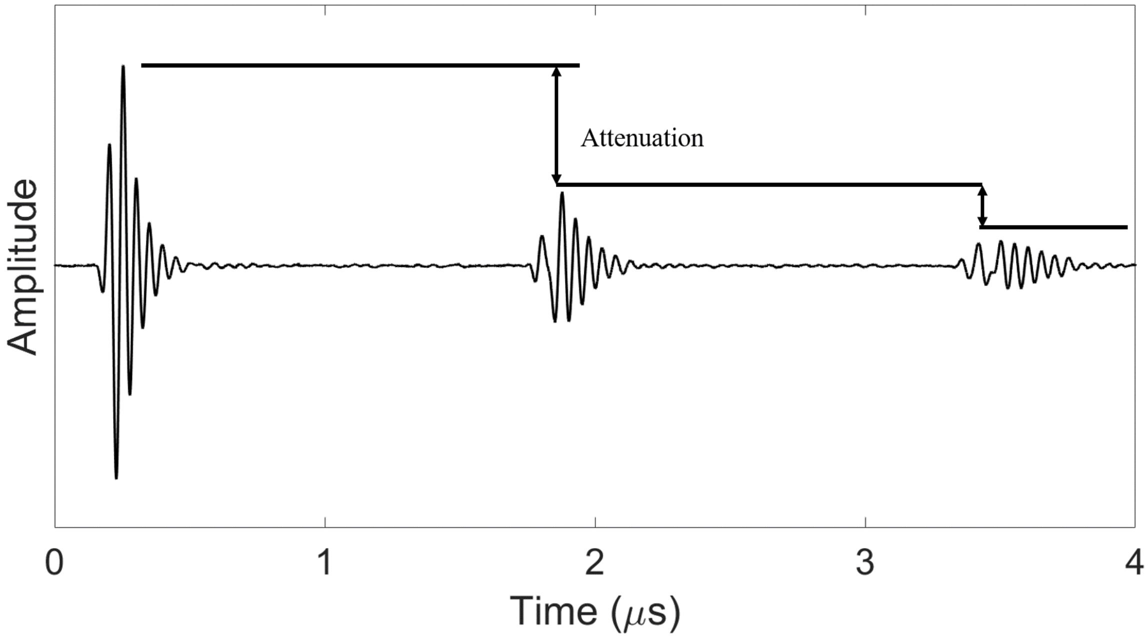

Figure 3.3: A-scan displaying multiple ultrasonic reflection from an air boundary, highlighting the attenuation in a medium.

3.2.5 Wave propagation at boundaries

The interaction that an ultrasonic wave has with a boundary depends upon the materials on either side and the contact between the two media. Under the assumption that two media are perfectly bonded (no air gaps, see Figure 3.4) when an ultrasonic wave strikes a boundary between two dissimilar materials (significantly different acoustic impedances) a portion of the wave is transmitted and a portion is reflected.

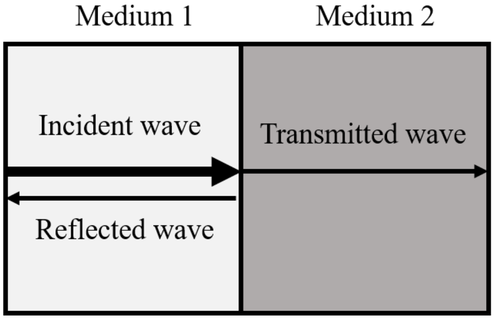

Figure 3.4: The interaction of an ultrasonic wave at a perfect solid-solid interface.

There is also continuity of the wave pressure (Equation 3.9) and wave velocity (Equation 3.10). Note the subscripts are defined as follows: i – incident, r – reflected and t – transmitted.

$$P_i = P_r + P_t \tag{3.9}$$

$$c_i = c_r + c_t \tag{3.10}$$

Manipulation of Equations 3.9 and 3.10 along with the acoustic impedance defined in Equation 3.7 produces Equation 3.11. By also applying knowledge that the wave is propagating from Medium 1 to Medium 2, therefore, the acoustic impedance of the reflected portion of the wave is in the negative direction.

$$\frac{Z_1}{Z_2} = \frac{P_i + P_r}{P_i - P_r} \tag{3.11}$$

The reflected portion of the wave can be expressed in terms of the acoustic pressure incident to the boundary compared to the reflected acoustic pressure, shown in Equation 3.12. Substituting this equation into Equation 3.11 gives an equation to quantify the amount of an ultrasonic wave that is reflected at a boundary and is termed the reflection coefficient, see Equation 3.13. This is purely dependent on the acoustic impedances of the two media. The value of the reflection coefficient varies between $-1 \leq R \leq 1$, in which $R = 0$ shows perfect contact as there is no reflection of the wave. The positive or negative sign of the reflection coefficient value denotes the phase of the wave.

$$R = \frac{P_r}{P_i} \tag{3.12}$$

$$R = \frac{Z_2 - Z_1}{Z_2 + Z_1} \tag{3.13}$$

3.3 Ultrasound generation

To instigate an ultrasonic wave in a material a line of particles must be displaced such that they vibrate at the desired frequency. There are several routes to transmit and receive ultrasonic signals; mechanical, thermal, electrostatic, piezoelectric and optical to name a few [69]. This work generates ultrasound via the piezoelectric effect.

3.3.1 Piezoelectric effect

The principle of piezoelectricity is shown in certain materials when subject to an electrical charge, this causes a mechanical deformation in the order of nanometers. These materials also experience the opposite effect when subject to a mechanical displacement. Therefore, an alternating current can generate a mechanical stress that induces a sound wave and vice versa enabling the piezoelectric effect to be capable of instigating and measuring ultrasonic signals.

3.3.2 Transducers

A large range of ultrasonic transducers are available, specialised to different aspects of NDT such as crack detection or acoustic emission. A series of typical ultrasonic transducers are shown in Figure 3.5a. The components of such transducers are labelled in Figure 3.5b.

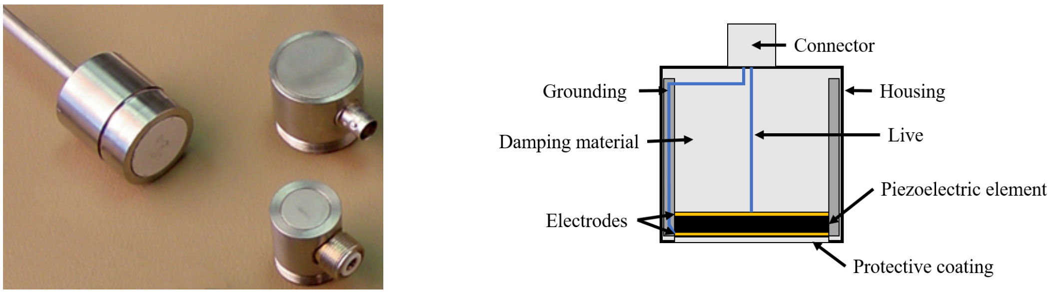

(a) Typical ultrasonic transducers [70]. (b) Transducer components.

Figure 3.5: Typical ultrasonic transducers and components.

The generic configuration is for a piezoelectric element such as lead zirconate titanate (PZT) or bismuth titanate to have an electrode on either side with a damping material on the back face of the transducer to damp vibrations after the initial pulse. The unit is encased in a housing that has a protective coating on the front face to protect the electrode. Ultrasonic transducers can either be probed onto a surface with ultrasonic transmission gel or permanently bonded if extended use is required. The relatively simple configuration of the transducer allows there to be freedom in size and shape of the transducer enabling potentially complex transducer arrays to be built up if required.

For a material to maintain its piezoelectricity, it must remain below its Curie temperature which ranges from 120-1000+°C depending on the material [69]. Therefore, for some applications such as cylinder liners in fired engines whose temperatures are often greater than 120°C specially manufactured transducers may be required to provide transducers that can operate for an extended time.

3.3.3 Transducer characteristics

A piezoelectric element is characterised by its centre frequency, amplitude and bandwidth. The centre frequency, f_c, of the transducer is determined by the thickness of the element, h, and the speed of sound through the element, see Equation 3.14. The equation shows that shear elements are thinner than longitudinal elements as the speed of shear waves is roughly half that of longitudinal waves.

$$h = \frac{c}{2f_c} \tag{3.14}$$

The bandwidth is dependent on the level of damping of the piezoelectric element and is characterised by the value of the bandwidth after a 6 dB (or 50%) decrease in the original signal amplitude in the frequency domain (see Figure 3.6b) as defined in E1065 ASTM Standard [71]. Transducers can also be characterised in terms of their bandwidth percentage as calculated in Equation 3.15.

$$Bandwidth\,(\%) = \frac{Bandwidth}{f_c} \tag{3.15}$$

An example of a typical ultrasonic reflection in the time domain and the frequency domain by applying a fast Fourier Transform (FFT) is shown in Figure 3.6 with the main factors labelled. The shape of the waveform is controlled by the frequency and the damping applied. Transducer damping controls the frequency response of the waveform by affecting the initial excitation after the ultrasonic pulse (ringing). Through the ability to attenuate the signal by applying damping material to the rear face of the active element it is possible to control the duration of the signal in the time domain.

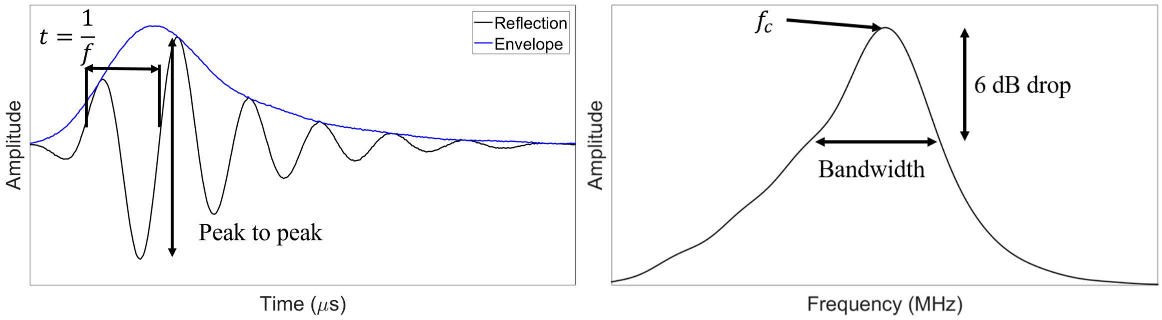

(a) Time domain ultrasonic reflection.

(b) Frequency domain of an ultrasonic reflection.

Figure 3.6: Time and frequency domain views of an ultrasonic reflection.

Highly damped ultrasonic transducers produce a short signal in the time domain whilst having a broadband signal in the frequency domain. Whereas poorly damped transducers produce a long duration signal in the time domain and a narrowband frequency domain.

3.3.4 Near field effect

Piezoelectric transducers follow Huygens' Principle of Diffraction when a sound wave is emitted from a transducer. The wave is instigated from a series of discrete points on the surface. Close to the transducer, these signals interact constructively and destructively which, therefore, leads to fluctuations in the overall signal produced in this region. This effect is defined as the near field effect. The fluctuation in the signal causes difficulties in identifying the desired reflections/regions in the signal in this region as shown in Figure 3.7, the near field is the region denoted by N.

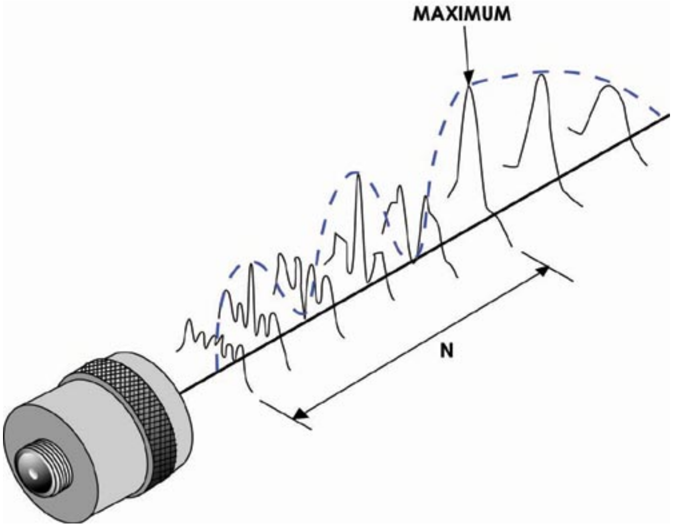

Figure 3.7: A schematic displaying the near field and far field regions [72].

Following the near field, is the far field in which the sound waves have sufficiently spread out such that there is a significantly lower level of variation in the output signal. The wave is now equivalent to a sound wave produced from a single-point source in the centre of the transducer. The length of the near field, N, can be calculated by using Equation 3.16 where D_t is the diameter of the transducer and λ is the wavelength of the signal used. Ideally, the transducer should be sized such that the near field ends just before the signal is captured as this has the maximum amplitude of the signal with minimal noise interference.

$$N = \frac{D_t^2}{4\lambda} \tag{3.16}$$

3.3.5 Transducer measurements

There are two configurations for ultrasonic transducers; pulse transmission and pulse reflection, see Figure 3.8. Pulse transmission measurements have a transducer on either side of the medium and can show discontinuities in a material due to the lack of signal being sensed from the receiver. Although this technique does not allow for the depth of the imperfection to be identified.

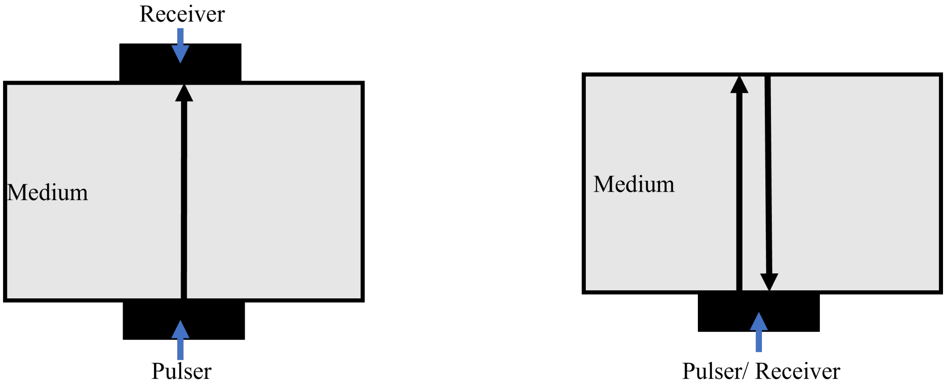

(a) Pulse transmission.

(b) Pulse reflection.

Figure 3.8: Pulse transmission and pulse reflection.

Alternatively, pulse reflection has the pulser and receiver on the same side of the specimen. The transmitter generates the ultrasonic wave which is propagated into the media. This wave is then reflected from the back surface of the media, in addition to any reflections from an imperfection in the media. The reflected wave is detected by the receiver, this combined with knowledge of the speed of sound through the media, the thickness of the component and the location of cracks/discontinuities can be found by time-of-flight analysis.

Pulse reflection analysis can be split into two subgroups; pulse-echo and pitch-catch, see Figure 3.9. Pulse-echo uses one transducer to both pulse and receive the signal whereas pitch-catch has a separate pulser and receiver. Whilst both techniques enable a similar analysis to be performed, the pitch-catch approach can be used for analysis such as how the ultrasonic wave propagates along/around a component by the spacing set between the two piezoelectric elements.

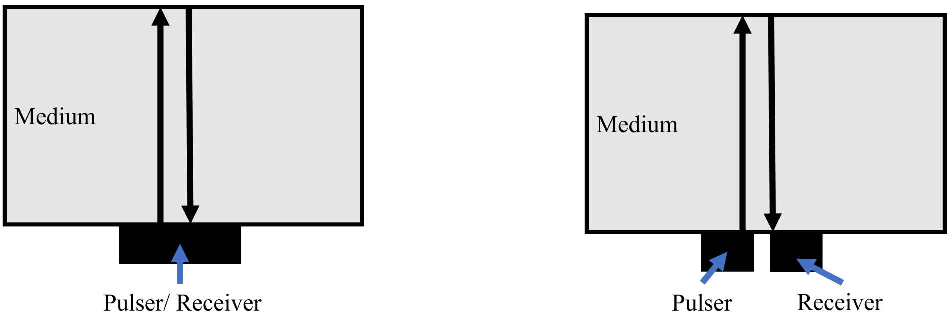

(a) Pulse-echo.

(b) Pitch-catch.

Figure 3.9: Pulse-echo and pitch-catch configurations.

3.4 Reflections at real boundaries

The reflection of an ultrasonic wave at an idealised perfect boundary can be improved to account for two real engineering surfaces, such as those seen in Figure 3.10 with each surface having a degree of roughness preventing complete contact. This results in only the asperities of the surfaces touching whilst the rest of the 'contact area' consists of air gaps.

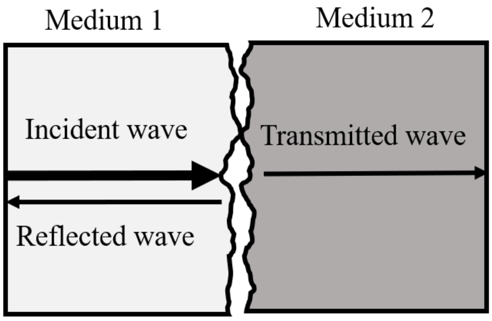

Figure 3.10: Two real engineering surfaces.

To improve the model, the interfacial stiffness needs to be considered as modelled using the Quasi-static spring model as developed in [73]. This model treats the two bodies as if they are connected via a series of springs (Figure 3.11) with the stiffness of K, defined in Equation 3.17 where P, is the contact pressure and u, is the deflection.

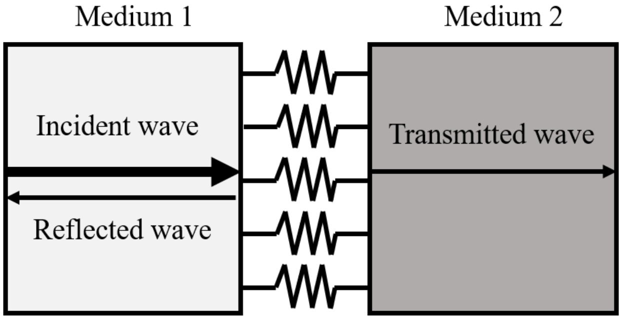

Figure 3.11: Spring model surface approximation.

$$K = \frac{dP}{du} \tag{3.17}$$

The interfacial stiffness replicates the asperities that are in contact, as the two surfaces get closer and the surface deformation increases, the interfacial stiffness tends to infinity. By incorporating the interfacial stiffness into Equation 3.13 a new equation for the reflection coefficient can be defined, in Equation 3.18.

$$R = \frac{Z_2 - Z_1 + i\omega(\frac{Z_1 Z_2}{K})}{Z_2 + Z_1 + i\omega(\frac{Z_1 Z_2}{K})} \tag{3.18}$$

Equation 3.18 contains an imaginary component providing the vector and phase of the reflection coefficient. The magnitude of the reflection coefficient is shown in Equation 3.19.

$$|R| = \sqrt{\frac{(Z_2 - Z_1)^2 + (\frac{\omega Z_1 Z_2}{K})^2}{(Z_2 + Z_1)^2 + (\frac{\omega Z_1 Z_2}{K})^2}} \tag{3.19}$$

A common simplification can be made if the two media are made of the same material (thus same acoustic impedance, $Z_1 = Z_2$). This simplifies Equation 3.19 to Equation 3.20.

$$|R| = \frac{1}{\sqrt{1 + (\frac{2K}{\omega z})^2}} \tag{3.20}$$

3.4.1 Reflections at boundaries with lubricant films

The reflection coefficient in Equation 3.19 is only applicable to two real unlubricated solid surfaces in contact. Additional steps can be applied to study two real surfaces separated by a thin lubricant film. This adapts the model to consider three media (Figure 3.12) each media has its own respective acoustic impedances, therefore, there is a partial reflection/partial transmittance occurs when the wave interacts with the boundary between Medium 1 and Medium 2 as well as the boundary between Medium 2 and Medium 3. This leads to the transducer receiving a second ultrasonic reflection marginally after the first. This causes difficulties in thin films (less than 100 μm), to identify which reflections are from which boundary. To overcome this, higher frequencies of ultrasound must be used although this increases the attenuation of the wave. In general, if the wavelength of the signal is large compared to the fluid film thickness then the two boundaries can be treated as a single reflector.

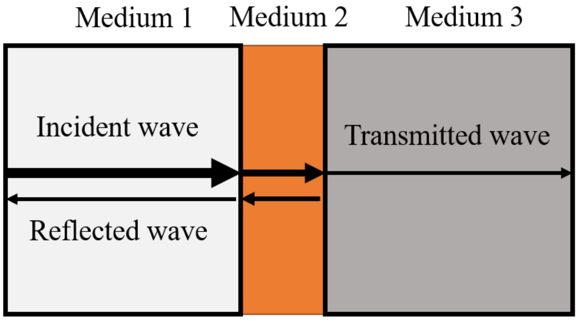

Figure 3.12: The interaction of an ultrasonic wave at a solid-liquid-solid interface.

The stiffness of the separating lubricant layer can be defined by the bulk modulus, B, and the layer thickness, h, shown in Equation 3.21.

$$K = \frac{B}{h} \tag{3.21}$$

The bulk modulus of a fluid can be rewritten in terms of the product of its density, ρ and wave velocity, c (Equation 3.22).

$$K = \frac{\rho c^2}{h} \tag{3.22}$$

Incorporating Equation 3.22 into Equation 3.19 with several stages of rearrangement gives an equation for the thickness of a thin oil film between two real bodies, Equation 3.23, [74].

$$h = \frac{\rho c^2}{\omega Z_1 Z_2}\sqrt{\frac{|R|^2(Z_2+Z_1)^2-(Z_2-Z_1)^2}{1-|R|^2}} \tag{3.23}$$

Similar to Equation 3.20, the same simplification can be applied if the two solid media have the same acoustic impedances, providing Equation 3.24.

$$h = \frac{2\rho c^2}{\omega Z}\sqrt{\frac{|R|^2}{1-|R|^2}} \tag{3.24}$$

Previously, Equation 3.23 [74] was used to show the expected oil film thickness over a range of frequencies for hydrodynamically lubricated machine elements, the resulting reflection coefficients and corresponding film thickness are shown in Figure 3.13.

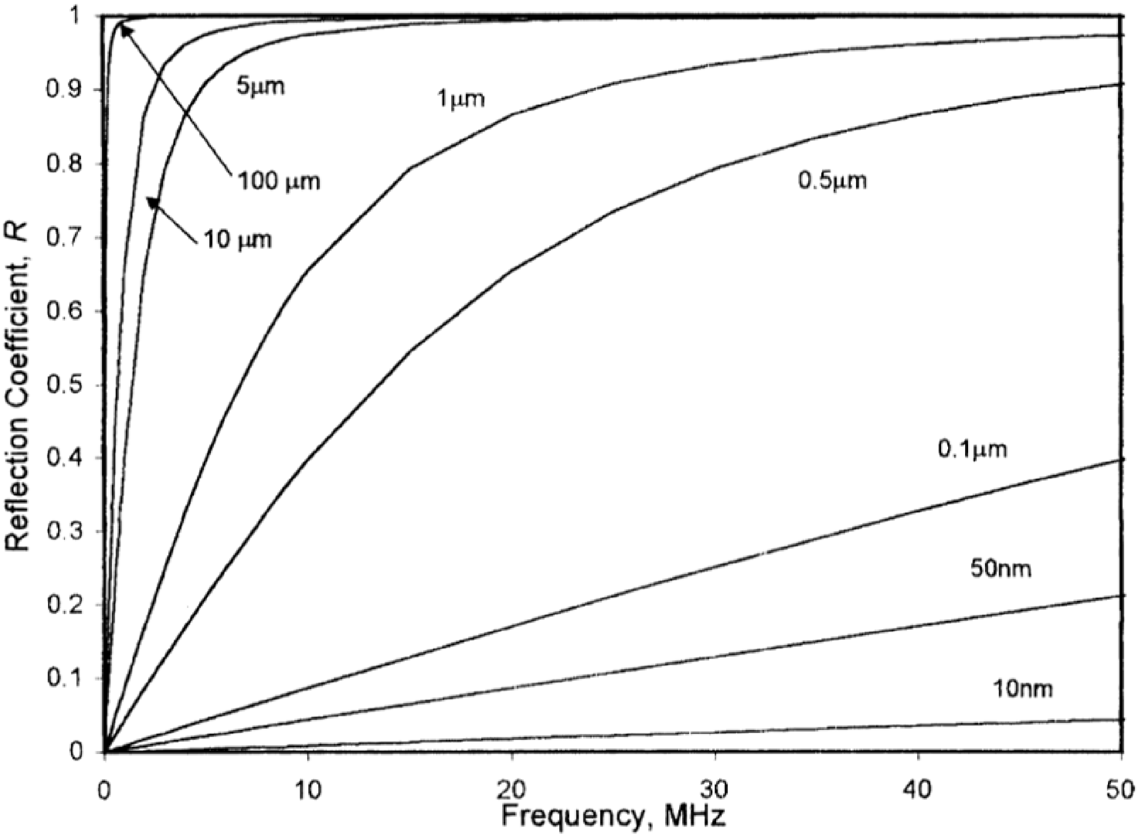

Figure 3.13: Reflection coefficients for a range of oil film thickness at various transducer frequencies, reproduced from [74].

In Section 2.10, a review of techniques to measure piston ring oil film thickness highlighted the expected oil films to range from $0.5\mu m$ to $20\mu m$ (Table 2.4). Therefore, using Figure 3.13 it shows that there is a large range of suitable transducer centre frequencies available to study this oil film with the most applicable being up to 10 MHz.

There are several assumptions made so that the spring model is applicable, these include:

- The region between Medium 1 and Medium 3 is fully flooded with fluid, therefore, no cavitation occurs.
- The fluid film completely separates Medium 1 and 3 such that no asperities are in contact.
- The two surfaces are parallel.

- The interaction between the two surfaces is equivalent to a series of springs such that when the loading on the springs increases this changes the deformation between the two and this deformation remains within the elastic region at all times.

3.4.2 Experimentally measuring the reflection coefficient

The reflection coefficient can be experimentally defined by measuring and normalising the ultrasonic reflection relative to a reference reflection. The reference reflection is taken when the back surface of the contact is free and unloaded i.e. an air contact. Air reflections can be used as a reference reflection as 99.998% of the signal is reflected, thus this reflection is a near equivalent to the incident wave input to the medium. This defines another definition of the reflection coefficient, Equation 3.25.

$$R = \frac{Ring\ Aligned\ Reflection}{Incident\ Signal/Air\ Reference} \tag{3.25}$$

The difference in the two reflections is visible in the A-scan via a change in amplitude between the reference and piston ring aligned reflection, see Figure 3.14. In the case of piston ring and liner studies, the reference is often defined when the piston is significantly far away from the sensor. The enables a representative reference to be recorded for each data capture.

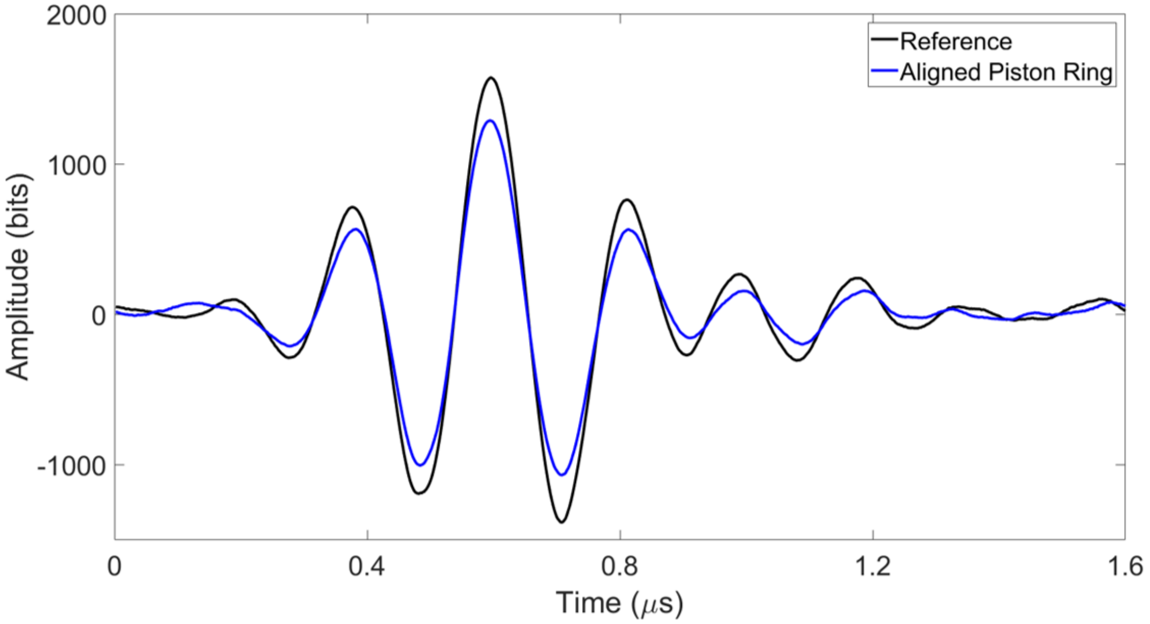

Figure 3.14: A reference reflection versus a piston ring aligned reflection.

The reflection coefficient parameter is defined by indexing the signal in the frequency domain at the transducer central frequency and comparing that to the reference reflection. See

Figure 3.15 for a visualisation of this of a sensor whose central frequency in 1 MHz. In Figure 3.15b the reflection coefficient is shown over the complete frequency domain. This technique has been used in previous ultrasonic piston ring oil film thickness research. The test rigs from these previous studies are discussed in Section 3.7.

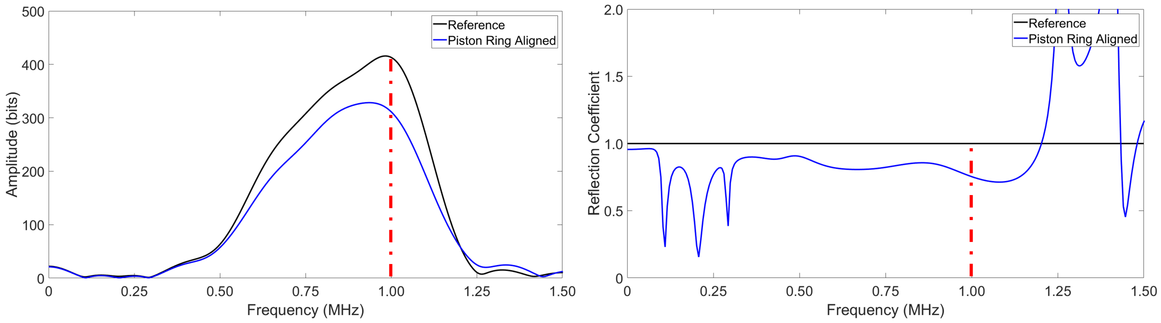

(a) Frequency domain.

(b) Normalised frequency domain.

Figure 3.15: A typical reference and piston ring aligned reflection in the frequency domain.

In Chapter 7, an alternative route to define the reflection coefficient is used. This is based upon the peak of envelope in the time domain signal using the Hilbert function. The time domain signal can be normalised relative to the reference envelope.

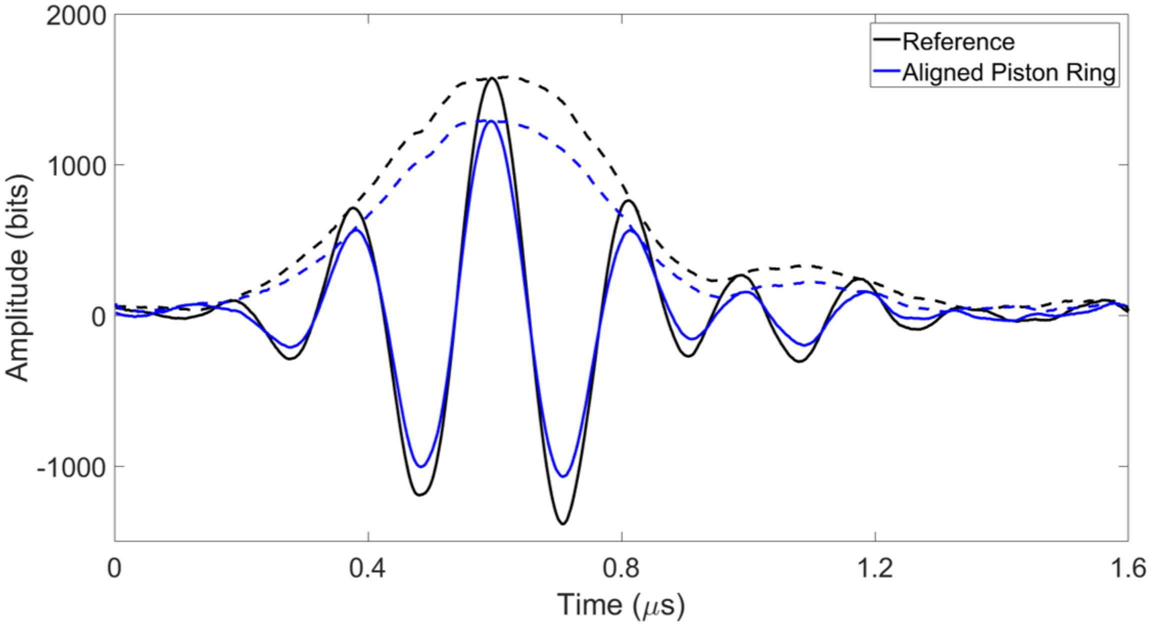

Figure 3.16: A reference reflection versus a piston ring aligned reflection with the Hilbert envelope overlaid.

The Hilbert envelope definition of the reflection coefficient primarily benefits over the frequency domain definition as it avoids difficulties in defining the start and end of a reflection and it is not subject to undesired ultrasonic reflections that are combined into the main body of the reflection when using the frequency index approach. This is covered extensively in Chapter 7.

3.5 Method validation

The ultrasonic methodology has previously been validated in [75, 76] by using ultrasonic transducers that were immersed in a water tank and positioned above a liquid wedge. The wedge was formed by using two glass sheets that were separated at one side by a ranges of shims of known thickness. The setup is shown in Figure 3.17.

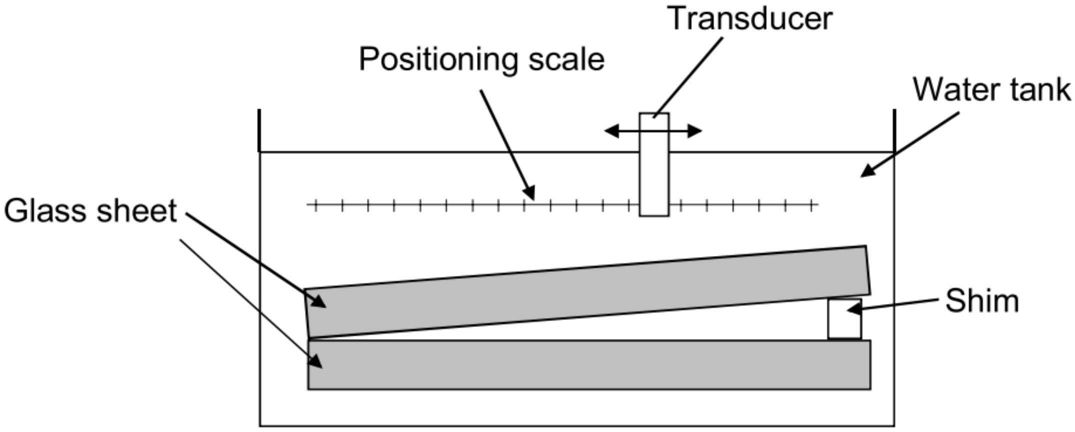

Figure 3.17: The ultrasonic method validation experiment setup performed in [75, 76].

The results show a good alignment between the ultrasonic measurement and the geometrical prediction of the lubricant film thickness within the range applicable to the Spring Model (up to 25 μm). Above 25 μm the resonance approach (explored in Section 6.3.2) was used which also showed good agreement with the experimental and geometric results.

A similar methodology was also performed in [75] to validate ultrasonic film thickness measurements between: a ring and shaft, elastohydrodynamic lubricated contacts (ball on disc, also covered in [76]) and for a roller bearing lubricant film. The results from all four of the scenarios studied provided good agreement between the measured and predicted results. In [75] the measurement between the glass plates (3.17) showed the greatest alignment between the shim thickness and ultrasonically measured results.

In the case of journal bearings, further validation has been performed in works such as [74, 77] as the ultrasonic results have been compared to the Raimondi-Boyd prediction [78], which showed good alignment to the experimental results, as the experimental results remained within the prediction boundaries.

3.6 Shear waves at solid-liquid boundaries

The previous section covers ultrasonic wave interaction at real engineering surfaces separated by a thin fluid film, this can only be applied to longitudinal transducers as shear waves are unable to support shear stresses and, therefore, do not propagate through fluids. Shear waves are only able to penetrate short distances into fluids, the penetration depth can be calculated using Equation 3.26, [79].

$$\delta = \sqrt{\frac{\eta}{\pi f_c \rho_l}} = \sqrt{\frac{4.5 \times 10^{-5}}{\pi \times 10 \times 10^6}} = 1.2\,\mu m \tag{3.26}$$

In which η, is the dynamic viscosity, ρ_l, is the density of the fluid and, f_c, is the centre frequency of the transducer. In the example shown above, using a transducer with a centre frequency of 10 MHz, the shear wave only propagates 1.2 μm into the oil film. However, the oil films between piston rings and cylinder liners typically reaches up to 20 μm, thus showing in most cases shear waves would not propagate through the film. As these high-frequency ultrasonic waves propagate a short distance into to oil film is enables the scenario to be treated as a semi-infinite half-space [80].

The fact that shear waves are unable to penetrate through a fully formed lubricant film in the orders expected for the piston ring-cylinder liner contact provides the potential for other parameters to be studied. An example of this is asperity contact between the ring and liner, hence showing a break down of the lubricant film. At any point where the oil film breaks down and boundary lubrication occurs (solid-solid contact) shear waves would then be able to propagate into the piston ring instead of being reflected at the boundary. Therefore, shear transducers provide a viable route to measure metal-metal contact.

3.7 Ultrasonic reflection piston ring rig design

In the several ultrasound sensing based piston ring oil film thickness works discussed in Section 2.10.6, a range of test rigs were manufactured to enable such measurements. This section provides a brief overview of the main features of those test rigs.

An early test rig for motored and fired testing was developed in [28] using a single-cylinder four-stroke engine on a dynamometer test platform. The barrel of the engine was modified to allow for wet liners to be used so that ultrasonic transducers could be instrumented on the external surface of the liner aligned with the piston skirt at the TDC. The TDC pulse was obtained using a digital rotary encoder to trigger the data acquisition system.

In [81] a four-cylinder Perkins 1100 series engine was driven by a 7.5 kW three-phase motor. The engine was run without the cylinder head/valves, therefore, a top plate was produced to seal the top of the water jacket and oil feeds. A shaft encoder was used to monitor crankshaft speed and position using a National Instruments USB-6009. Thermocouples were located at various points around the engine such as to monitor the temperature of the coolant and ultrasonic transducers. Slots were machined through the engine block to expose the back surface of the steel cylinder wall to enable ultrasonic instrumentation. Plates were machined to seal the coolant jacket post instrumentation. Bare piezoelectric transducers with a delay line, contact transducers and focusing transducers were all implemented onto the engine with varying degrees of success to measure the piston skirt. The test rig was also used in [32] with a 5 MHz contact transducer to measure the oil film thickness of each piston ring on the neutral side of the engine. As the contact transducer was not permanently bonded to the liner, this enabled the transducer to be used at a range of locations down the length of the piston stroke.

A single-cylinder Briggs and Stratton Quantum engine as used in [30] in which a hydraulic disc brake was coupled to a load cell to apply loading on the engine. The lawn-mower engine had side-valve aspiration limiting ultrasonic instrumentation to the anti-thrust side of the engine. Cooling fins on this side of the cylinder were removed to provide a flat area to instrument the transducers. An array of 7 transducers were instrumented, each with a width of 1.5 mm, a similar size to the thickness of the compression rings, the instrumented transducers are shown in Figure 3.18. The reduction in transducer size enabled measurements of all three piston rings and the piston skirt in each stroke of the engine.

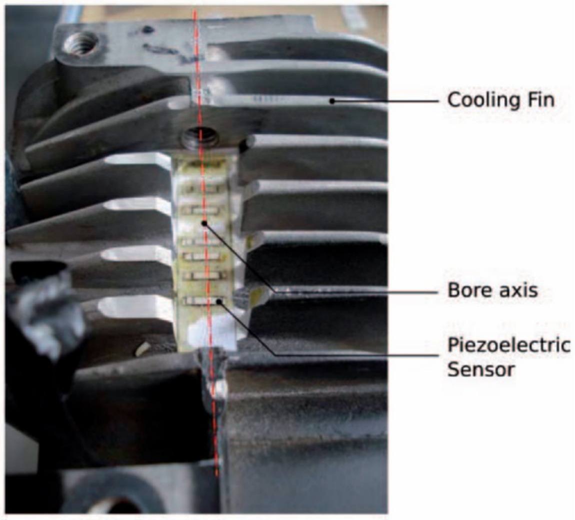

Figure 3.18: Ultrasonic instrumentation applied in [30].

Further works by Mills in [29, 31, 65] used a single-cylinder Honda CRF450R gasoline engine for motored and fired testing. A small flat was machined on the thrust, anti-thrust and neutral side of the engine to enable complex arrays of 15 transducers to be instrumented on each side of 7 mm x 1 mm. The coolant jacket was sealed post instrumentation and used in motored and fired testing to produce a significantly more detailed picture of the lubricant film than previous works. In addition, as measurements were recorded on multiple sides of the liner piston secondary motion could be inferred from the ultrasonic measurements.

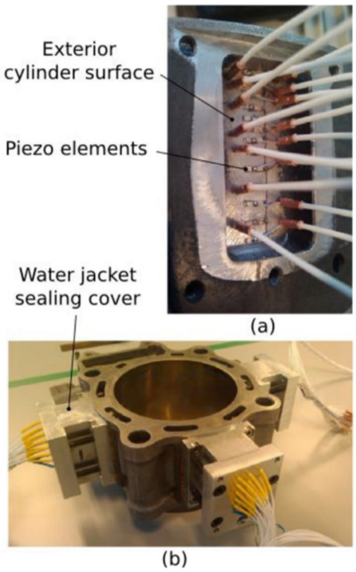

Figure 3.19: Ultrasonic instrumentation applied in [65].

From the literature surveyed, most test engines used with the ultrasonic approach or those using alternative techniques mentioned in Section 2.10 use single-cylinder engines except for a small range [32, 39, 81] who used a four-cylinder and six-cylinder engines respectively. A sizeable portion of the ultrasonic research was based upon single transducers or measurements from one side of the liner. To enable ultrasonic transducers on the AJ200 engine, a tailored rig was designed that was inspired upon the previous works such as [29, 31, 32, 65].

3.8 Ultrasonic testing equipment

Specialised equipment is required to perform ultrasonic analysis, a generic set-up is shown in Figure 3.20.

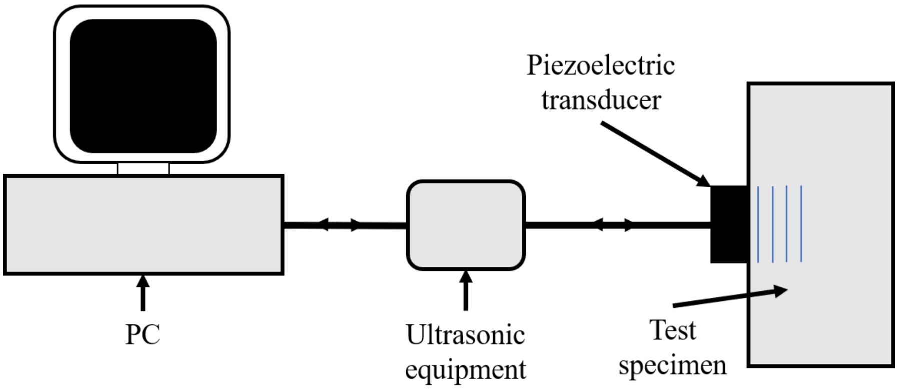

Figure 3.20: A typical ultrasonic set-up for basic data acquisition with the major components labelled.

The main functions of the system are detailed as follows:

- Pulser - Generates the voltage pulses that are used to actuate the ultrasonic sensor. The system used had 8 channels that could: pulse up to 200 V with pulse rates up to 80 kHz.
- Receiver - Receives the voltages from the ultrasonic transducer and directs the voltage to the digitiser. The system allows for the specification of the recorded waveform. Variable parameters include: gain of the signal, filter to remove noise from the raw signal, delay to focus the recorded signal on the time range of interest, and overall range of the recorded signal as a reduced time recording enables greater pulse rates to be used.
- Digitiser - Converts the received analogue signal to a digital signal.

- PC - A LabVIEW programme controls the system to enable optimisation of the input signal and recorded ultrasonic reflections.
- Piezoelectric sensor - Bonded to the test specimen and receives the voltages from the pulser. The piezoelectric element converts the voltage to an ultrasonic wave in the test specimen. The reflections in the test specimen are converted back to a voltage by the piezoelectric material and the voltage is sent to the receiver.

In this project an FMS100 PC was used. This unit houses a UPR (ultrasonic pulser/receiver) and a digitiser as well as a PC to run the system.

3.9 Ultrasonic wave propagation simulations

There are numerous systems to simulate ultrasonic wave propagation, this work used k-Wave [82, 83] an open-source, third-party, MATLAB toolbox that is capable of simulating ultrasonic waves in the time domain for 1D, 2D and 3D simulations. The toolbox works by defining a grid of nodes and solving a series of first-order partial differential equations, momentum conservation Equation 3.27, mass conservation Equation 3.28 and pressure-density relation Equation 3.29 for each node in the grid. The particle velocity is u, p is the acoustic pressure, ρ is the density and c is the speed of sound. The boundary of the media is surrounded by an anisotropic layer (perfectly matched layer) to attenuate a wave impacting the layer and to prevent reflections back into the medium.

$$\frac{\partial u}{\partial t} = -\frac{1}{\rho_0}\nabla p \tag{3.27}$$

$$\frac{\partial p}{\partial t} = -\rho_0 \nabla u \tag{3.28}$$

$$p = c_0^2 \rho \tag{3.29}$$

A comprehensive guide and numerous examples using the toolbox can be found at [82]. The toolbox has been applied to a range of ultrasonic applications including:

- Reconstruction of 3D photoacoustic imaging of vascular networks in pregnant female mice in [84].
- Simulating photoacoustic wave propagation in heterogeneous media (human tissue) in [85].

- In [86] k-Wave simulations were validated against acoustic pressure measurements in water and layered absorbing fluids with some simulations agreeing within 3% of the experimental results.

3.9.1 Toolbox overview

The set-up for k-Wave simulations can be split into four areas each of which must be defined: computational grid, acoustic medium, acoustic source and sensor. A brief summary of these areas is provided for the reader.

Computation grid
This defines the grid of discrete nodes used for the simulation in which the governing equations are solved for each node in the grid. Therefore, an increased grid size has exponentially greater requirements to timely run the simulation. The grid size is dependent upon the required domain size and the maximum frequency, for linear simulations it is recommended to use at least four grid points per wavelength.

Acoustic medium
The acoustic properties at each grid point must be defined. These include the speed of sound, density for lossless simulations. The addition of the power-law absorption coefficient/exponent and a non-linearity parameter enables system losses to be simulated.

Acoustic source
The properties and location of the source in the medium can be defined in three ways either; initial pressure distribution, time-varying pressure source (mass source in mass conservation) or a time-varying particle velocity source (force source in momentum conservation).

Sensor
The properties and location of the sensor nodes are defined within the computational grid and record the acoustic field at each time step. In a 3D grid, a transducer can be defined to replace the source and sensor definition. The additional parameters in the transducer function such as the focus distance or steering angle enable realistic input signals to be replicated.

To use the toolbox the following parameters are required:

- Domain size

- Medium properties (speed of sound and density)
- Source (location, type and size)
- Sensor (location, type and size)

These are the minimum input requirements although a much more exhaustive list of input parameters can be provided for more complex models.

The toolbox comes with a series of predefined examples. One example, ”defining an ultrasonic transducer” from [82] is summarised here for visualisation of the function of the toolbox. This simulation defines a transducer along the top of the domain which initiates a 1 MHz ultrasonic wave and there are 3 sensors at discrete nodes along the x-axis. In Figure 3.21 the wave propagation at three-time intervals as the simulation runs is shown. The transducer and sensor numbering convention is labelled in the figure.

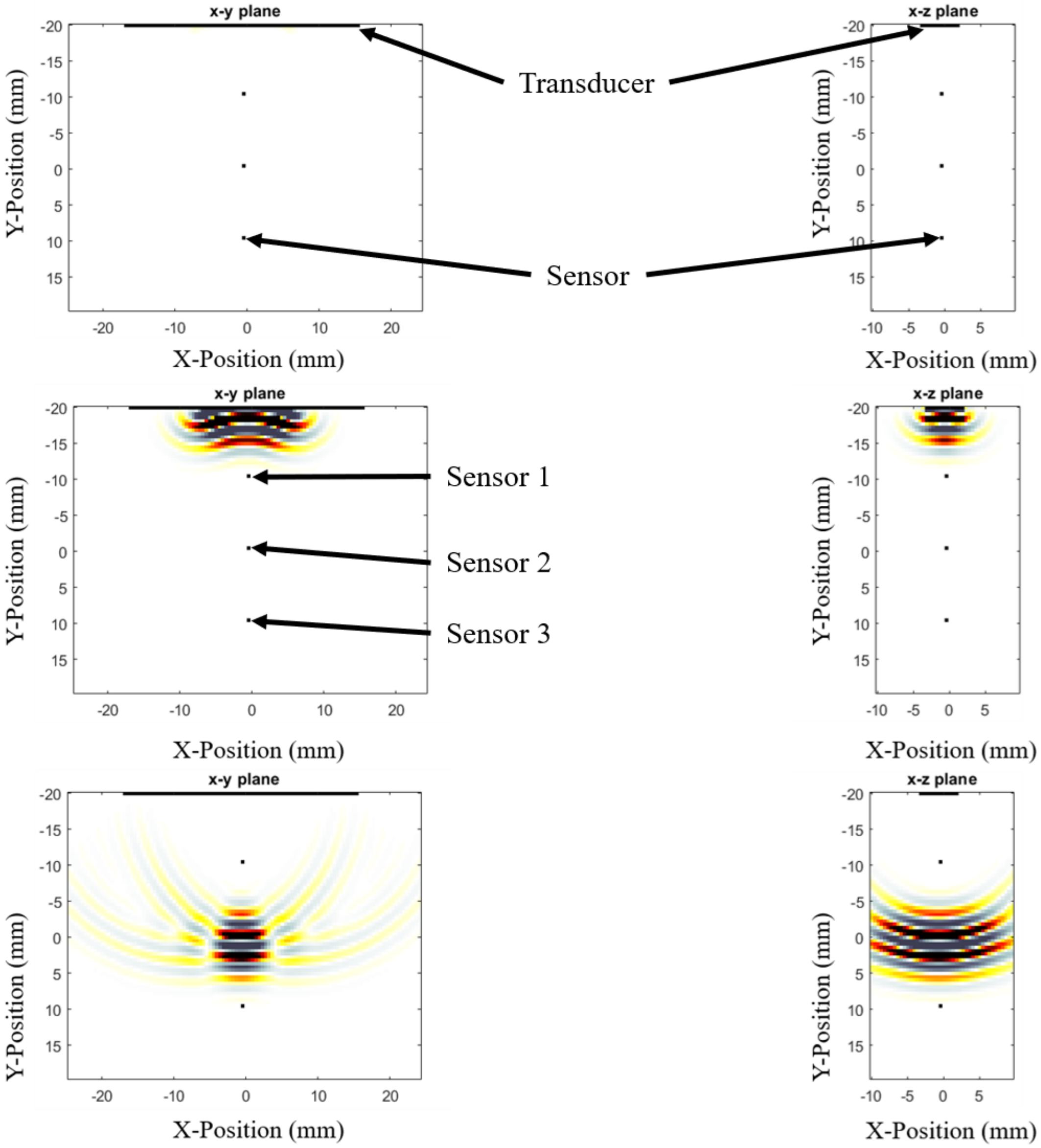

Figure 3.21: k-Wave ultrasonic wave propagation along the X-Y and X-Z planes from the example simulations in the k-Wave toolbox [82].

The k-Wave toolbox provides a real-time output of the visualisation of the wave propagation through the medium. The A-scan and FFT for each sensor in this example are shown in Figure 3.22.

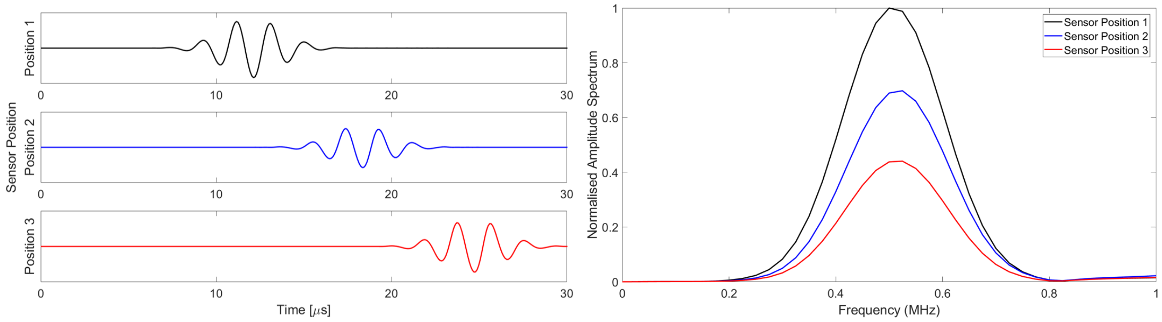

(a) A-scan from the three sensors. (b) FFT of the reflection from each sensor.

Figure 3.22: A-scan and FFT from an example simulation in the k-Wave toolbox [82].

The example results shown in Figure 3.22a shows for a sensing location further from the transducer a longer time of flight is recorded, as the wave is propagating a greater distance. The FFT shown in Figure 3.22b, shows that a greater propagation distance results in greater attenuation of the wave indicated by a reduction in FFT amplitude.

3.10 Conclusions

This chapter has provided an introduction to ultrasound, the basics of ultrasonic wave propagation and sensors. In addition, it has detailed a review of how ultrasonic sensors have been used to measure piston ring oil film thickness. A concluding summary of this chapter is as follows:

- Ultrasound is used in various engineering fields and nature, these are all based on the principle that a ultrasonic wave which is propagating through a medium has a partial reflection partial transmittance at each boundary. This reflection provides a measure of the contact between the two media.

- Ultrasonic waves can be instigated in a medium by a material that experiences piezoelectricity and these materials can be used to pulse and receive ultrasonic signals. A range of instrumentation routes of ultrasonic sensors has also been covered.

- The Quasi-static spring model provides a measure of the contact between real engineering surfaces. This model has been further refined to provide a measure of the reflection from two engineering surfaces that are separated by a thin lubricant film ($<$ 25 μm).

- Previous piston ring film thickness research has produced a series of test rigs capable of ultrasonic research, these have been reviewed concerning their applicability to the test rig required in this project.

- k-Wave provides a simple, reliable toolbox to simulate ultrasonic wave propagation through a medium. A brief overview of this MATLAB toolbox has been defined.

Chapter 4

Motored rig design

This chapter provides the reader with a brief overview of the motored AJ200 engine test rig that was designed and built for the project. The main design aspects of the rig have been identified and discussed to aid in the design of a similar test rig. The closing section of the chapter shows the reader the final assembled version of the AJ200 rig.

4.1 Engine block test rig

The engine selected for the motored test rig was a Jaguar Land Rover AJ200 Ingenium engine, specifically an I4, a 2-litre four-cylinder gasoline engine. This engine model is used in Jaguar Land Rover XE and XF models. The engine block bore is 83 mm with a piston stroke of 92 mm and the engine block itself is shown in Figure 4.1.

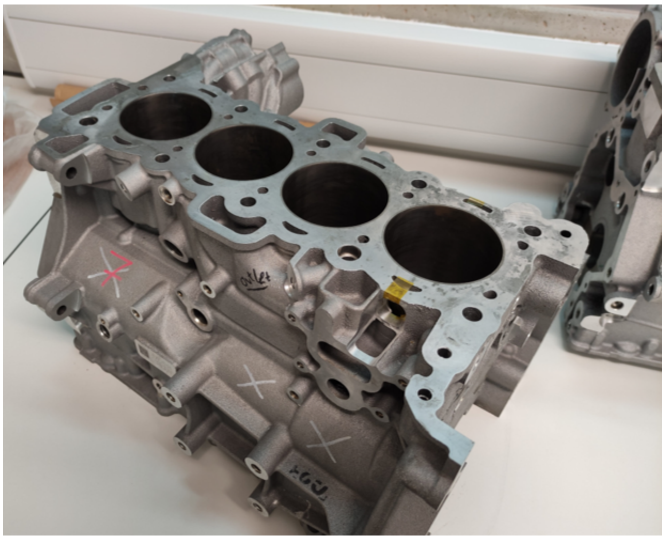

Figure 4.1: Engine block from the AJ200 I4.

The motored test rig was based upon previous similar ultrasonic OFT piston ring test rigs discussed in Section 3.7. This led to the overall design shown in Figure 4.2 in which a cross-section across the test rig is shown to highlight the key features of the test rig. The rig casing and inverter is excluded for visualisation purposes.

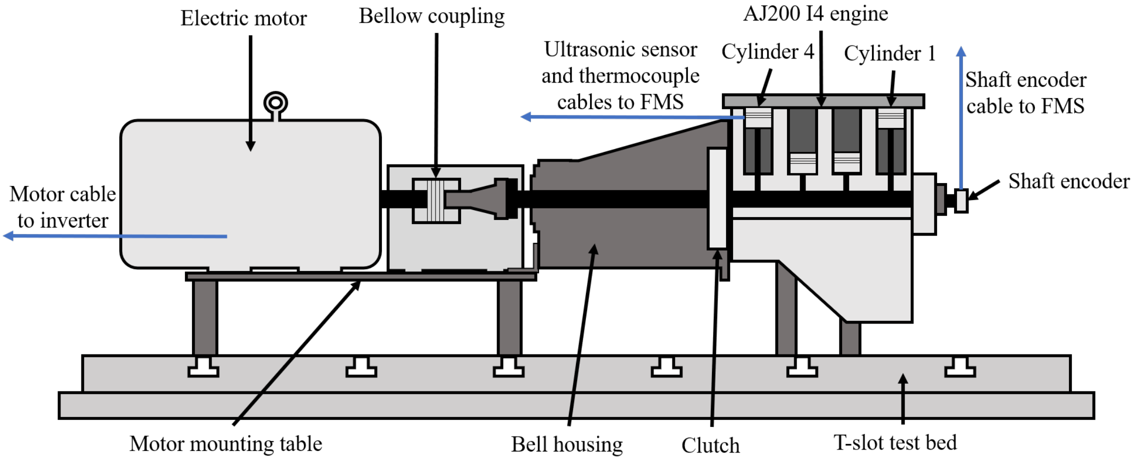

Figure 4.2: Cross-section of the motored AJ200 test rig.

The AJ200 engine block is driven by an 18.5 kW Baldor electric motor that is raised above a T-slot testbed by a custom mounting table. The motor is coupled by a bellow coupling to an intermediate shaft that is mounted onto the rear flange of the AJ200 bell housing which in connected to the crankshaft. The standard engine components have been used where possible to run the oil system with the cylinder head removed. Several oil and coolant pathways have been blocked to enable the test rig to be run in this state. The engine block itself is mounted using the standard engine mounts and fixed to the T-slot testbed by four mounting legs. The engine block is rigidly connected to the testbed removing the requirement for vibration isolation. The system is controlled by an ABB ACS580 inverter that allows simple control of the motor rotational speed. This test rig design enables the engine rotational speed and crank angle to be recorded in conjunction with the ultrasonic data from piezoelectric transducers. Ultrasonic reflections from the piston rings can be recorded as minor slots were machined into the engine block to expose the backface of the liner. An isometric view of the test rig using Solidworks is shown in Figure 4.3.

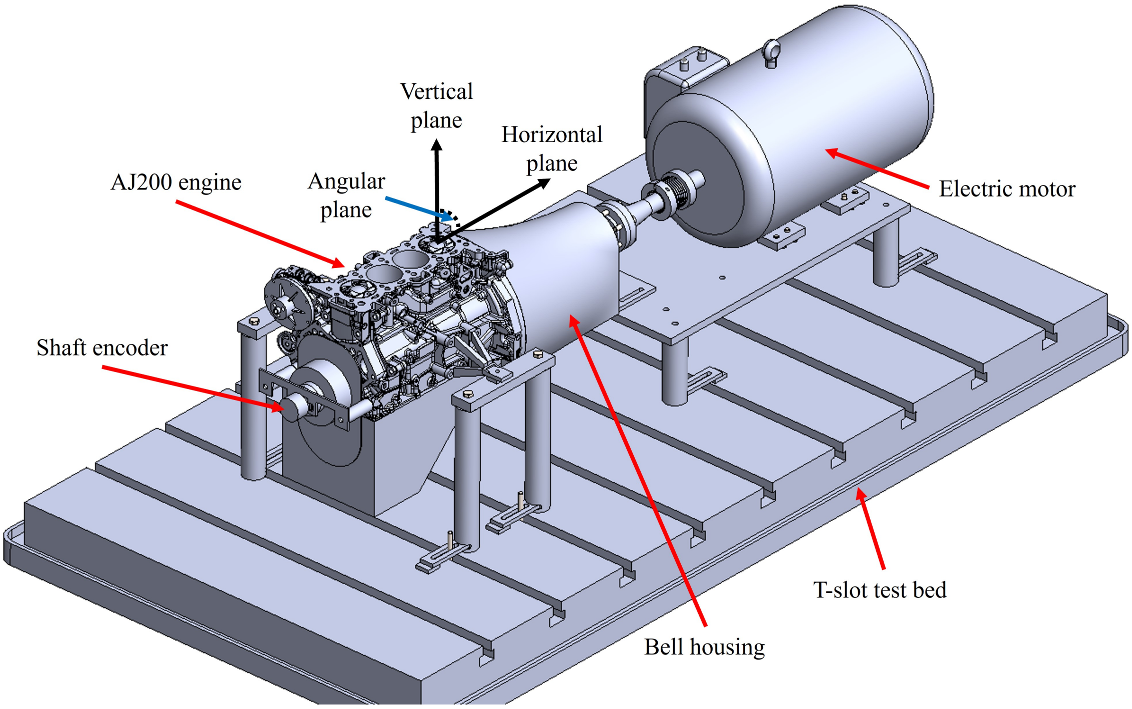

Figure 4.3: Solidworks of the motored AJ200 test rig.

4.2 Design features and constraints

Through the design of the motored test rig, there have been numerous constraints and design iterations that have adjusted the test rig to its final design. This section highlights some of those key features.

4.2.1 Engine block modifications

The primary design feature of the motored test rig was to enable ultrasonic measurements of the AJ200 piston ring oil film thickness. The piezoelectric ceramic in the sensor is brittle and therefore, is unable to support a bending stress without shattering. To enable these measurements, a flat on the external surface of the liner had to be exposed to enable ultrasonic instrumentation like those detailed in Chapter 3. From the literature review outlined in Chapter 2 the region close to the TDC has the largest contribution to; oil throw off, friction and has the thinnest oil film thickness with the potential of lubricant film breakdown (metal-metal contact). Therefore, any modifications made to the engine block were to enable the oil film to be studied close to the TDC. A series of potential engine modifications were considered, see Figure 4.4. Each modification was machined on a large CNC milling machine with a specialised long series slot drill.

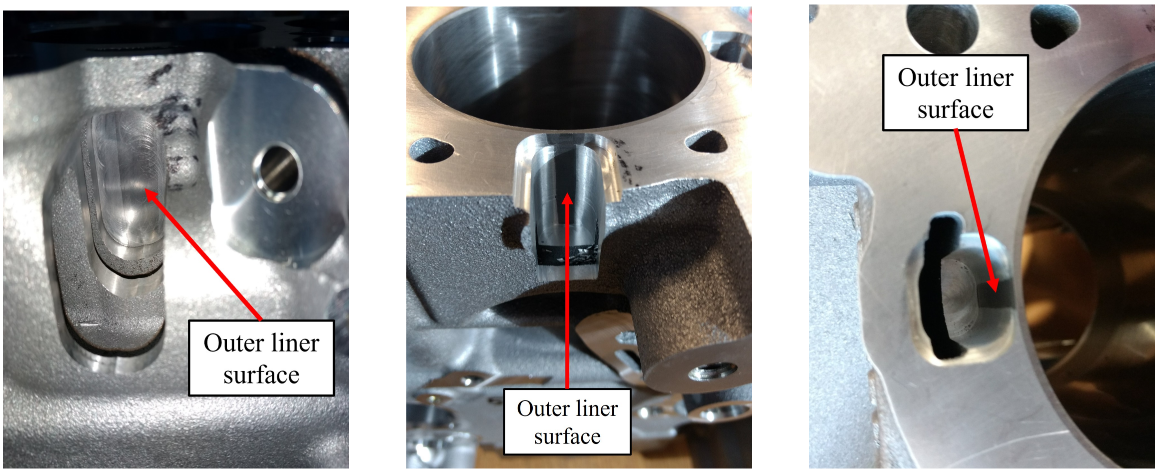

(a) Modification 1. (b) Modification 2. (c) Modification 3.

Figure 4.4: Three engine block modifications considered.

The three modifications can be summarised as:

1. Modification 1 - Slot machined through the water jacket at two points exposing a relatively large flat surface on the back face of the liner. The slot would lead to difficulties resealing the coolant jacket but the fired face of the block is unaffected. Limitations in slot drill availability led this modification to be performed on Cylinder 3 instead of an end cylinder.

2. Modification 2 - Corner segment machined off an end cylinder. This machining cut through the water jacket and removed a section of the fired face of the block. A 5 mm wide gap was exposed on the liner. The modification would hinder sealing of the coolant jacket and sealing the fired face.

3. Modification 3 - The slot machined through through the fired face also affecting the water jacket. Similar to Modification 2, a 5 mm flat on the liner was exposed. This modification although only machining on the fired face affects both the sealing of the fired face and the coolant jacket.

Each machined slot was subject to a series of ultrasonic sensor instrumentation to evaluate the feasibility of high-quality sensor arrays being instrumented using each modification. The modification shown in Figure 4.4a was ultimately selected as the ideal machining route. Even though this modification led to more limited access to the liner, as the fired face of the block was unaffected this enabled the potential of fired operation of the block in the future. As each modification considered removes a portion of the material around the cylinder liner, the distortions of the block will have likely been altered by this machining.

Although a degree of modification is required to enable ultrasonic instrumentation on the back surface of the liner. It is worth noting though, that the modifications to the block here are significantly less than those required for other techniques outlined in Section 2.10.

Cylinder 4 (see Figure 4.2) was selected as the ideal cylinder for machining as it is an end cylinder providing the potential to study the neutral side in addition to the thrust/anti-thrust sides. Cylinder 1 was omitted as the coolant pump is located next to this cylinder and it is believed it would lead to greater complications if the coolant pump was set to be used with the test rig. A lip was also added around the circumference of the slot so that the coolant jacket could be re-sealed post instrumentation if the coolant jacket was required to heat or cool the test rig. The locations of the machined slots are shown in Figure 4.5.

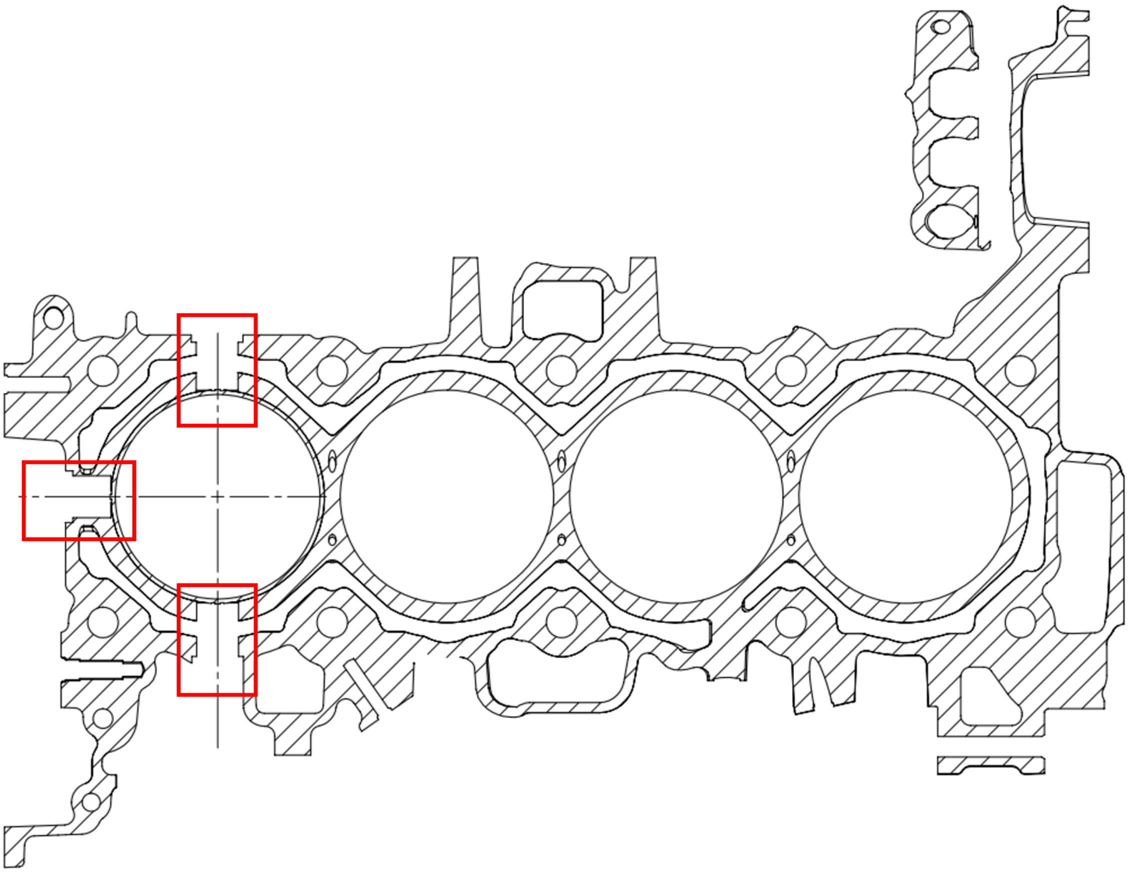

Figure 4.5: Engine block cross-section highlighting the three machined slots on Cylinder 4.

The machined slots dictate the position of the piezoelectric transducers. The block modifications exposed an 18 mm flat on the outside of the cylinder liner from 7 mm to 25 mm from the fire face of the block, see Figure 4.6. The design of this was based upon the leading edge of the rings at their TDC position. The first compression ring peaks at 7.6 mm from the fire face of the block whilst the oil control ring peaks at 20.7 mm. Therefore, the machined slots are capable of studying all piston rings at their TDC positions and on the approach to the TDC as the machining extends down to 25 mm from the fired face. The engine stroke length is 92 mm and this allows for the entry of the first compression ring to be close to its maximum velocity when it initially passes over the exposed region. Therefore, the lubrication regime should vary from a fully formed hydrodynamic film potentially down to boundary lubrication over the exposed region.

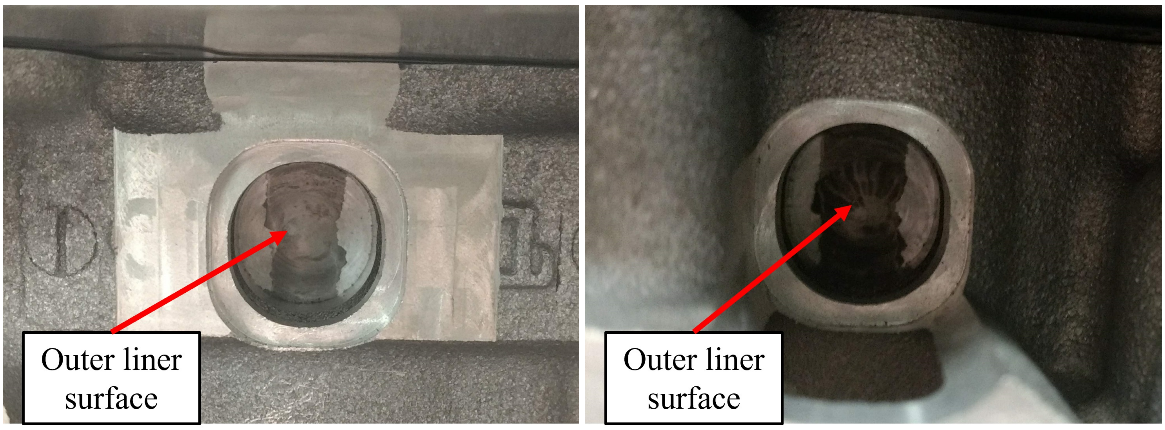

(a) Thrust side.

(b) Anti-thrust side.

Figure 4.6: Machined slots on the thrust and anti-thrust sides.

The size of the piezoelectric transducers themselves is a compromise between being large enough to instrument to a high standard whilst being small enough to provide results with a suitable spatial resolution. To achieve this, the height of the transducers should not be greater than the thickness of the ring being studied as the ultrasonic reflections recorded are an average over the whole measurement area. The piezoelectric transducers used on this test rig were therefore, deemed to be no larger than 0.9 mm in height as the width of the first compression ring is 0.9 mm. The width of the transducer is dictated by the width of the exposed surface of 5 mm. The ultrasonic elements were chosen to be no greater than 4 mm in width to ease instrumentation whilst limiting the impact of piston ring curvature.

The cylinder liners are press fit into the engine block which enables the transducers to be ground on the block itself and to locate the thermocouples here providing greater room for additional transducers.

4.2.2 Oil system

The oil system is largely unchanged from that of standard operation for the engine even whilst the cylinder head is removed from the engine. The absence of the cylinder head causes some of the oil pathways to be obsolete, therefore, to prevent major leaks these have been plugged. The plug sites have been highlighted in red in Figure 4.7 and the overall oil route is shown in brown. The AJ200 engine uses a solenoid driven oil pump which causes the oil pressure in the engine to remain at the required level with several oil routes blocked. Although as the motored test rig is run without the engine control unit the oil pump is purely ran by the crankshaft. The oil filter, oil cooler, and oil pump have been incorporated into the test rig and the standard oil for this commercial engine is used (0W-20 Castrol GTX SynBlend).

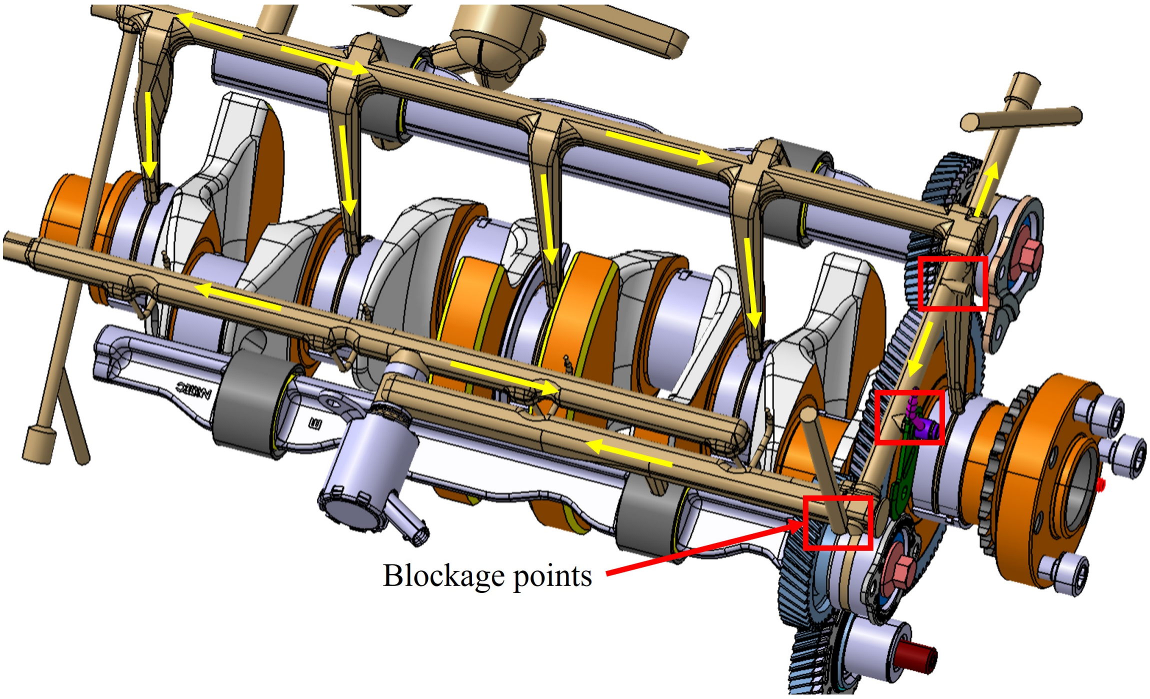

Figure 4.7: AJ200 oil routes highlighting required blockage points. The oil route is shown in brown with flow direction indicated by the yellow arrows.

4.2.3 Rig set up and usability

The electric motor is a Baldor 1044M, 18.5 kW motor with the main parameters shown in Table 4.1. This motor was selected due to the availability, the maximum rotational speed (2900 rpm) and full load torque (60 Nm) being greater than required for the desired operation of the partially assembled AJ200 engine. The maximum motor speed of 2900 rpm was deemed satisfactory for the test rig by study of Table 2.4 and previous ultrasonic piston ring test rigs outlined in Section 3.7. These areas showed the Baldor motor enabled ultrasonic testing at similar engine speeds to other works and would support an improved resolution of data points captured per piston ring passage. The motor is run by an ABB ACS580 inverter, this set-up enables the engine to be spun at a set engine rotational speed up to the maximum for the motor enabling steady-state operation of the engine and allows dynamic state operation for start-up and shut-down tests.

Table 4.1: Main parameters of the Baldor 1044M motor.

Parameter	**Value**	**Unit**
Horsepower	25	-
Voltage	400	V
Rotational speed	2900	rpm
No. of poles	2	-
Full load torque	60	Nm

The design of the motored engine test rig is such that the rotational speed of the motor is set on the inverter and parameters such as; engine revolution count, transducer temperature, recorded ultrasonic reflections and reflection coefficient are displayed in a LabVIEW programme on a PC that is connected to the rig. This gives a real-time representation of how the rig is running and allows for quick modification of the running parameters.

4.2.4 Coupling

The coupling between the motor and the engine block is key to the running of the test rig for the transmission of torque and smooth operation of the motored engine. A bellow coupling was deemed appropriate as the coupling gives zero-backlash and has large flexibility allowing for up to 5° of angular misalignment or 0.9 mm parallel misalignment. The main flaw in this coupling is the attachment method to the shaft as it must be tight enough to prevent the slip and backlash. A Mayr 3/932.333 coupling was selected as the transmittable torques are up to 200 Nm which is relatively low for couplings but significantly greater than those required for the test rig (80 Nm at highest speed under motored conditions). This bellow coupling also has split hubs enabling it to be clamped to the shafts to prevent any possible slip or backlash.

4.2.5 Shaft alignment

The alignment of the test rig is key to preventing uneven operation or damaging of test rig components. Therefore, the test rig required aligning in both the vertical and horizontal planes as well as angularly aligning, see axes system on Figure 4.3. From Figure 4.3 the reader can see that the test rig can be split into two halves, the engine side and the motor side which interconnect via the bellow coupling. To reduce the difficulty in shaft alignment of the two sections it was clear to assemble and mount the engine side of the test rig at a fixed height and levelled to within 0.1 mm in each plane. Following this, the height of the motor side of the rig was finalised hence reducing the potential cause of error in the design of this half.

The alignment procedure between the two halves used dial indicators at a range of locations on the test rig with a series of shims with the final alignment being within 0.1 mm in both the vertical and horizontal planes and within 1° of angular misalignment. These values are within the coupling misalignment tolerances to enable smooth operation of the test rig.

4.3 Final rig assembly

The final assembled version of the motored AJ200 test rig can be seen in Figure 4.8.

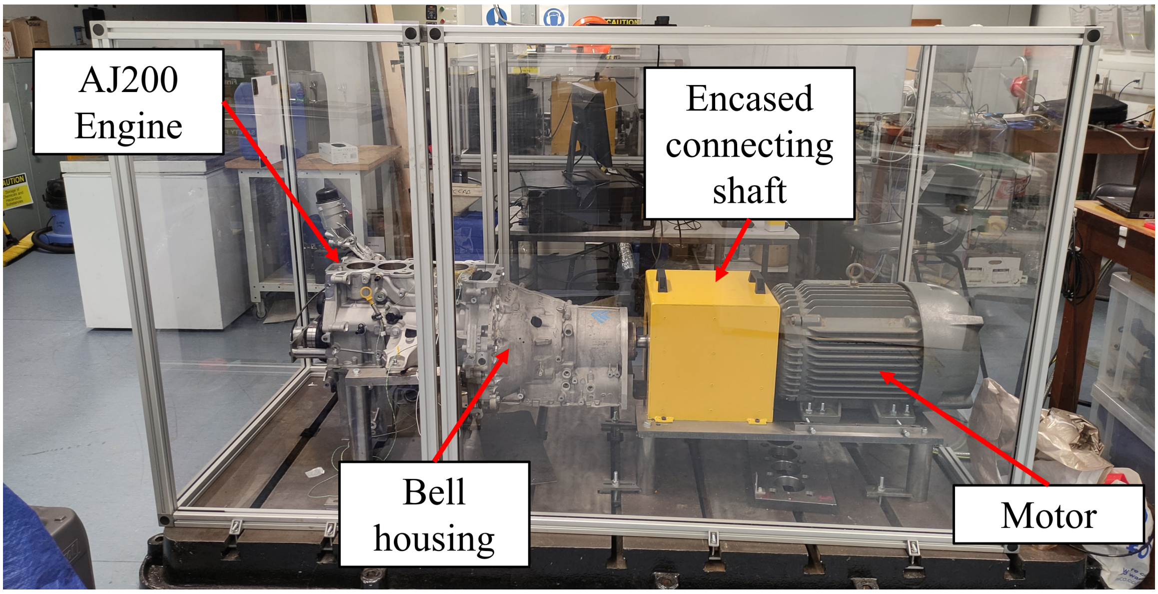

Figure 4.8: The fully assembled motored AJ200 test rig.

4.3.1 Instrumentation

The ACS580 inverter allows for the rotational speed of the motor to be set and monitored using a closed-loop feedback system to provide steady-state operation of the engine. This allows for precise control of the rotational speed to a suitable level required for this thesis. The inverter and controller are shown in Figure 4.9a.

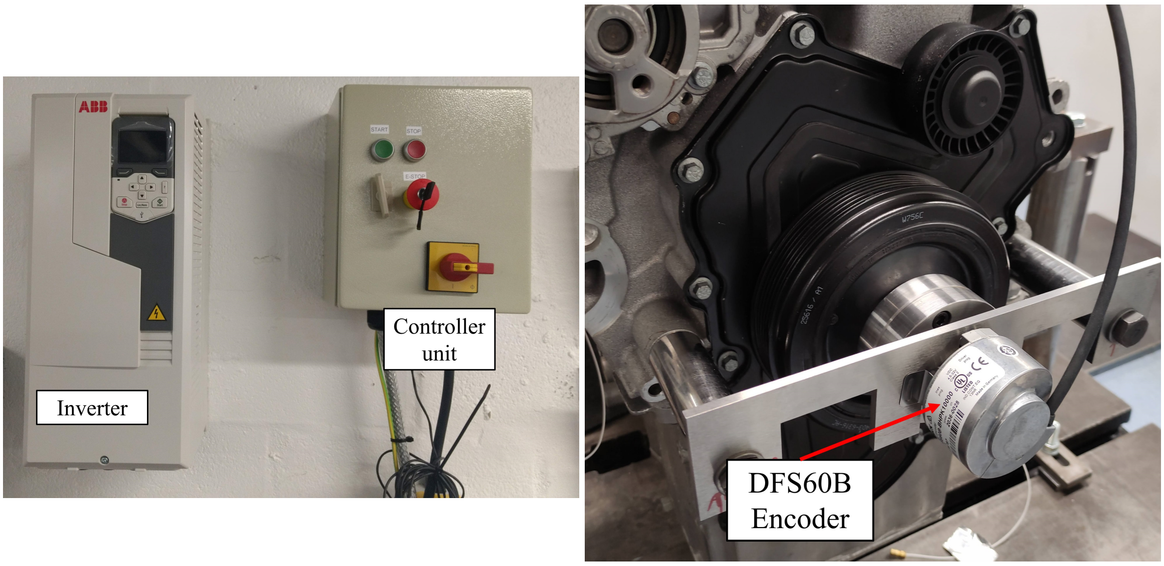

(a) ACS580 inverter and controller unit.

(b) Mounted DFS60B encoder.

Figure 4.9: The inverter, controller and encoder of the AJ200 rig.

The crankshaft rotational speed is measured by a Sick DFS60B encoder (Figure 4.9b) that is mounted to the front of the engine. The encoder is programmable and enables up to 10,000 pulses per revolution which is excessively higher than any requirements for this project. For this test rig, the encoder was programmed to produce 1000 pulses per revolution and a single tick per every revolution of the crankshaft.

The temperature next to the transducers was monitored using K-Type thermocouples that were connected to a TC-08. The TC-08, ultrasonic transducers and shaft encoder were all connected to the FMS100 PC and through the use of an in-house LabVIEW programme all measurements were captured.

4.4 Test rig further work

The motored engine block test rig was initially designed with an exhaustive testing regime in mind. Here, a brief outline of the considered test rig advancements are discussed:

1. Adding a dynamometer - A dynamometer was planned to be added to the motored rig so that load could be tested on the engine.
2. Heated coolant jacket - Due to the motored operation of the block, the sole heating source was due to frictional heating. Therefore, the engine block did not achieve temperatures like those from fired operation of the engine. The engine block modifications were designed such that the coolant jacket could be resealed post instrumentation. Then, through the use of an external heating reservoir, the coolant jacket could have been used to heat the block to temperatures like those of fired operation leading to the test rig being at temperatures more similar to those from fired operation.
3. Oil deterioration - The motored engine block was planned to be run with fresh and aged lubricants. This would enable ultrasonic sensors to study how the state of the lubricant affects the piston ring oil film thickness.
4. Complex transducer arrays - The three-block modifications exposed a portion of the liner covering the piston rings at their TDC positions on the thrust, anti-thrust and neutral sides. A more complex instrumentation of ultrasonic sensors would have provided a greater value of ultrasonic result, such as visualising how the piston ring oil films varied as they approached the TDC.
5. Fired operation - The block modifications to instrument the ultrasonic sensors were designed so that the fired face of the block was unaffected. This was to enable the block to be used in fired testing in the future so a comparison between fired and unfired operation could be studied.

4.5 Conclusions

This chapter has detailed the design, assembly and instrumentation of the key aspects of the motored AJ200 test rig designed for this thesis. The main points of the chapter are summarised as:

- A bespoke motored test rig for the AJ200 I4 engine has been designed and manufactured to enable quantification of the piston ring and liner oil film thickness using an ultrasonic methodology.
- The design process has been outlined detailing the minor modifications to the engine block to provide a route for piezoelectric sensor instrumentation.

- The closing section of the chapter shows the assembled test rig and summaries the additional instrumentation on the test rig to enable data acquisition.

Chapter 5

Motored gasoline automotive engine

This chapter uses the motored test rig whose design and assembly was covered in Chapter 4. The test rig was instrumented with ultrasonic transducers and the data was processed to produce piston ring oil film thickness measurements from the motored engine block at a range of engine speeds.

5.1 Engine summary

The motored test rig uses the engine block from a AJ200, a four-stroke gasoline Jaguar Land Rover engine. Although, the block is driven with the cylinder head removed, this effectively makes the engine only have two strokes (up and down stroke). The main parameters of this engine are shown in Table 5.1. The engine block has four cylinders and as outlined in the previous chapter the instrumentation was set to be focused on Cylinder 4 in the machined slots shown in Figure 4.6. The ring pack of the AJ200 includes three piston rings; two compression rings and a three-piece oil control ring. The cylinder liner and piston ring surface roughness values are similar to other automotive engines, in the low order of microns.

Table 5.1: Main engine parameters for the AJ200 engine.

Engine parameter	**Value**	**Unit**
Maximum power	184 [87]	kW
Cylinder bore	83	mm
Piston stroke	92	mm
No. of cylinders	4	-
No. of piston rings	3	-

The engine block is cast aluminium whilst the cylinder liner itself is cast iron. The body of the piston is also made from an aluminium alloy whilst the piston rings are a steel alloy. The standard acoustic properties of these materials are shown in Table 5.2.

Table 5.2: Acoustic impedance of AJ200 engine components.

Engine component	Material	**Acoustic impedance (MRayl)**
Cylinder liner	Cast iron	36
Piston	Aluminium alloy	17.3
Piston ring	Steel alloy	46

The equation for oil film thickness (Equation 3.23), requires the speed of sound and density of the oil. In the AJ200 engine the standard engine oil is Castrol GTX SynBlend 0W-20, this oil was used in the motored rig. To measure the longitudinal wave velocity in the oil the 'Speed of Sound' rig was used, see Figure 5.1. The rig is made from invar due to the material's low thermal expansion coefficient and instrumented with a 10 MHz longitudinal transducer to record the time of flight between two successive reflections over a know path length (100 mm). Measurements of the time-of-flight of the ultrasonic wave as the oil was heated and cooled in an oven provided a measure of the longitudinal wave velocity variation with temperature, see Equation 5.1.

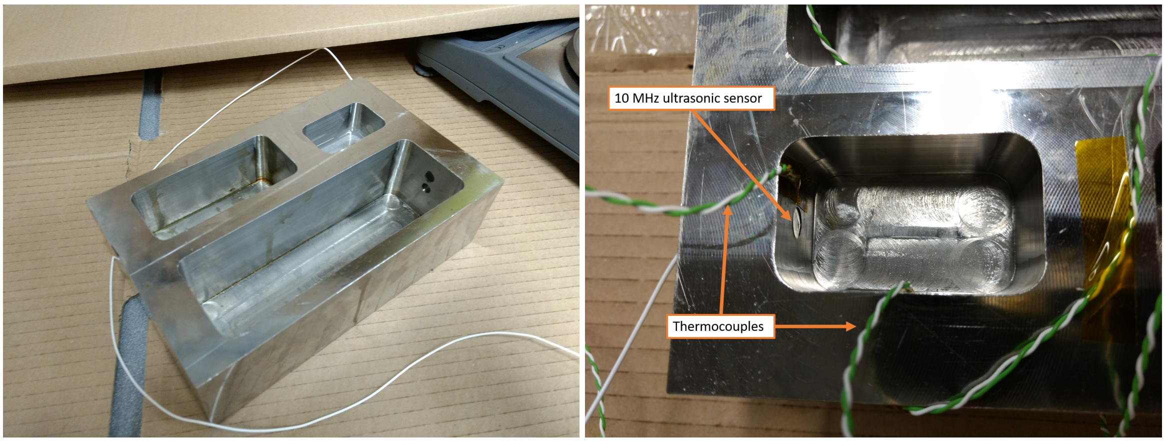

(a) Speed of sound test rig. (b) Instrumented 'Speed of Sound' rig.

Figure 5.1: Lubricant speed of sound test rig.

$$Speed\ of\ sound(c) = \frac{Path\ length}{Time\ of\ flight(T)} \tag{5.1}$$

Equation 5.1 was used to define the speed of sound in the 0W-20 oil for heating and cooling for the temperature range applied as shown in Figure 5.2. The density variation over this temperature range is included in this plot, whilst this temperature variation data was provided by Jaguar Land Rover.

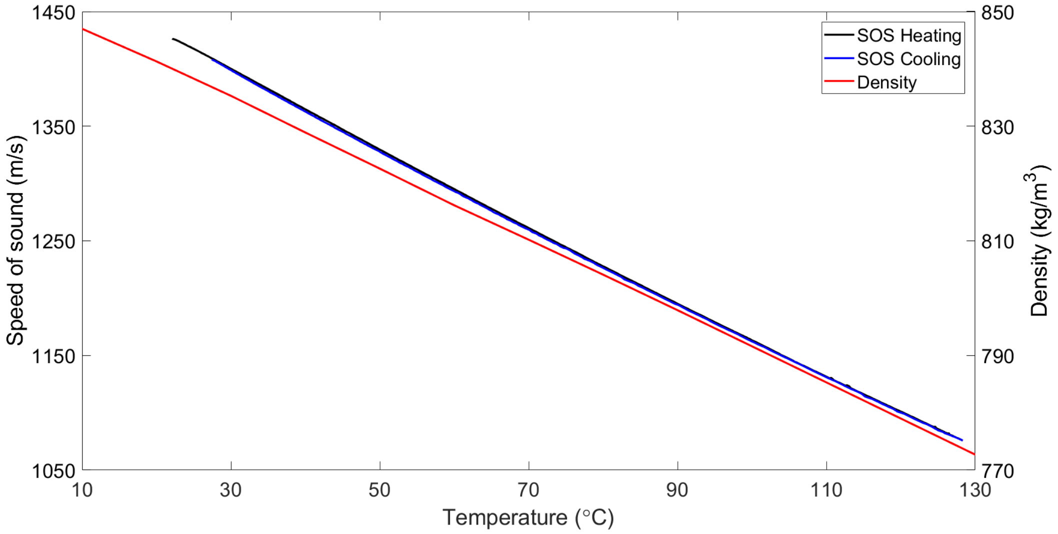

Figure 5.2: Speed of sound and density variation of 0W-20 over a temperature range.

Applying a linear regression to the data for 0W-20 density and speed of sound provides Equations 5.2 and 5.3 for the density and speed of sound respectively.

$$\rho = -0.624T + 854 \tag{5.2}$$

$$c = -3.350T + 1500 \tag{5.3}$$

The pressure effect on the oils density and acoustic wave velocity can also be accounted for. Although, because the engine block is driven with the cylinder head removed the pressure variation is not considered here.

5.2 Ultrasonic instrumentation

The piezoelectric transducers were located on the back surface of the cylinder liner that was exposed during the CNC machining on the engine block as outlined in Section 4.2.1. A range of varying central frequency transducers were instrumented onto the liner to evaluate their response through cast iron. The ideal sensor selection was based upon optimal transducer response and instrumentation success, this resulted in 5 MHz DL-10 (curie temperature: 350°C) transducers being selected for instrumentation arrays. As previously considered in Section 3.7, to provide a suitable spatial resolution of the ultrasonic transducers the transducer width should be less than the piston ring width. The final dimensions of the transducers were 1 mm x 4 mm, equal to the thickness of the thinnest ring (when considering the overall dimensions of the oil control ring), see the ring dimensions in Figure 5.3.

The machined slots that were sufficient to enable fired engine testing in the future restricted access to the liner, this limited instrumentation to four sensors in the machined slots on the thrust and anti-thrust side of the engines. The location of the sensors and numbering convention are defined in Figure 5.3. The spread of ultrasonic transducers over this range was defined such that it was capable of studying each piston ring close to its TDC position and for measurements of the upper portion of the piston skirt.

The sensors were bonded using M-Bond 610, an industrial adhesive that was cured at elevated temperatures using a hot air gun directed onto the sensor area for a two hour interval. Ideally, the sensors would have been cured in a thermostatic oven, although the size of the engine block prevented this possibility. The cured sensors with a protective layer of kapton tape can be seen in Figure 5.4a. A coaxial cable was connected to the live of each sensor using a silver epoxy and ground onto the engine block. Figure 5.4b shows the sensors post one sensor having a cable connected. Following cabling, the sensors were covered with an

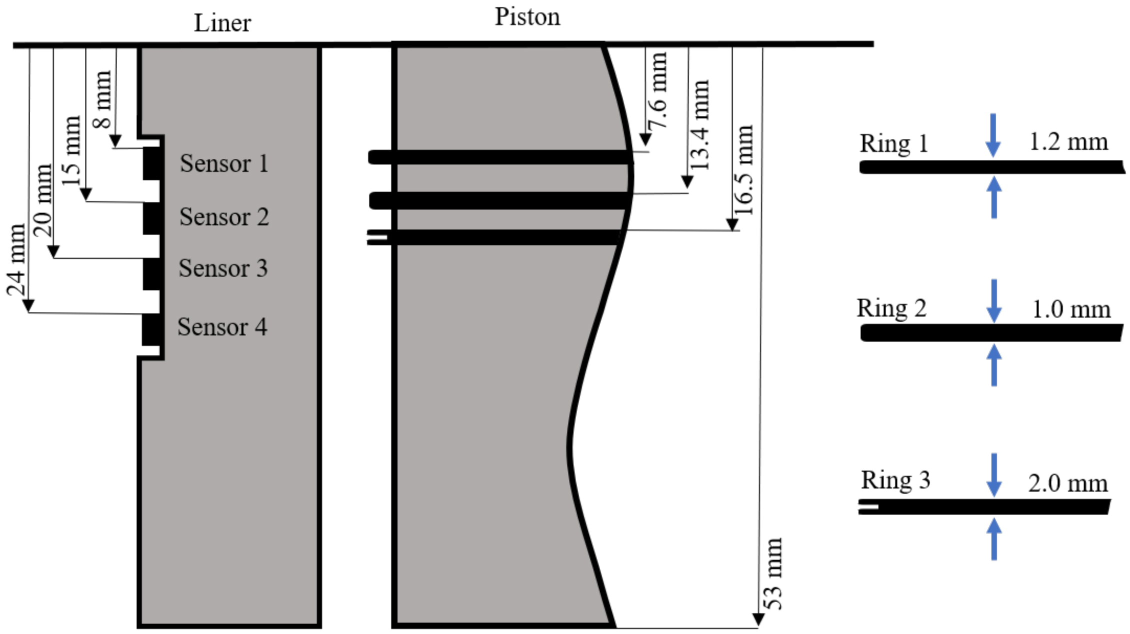

Figure 5.3: Sensor instrumentation in the slot on the thrust and anti-thrust side of Cylinder 4.

epoxy potting compound to protect the transducers from damage and seal against coolant if the coolant circuit was to be used in the future.

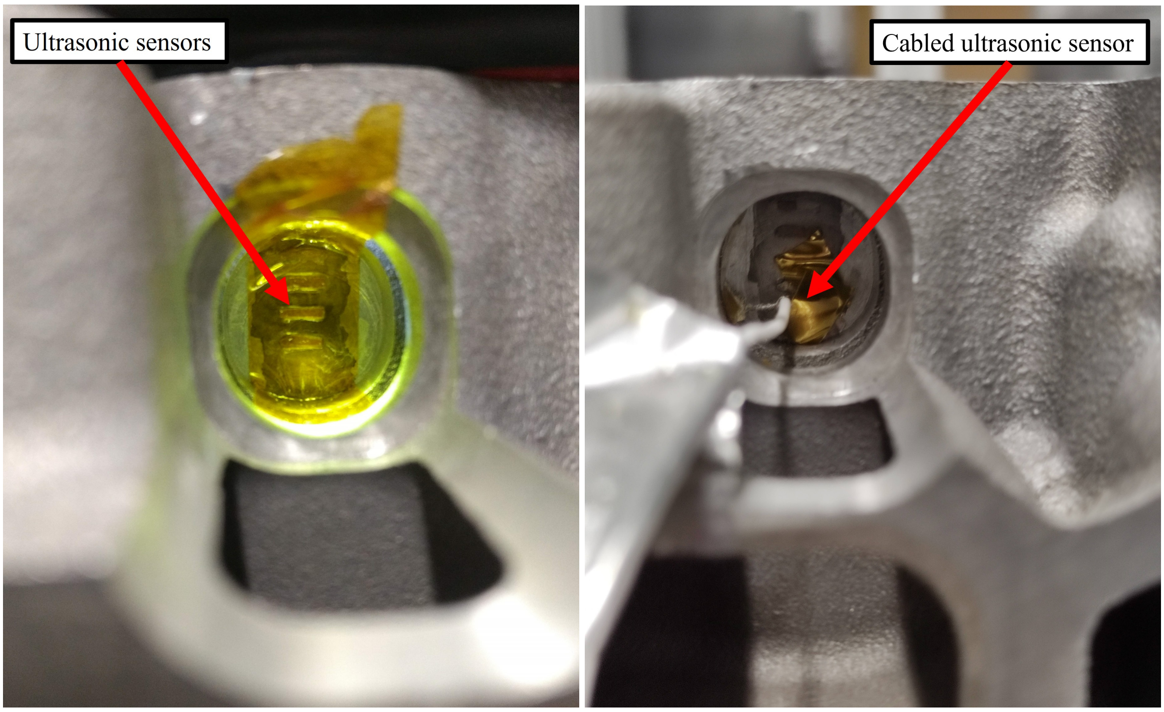

(a) Instrumented piezoelectric sensors.

(b) Cabled piezoelectric sensor.

Figure 5.4: Bonded and cabled piezoelectric sensors on the anti-thrust side.

5.3 Test conditions

The motored engine block test rig was capable of steady-state and dynamic testing. This led to the testing program as outlined in Table 5.3. The speed variation testing was all performed at steady-state operation, this was defined by running the test rig for extended intervals and monitoring the thermocouple variation over time. A comprehensive plan of future proposed testing conditions on the test rig was shown in Section 4.4. In between each engine speed, the test rig was turned off, this provided start-up and shut-down intervals of the engine to record further data.

Table 5.3: Matrix of tests performed.

Test type	**Test conditions**	**Units**
Speed variation	360, 540, 800, 900, 1000	rpm
Start-up	At each speed	-
Shut-down	At each speed	-

The speed variation included two speeds below idling speeds of the fired engine (360, 540 rpm) during which the oil pump would not have been fully engaged during normal operation. As the engine control unit was not used in the test rig, the oil pump was purely run from the crankshaft and, therefore, the pump ran at full operating conditions at each engine speed. This was done to access the difference in the build-up of the lubricant film during non-standard engine block operation.

5.4 Data acquisition

An FMS100 PC was used to perform the ultrasonic analysis. This unit contains a PC that runs an in-house built LabVIEW programme that controls various factors of how the ultrasonic wave was initiated and recorded. Furthermore, within the UPR there is a wave generation card to generate short voltage pulses that are sent to the sensors. The reflected waves are received by the oscilloscope that is digitised and fed into the LabVIEW program. The FMS also enables the encoder output from the Sick shaft encoder to be fed directly into the PC and the thermocouples located next to the transducers were connected to the PC via a TC-08. A summary of the ultrasonic setup is shown in Figure 5.5.

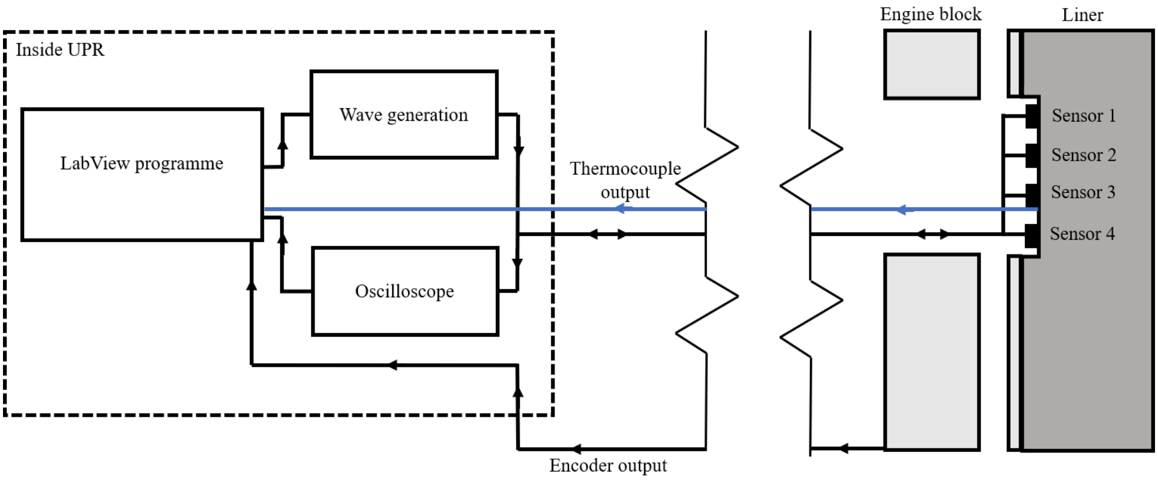

Figure 5.5: Summary of the ultrasonic equipment for the motored AJ200 testing.

The ultrasonic recordings lasted for 3 seconds for the steady-state captures at all tested speeds, whilst any start-up/shut-down tests lasted for an extended time interval (up to 30 seconds) to cover the initial build-up or breakdown of the lubricant film. Typical settings for the ultrasonic transducers are shown in Table 5.4. These settings were set such that the ultrasonic reflection was optimised within the captured window. This utilised the FMS100

PC resolution for a greater recorded reflection amplitude and purely the ultrasonic reflection of interest was captured, see Figure 5.6c for a series of captured reflections.

Table 5.4: Typical settings of the piezoelectric sensors.

Setting	**Value**	**Units**
Gain	230	-
Pulse width	5	ns
Range	8	ns
Filter	4	-
Voltage	75	V
Pulse rate	75	kHz

5.5 Data processing

A series of data processing steps were performed to the raw ultrasonic reflections to provide the oil film thickness, these stages are shown in Figure 5.6. The raw data consisted of a continuous series of the time domain reflections of the ultrasonic wave as shown in Figure 5.6a. The reflections across a ring pack passage are shown in Figure 5.6b and the stream of sequential reflections can be seen in Figure 5.6c. To determine the reflection coefficient each reflection was isolated and converted to the frequency domain, see Figure 5.6d, the central frequency and bandwidth are overlayed figure. The ring alignment signal was normalised relative to the reference signal to define the reflection coefficient in Figure 5.6e. The reference signal was defined by the mean reflection from the region where the ring pack was significantly far from the sensor, the area where there is no variation in the recorded reflection, see the green region in Figure 5.6a. It can be seen in Figure 5.6e that there are large variations in the reflection coefficient outside of the bandwidth whilst in the bandwidth there is a reduced variety in the reflection coefficient. The oil film thickness over the frequency range is shown in Figure 5.6f that was determined by the application of Equation 5.4 with the addition of the equations for the oil's density and speed of sound as seen in Equations 5.2 and 5.3. The temperature used in those equations was set by the thermocouple measurements from next to the ultrasonic sensors.

$$h = \frac{\rho c^2}{\omega Z_1 Z_2}\sqrt{\frac{|R|^2(Z_2+Z_1)^2-(Z_2-Z_1)^2}{1-|R|^2}} \tag{5.4}$$

The crank angle (CA) at which a piston ring was aligned with a sensor was calculated from the location of the sensor position relative to the piston at the TDC and the piston displacement through the piston stroke such as that seen in Section 2.3. Therefore, the figures are presented in terms of CA after TDC (aTDC).

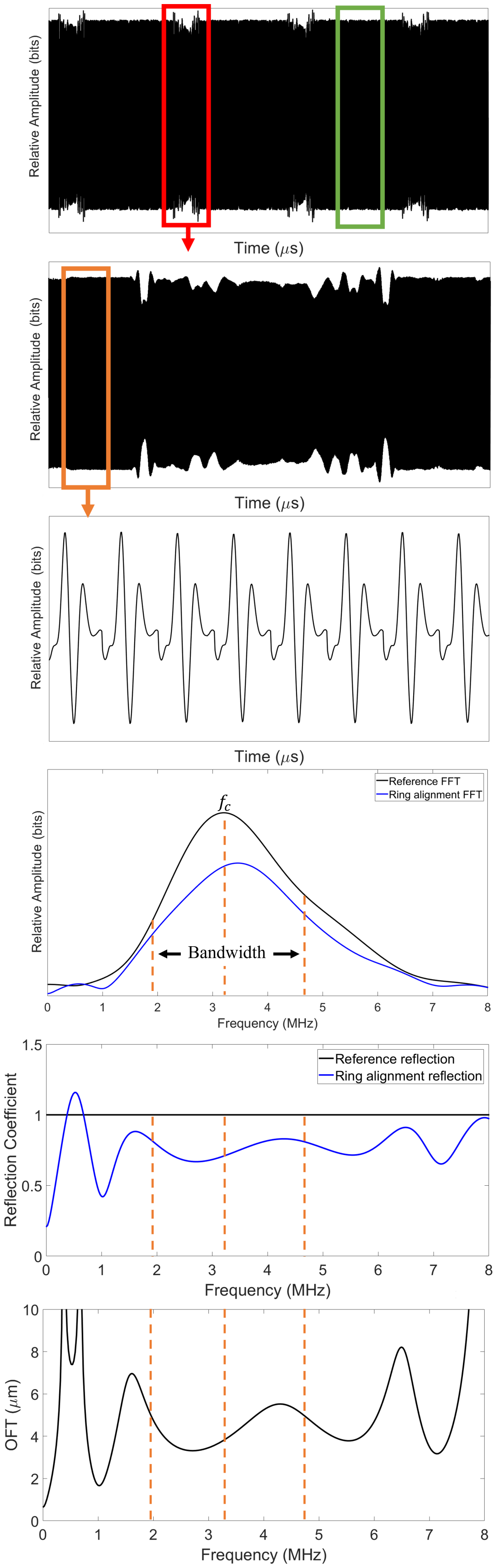

a) Raw recorded data

b) Zoomed in view of a ring pack passage

c) Series of reflections

d) Frequency domain view of ring alignment signal relative to reference signal

e) Reflection coefficient over a frequency range

f) Oil film thickness over a frequency range

Figure 5.6: Data processing stages from raw data to oil film thickness.

5.6 Reflection coefficient

The reflection coefficient used for the OFT measurements was defined using the central frequency of the sensor, isolating this reflection coefficient from each signal for each reflection provided the variation as the ring pack moves past the sensor. The reflection coefficient from a typical ring pack passage from a slow crankshaft revolution can be observed in Figure 5.7.

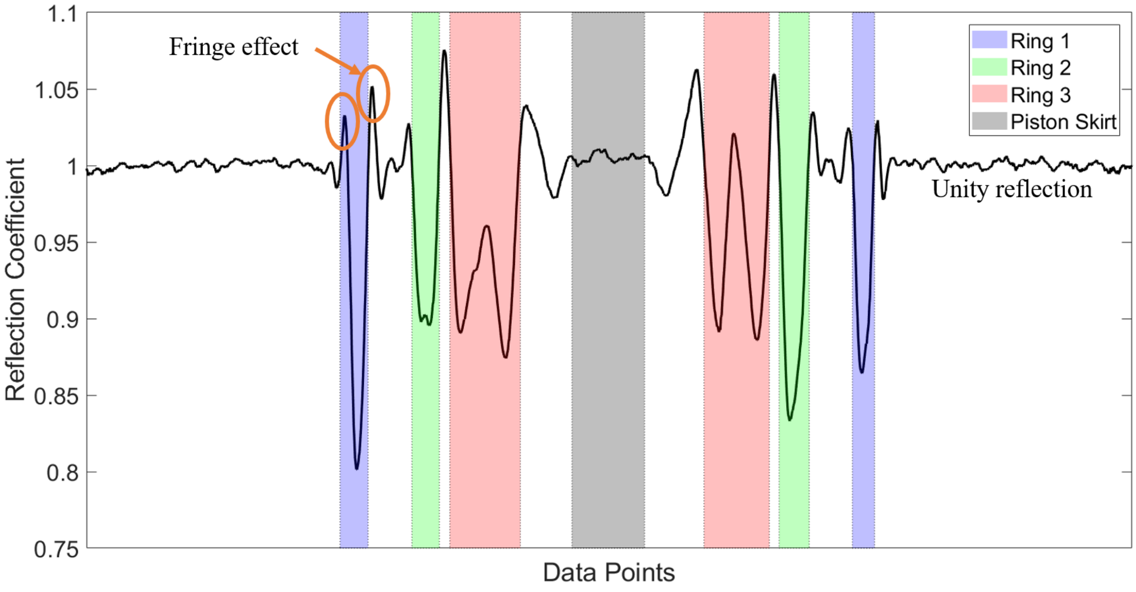

Figure 5.7: Reflection coefficient from slow test rig spin highlighting each piston ring.

The reflection coefficient for Sensor 3 on the anti-thrust side is shown in Figure 5.7. This sensor covers all three piston rings and all the rings are identifiable in the reflection coefficient, including the two rails of the oil control ring. The piston skirt was aligned with the sensor at the TDC and is, therefore, in-between the ring pack passage on the up- and down-stroke.

The variation in reflection coefficient in Figure 5.7 displays a few factors that are common in ultrasonic reflection coefficient results:

- The alignment of a piston ring leads to a reduction in reflection coefficient as a portion of the wave was transmitted into the piston ring.
- A anomalous fringe effect was seen on either side of the ring passage (anomalous as reflection coefficients greater than R=1 are unexpected).

- A unity reflection (R=1) was seen at all points outside of the ring pack passage and any variations in this region are anticipated to be due to noise in the system.

5.7 Oil film thickness

The oil film thickness for the regions of ring/skirt alignment with the sensors were calculated according to Equation 5.4 with the refinement from the density and speed of sound measurements of the oil. Two sensors are focused on during this section, selected for their optimal location and results, Sensor 1 on the thrust side and Sensor 3 on the anti-thrust side.

The oil film thickness over Sensor 1 on the thrust side is shown in Figure 5.8 for a range of test rig speeds at steady-state. Four differing regions of lubricant film thickness are highlighted via the orange vertical lines.

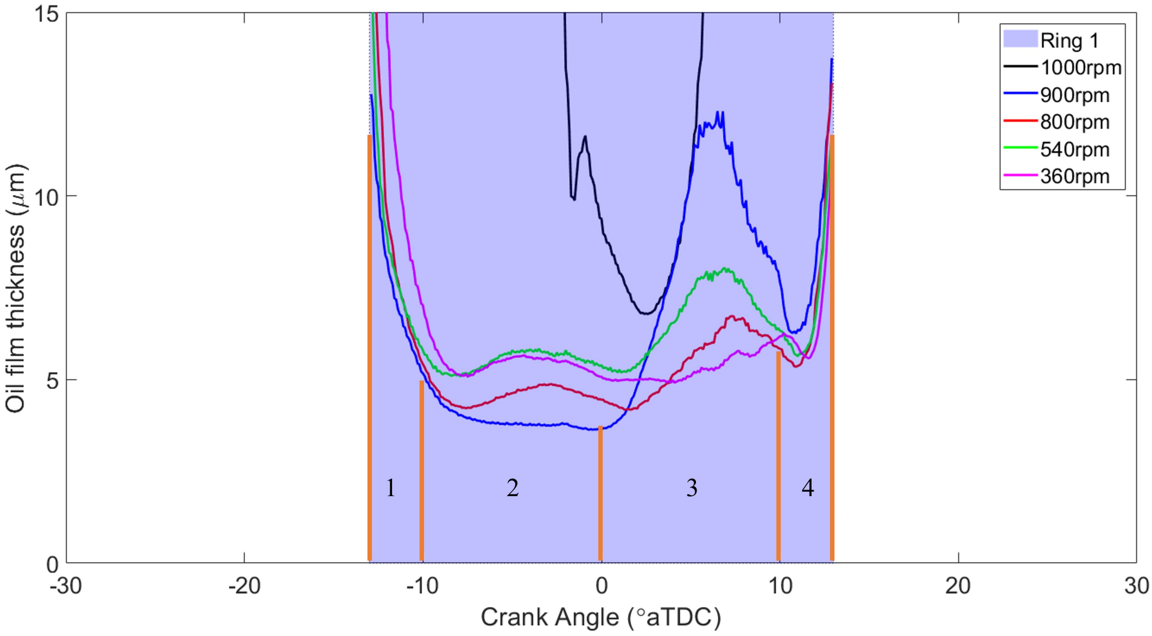

Figure 5.8: Oil film thickness for a series of steady-state test rig speeds over Sensor 1.

In Figure 5.8, oil films of a similar magnitude (up to 12 μm) are seen for all speeds considered although some unexpected trends are observed. Firstly, at 1000 rpm, significantly differing OFT values and trends are seen. The Spring Model only rendered appropriate lubricant film thickness measurements over a narrower CA range (-3° to 5° CA) than expected. Therefore, this speed should be treated as erroneous for this sensor. The cause of which is unknown as the test rig was given the same time to achieve steady-state operation for each speed. Furthermore, it was expected to see an increase in the lubricant film thickness as the engine speed increased due to greater entrainment of lubricant. Therefore, the cause of these trends requires further study.

Inspection of the OFT for the four remaining test rig speeds highlights several regions of OFT variation (orange lines in Figure 5.8):

1. -13° to -10° CA: Sharp reduction in OFT as the piston ring initially moves over the sensor. The averaging effect of piezoelectric transducers will have led to an overestimation of the film thickness here due to minor alignment of piston ring and sensor. This is also discussed in Section 6.5.
2. -10° to 0° CA: Each speed has a stable OFT ($< 1\ \mu$m variation at each speed) with the unexpected general trend of an increased speed producing a thinner lubricant film thickness. Due to the engine block being motored, the differences in film thickness may have arisen from the steady-state temperature variation at different engine speeds. At 900 rpm the steady-state temperature was greater than that at 360 rpm leading to differing oil properties (viscosity, density and speed of sound) and thus differing OFT values were calculated from Equation 5.4.
3. 0° to 10° CA: After the TDC of the piston there was a reversal in the OFT trends. A sharp rise in the film thickness is seen that has an inflexion point at 5°-7° CA before the film thickness decreases again. The cause of these trends in the preliminary work is unknown and requires further study.
4. 10° to 13° CA: A sharp rise in the OFT, the opposite of -13° to -10° CA. The film is thicker than that in Region 1 as more oil is being entrained into the contact.

The lubricant film thickness is plotted for Sensor 3 on the anti-thrust side for a range of steady-state test rig speeds in Figure 5.9. This sensor covers all three piston rings and the piston skirt and, therefore, has a greater level of complexity than the previous OFT figure. The different piston rings and the skirt are highlighted in Figure 5.9 via the varying shaded regions.

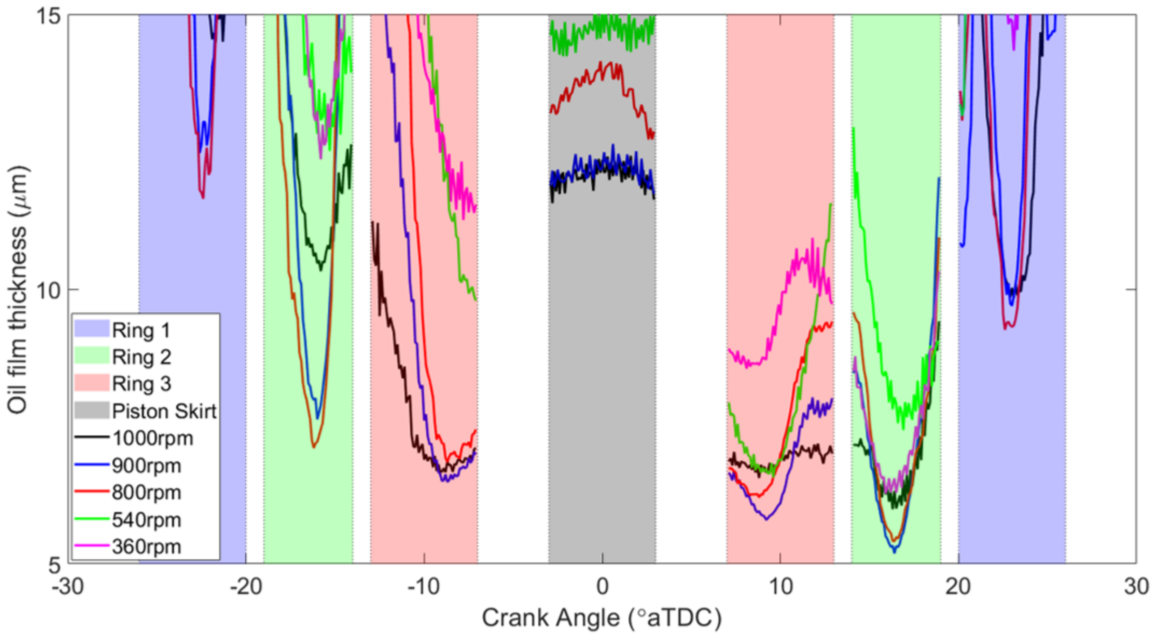

Figure 5.9: Oil film thickness for a series of steady-state test rig speeds over Sensor 3.

It can be seen in Figure 5.9 that each piston ring and the skirt is identifiable over Sensor 3 at each steady-state level as highlighted in the various CA ranges. The erroneous 1000 rpm for Sensor 1 (Figure 5.8) does not appear clearly anomalous for Sensor 3 as similar trends to the other engine speeds are seen.

Overall, the same trends are shown as with Sensor 1, that a sharp rise in the OFT on either side of a ring passage is seen. Furthermore, a narrower measurement of the OFT is seen as the piston rings moved over the sensing region at greater velocities than for Sensor 1. Sensor 3 does not display the peculiar inflexion trend that was seen by Sensor 1 in Figure 5.8 although this may be due to no piston ring being aligned with this sensor at the TDC. Instead, the piston skirt was aligned with this sensor at the TDC, which for all engine speeds excluding 800 rpm provided relatively level film thickness values (standard deviations of ± 0.4 μm). Whilst 800 rpm displayed a build-up (13 to 14 μm) and reduction (14 to 12.5 μm) in film thickness, reversing at 1° CA.

Similar to Figure 5.8, a greater test rig speed led to a reduced minimum lubricant film thickness for the majority of piston rings and skirt, which is observed for all speeds, even with 1000 rpm which produced erroneous results over Sensor 1. The starkest deviation from this trend was for the second ring on its upward stroke, in which 1000 rpm produced lubricant films of 10.2 μm whilst at 800/900 rpm measurements of 7.5 μm were recorded.

In theory it would have been expected that a greater lubricant film thickness was seen at higher engine speeds due to greater lubricant entrainment, therefore, the cause of these trends requires further study.

At each test rig speed, Ring 1, the first piston ring had the greatest lubricant film thickness which is not typically expected in a fired engine as this ring forms the primary buffer between high and low pressure during the combustion process and lubricant film breakdown of the piston rings close to the TDC is not unexpected. Instead, in the motored test rig, the lack of combustion pressure did not expel lubricant down the liner leading to more oil remaining at the top of the liner. This led to an excessive amount of oil being retained at the top of the liner which is directly reflected in terms of thicker lubricant films being measured for the first piston ring. A likewise trend is observed for the other piston rings as thick films were measured for all rings.

A reduction in the film thickness is seen for the downstrokes relative to the upstrokes for all piston rings. For example, the first ring shows a 30% reduction between the up and down stroke for 800 and 900 rpm. This reduction is an indicator of the piston ring pack operating as designed, that between the two passages of the compression ring, the oil control ring passes twice. Each control ring passage removes an amount of excess oil leading to a reduction in film thickness. This trend is expected to be enhanced during fired operation due to combustion pressure and combustion of lubricant.

5.8 Minimum oil film thickness

The minimum oil film thickness (MOFT) has been isolated for each piston ring and the skirt for each ring pack passage. The mean of these values has been used to produce the MOFT for each ring in each data capture with the addition of the standard deviation. The MOFT for the first compression ring over Sensor 1 at each test rig speed is shown in Figure 5.10. Note 1000 rpm has been removed due to the anomalous results in Figure 5.8.

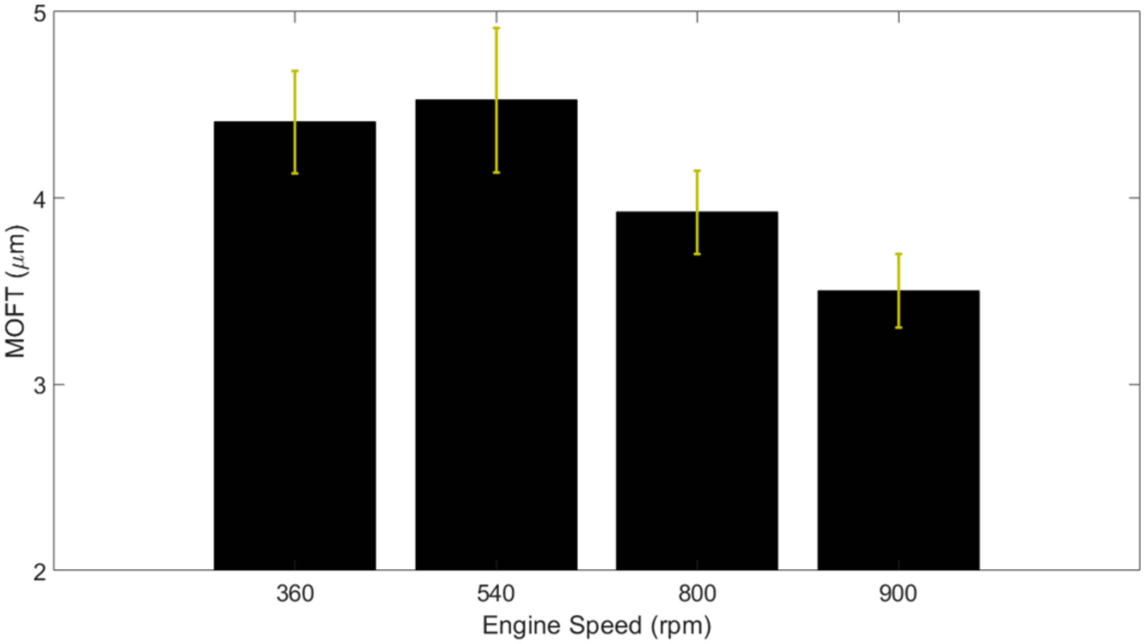

Figure 5.10: Minimum oil film thickness for Sensor 1 at a range of test rig speeds, 1000 rpm has been excluded due to erroneous results in Figure 5.8.

Observation of the MOFT over Sensor 1 at steady-state shows the two speeds below typical idling of the engine (360 and 540 rpm) produced similar MOFT values around 4.5 μm with similar standard deviations (± 0.3 and ± 0.4 μm for the speeds respectively). Above the idling speeds of the engine, an increase in the test rig speed is shown to reduce the MOFT. At 800 rpm, the MOFT is 3.9 μm ± 0.2 and at 900 rpm 3.5 μm ± 0.2. Minor reductions in the standard deviations are also seen as the engine speed increased (± 0.40 to 0.22 to 0.18 for 540 to 900 rpm).

The sensor on the anti-thrust side (Sensor 3) enables a comparison between the up and down strokes of each piston ring. Figure 5.11 shows the MOFT and standard deviation for the first and second ring at steady-state.

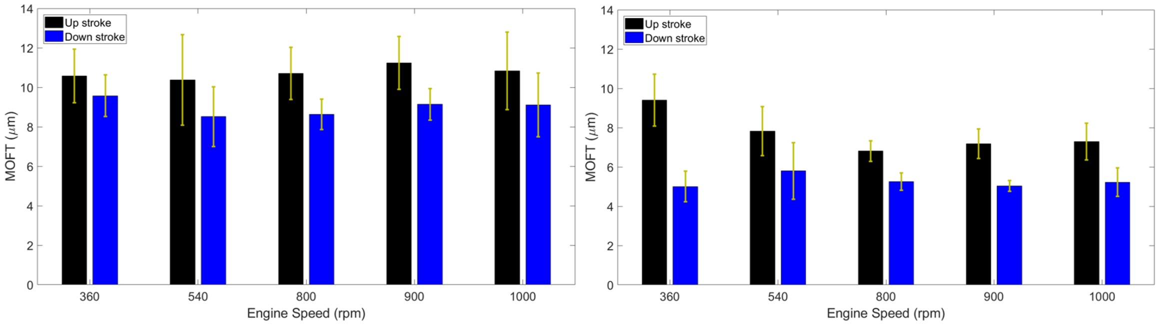

(a) First compression ring.

(b) Second compression ring.

Figure 5.11: MOFT variation for Sensor 3 between up- and down- strokes for two piston rings at steady-state operation.

Both figures within Figure 5.11 clearly show the difference between the MOFT on the up and down strokes of the piston. The downstroke is consistently thinner, typically in the order of a 20% reduction in the MOFT and a reduced variation in the standard deviation. Between the two passages of each of these piston rings the oil control ring moved over the sensing region twice, removing excess oil. For both piston rings a reduced standard deviation is seen on the downwards stroke, this indicates that following the oil control ring a more consistent lubricant film remains on the liner. Whilst on the upstroke, excessive pooling of lubricant led to greater variety in the minimum film thickness measured.

Similar to the general OFT trend seen in Figure 5.9 a greater MOFT is seen for the first ring than the second. This is primarily anticipated to be due to the motored operation of the engine with the cylinder head removed. Therefore, the lack of combustion pressure did not expel lubricant down the liner, leading to more being retained at the top near the TDC of the piston rings. Therefore, significantly more lubricant was present here than would have been expected under fired operation of the engine. Due to this, the trends between the first and second ring are likely unrepresentative of those of fired operation of the engine.

The lambda ratio ranged from 2.5 to 3.2 over Sensor 1, indicating that the first compression ring was under mixed mode lubrication when the ring was close to the TDC. Whereas when the ring moved over Sensor 3, the lambda ratio was 5.7 to 7.8, which is in the hydrodynamic regime. Therefore, when the piston ring velocity was reduced, the film thickness decreased sufficiently to change the lubrication regime of the piston ring.

5.9 Conclusions

The OFT measurements from the motor-driven AJ200 engine have demonstrated how the lubricant film varies with engine speed. However, through the course of this testing, several factors have limited the magnitude of substantive results.

The machined slots were designed to enable minimal modification to the engine block to instrument the dry liner with ultrasonic transducers. Whilst enabling the potential for either a driven engine with the coolant circuit running or for full fired operation in the future. These requirements hindered the complexity of transducer arrays that could be instrumented onto the liner to a high-quality standard, leading to arrays of four ultrasonic transducers in the slots on the thrust and anti-thrust sides of the block.

The piezoelectric transducers have successfully measured the OFT variation as a ring moved past the sensing region and the MOFT for each ring at each speed has been defined. However, due to the inability to measure the temperature of the oil in the contact, all measurements will have a temperature shift (and, therefore, a speed of sound and density shift) shifting the calculated OFT from the true OFT. The nearest practically achievable temperature measurements were from the thermocouples located next to the transducers, which will have been cooler than the oil in the contact by an unknown factor. However, as a consistent temperature sensing location was used, the trends between test rig speeds should remain unchanged. Further to this, the averaging effect of ultrasonic transducers will have led to overestimations in the lubricant film thickness, especially in the regions of major misalignment between the piston ring and sensor. Therefore, the true lubricant film thickness will have been thinner than those shown here.

The trends in the driven engine block are also inconclusive at points, with Sensors 1 and 3 showing opposing indications of engine operation at the top end of the speed range. Sensor 1 indicated a potential engine block issue at 1000 rpm preventing the test rig from achieving steady-state operation whilst Sensor 3 provided more anticipated results. Furthermore, the top piston ring was found to have a thicker lubricant film than the other piston rings which opposes the expected trends. The pooling of excess lubricant led to a greater film thickness being measured for the first ring (and likely to impact the other piston rings to a lesser extent) than would have been seen under fired operation of the engine. Therefore, the results presented here are likely unrepresentative of the engine under fired operation. A summary of the concluding findings from this chapter can be condensed to the following:

- Ultrasonic transducers have been instrumented onto the thrust and anti-thrust side of the cylinder liner in a motored AJ200 engine. The press-fit liner increased the difficulty in ultrasonic instrumentation limiting the complexity of possible transducer arrays.

- The piezoelectric transducers have been capable of identifying each piston ring and the piston skirt at a range of speeds. Although the trends found in the preliminary results require further study for conclusive findings.

- The first piston ring has been found to consistently produce thicker films than the other piston rings. This result is expected due to the lack of combustion pressure. Therefore, the lubricant is not expelled down the liner leading to more oil being retained close to the TDC position of the piston rings. In addition, upstrokes produced thicker films than the downstrokes.

- The motored AJ200 block has enabled high-resolution measurements of the oil film thickness between the piston ring and liner. Although some of the identified trends are unexpected and applicability of the results to those of fired engine operation are limited. In addition to a number of practicality limitations hindering the quantity and quality of results measured. Therefore, application to a fired ICE with either an already exposed liner or removable liner has the potential for more substantive results.

Chapter 6

Lubricant injector comparison in a fired marine diesel

This chapter furthers the piston ring oil film thickness measurements applied to the AJ200 motored engine block in Chapter 5 onto a fired marine diesel engine, an RTX-6 Winterthur Gas and Diesel (WinGD) engine. Marine engines are much larger and operate at significantly slower rotational speeds than their automotive counterparts. Therefore, giving the potential for greater resolution in oil film thickness measurements at a cost of a greater path length for the ultrasonic wave to spread over. This chapter summarises and expands upon the findings shown by the author in [6].

6.1 Test engine

Following the ultrasonic instrumentation and motored engine block testing on the AJ200, it was desired to apply a similar instrumentation route to a larger engine. This was aimed to provide several benefits: the larger engine size was likely to reduce the complexity in ultrasonic instrumentation, the slower engine operation allows for a higher resolution of ultrasonic result and little research had been performed on piston ring oil films in marine engines from an ultrasonics perspective. This led to the selection of a large two-stroke diesel marine engine, an RTX-6 WinGD engine seen in Figure 6.1. This engine is a test engine of the same design that is typically used in cargo vessels. The test engine is located at a WinGD test site in Winterthur. The main engine parameters are shown in Table 6.1 and all three piston rings are barrel-faced single pieces of steel coated with chromium-ceramic. The R_a of all the piston rings was less than 1 μm and a similar roughness was achieved on the cylinder liner.

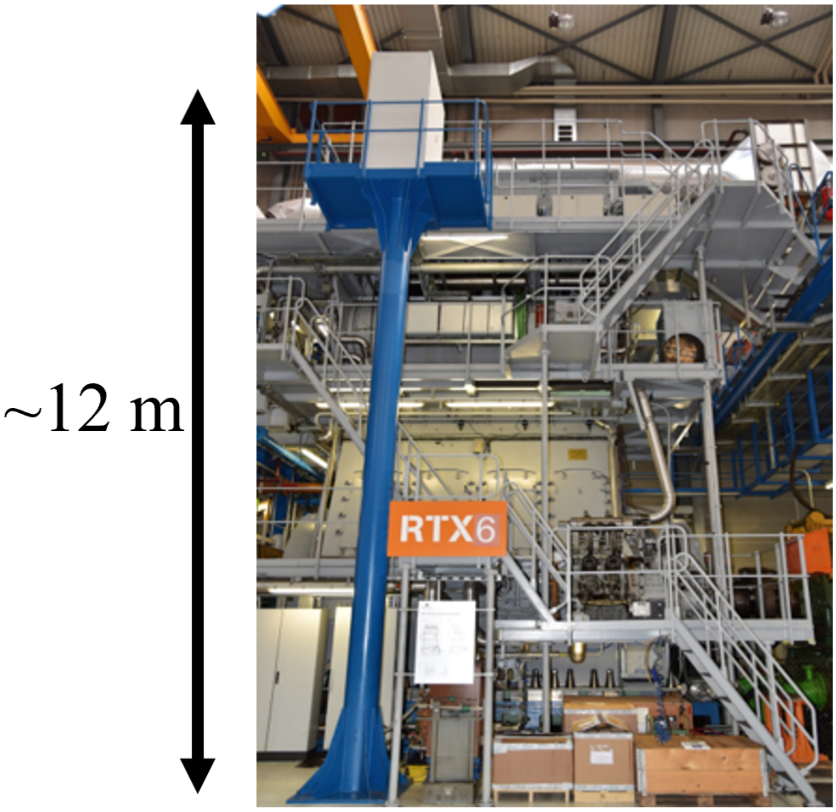

Figure 6.1: RTX-6 engine [6]. © SAE International

Table 6.1: Main engine parameters for the RTX-6 engine [6]. © SAE International

Engine parameter	**Value**	**Unit**
Maximum power	6470	kW
Cylinder bore	500	mm
Piston stroke	2250	mm

The piston stroke in a marine engine is significantly larger than its automotive counterpart, in the case of the RTX-6 engine the piston stroke is 2250 mm. Marine engines are generally two-stroke and significantly larger, this is due the increased efficiency relative to four-strokes and a greater power density as combustion occurs every TDC of the piston. The RTX-6 test engine is fitted with two lubricant injector rails, the upper and lower injection systems are located 400 mm and 800 mm from the TDC of the piston, as shown in Figure 6.2. A complex distribution system is required to provide lubricant over the whole piston stroke. The standard lubricant distribution in this engine is to inject 80% of oil above the ring pack, 10% into, and 10% below the ring pack.

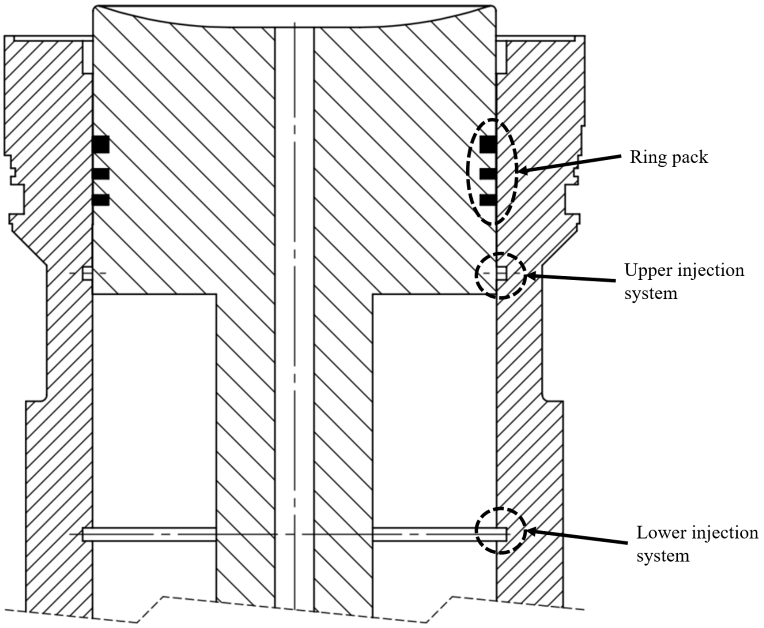

Figure 6.2: Lubricant injection rail locations relative to the piston at the TDC [6]. © SAE International

In this study two different injector designs were tested, pulse jet (PJ) injectors and needle lift type (NLT) injectors. PJ injectors are a more traditional technique implemented in marine engines. This system consists of the lubricant oil injectors, lubricant tank, filter system, and lubricant oil dosage pumps; the lubricant system's main components and a schematic of the injector system is shown in Figure 6.3 (a) and (b) respectively. The dosage pump delivers lubricant to the injectors, powered by pressurized servo oil from the engine's oil circuit. The lube oil feed rate and timing are electronically controlled by a solenoid valve in the dosage pump, providing full flexibility in setting the injection timing over the full load range of the engine.

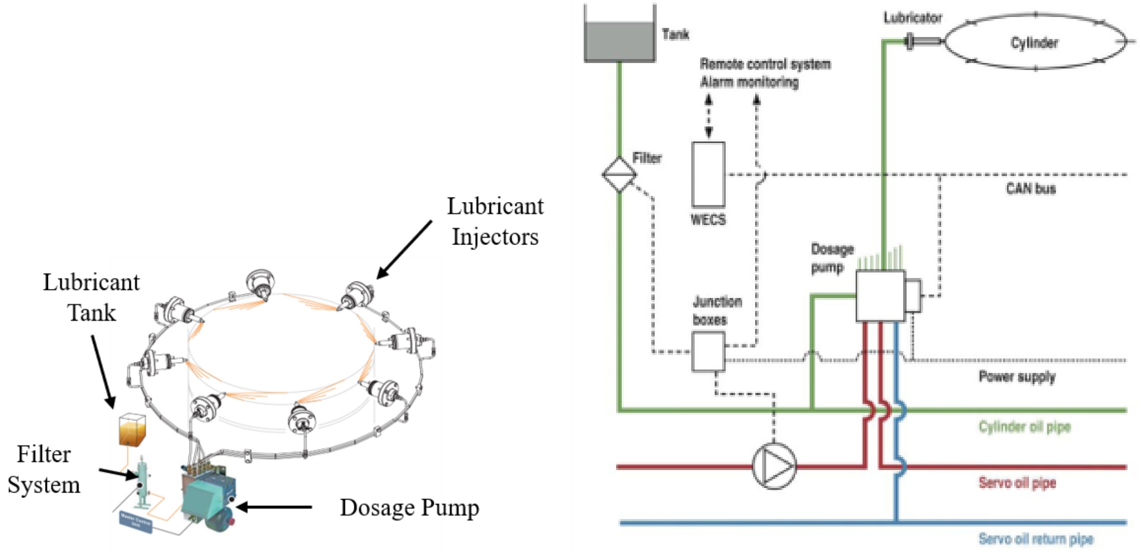

(a) Pulse jet injector components [6]. © SAE International

(b) Schematic of the complete PJ system [66]. © SAE International

Figure 6.3: Pulse Jet oil injection system.

A shortcoming of the PJ injector system is found in significant variations of the lubricant spray pattern. The necessity to control the spray characteristics, to optimise lubricant utilisation led to the development of a needle lift type injection system in conjunction with a common rail approach. NLT injectors are a prototype design that reduces lubricant atomisation and thus provides greater control over lubricant consumption relative to PJ injectors. The NLT injection system is shown in Figure 6.4.

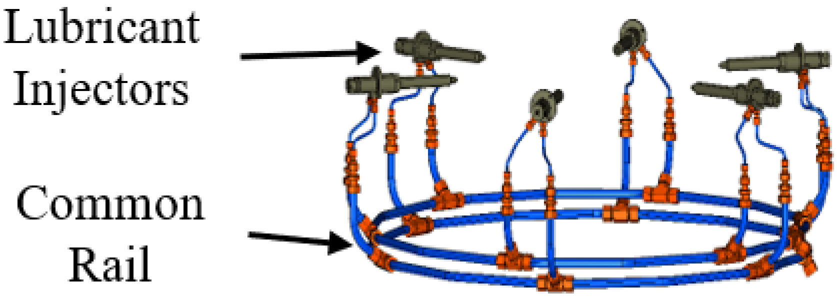

Figure 6.4: Needle lift type injector system [6]. © SAE International

These two injection systems were used to make up three injector configurations as shown in Table 6.2. In Configuration 3, the lower lubricant injection system consisted of modified PJ injectors to provide a more comparable injector nozzle design to NLT injectors.

Table 6.2: Lubricant injector setup summary [6]. © SAE International

Parameter	**Value**	**Unit**
Configuration 1	Upper System	PJ
	Lower System	NLT
Configuration 2	Upper System	NLT
	Lower System	PJ
Configuration 3	Upper System	PJ
	Lower System	PJ-Modified

6.1.1 Ultrasonic instrumentation

In this work, seven 1 MHz (curie temperature: 350°C) piezoelectric transducers were instrumented onto the liner. This chapter covers 4 of those sensors that were instrumented for oil film thickness measurements, each sensor had a 14 mm active element diameter. The additional sensors are covered in Chapters 7 and 8. Lower frequency ultrasonic sensors were used on the RTX-6 than the AJ200 due to the cylinder liner being significantly greater on the RTX-6. As higher frequency ultrasonic waves attenuate more, lower frequencies were required to be able to detect a reflection from the internal surface of the liner/piston ring. The sensors were coupled to the external surface of the liner by applying an industrial adhesive and curing overnight at room temperature. Limitations in access to the liners external surface caused the instrumentation to be restricted to the neutral side of the end cylinder of the RTX-6. To avoid any transducer being aligned with a cooling channel within the liner, the sensors were positioned at a series of locations on the liner centred around the neutral axis of the engine, as shown in Figure 6.5a. Critically, no modifications were made to the engine to perform this work.

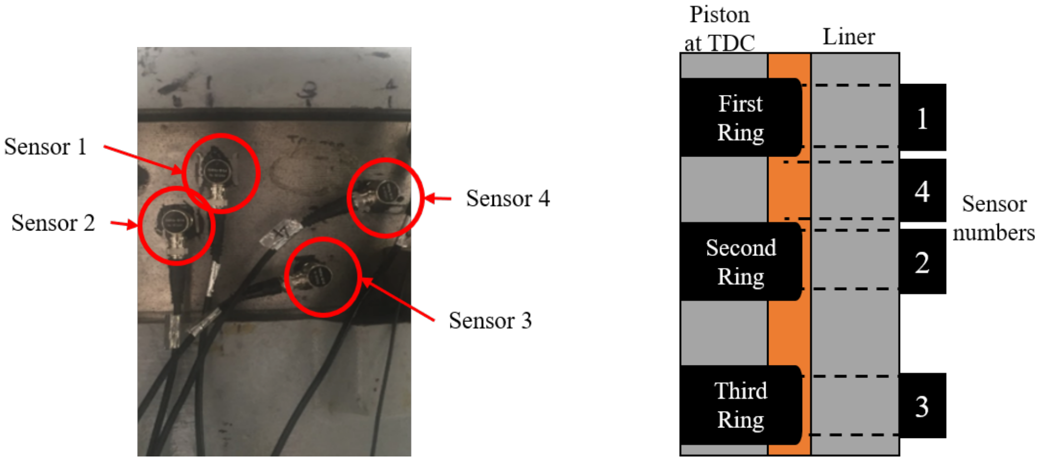

(a) Instrumented sensors.

(b) Sensor numbering convention.

Figure 6.5: Instrumented transducers and transducer notation [6]. © SAE International

One transducer was aligned with each piston ring (first ring, second ring, and third ring) when at their respective TDC positions. Whilst the fourth transducer was positioned between the top two rings at the TDC, as shown in Figure 6.5b. Each transducer was circular, with the active element diameter less than the thickness of the piston rings; minimising the averaging effect of piezoelectric transducers when the rings were at the TDC. The crank angle corresponding to each piston ring being aligned with a transducer is summarised in Table 6.3.

6.1.2 Data acquisition

The same data acquisition system as discussed in Section 5.4 was applied to record the ultrasonic measurements. The ultrasonic pulses were controlled via an in-house LabVIEW program. Each data capture duration lasted for 5 seconds, this enabled multiple engine cycles to be covered during one capture and averaging of the oil film data. Through the course of the engine testing the ultrasonic pulse rate was varied; with some tests capturing ultrasonic reflections at 1.05 kHz per channel whilst other data captures focused on each transducer in turn at higher pulse rates of 12.4 kHz. At full engine load, single-channel measurements enabled ultrasonic reflections to be recorded up to a rate of one capture per

Table 6.3: Piston ring and sensor alignment crank angle [6]. © SAE International

Piston ring	Sensor	Piston ring alignment crank angle (°aTDC)
First	1	-8.5 to 8.5
	4	-12.6 to -3.5 and 3.5 to 12.6
	2	-15.6 to -9.9 and 9.9 to 15.6
	3	-21 to -17 and 17 to 21
Second	2	-8 to 8
	3	-16 to -11 and 11 to 16
Third	3	-9.2 to 9.2

0.05° CA. The data was aligned to the engine crank angle using an encoder which produced a tick count from every TDC and every degree rotation of the crankshaft. A summary of the ultrasonic equipment used is shown in Figure 6.6.

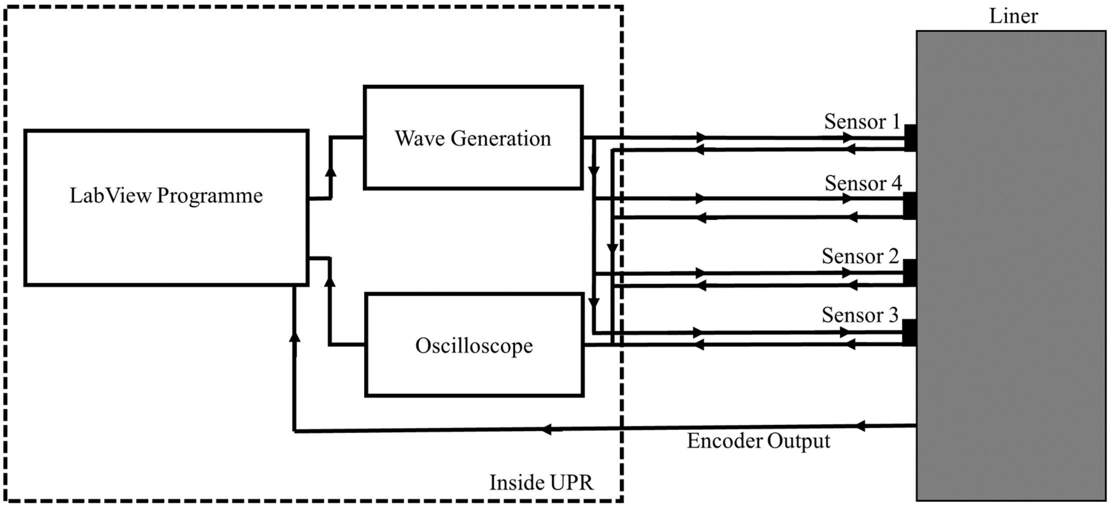

Figure 6.6: Summary of data acquisition equipment used to record ultrasonic data [6]. © SAE International

6.1.3 Speed of sound and density

To define the speed of sound and density relations of the oil, the speed of sound test rig, as previously shown in Figure 5.1 and a pressure calibration rig was used. This enabled the definition of a speed of sound and density relationship that accounted for pressure and temperature measurements. The raw measurements of the speed of sound variation with temperature and pressure are shown in Figure 6.7.

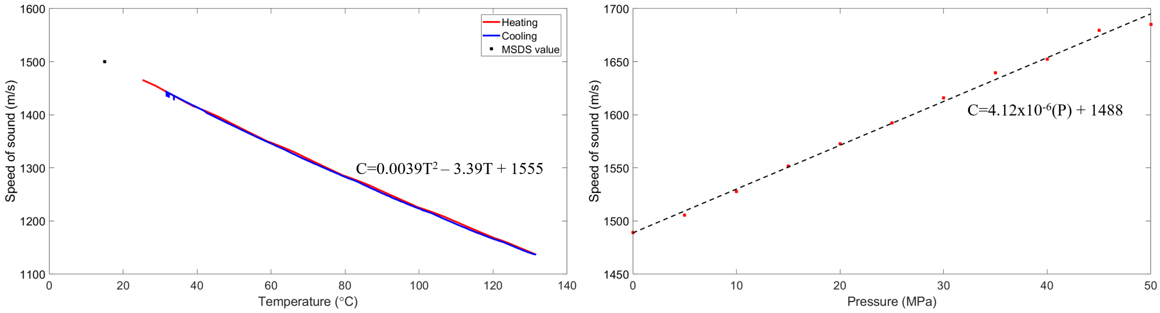

(a) Temperature.

(b) Pressure.

Figure 6.7: Speed of sound variation with temperature and pressure, reworked from [88].

A second order fit for the speed of sound relation with temperature is shown in Equation 6.1. A first order fit for the speed of sound relation with pressure as shown in Equation 6.2

$$c(T, p \ = \ 0) = 0.0039T^2 - 3.39T + 1555.2 \tag{6.1}$$

$$c(T \ = \ 20, \ p) = 4.13 \times 10^{-6} p + 1488.8 \tag{6.2}$$

Combining Equations 6.1 and 6.2 and through a series of rearrangements, a speed of sound equation accounting for both temperature and pressure variations was defined, Equation 6.3. The speed of sound variation with pressure at a series of temperatures is shown in Figure 6.8a.

$$c(T, p) = 0.0039T^2 - 3.39T + 4.13 \times 10^{-6} p + 1555.2 \tag{6.3}$$

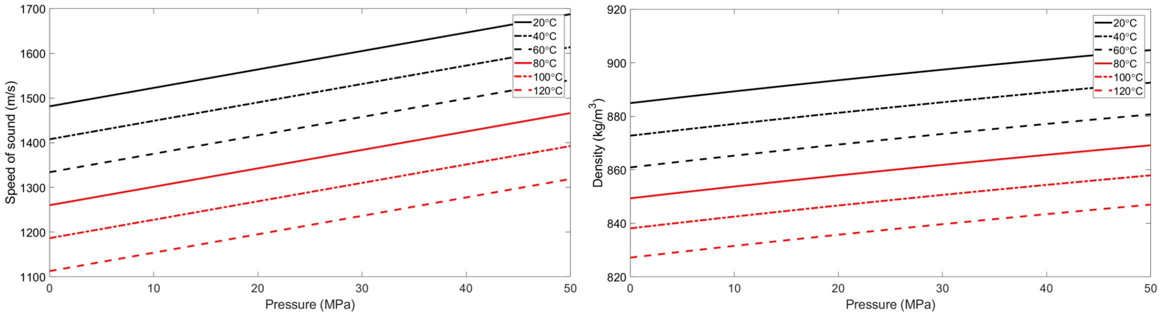

(a) Speed of sound.

(b) Density.

Figure 6.8: Speed of sound and density change with pressure at a range of temperatures, reworked from [88].

To define the density relationship, the definition of the bulk modulus as shown in Equation 6.4 was used. A series of rearrangements and substitutions led to Equation 6.5 to account for density variation with temperature and pressure. The derivation of Equation 6.4 is covered in Appendix B. Figure 6.8b provides a visualisation of density variation with pressure at a range of temperatures.

$$B = \rho \frac{dp}{d\rho} = \rho c^2 \tag{6.4}$$

$$\rho(T,p) = 162.85 + \frac{888}{1 + 0.007(T-20)} - \frac{5.88 \times 10^{1}0}{p + 3.61 \times 10^{8}} \tag{6.5}$$

Through the combination of Equations 6.3 and 6.5 with temperature and pressure measurements from the internal surface of the liner, accurate measurements of the lubricating oil properties are capable of being defined at all operating conditions.

6.1.4 Test conditions

The engine testing took place at three fired loading levels (100%, 50%, and 25%) each related to a different engine speed (105.5, 83.6, and 66.2 rpm respectively). The three loading steps are each associated with a different torque demand levels. Figure 6.9a shows the engine loading sequence over 8 hours (length of testing on each engine configuration).

Once the engine had achieved steady-state operation, the oil feed rate was varied from a nominal rate of 0.8 g/kWh to a low flow case of 0.6 g/kWh and then a high flow case of 1.2 g/kWh over the course of 20 minutes. This oil feed rate variation is summarised in Figure 6.9b and was repeated at each engine load and for each of the three engine configurations as previously shown in Table 6.2.

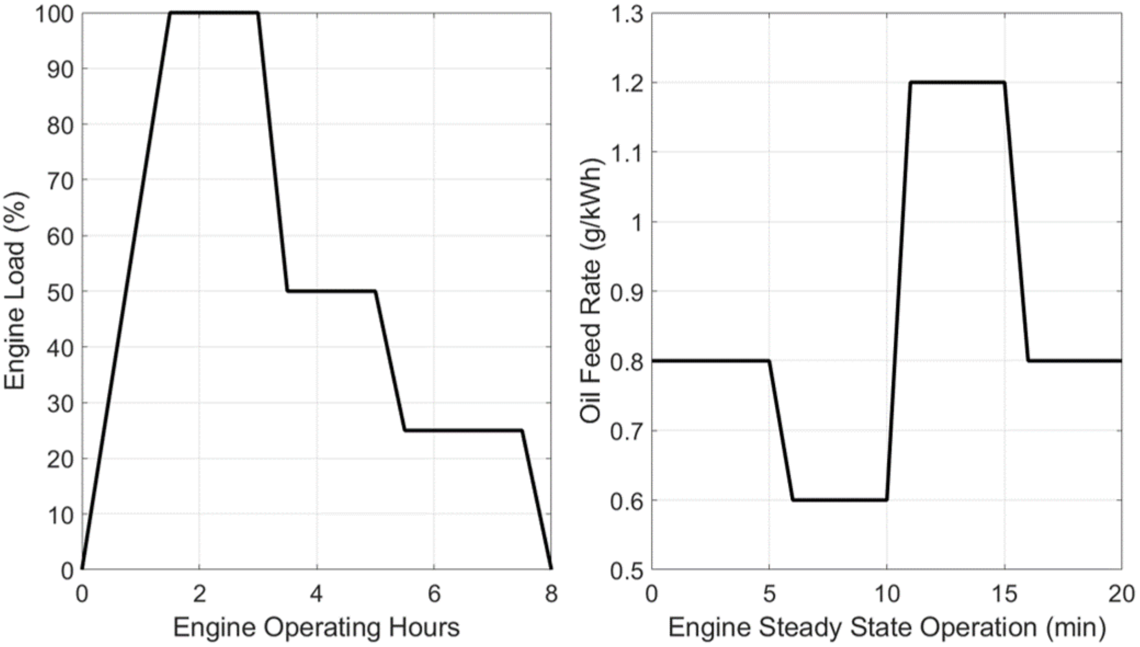

(a) RTX-6 loading sequence.

(b) Steady-state oil feed rate variation.

Figure 6.9: Testing loading cycle for each engine configuration and the oil feed rate variation within each steady-state loading period [6]. © SAE International

6.2 Signal Processing

The same data processing technique as applied to the driven AJ200 engine was applied to the RTX-6. A summary of the data processing technique is outlined in Figure 6.10. The raw data was captured as a series of isolated ultrasonic reflections see, Figure 6.10 (a) and (b). To convert this into oil film thickness measurements the preceding steps of Figure 6.10 were required.

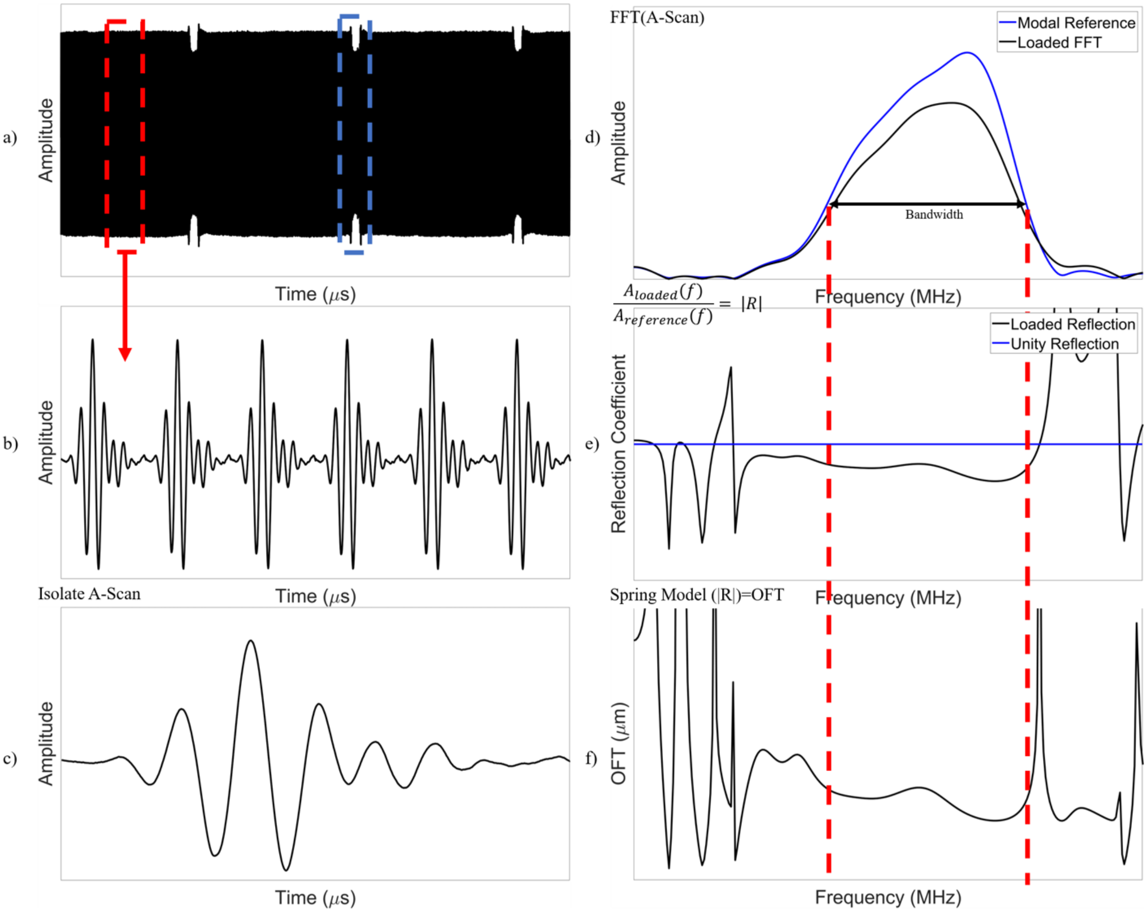

Figure 6.10: Signal processing summary [6]. © SAE International

The ultrasonic reflection was isolated (Figure 6.10c)) and converted into the frequency domain using an FFT (Figure 6.10d)). Each signal was normalized relative to the modal signal to provide the reflection coefficient (Figure 6.10e)). The reflection coefficient was input into Equation 6.6, to output the oil film thickness (Figure 6.10f)). The oil film thickness calculation was refined by the application of Equations 6.3 and 6.5 from temperature and pressure measurements from the liner's internal surface.

$$h = \frac{\rho c^2}{\omega Z_1 Z_2}\sqrt{\frac{|R|^2(Z_2+Z_1)^2-(Z_2-Z_1)^2}{1-|R|^2}} \tag{6.6}$$

The same method as previously applied to the AJ200 engine has been implemented to provide a reference for ultrasonic measurements. By defining the modal reference waveform, when the piston is significantly far away from the transducer.

6.3 Determination of reflection coefficient

The technique outlined in the signal processing section has been applied to the ultrasonic reflections captured for the three injector configurations. In the case of Sensor 2, this experienced the first ring on its upstroke followed by the second ring at the TDC and finally the first ring again on the downward stroke of the engine. These three stages are summarised in Figure 6.11.

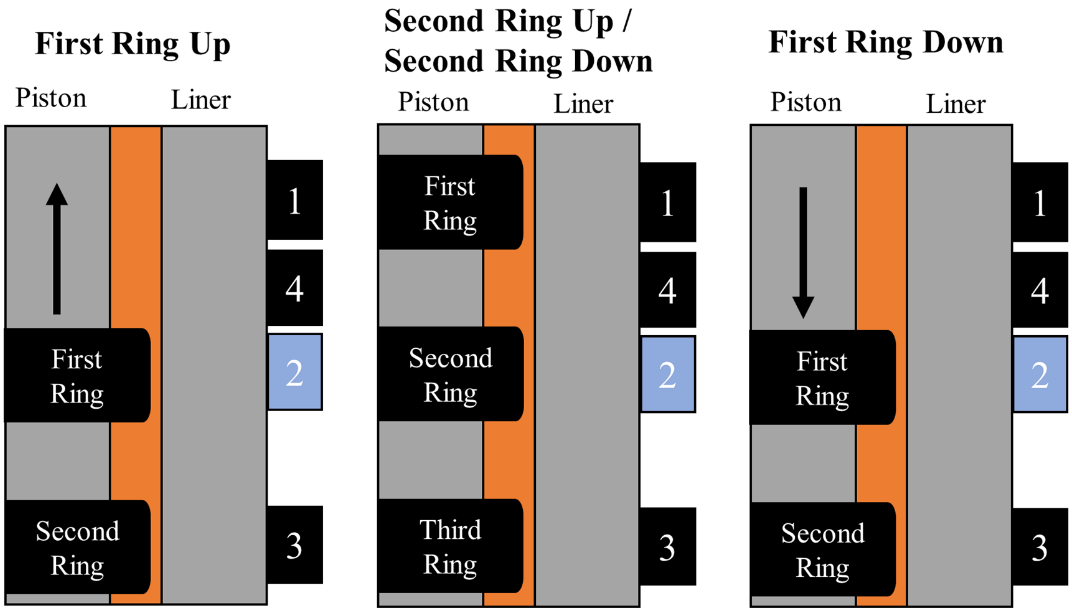

Figure 6.11: Piston ring passage over Sensor 2 [6]. © SAE International

A labelled breakdown of the variation in reflection coefficient over Sensor 2 for a steady-state capture at 100% loading for all engine configurations is shown in Figure 6.12. Equivalent reflection coefficient variations are shown for Sensors 1, 3, and 4 in Figures 6.13-6.15 respectively. The crank angle measurement at the transducer location has been determined by calculation of piston ring displacement relative to its TDC location for the whole engine stroke. The crank angle corresponding to each piston ring moving over a transducer is highlighted in Figures 6.12-6.15 by the shaded regions and is presented in terms of CA after TDC (previously shown in Table 6.3). This breaks down complex variations in reflection coefficients into simpler trends.

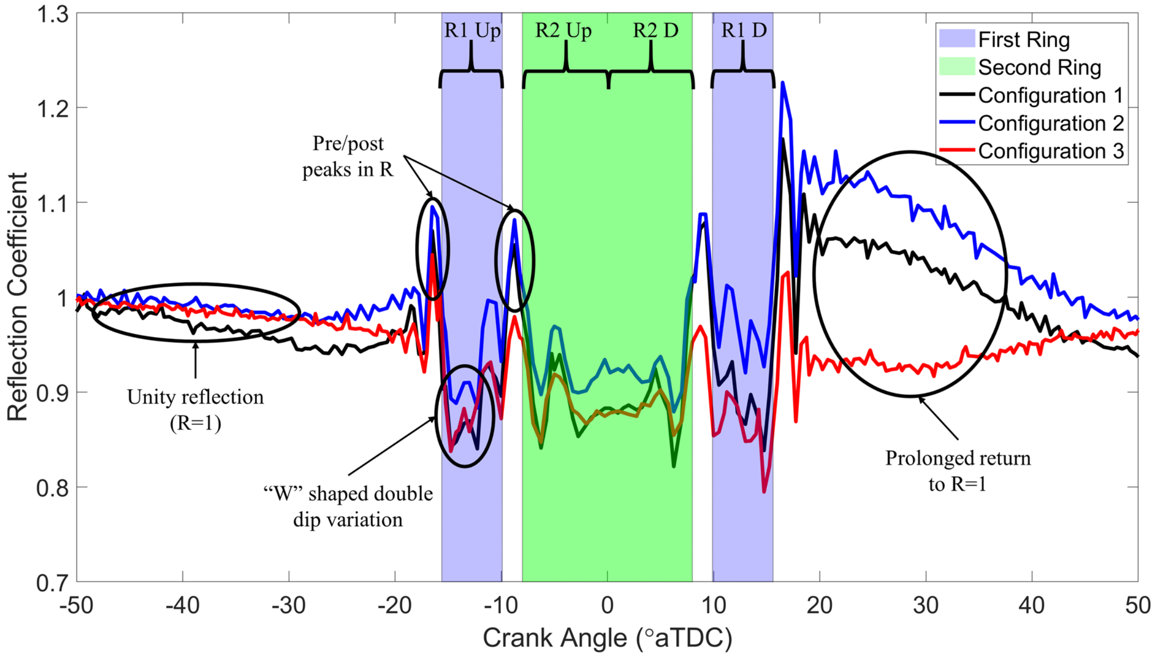

Figure 6.12: Reflection coefficient over Sensor 2, highlighting the two rings passing over the transducer [6]. © SAE International

Figure 6.12 covers Sensor 2 over a 100° CA range centred about the TDC. On the piston approach to the TDC, the first ring passes at -15.6° to -9.9° CA, this corresponds to the R1 Up highlighted region in this figure. The reflection coefficient decreases from unity when the ultrasonic wave is partially transmitted through the oil film to the piston ring, with a greater reduction in reflection coefficient indicating greater transmission. Therefore, a lower value of reflection coefficient indicates a thinner lubricating film.

The green highlighted section signifies when the second ring is over Sensor 2, spanning from -8° to 8° CA, which is for the upward stroke of the second ring (R2 Up), the ring at the TDC, and the preceding downward stroke of the ring (R2 D). As the piston is close to the TDC in this region it is moving at a lower velocity leading to the second ring being positioned over Sensor 2 for a greater CA range. The ring is shown to be over this transducer at the TDC as there is no increase in reflection coefficient at 0° CA.

The final region is the first ring moving over this transducer on the downward stroke (R1 D). The piston is at a greater velocity here leading to the ring moving over the transducer in a shorter CA range, leading to a narrower dip in reflection coefficient. With the increase in cylinder pressure typically leading to a greater reduction in reflection coefficient for this downward stroke than the upward stroke of the first ring (R1 Up).

In addition to major variations in the reflection coefficient due to the rings moving over the sensing area of Sensor 2, there are other trends displayed in Figure 6.12. Outside of the measurement region of the piston rings the reflection coefficient largely remains around unity as this shows the complete reflection of the ultrasonic wave from the internal surface of the cylinder liner (i.e. no contact and no expected residual oil film). Whilst the reflection coefficients from when a piston ring was aligned with the transducer dips to 0.7 in some cases.

The general trend in the reflection coefficient was the same for each engine configuration with the most prominent variations being from either; the magnitude of the dip, leading to changes in oil film thickness determined from the Spring Model (Equation 6.6) or the variation in reflection coefficient after the last ring passed on the downward stroke for an extended crank angle range (> 20° CA). This may be an indication that an excessive oil film was left on the liner after the last ring passed, which dissipates as the reflection coefficient returns to unity. This is explored further in Section 6.3.2 and Chapter 9.

For the regions of piston ring and sensor alignment, Configurations 1 and 3 provide near-identical reflection coefficient values whilst Configuration 2 is consistently higher. The upper rail injection system for Configuration 1 and 3 was the PJ injector whilst the NLT injector was used for Configuration 2. Displaying that the NLT injectors, with a reduced rate of lubricant atomisation, led to a greater reflection of the ultrasonic signal and, therefore, thicker lubricating film.

Immediately before and after a piston ring moved over a transducer there was a sharp peak in the reflection coefficient above unity. These peaks are to a greater amplitude than was previously seen on the driven AJ200 in Section 5.6. The cause of these peaks requires further study (See Section 7.5) but there are a few potential causes; a leading/trailing oil wave, stress in the liner induced by the piston ring, the piston ring marginally outside of the measurement region causing a greater amount of ultrasonic energy to reflected towards to the sensor [89, 90].

The micro variations within the dips in the reflection coefficient are also noteworthy as in most cases there is a double-dip within each dip, leading to a 'W' shape. The cause of this variation is unknown but may be due to several reasons; the movement of the piston ring traversing the piston ring groove, the piston ring itself tilting, or lateral movement of the ring towards and away from the liner on the neutral side [42]. For Sensor 2 this 'W' shape is also more prominent in the upward stroke than downstroke, although this is not always the case, see Figure 6.14, Sensor 3. This pattern has been found in several other ultrasonic applications; piston skirt [64], roller bearing [89], and cold rolling [90]. Each of these applications differ from each other in geometry, lubricant presence, and speed of component displacement suggesting the cause of this is related to ultrasonic wave propagation instead of a geometric parameter of the engine.

The decrease in reflection coefficient is consistently greater for a ring on the downward stroke than the upward stroke, this is true for Sensor 2 (Figure 6.12) and the other sensors (Figures 6.13-6.15). This is likely due to a combination of the two passes of the control ring directing oil down the liner and the combustion process leading to an increased pressure in the cylinder thus causing the piston rings to conform more to the liner. This trend was also observed in the driven AJ200 engine block in which the sole factor was the oil control ring removing excess oil from the liner.

Similar variations are also seen for the other sensors, the same test case as Sensor 2 in Figure 6.12 is shown for Sensors 1, 3, and 4 in Figures 6.13-6.15 respectively. Note the differing highlighted regions for the sensors as each sensor experienced the piston rings moving over the sensing area at varying CA ranges as previously shown in Table 6.3.

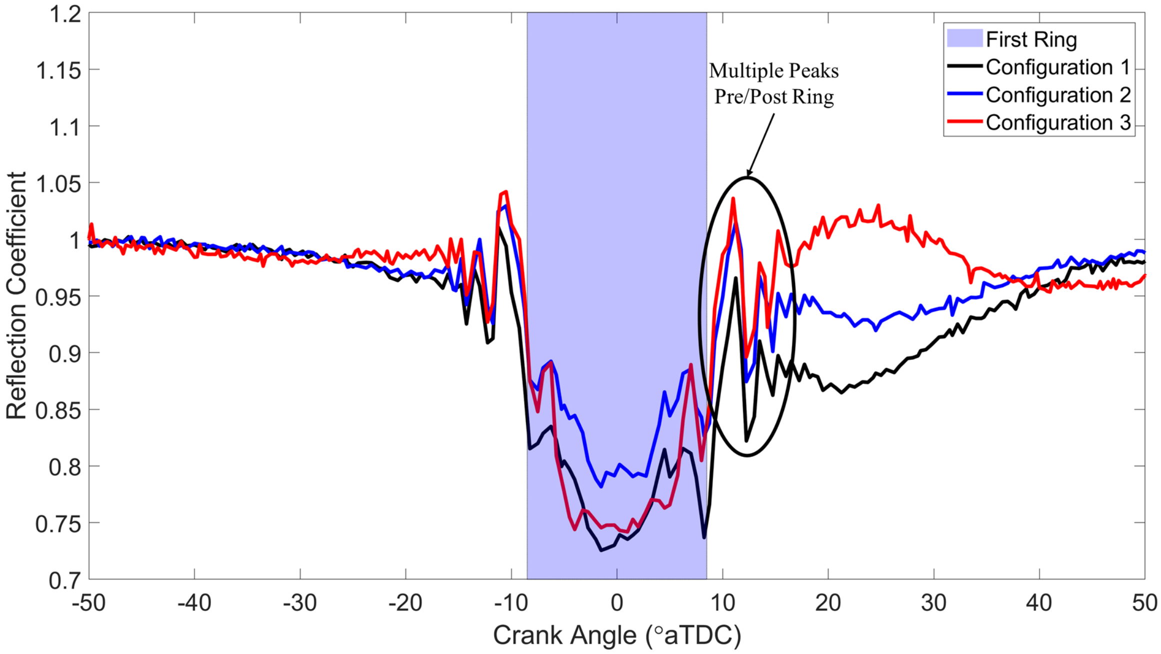

Figure 6.13: Reflection coefficient over Sensor 1, highlighting the first ring passing over the transducer [6]. © SAE International

The first ring was aligned with Sensor 1 at the TDC, see Figure 6.13, this piston ring had a greater width than the other two piston rings and was, therefore, over the sensing area for a marginally greater range (-8.5° to 8.5° CA). In this plot, an additional trend is more pronounced, primarily as only one ring transversed this sensor. Further to the single peak in the reflection coefficient pre/post ring observed in Figure 6.12, there is a series of cyclic peaks in the reflection coefficient, highlighted in Figure 6.13. This pattern is more comparable to those seen in roller bearings [89] in which the cyclic peaks were shown to be independent of loading and occurred due to a roller approaching the sensing area leading to a greater amount of energy being directed back to the sensor.

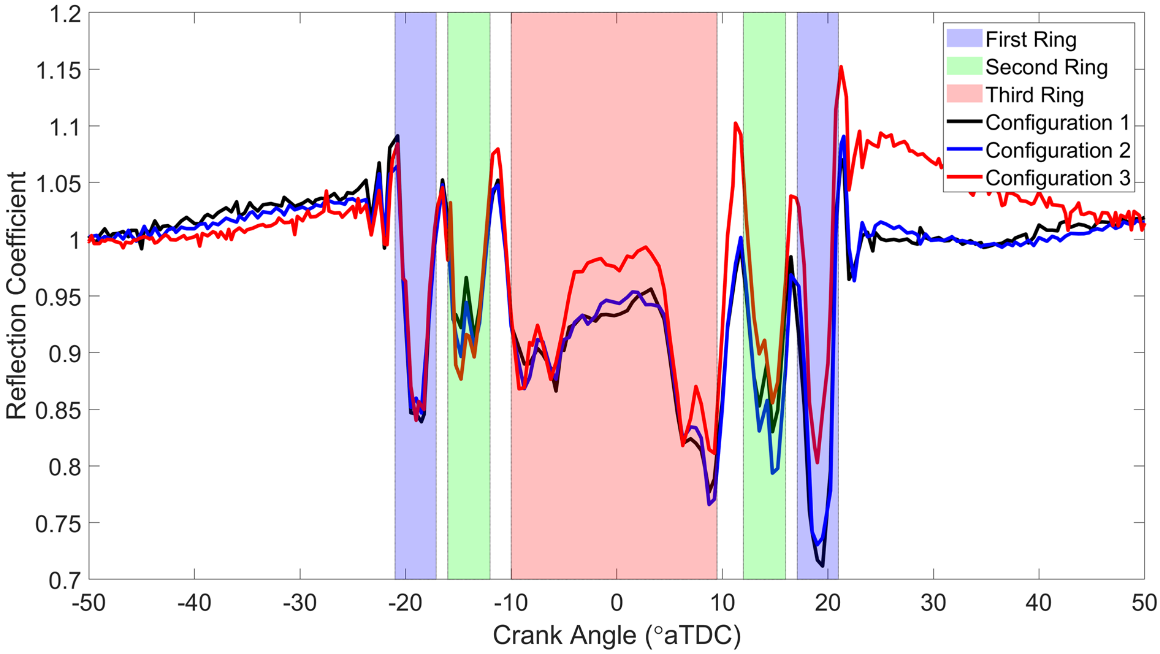

Figure 6.14: Reflection coefficient over Sensor 3, highlighting all three rings passing over the transducer [6]. © SAE International

The third sensor, Figure 6.14, has the most complex variation in the reflection coefficient as all three piston rings moved past this sensor with the third ring aligned with it at the TDC. The first ring moved over this sensor at -21° to -17.1° CA followed by the second ring at -16° to -11° CA. The two have largely similar trends in reflection coefficient over a comparable sized CA range although the second ring experienced the ’W’ shape highlighted for Figure 6.12 yet the first ring did not. The third sensor was aligned with the third ring over a large range (-9.2° to 9.2° CA) covering the TDC. Although the reflection coefficient returns to near unity over -5° to 5° CA. This may indicate the transducer was positioned marginally too far down the liner and is beneath the third ring at the TDC.

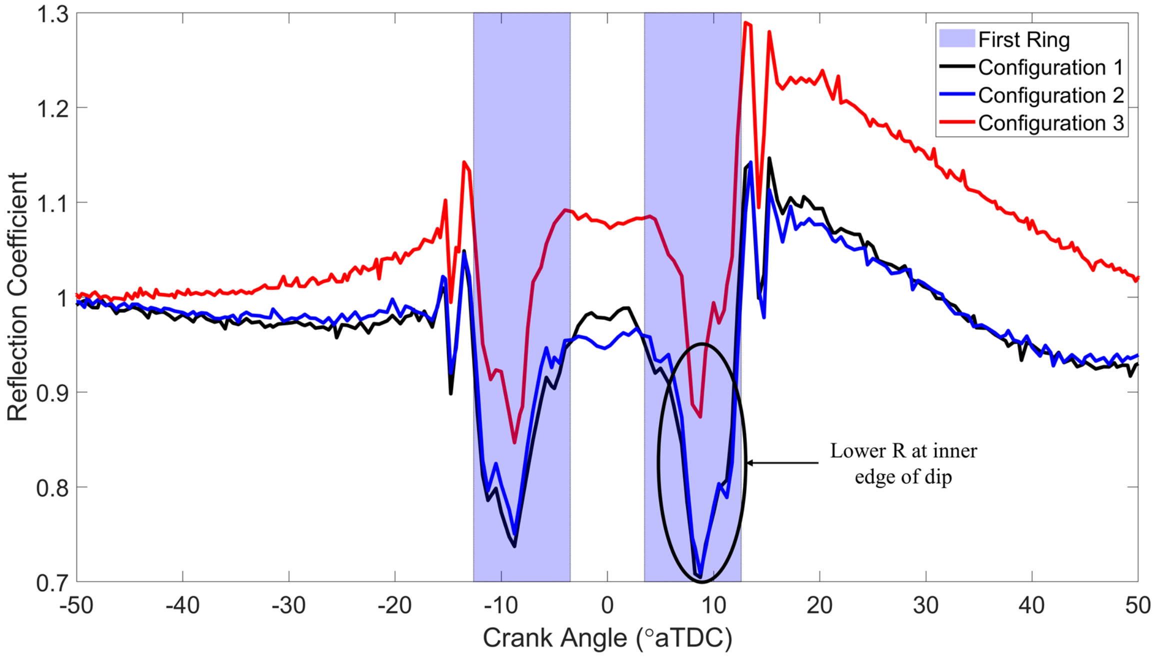

Figure 6.15: Reflection coefficient over Sensor 4, highlighting the first ring passing over the transducer [6]. © SAE International

Sensor 4, seen in Figure 6.15, was positioned between the first and second ring at the TDC. This led to the first ring moving past this transducer shortly before and after the TDC, hence two dips in the reflection coefficient. This sensor displays a deviation on the 'W' dip variation experienced by other transducers, with the inner edge (edge closer to the TDC) having a lower reflection coefficient. This may indicate the ring is tilted with the lower section of the piston ring closer to the liner. The cause of this is further explored in Section 7.5.

6.3.1 Effect of changing pulse rate

Through the course of this work, there were two different methods to record ultrasonic reflections, recording all channels (sensors) at once at a lower pulse rate of 1.05 kHz, or focusing on a single channel to allow a higher pulse rate of 12.4 kHz. This is detailed in Section 6.1.2. Figure 6.16 shows the variation in reflection coefficient for Sensors 1-4 for the two different pulse rates used at 50% engine loading. Each pulse rate considered here, is significantly higher than the rate at which a piston ring moves past a sensor, therefore, the higher rate is not necessarily required for OFT measurements. The higher pulse rates were tested in order to highlight any micro-variations that would have been otherwise misrepresented.

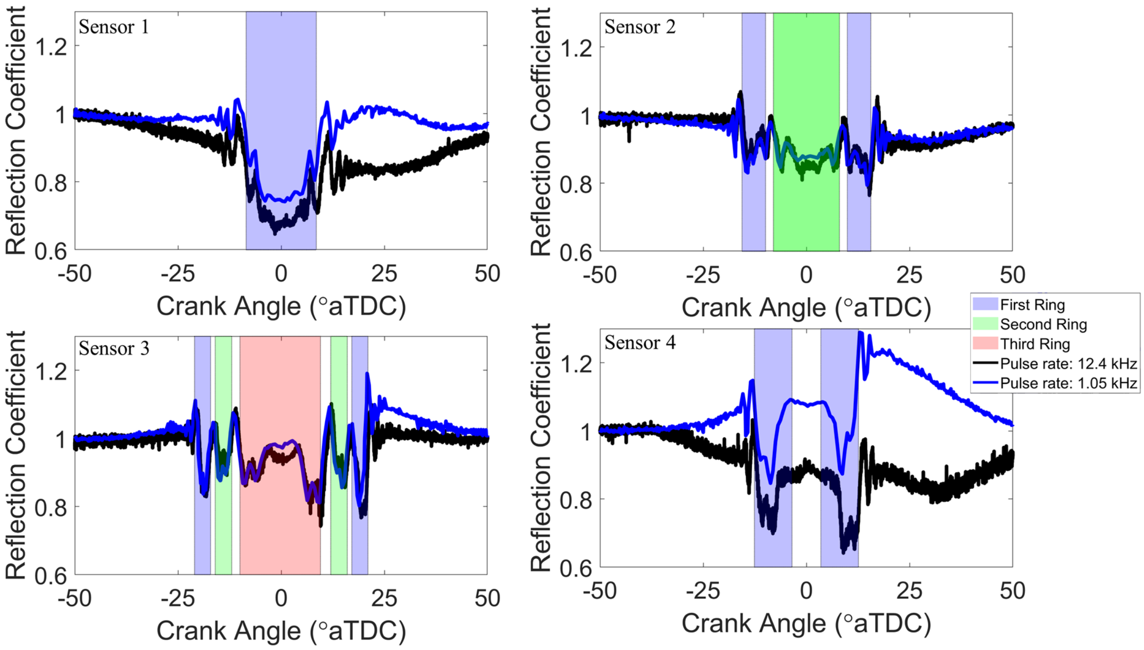

Figure 6.16: Reflection coefficient variation for changing pulse rate [6]. © SAE International

A pulse rate of 1.05 kHz led to an ultrasonic reflection every 0.6° CA whereas using 12.4 kHz provides a measurement every 0.05° CA but limited the data to be recorded on each channel in turn. The effect of increasing the pulse rate on the reflection coefficient is only clear for Sensors 1 and 4 which provided a significant reduction in the reflection coefficient. The large reduction in reflection coefficient post ring pack passage is thought to be due to the higher pulse rate capture being marginally outside of steady-state leading to a differing residual oil film on the liner surface.

Figure 6.15, Sensor 4, previously displayed a lower reflection coefficient at the inner edge of the ring implying ring tilt. However, the increased pulse rate has removed this trend for Sensor 4 and it now displayed a ’W’ shape such as seen for the other sensors.

Observation of the plots for Sensors 2 and 3 show minor differences between the two pulse rates with the most prominent change arising close to the TDC with the increased pulse rate leading to a lower reflection coefficient value. Note, the single-channel measurements were taken over a short period of 50% loading marginally outside of the steady-state testing period whilst the slower pulse rate was within the steady-state operation period.

6.3.2 Spectrograms and residual oil film thickness

Observation of the reflection coefficient over the whole bandwidth of the transducers provides a more complete view of the variation in the reflection coefficient over an engine cycle. This is shown in Figure 6.17 for Sensor 1 for the three engine configurations at 100% loading. In these plots, 1 MHz has been highlighted with a dashed line as this is the frequency used previously in Figure 6.12-6.16, in addition to being used for oil film thickness calculations in the following section. The spectrograms have been limited to the range of 0.9 < Reflection coefficient < 1.1, this has been done for visualisation purposes to centre the reflection coefficient around unity (R=1) and to display the trends in the reflection coefficient clearer.

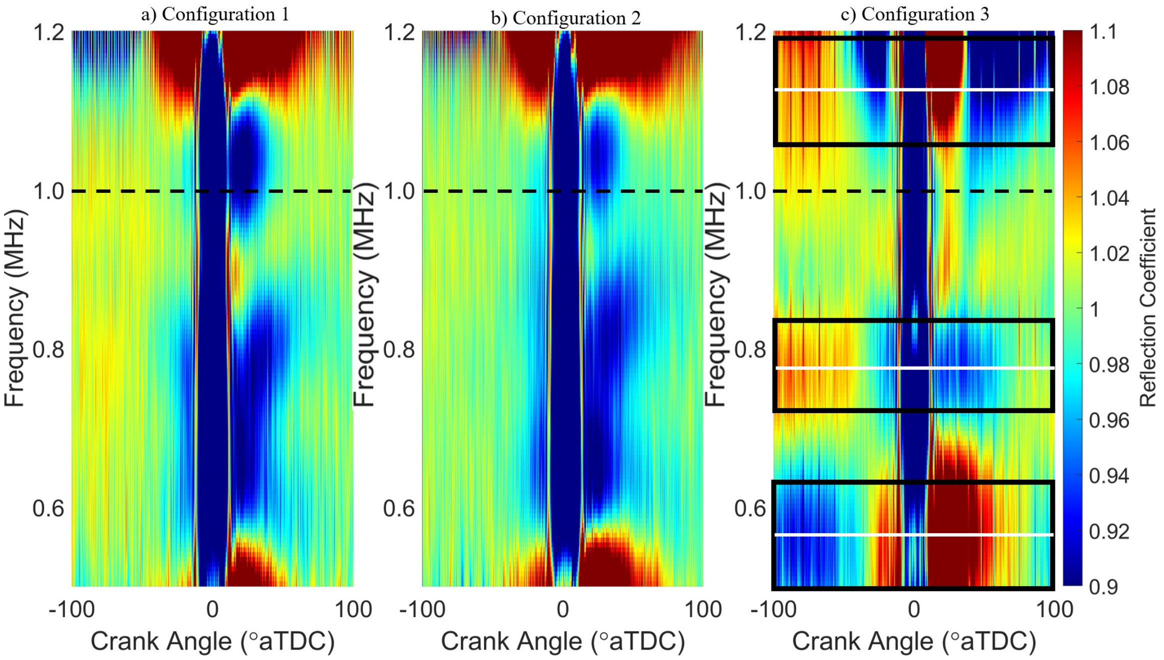

Figure 6.17: Reflection coefficient over the transducer bandwidth for Sensor 1 for all three configurations. Plots a-c correspond to Configurations 1-3 respectively. 1 MHz is highlighted as this frequency was used for oil film thickness calculation [6]. © SAE International

The spectrograms for the three engine configurations over the bandwidth of Sensor 1, Figure 6.17, largely show a consistent decrease in reflection coefficient beyond 0.9 reflection coefficient across the whole bandwidth for -8.5° to 8.5° CA which corresponds to when the first ring was aligned with this transducer.

Outside of the region corresponding to the first ring, there are bands of increased and decreased reflection coefficient which vary with frequency across the bandwidth of the transducer, see the black rectangles in Figure 6.17c. The trends are more identifiable on the YTR engine in Section 9.6.2. Along the 1 MHz line the band of increased/decreased reflection coefficient post ring is the same as the 'Prolonged return to R=1' section seen in Figure 6.13. The cause of these frequency-dependent bands of reflection coefficient variation is unknown but may be an indication of the residual oil film left on the liner post ring. The OFT of these resonant bands can be defined using the resonant dip technique [77], in which the equation and calculation are shown in Equation 6.7 in which f_m is denoted as the frequency range between two resonant bands (white horizontal lines in Configuration 3 of Figure 6.17).

$$h = \frac{cm}{2\Delta f_m} = \frac{1007}{2(1.1 \times 10^6 - 0.75 \times 10^6)} = 1400\ \mu m \tag{6.7}$$

The resonant dip technique implies a lubricating film thickness of over 1000 μm on the liner in the regions that see the frequency-dependent bands. The residual film calculation is based upon the two upper bands (0.75 MHz and 1.1 MHz) whilst the two lower bands (0.55 and 0.75 MHz) imply a residual film of 2000 μm. These film thicknesses are obviously significantly greater than the film thicknesses measured from the Spring Model when a piston ring was aligned with the sensor which was in the order of 10 μm. Residual films of this magnitude are unexpected due to minimal lubricating oil adhering to the liner surface although not infeasible. Resonant oil levels have only previously been quantified in automotive engines and, therefore, their levels are not necessarily applicable for comparison to marine engines. As 10% of the oil is injected into the ring pack in the RTX-6 test engine, the sensor may well be exposed to a large portion of that injected lubricant. The bandwidth of the transducer only provides a useful measurement range of 0.7 MHz leading to only three resonances being found in this range, higher centre frequency transducers would have provided additional resonances potentially capable of improving the resonant dip calculation. Unfortunately, the thickness of the liner and it being made of cast iron prevented higher frequency transducers from being capable of providing these measurements. This is due to higher frequency ultrasonic waves being attenuated more over a greater propagation distance than lower frequencies, limiting these measurements to a relatively lower frequency range. This measurement is applied to the YTR engine in Section 9.6.2 in which a greater bandwidth enables a measurement over a greater CA range.

Observation of Figure 6.17(a) and (b) which resembles Configurations 1 and 2 shows a near-identical variation in the reflection coefficient across the whole bandwidth. Yet the third configuration displays significantly different patterns outside of the first piston ring zone. This may be an indication of transducer deterioration over time or a largely differing residual oil film left from the third configuration which is unexpected due to the upper rail for Configuration 1 and 3 being the same.

For the preceding work, a frequency index of 1 MHz was used, this was primarily due to the centre frequency of these transducers being 1 MHz, although it is clear from Figure 6.17 that the selection of this frequency index has an effect on the resulting reflection coefficient and thus oil film thickness.

6.4 Oil film thickness

The reflection coefficient of Figures 6.12-6.15 has been used to determine the OFT between the piston ring and cylinder liner using Equation 6.6. The same 100% loading test case as shown in Figure 6.12 is shown in Figure 6.18 which refers to Sensor 2. Whilst Figures 6.19-6.21 show Sensors 1, 3, and 4 respectively.

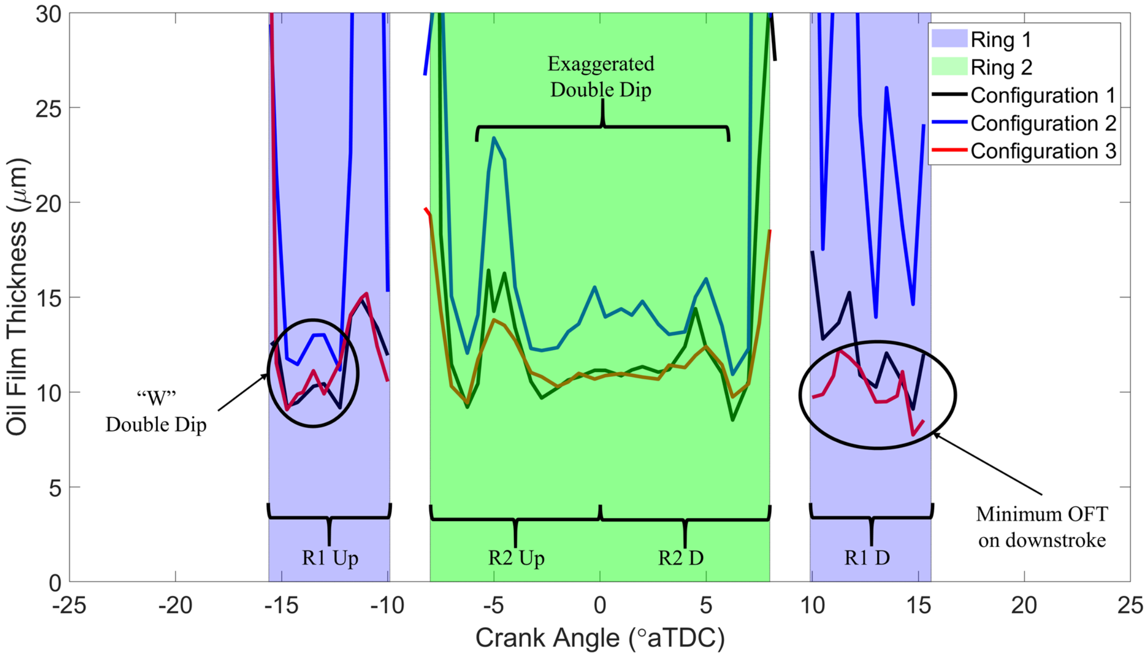

Figure 6.18: Oil film thickness measurements over Sensor 2 for 100% engine loading steady-state operation [6]. © SAE International

The oil film thickness shown in Figure 6.18, for Sensor 2, is of the same order of magnitude for each engine configuration. The upper rail in the second configuration was the NLT injector (the injector design that reduced atomisation of the lubricant) reducing lubricant presence in the exhaust manifold. This is directly reflected in the OFT, with Configuration

2 providing thicker lubricating films, roughly 4 μm thicker at the TDC than the other configurations. Whilst Configurations 1 and 3, both with PJ injectors on the upper rail provided near identical film thicknesses.

The 'W' shaped double-dip present in the R1 Up reflection coefficient of Sensor 2 (Figure 6.12) remains present in the OFT over this sensor. Whilst the second ring (R2 Up and R2 D) now displayed an exaggerated version of the double-dip, with a 'W' at either side of the ring passage. No double-dip is displayed for R1 D, instead, the OFT decreases over the passage of the ring with minimum oil film thickness at 14.5° CA, once the ring has almost moved completely past the transducer. This is shortly after the maximum combustion pressure and, therefore, may be due to the cylinder pressure causing the ring to conform more to the liner, potentially with the addition of ring tilt or ring lateral movement.

The OFT greatly increases either side of all the rings, Takiguchi [33] and Seki et al. [34] argued this was likely a bow wave pre-and post- ring passage. Yet works such as Garcia-Atance Fatijo et al. [42] who used capacitance transducers, showed the rings operated under starved conditions and indicated potential flow detachment, therefore, it is unlikely to be a bow wave of lubricant.

The same general trends in oil film thickness are observed for Sensors 1, 3, and 4 as shown in Figures 6.19-6.21 respectively. Note the differing highlighted regions for each sensor as each experienced piston rings moving over the sensing area at varying CA ranges.

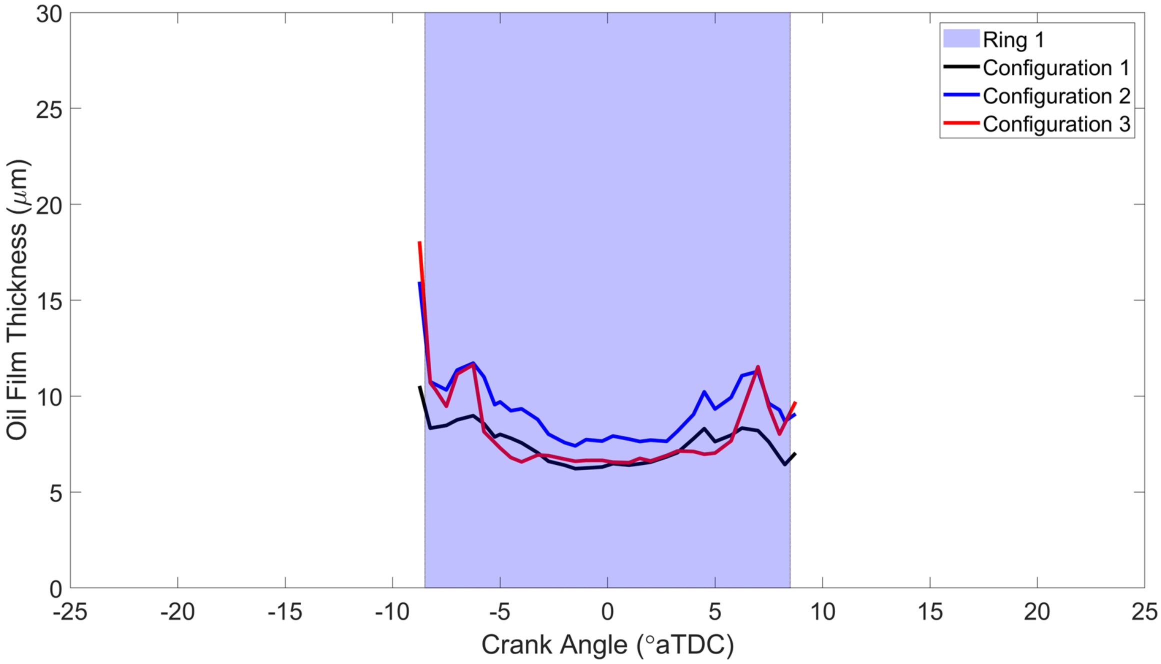

Figure 6.19: Oil film thickness measurements over Sensor 1 for 100% engine loading steady-state operation [6]. © SAE International

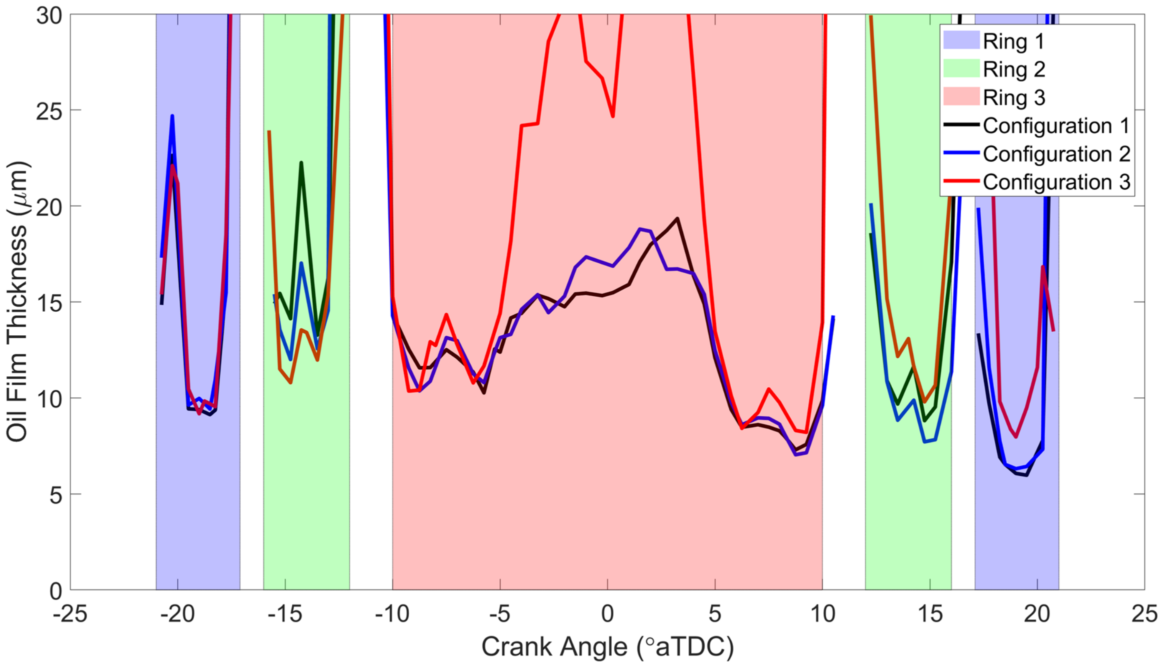

Figure 6.20: Oil film thickness measurements over Sensor 3 for 100% engine loading steady-state operation [6]. © SAE International

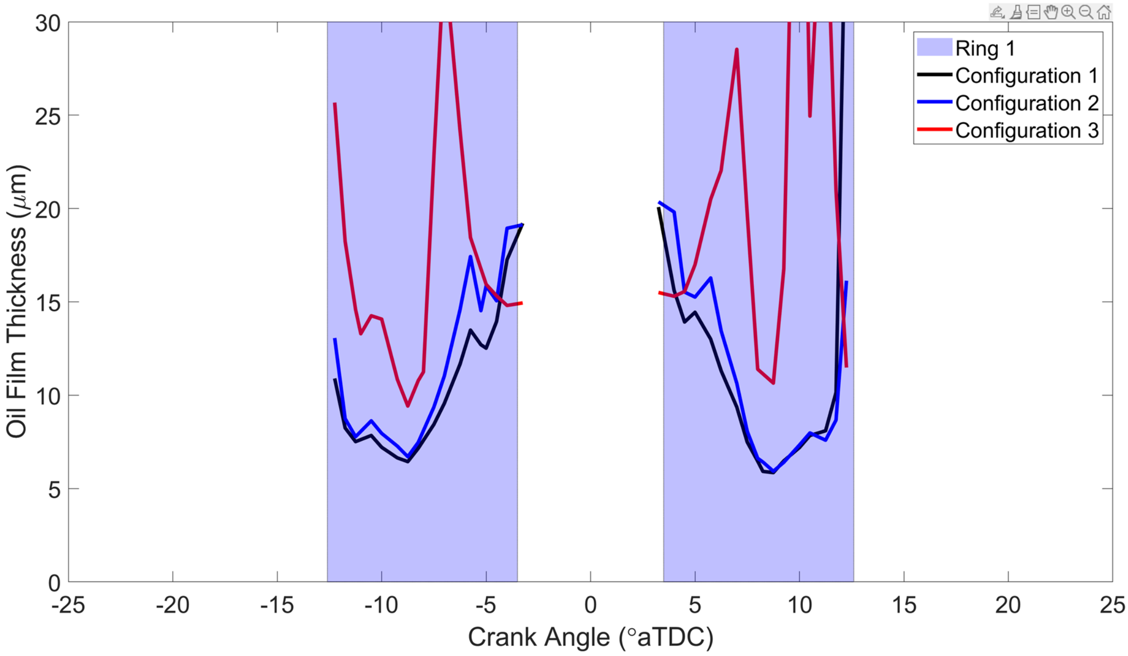

Figure 6.21: Oil film thickness measurements over Sensor 4 for 100% engine loading steady-state operation [6]. © SAE International

Similar trends are shown for the three engine configurations for all piston rings in Figures 6.18-6.21, except for the third configuration in Sensor 3 Ring 3 (Figure 6.20) and Sensor 4 Ring 1 (Figure 6.21) which shows significantly differing patterns. This is thought to have been due to either the sensors having moved or malfunctioned after extended use as Configuration 3 was the last to be tested.

The OFT in Figures 6.18-6.21 shows the rings further up the liner (Sensors 1 and 4) to have minimum OFT values of significantly less than 10 μm, typically around 7 μm whereas sensors further down the liner (Sensors 2 and 3) have minimum OFT values around 10 μm. This is likely the case as the first ring can be seen as a buffer ring between high and low pressure regions and this ring moved over Sensors 1 and 4 closer to the TDC when the combustion chamber experienced greater pressures. The high pressure of the combustion chamber causes the ring to conform to the liner more leading to a thinner oil film between the two. The combustion pressure also affects Sensors 1, 3, and 4 as previously mentioned for Sensor 2 (Figure 6.18) causing the downstrokes for each ring to be thinner than their respective upward strokes.

Comparable to Sensor 2 (Figure 6.18) double dips in the OFT are displayed for Sensor 3 (Figure 6.20) although they are not prevalent for the first ring moving over this transducer for either the up or the downstroke. This piston ring moved over the sensing area of Sensor 3 at a greater velocity, therefore, there were fewer reflections captured in this timeframe, potentially leading to there not be enough data points to show the double-dip. Whilst Sensor 4 (Figure 6.21), like its reflection coefficient, shows the inner edge OFT to be the thinnest point.

The first sensor (Figure 6.19) shows a similar trend in OFT pre- and post-TDC, unlike the sensor that was aligned with the first ring on the driven AJ200 (Figure 5.8). The motored operation of the AJ200 which led to lubricant pooling on the top of the liner and greater fluctuations in the film thickness post TDC. Whilst the excess lubricant at the top on the liner in the RTX-6 will have been fed down the liner by the combustion pressure or combusted. Therefore, the OFT trends seen for the RTX-6 are more representative of engine operation than those from the AJ200.

Sensors 1-3 are aligned with the first, second, and third piston rings respectively at the TDC. At this location in Figures 6.18-6.20, Configuration 2 consistently provided a thicker lubricant film than the other two configurations, excluding Configuration 3 for Sensor 3 as the sensor is thought to have moved or malfunctioned here.

6.4.1 Minimum oil film thickness

The minimum oil film thickness for each data capture has been determined by isolating the minimum OFT of each piston ring recorded in each engine revolution and averaging the data. Comparison of the MOFT for the three engine configurations for the first piston ring at the TDC is shown in Figure 6.22 with the corresponding engine speed for that capture. The repeatability of the MOFT measurements is explored in Section 6.4.4. There is no data presented for Configuration 3 at 50% loading as no ultrasonic data was captured in this period.

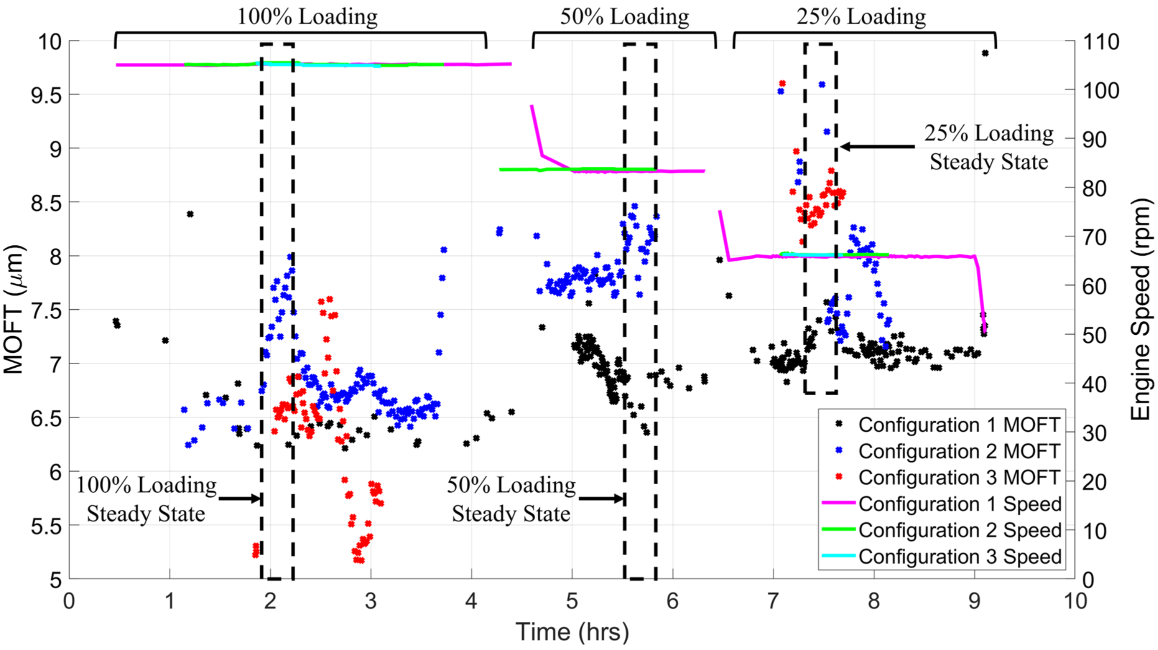

Figure 6.22: Minimum oil film thickness of Ring 1 over Sensor 1 plotted for the three configurations and all engine speed levels. The three steady-state operation periods are highlighted via dashed boxes [6]. © SAE International

Across all three engine configurations, the trend of increased lubricant film thickness with decreased engine load is observed. For example, Configuration 1 steady-state MOFT values are 6.3 μm, 6.7 μm, and 7.3 μm for 100%, 50%, and 25% loading respectively. There are several contributing factors to this trend, at higher engine loading, the combustion pressure is greater, leading to greater ring conformity to the liner. In addition to this, the higher internal liner temperature and pressure results in a lower oil speed of sound and oil density (Equations 6.3 and 6.5), reducing the lubricant film thickness. The increased liner temperature also causes an increased rate of lubricant evaporation, therefore, there is less lubricant present to form an oil film at higher engine loads. The MSDS of the lubricant quotes the lubricant flash temperature to be 220 °C and at 100% engine loading the liner's internal surface temperature is 216 °C at the location of Sensor 1. The piston ring surface temperature is likely higher than this leading to lubricant potentially igniting at 100% engine loading. All of these factors compound to results in a thinner lubricant film at higher engine loading.

Figure 6.22 shows that the MOFT of the first ring over Sensor 1 is greater for Configuration 2 than Configurations 1 and 3, during steady-state operation, except at the end of the 25% loading period. A greater MOFT consequently reduces the likelihood of boundary lubrication (metal-metal contact) occurring between the piston ring and cylinder liner. For steady-state testing at 100% and 50% loading, Configuration 2 provided a film that was consistently at least 17.5% thicker than the two other engine configurations. This configuration was the lubricating system with a reduced rate of lubricant atomisation, ultimately reducing lubricant losses to the exhaust manifold. This led to a greater amount of injected oil remaining within the cylinder which was directly reflected in terms of a greater MOFT for Configuration 2.

Outside of steady-state operation (i.e. outside the dashed boxes in Figure 6.22), the MOFT for Configuration 2 is greater than that of the other two configurations at all points except a short period of Configuration 3 during 100% loading where the MOFT increased. In general, the MOFT is relatively consistent outside of steady-state loading except for brief instances for Configuration 3 100% loading and Configuration 2 25% loading the cause of which is unknown.

6.4.2 Effect of change in oil feed rate

The RTX-6 engine experienced a 20-minute steady-state operation period for each engine loading step for each injector configuration. Within these steady-state periods, the oil feed rate (OFR) was varied as shown previously in Figure 6.9b. The MOFT values measured during this period are shown in Figure 6.23 for the first piston ring moving over the four sensors in CA order, with the change in OFR plotted in green. For example, the order the first piston ring passed the sensors is 3, 2, 4, 1 (TDC), 4, 2, 3, hence left to right for upstrokes followed by the right to left for downstrokes. The equivalent plots for the second and third piston rings moving over their respective transducers are shown in Figure 6.24.

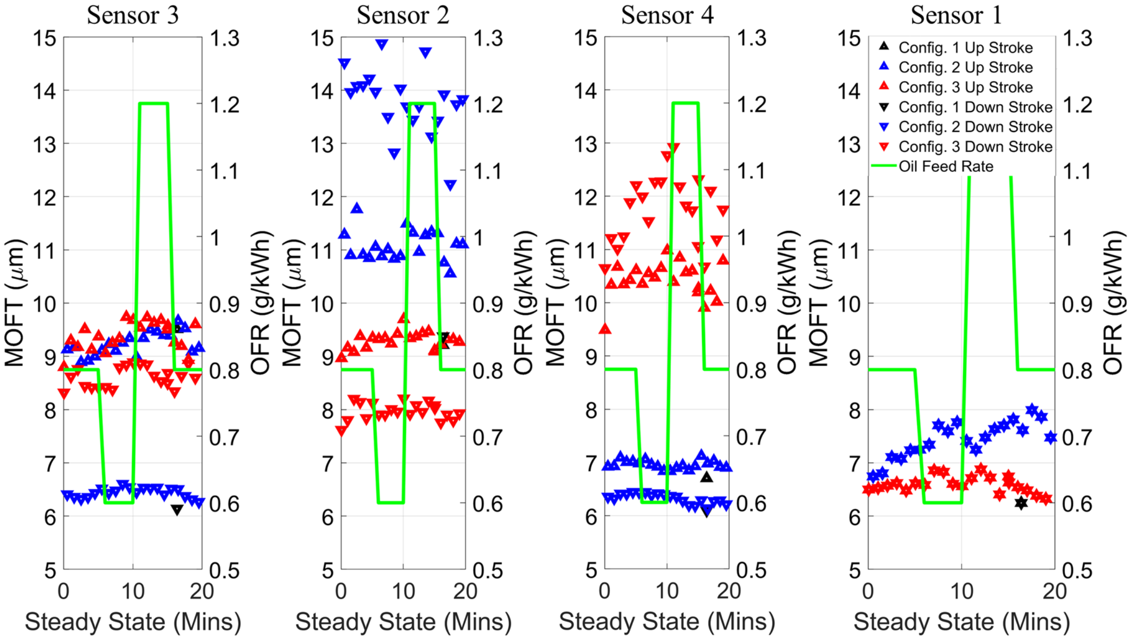

Figure 6.23: MOFT of the first piston ring over Sensors 1-4 for up and down strokes for all configurations at 100% loading with the addition of oil feed rate change [6]. © SAE International

All four plots in Figure 6.23 display no clear variation in the MOFT with the change in OFR for the first piston ring, this was also demonstrated for the 50% and 25% loading. It is not clear why there is no definitive variation in MOFT with OFR. Possibly the thickness of the film formed is simply not sensitive to the amount of oil present, provided a certain threshold volume is supplied; and testing was all carried out above that threshold. Additionally, the OFR steps were in intervals of 5 minutes which may not have been a significant enough time to lead to a change in the lubricating film thickness. Based on the Engine slowdown testing (Section 6.4.3) an interval of at least 20 minutes is required for definitive changes in the reflection coefficient.

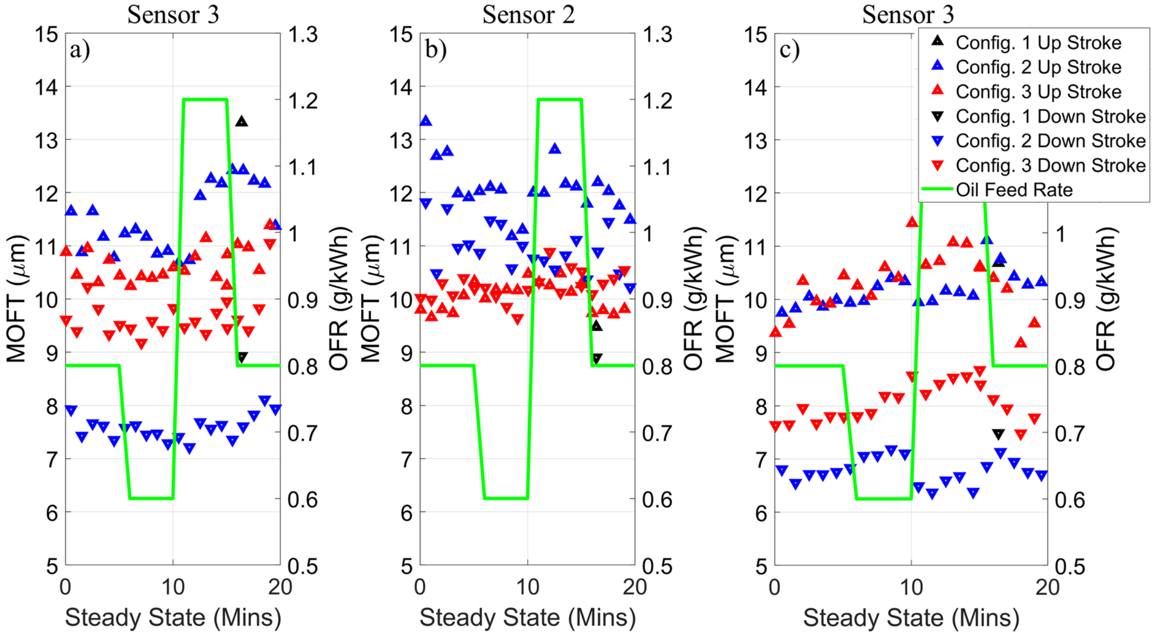

Figure 6.24: MOFT of the second and third piston ring over Sensors 2-3 for up and down strokes for all configurations at 100% loading with the addition of oil feed rate change [6]. © SAE International

Figure 6.24 (a) and (b) show the change in MOFT with OFR for the second ring moving over Sensors 3 and 2, respectively. Whilst Figure 6.24c is for the third ring over Sensor 3. Similar to the results for the first ring (Figure 6.23) there is no clear change in MOFT with OFR for either of the other two piston rings.

6.4.3 Engine slowdown

The RTX-6 engine was operating continuously for each engine configuration covering all loading steps, as shown in Figure 6.9a. This provided a period in which the engine changed loading and rotational speed, capable of providing incremental changes between two loading levels. In the case for Configuration 2 between 50% and 25% loading, interval data was recorded for a 44-minute duration. This involved capturing data at a pulse rate of 1.05 kHz for 5 seconds every minute. The minimum reflection coefficient for each engine cycle of the first piston ring over Sensor 1 is shown over the engine slowing period in Figure 6.25, the slowing engine speed interval is highlighted in the blue dashed box. The results are not plotted in terms of MOFT as there was insufficient temperature and pressure measurements from this transient period to reasonably determine the MOFT.

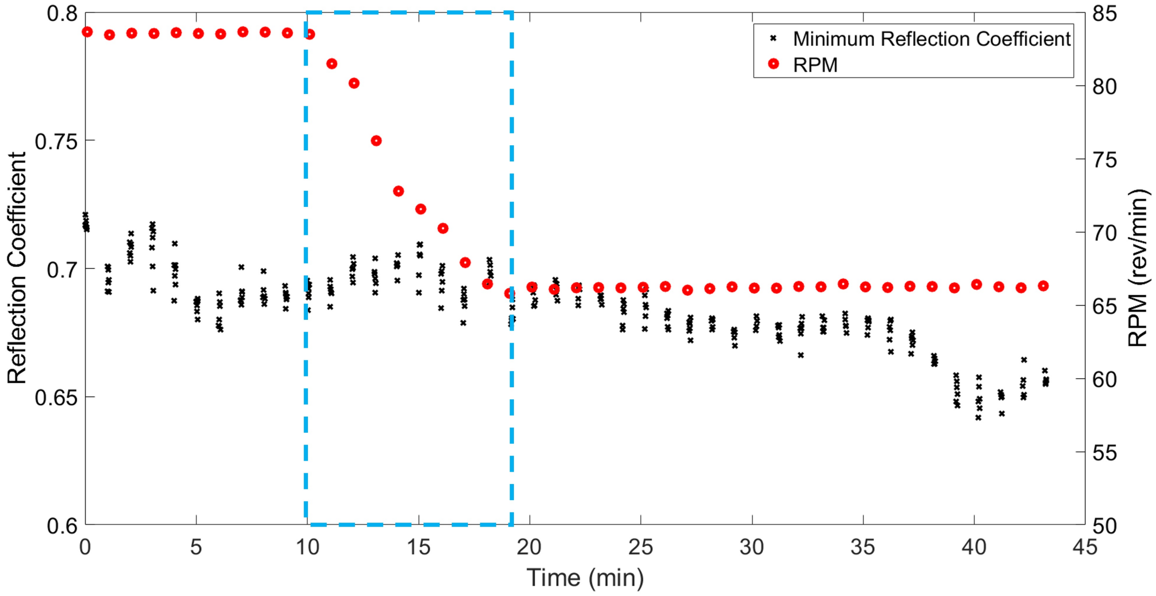

Figure 6.25: Sensor 1 minimum reflection coefficient over the 44-minute engine slowing period from 50% to 25% engine loading. The slowing engine speed interval is highlighted in the blue dashed box.

The progression of the minimum reflection coefficient over time shows a graduation reduction throughout the recording interval as the engine slowed to 25% loading. Observation of the engine speed variation over this period indicates that the engine speed varied over 10 minutes (Minute 10 - Minute 20). Although the slowing of the engine is not immediately reflected in terms of a change in the minimum reflection coefficient. The reflection coefficient remains near constant for the Minute 10 to Minute 25 until it then begins a gradual reduction to the lower loading level.

The oil feed rate is dependent on engine speed this, therefore, suggests that after the engine had slowed (Minute 20), sufficient oil remained in the cylinder to provide the same lubricant film for an additional 5 minutes before a noted marked change in film thickness. This further adds to the results in the previous section covering the change in MOFT as the oil feed rate was varied, as no discernible change was identifiable over the 5-minute intervals. Therefore, indicating that the change in oil feed rate time intervals were not sufficient to study the change in the quantity of oil on the liner. The delayed response in the reflection coefficient is not consistently observed by all sensors. Consider the same piston ring passing Sensor 2 in both the up and downstroke, the reflection coefficient for these two cases is plotted in Figure 6.26 respectively. The engine slowing interval is highlighted in the blue dashed box.

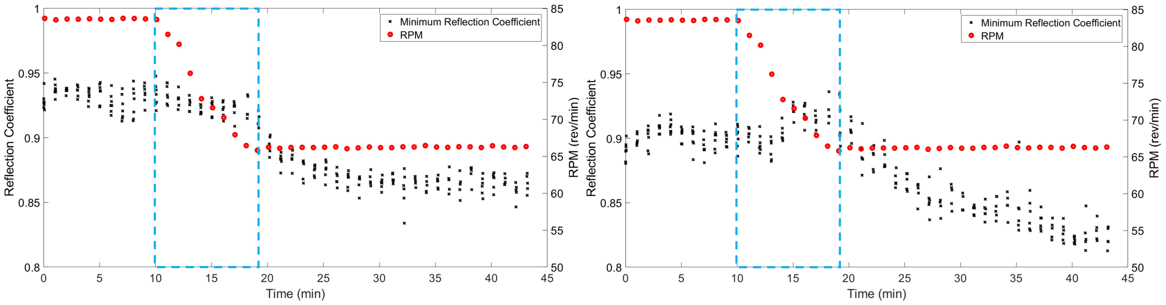

(a) Sensor 2 Ring 1 up stroke reflection coefficient.

(b) Sensor 2 Ring 1 down stroke reflection coefficient.

Figure 6.26: Sensor 2 reflection coefficient as the engine slowed from 50% to 25% loading for both strokes of Ring 1. The slowing engine speed interval is highlighted in the blue dashed box.

In both strokes shown in Figure 6.26 the reflection coefficient appears to have a more immediate change. Figure 6.26a shows a drop post Minute 18 whilst Figure 6.26b shows a brief increase at Minute 15 before starting a consistent decrease from Minute 19.

Both Figure 6.25 and Figure 6.26 display that a decrease in engine loading leads to a reduction in the minimum reflection coefficient for the first ring moving over a sensor. Although this reduction is not immediately displayed, this may be due to the engine being in transient operation as the marine engine takes time to move between steady-state operation at differing loading levels.

It is worth noting that a reduction in reflection coefficient does not necessarily represent a reduction in the MOFT, see Figure 6.22 which shows the MOFT to increase with reduced engine loading. As when the engine is at steady-state, the lower loading conditions leads to the lubricant being subject to a lower temperature and pressure leading to different lubricant properties as previously shown in Equations 6.3 and 6.5.

6.4.4 Measurement repeatability

In Section 6.4.3 the MOFT across the steady-state period for 100% engine loading was studied. The change in the MOFT over this interval is explored in greater detail for all engine loading levels in Figures 6.27-6.29. These figures show the mean MOFT over this period for each engine configuration and loading with the addition of the standard deviation.

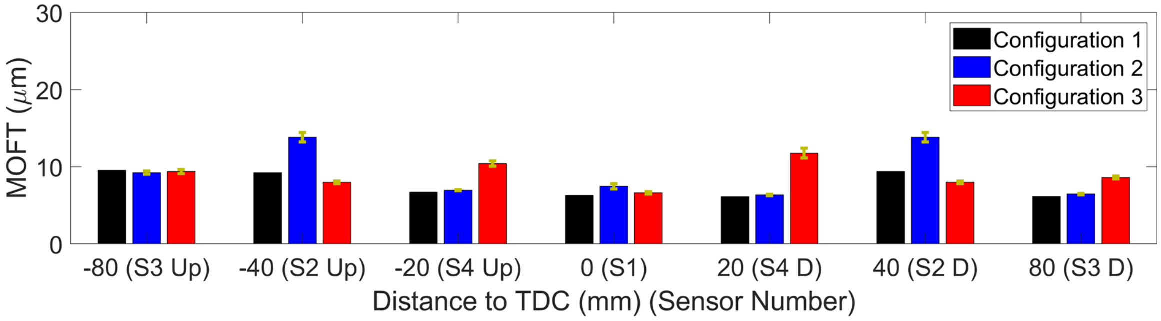

Figure 6.27: MOFT of 100% engine loading for the first ring moving across the sensors with the standard deviation of the MOFT. Note, there are no standard deviations for Configuration 1 as there was only one measurement taken within this steady-state period [6]. © SAE International

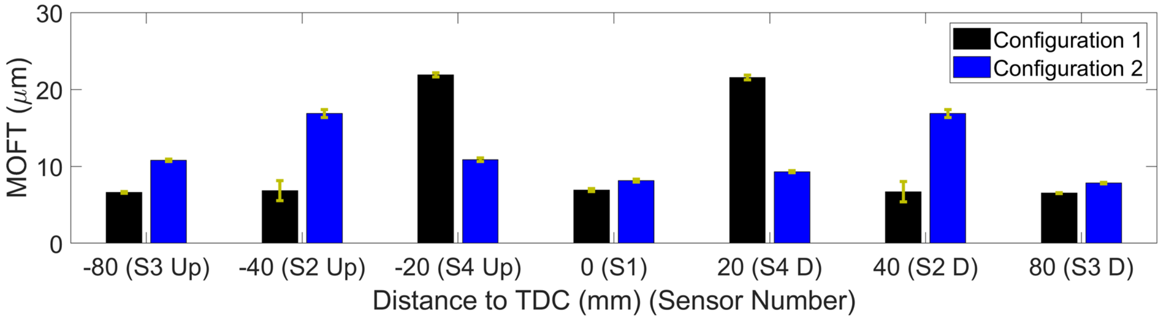

Figure 6.28: MOFT of 50% engine loading for the first ring moving across the sensors with the standard deviation of the MOFT [6]. © SAE International

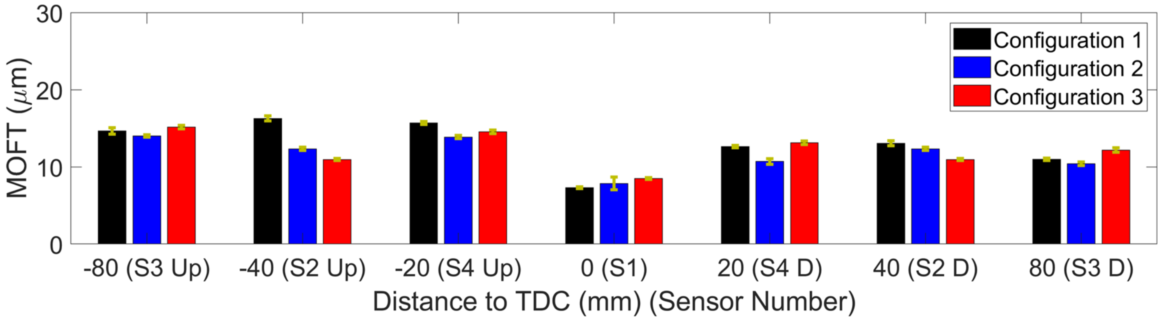

Figure 6.29: MOFT of 25% engine loading for the first ring moving across the sensors with the standard deviation of the MOFT [6]. © SAE International

Across all engine configurations and loading levels in Figures 6.27-6.29, the first piston ring has the thinnest oil film when the ring is at the TDC, with Configuration 1 providing a thinner film than the other two configurations. The standard deviation of the MOFT across the steady-state period varies from ±0.07 μm up to ±1.3 μm with the least variation consistently occurring at the TDC.

Sensor 2 often provided a thicker MOFT than the sensors on either side. With this sensor having the greatest standard deviation in results (±1.3 μm), it can be seen in Figure 6.23 and Figure 6.24 that this increased variation in results is no indication of a greater variety of the MOFT with OFR. This sensor may be providing thicker MOFT measurements with a greater variation due to a potential transducer issue such as a marginal error in transducer placement leading to a coolant channel being partially over the measurement area or insufficient bonding between the sensor and external liner surface. Alternatively, the second ring may fluctuate in its groove more leading to greater variability in the measured MOFT. Excluding Sensor 2, the maximum standard deviation over steady-state operation is ±0.9 μm across all rings traversing all sensors, further indicating there is no definitive change in the MOFT with OFR.

The lambda ratios of the three engine configurations at 100% loading range from 2.9 to 3.5 indicating a mixed lubrication regime when the first piston ring is at the TDC, therefore, metal-metal contact may be occurring. This is explored in greater detail in Chapter 8. Whereas further down the liner lambda ratios of up to 5.2 are achieved, indicative of a hydrodynamic lubricant film. Furthermore, at lower loading levels, as the film thickness increases, the lambda ratio increases, expanding the presence of hydrodynamic lubrication over the sensing region, although mixed lubrication still occurs over Sensor 1 (λ_r up to 4).

The MOFT is numerically shown in Tables 6.4-6.6 for the first piston ring moving across all sensors for the three engine configurations and loading levels. These tables include the addition of the coefficient of variance (COV) over the steady-state period.

Table 6.4: Steady-state MOFT across 100% loading for all configurations for the first piston ring passing all transducers. Note, there are no coefficients of variance values for Configuration 1 as there was only one measurement taken within this steady-state period [6]. © SAE International

Configuration	**Dist to TDC (mm)**	**-80**	**-40**	**-20**	**0**	**20**	**40**	**80**
	Sensor	**S3**	**S2**	**S4**	**S1**	**S4**	**S2**	**S3**
	Up/Down Stroke	**U**	**U**	**U**	**-**	**D**	**D**	**D**
1	MOFT (μm)	9.5	9.2	6.7	6.3	6.1	9.4	6.1
	COV (%)	-	-	-	-	-	-	-
2	MOFT (μm)	9.2	11.1	7.0	7.4	6.3	13.8	6.5
	COV (%)	2.3	2.6	1.2	4.6	1.5	4.5	1.4
3	MOFT (μm)	9.4	9.3	10.4	6.6	11.8	8.0	8.6
	COV (%)	2.9	2.0	3.3	2.3	5.4	2.0	2.3

Table 6.5: Steady-state MOFT across 50% loading for all configurations for the first piston ring passing all transducers [6]. © SAE International

Configuration	**Dist to TDC (mm)**	**-80**	**-40**	**-20**	**0**	**20**	**40**	**80**
	Sensor	**S3**	**S2**	**S4**	**S1**	**S4**	**S2**	**S3**
	Up/Down Stroke	**U**	**U**	**U**	**-**	**D**	**D**	**D**
1	MOFT (μm)	10.2	22.9	11.0	6.7	10.8	18.8	7.7
	COV (%)	1.2	6.5	2.5	3.0	2.9	7.0	0.9
2	MOFT (μm)	10.8	21.2	10.9	8.1	9.3	16.9	7.8
	COV (%)	1.4	3.1	2.1	2.4	1.6	3.1	1.2

Table 6.6: Steady-state MOFT across 25% loading for all configurations for the first piston ring passing all transducers [6]. © SAE International

Configuration	**Dist to TDC (mm)** **Sensor** **Up/Down Stroke**	**-80** **S3** **U**	**-40** **S2** **U**	**-20** **S4** **U**	**0** **S1** **-**	**20** **S4** **D**	**40** **S2** **D**	**80** **S3** **D**
1	MOFT (μm)	14.7	16.3	15.7	7.3	12.6	13.1	11.0
	COV (%)	2.9	2.2	1.3	1.8	1.3	2.4	1.4
2	MOFT (μm)	14.0	14.7	13.9	7.9	10.7	12.3	10.4
	COV (%)	1.1	1.7	1.5	10.4	3.5	1.7	2.1
3	MOFT (μm)	15.2	15.8	14.5	8.5	13.1	11.0	12.2
	COV (%)	1.5	1.2	1.5	1.5	1.9	1.2	2.5

6.5 Discussion

Ultrasonic reflectometry has been applied to a fired two-stroke RTX-6 engine to quantify the oil film thickness for three piston rings moving across four piezoelectric transducers. With MOFT values for the first piston ring ranging from 6-22 μm. To provide these values several assumptions have been made and limitations identified which are discussed in the following section. In addition, the MOFT from the RTX-6 is compared to oil film thickness measurements from alternative engines in this section.

6.5.1 Assumptions and limitations

The temperature used to define the oil speed of sound and density was determined from temperature measurements from the internal surface of the liner. It was assumed that the temperature of the oil in the contact was the same as this surface temperature. The flash temperature of the ring will have likely been significantly higher and vary with engine CA especially during the early stages of the power stroke. For 100% loading, all piston rings were assumed to be at 216 $^\circ C$, however, an increase of 10 $^\circ C$ reduces the oil film thickness calculated by 0.3 μm. This factor will have affected all measurements equally, therefore, the trends in results remain unchanged.

The ultrasonic transducers have provided OFT measurements that are similar to previous works with some of the same trends identified from alternative techniques, highlighting their robustness. Yet potential issues with either bonding, placement or damage, may have led to different trends in reflection coefficient to be seen for the third testing configuration. Sensor 2 for example provided consistently greater film thickness measurements than transducers on either side of the sensor indicating that the transducer may have been positioned incorrectly.

The spatial resolution of the sensors in this work was notably improved from previous ultrasonic ring-liner measurements [28, 29, 30, 31, 32, 64, 65]. As most of the previous research used piezoelectric transducers equal to or greater than the size of the first piston ring (piston ring to sensor size ratio of 1) yet this work used transducers smaller than any of the rings (14 mm active element diameter, piston ring to sensor size ratio of 1.2). Therefore, the averaging effect of the ultrasonic transducers was minimized when the sensing area was completely encompassed by a piston ring, aided further by the barrelled profile of the rings with the edges having small radii curvatures. However, the Spring Model applied in this work is only applicable for a solid-oil-solid system, therefore, it is only applicable when the piston ring is over the sensor. When the piston ring is marginally over the contact there is a combination of a partial solid-oil-solid system and a solid-oil system which inhibits the applicability of the Spring Model. The averaging effect of the ultrasonic transducers will have led to an overestimation of the lubricant film thickness in this region due to higher reflection coefficients being measured than caused purely by the piston ring itself. The averaging effect is summarised in Figure 6.30, through the use of three cases:

1. Case 1 No ring alignment: A complete reflection from the internal surface leading to a unity reflection, R=1.
2. Case 2 Partial ring alignment: The region not aligned with the piston ring experiences a reference reflection (same as Case 1). Whilst the region that is aligned with the piston ring has a reduced proportion that is reflected as a partial transmittance to the piston ring occurs. The resulting reflection coefficient recorded is an average over the whole surface, therefore, in the case shown R=0.85 due to half ring alignment and half reference reflection.
3. Case 3 Full ring alignment: The piston ring is completely aligned with the transducer leading to a partial transmittance over the whole alignment zone. This leads to a significant reduction in reflection coefficient such as those seen in Figure 6.12 from -6° to 6° CA.

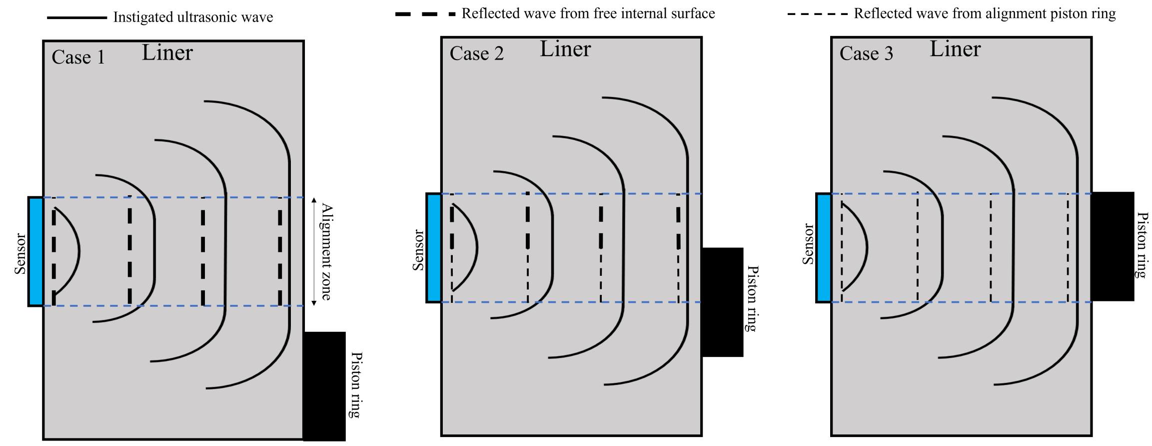

Case 1: $R = 1$ (reference)
Case 2: $R = \frac{1+0.7}{2} = 0.85 = \frac{50\%\ reference\ R + 50\%\ aligned\ R}{2}$
Case 3: $R = \sim 0.7$

Figure 6.30: Ultrasonic averaging effect summary.

It has been assumed that any changes in the reflection coefficient were purely from a piston ring moving over a transducer. For this to be the case the region between the piston ring and liner must be fully flooded with lubricating oil. Yet piston rings often operate under starved conditions or cavitation may occur in the lubricating film. Either of these factors would have led to a higher reflection coefficient than if the region were fully flooded with oil. Therefore, the OFT presented here is likely an overestimation of the true OFT especially for OFT values significantly far from the MOFT.

6.5.2 Comparison to other works

The oil film thickness between a piston ring and cylinder liner has been the focus of numerous works, with most of that research focusing on smaller engines. Due to this, their comparison to a large diesel marine engine is somewhat limited. The MOFT from previous research typically varies from 0.2-20 μm across all techniques [28, 29, 30, 31, 32, 33, 34, 35, 36, 39, 41, 42, 43, 44, 49, 50, 64, 65] with ultrasound providing measurements from 2-20 μm [28, 29, 30, 31, 32, 64, 65]. The OFT from the RTX-6 is thinnest for the first ring at the TDC (6.3 μm Configuration 1), which is close to the MOFT from a Winterthur Gas & Diesel RTX-4 engine of 6 μm [66]. These values are a factor of 3 larger than their automotive counterpart minimums which may partially be from a larger engine operating at much greater loads and partially from this work being on the neutral side of the engine as most previous works study the thrust or anti thrust side.

6.6 Conclusions

The lubricating film between a piston ring and cylinder liner in a large diesel marine engine has been quantified using ultrasonic reflectometry by positioning piezoelectric transducers close to the TDC on the outer surface of an RTX-6 liner. This oil film is a key contributor to engine emissions with lubricant thrown off into the combustion chamber raising particulate emissions and wasting oil. However, if the lubricating film is too thin it leads to metal-metal contact and damage to engine components. The findings from this work can be summarised as follows:

- The thickness of the piston ring lubricating film has been quantified for three engine loadings across three different cylinder injection configurations each with varying rates of lubricant atomisation. Across all three injection configurations, the oil film thickness increases with decreased engine loading. These findings agree with other research into piston ring film thickness using other techniques on a range of engines.
- Configuration 2 provided a thicker minimum oil film thickness for the first ring at the TDC than either of the other two engine configurations (7.4 μm instead of 6.3 μm and 6.6 μm). This engine configuration used a needle lift type injector on the upper rail which reduced the rate of lubricant atomisation reducing lubricant losses to the exhaust manifold whilst it also increased the thickness of the lubricating film. It is, therefore, reasonable to conclude that this engine configuration reduces engine emissions, by a smaller loss of lubricant whilst also improving the lubrication regime of the piston rings close to the TDC aiding to avoid boundary lubrication.
- Within each loading and engine configuration the oil feed rate was varied from its nominal rate to an upper and lower rate in 5-minute intervals. Measurements of the minimum oil film thickness during this time display no clear trend between minimum oil film thickness and oil feed rate. This is expected to be the case due to the short time intervals of the change in the oil feed rate. This is also represented in a delayed discernible change in minimum reflection coefficient from the engine slowdown results.

Chapter 7

Fired marine engine advanced analysis

The previous chapter (Chapter 6) covers the measurement of oil film thickness for multiple piston rings at four locations close to the TDC in an RTX-6 marine diesel engine to compare three lubricant injector configurations. The data processing presented was equivalent to that used in previous research in the field. This chapter expands upon the previous chapter to cover an additional sensor not previously considered and to evaluate various advancements in the data processing.

In total seven ultrasonic transducers were instrumented, all of which are detailed in Figure 7.1 with the additional sensors highlighted. The additional longitudinal transducer is highlighted in green and shear transducers in blue. The opening section of this chapter covers frequency index data processing (such as seen in Figure 6.6) for Sensor 5, a sensor above any piston ring at their TDC position before developing onto alternative data processing techniques. The shear sensors shown in blue are considered in Chapter 8.

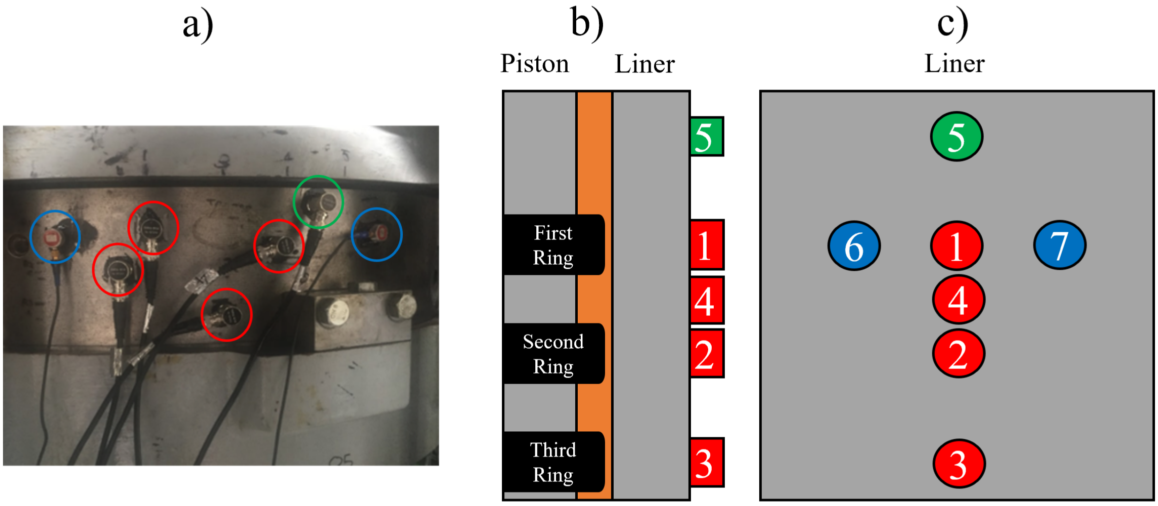

Figure 7.1: Full set of instrumented ultrasonic transducers on the RTX-6 liner. a) Photograph of the sensors. b) Side profile of the sensors showing the position relative to the piston rings at their TDC positions. Note, only the longitudinal sensors appear for visualisation purposes. c) The sensor numbering convention of all seven sensors; red were covered in Chapter 6, green is an additional longitudinal sensor, blue are two shear sensors and covered in Chapter 8.

7.1 Longitudinal transducer above first ring

The additional longitudinal sensor, Sensor 5, is of key interest as it is noticeably different from the other four longitudinal transducers. Like the other longitudinal sensors it is a 1 MHz sensor with a 14 mm active element diameter although in this case it was instrumented 20 mm above the first ring at the TDC. Therefore, no piston ring transverses this transducer at any point in the engines' cycle. In *theory* there would be no variations in the recorded ultrasonic reflections for this sensor and, therefore, the reflection coefficient would not vary at any crank angle.

By applying the same data processing technique as outlined in Figure 6.10 the reflection coefficient has been defined from a frequency index at the central frequency. The reflection coefficient variation over a 100° CA range centred at the TDC for 100% loading steady-state operation for Sensor 5 is shown in Figure 7.2 for all three engine configurations.

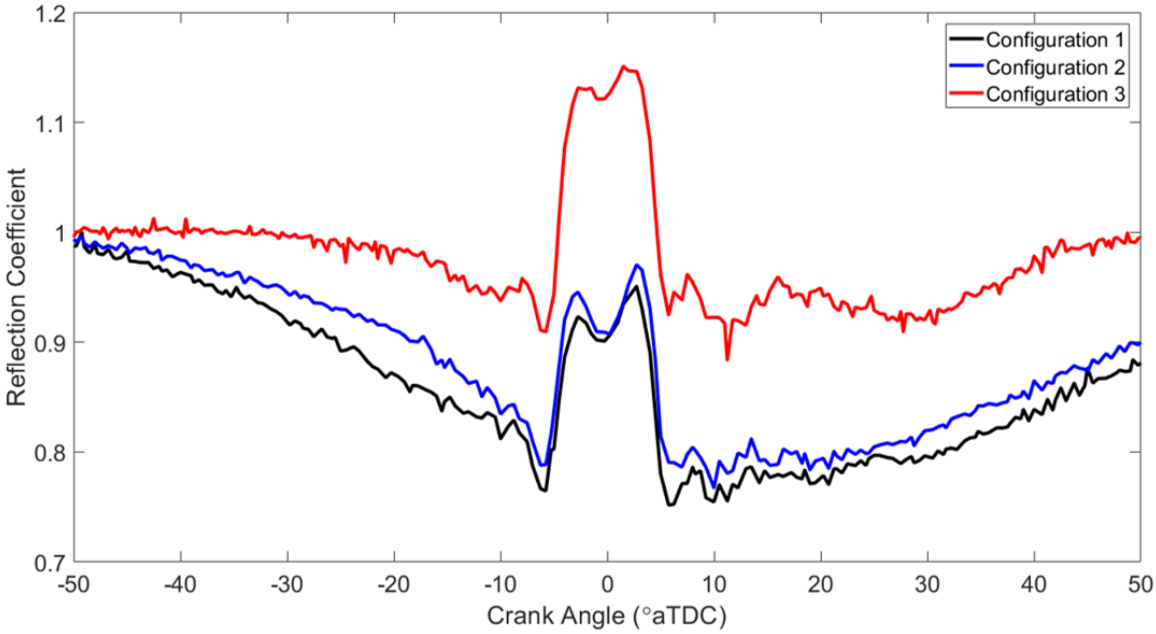

Figure 7.2: Reflection coefficient variation over Sensor 5 at steady-state 100% loading for all engine configurations.

Counter intuitively, Figure 7.2 shows that there is a significant change in reflection coefficient over the 100° CA range, with a decrease seen for the majority of the CA range, even with no piston ring aligning with this sensor. Noticeably the trend in variation is very different from those seen in the previous chapter for the other in-contact longitudinal transducers. All three configurations display the same trend in reflection coefficient, although in Configuration 3 there appears to be a vertical shift in the reflection coefficient typically in the order of 0.15 close to the TDC. The cause of the drop in reflection coefficient over the large CA range is currently unknown. The presence of this variation without a piston ring indicates a more complex interaction between a piston ring and sensor is occurring than previously considered.

It is theorised that the increase in reflection coefficient immediately before and after the TDC may be caused by the fringe effects of the approaching transducer. The fringes seen here are similar in magnitude to those seen in the previous chapter in Figure 6.12 however, in this case, the fringe effects are adjoined immediately before and after the TDC as a ring never reaches this transducer so no sharp reduction in reflection coefficient is seen. The concept of the ultrasonic wave reflecting outside of the alignment zone is shown in Figure 7.3 through three different reflection cases.

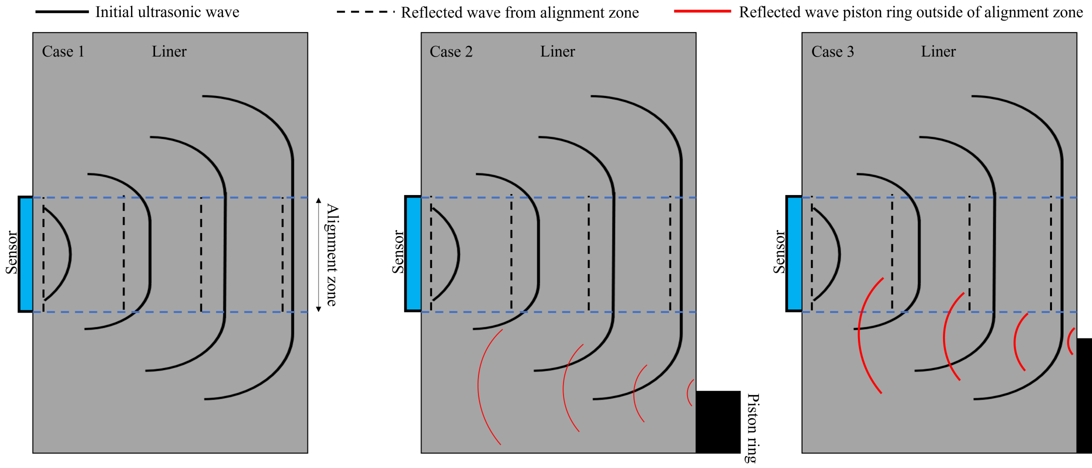

Figure 7.3: Theorised fringe effect interference.

In summary, as the ultrasonic wave propagates through the liner the beam spreads, part of that wave interacts with the approaching piston ring significantly far from the alignment zone. The magnitude of the wave that interacts with the piston ring outside the alignment zone increases as the piston ring moves up the liner leading to the peaks above unity reflection coefficient (R>1). These peaks were seen immediately before and after the rings for Sensor 1-4 and from -7° to 7° CA for Sensor 5 as the piston ring is close to the alignment zone for a greater CA range for this sensor.

7.1.1 Wave reflection simulation

To justify these theorisations, a k-Wave simulation (introduced in Section 3.9) equivalent to Sensor 5 has been developed. The developed model consists of pulsing an ultrasonic wave through a medium and recording the reflection from the other side that has a full lubricant film. The simulation is run multiple times (> 750) with each simulation moving the 'piston ring' across the domain, equivalent to a piston ring moving up the cylinder liner. In k-Wave, a domain is defined and the speed of sound and density at each node is set. In the case of a piston ring and cylinder liner example, the model parameters are defined in Table 7.1.

Table 7.1: k-Wave model parameters.

Model parameter	**Value**	**Unit**
Domain size	640x2560	-
	4x20	mm
Input signal	1	MHz
Liner	5000	m/s
	7300	kg/m^3
Oil	1007	m/s
	781	kg/m^3
Piston ring	6000	m/s
	7850	kg/m^3

An example of the domain for two simulations is shown in Figure 7.4 in which the upper plots show a simulation with the piston ring significantly far from the sensor, whilst the lower plots are for a near aligned piston ring. The solid mediums are shown in black, whilst the liquid (engine oil) is shown in white. The speed of sound plot for the near aligned piston ring case is highlighted for visualisation of the thin lubricant film between the solid media.

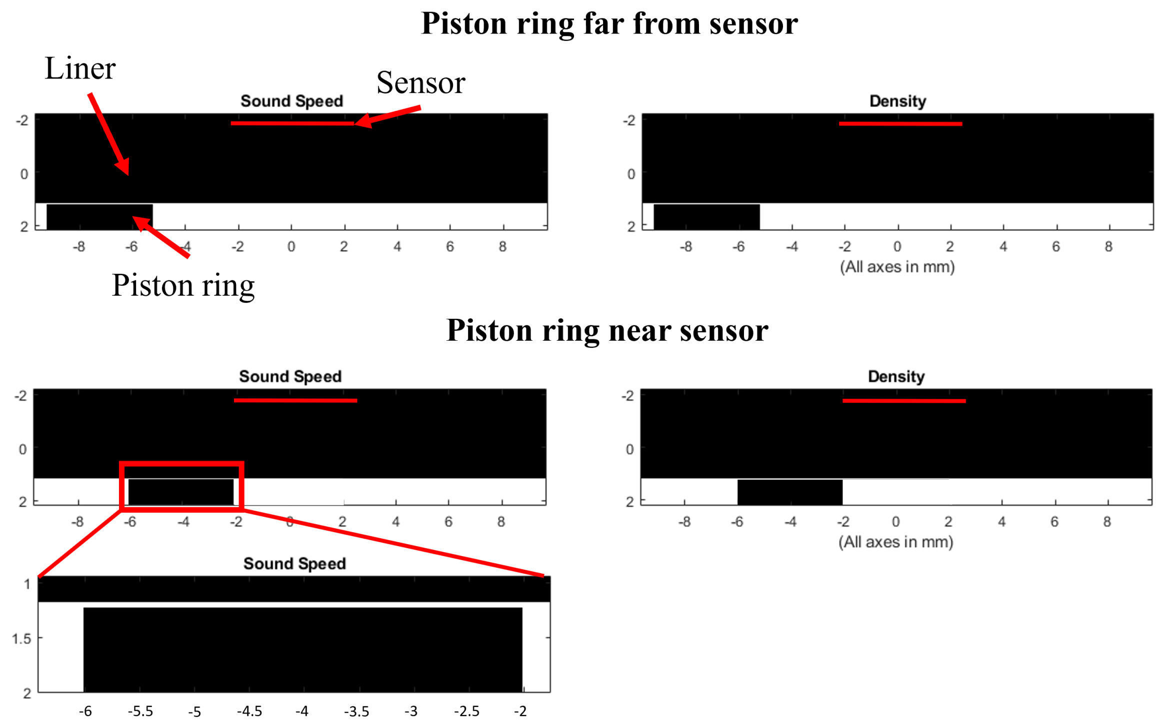

Figure 7.4: Domain of two simulation examples.

The series of simulations produces an ultrasonic reflection from each piston ring position. By processing these reflections to convert them to the frequency domain and defining the reflection coefficient at 1 MHz the reflection coefficient for the simulation is produced, as shown in Figure 7.5.

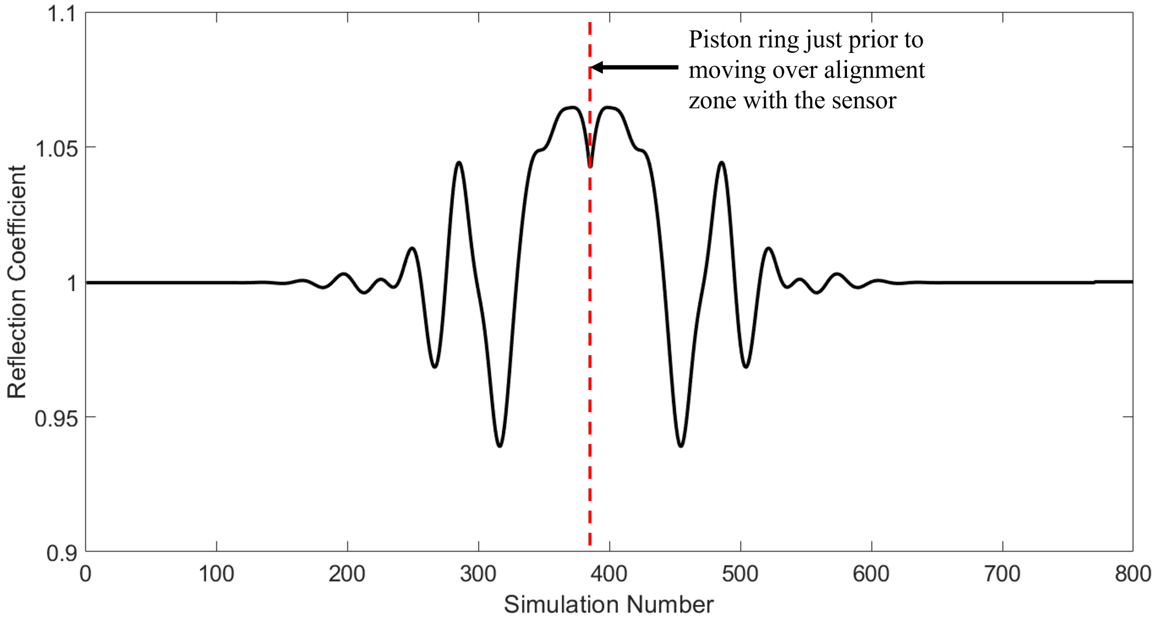

Figure 7.5: A simulation equivalent for Sensor 5.

The sharp rise and dip in the reflection coefficient immediately before and after the TDC similar to that previously shown in the experimental results in Figure 7.2 can be seen in Figure 7.5. Further indicating that the approaching ring combined with the spreading of the ultrasonic wavefront leads to additional energy to be reflected towards the sensor. All longitudinal transducers were located in vertical increments (up to 20 mm) from the next transducer it is, therefore, reasonable to conclude that each of the sensors will have been impacted by this effect when a piston ring was aligned with a different sensor. The magnitude of the effect being proportional to the CA range in which a ring was close to the sensor, therefore, the impact is reduced on rings further down the liner as the piston moved faster here.

Notably, there is no reduction in the reflection coefficient over an extended range in the simulation. There are several potential causes for this:

1. The model is entirely based on wave propagation, therefore, it does not consider engine factors impacting the sensor, such as the impact of cylinder pressure or combustion products.

2. Potential error in transducer instrumentation placement leading to the experimental transducer experiencing unanticipated reflections.

3. The liner is assumed to be an anisotropic elastic solid which is not the case in cast iron.
4. The model used a "perfect" 1 MHz input and assumes the ring is a constant distance from the liner of 12 μm. Both of these differ from the experimental results due to noise in the system and the piston rings relative freedom to vary the distance from the liner surface.

Sensor 5 is above all three piston rings at their TDC positions, this prevents any oil film thickness analysis using the results from this transducer. The analysis is purely focused on the reflection coefficient whose trends still provide informative information to deduce factors hidden in results for the other transducers.

7.2 Reflection window optimisation

Initial analysis in Chapter 6 studied the complete recorded reflection, primarily as from base analysis the length of the studied signal should be independent of the results providing that only the reflection of interest is within that captured window. In this section, the effect of varying the A-scan window length is studied further to optimise how a reflection is defined to minimise the effect of undesired reflections/noise in the system. A typical reflection from Sensor 1, Configuration 1 100% loading is shown in Figure 7.6. Each ultrasonic reflection consisted of a 1.6 μs recording although this section presents the data in terms of raw data points for ease of comparison of differing portions of the signal (one data point captured every 2 ns).

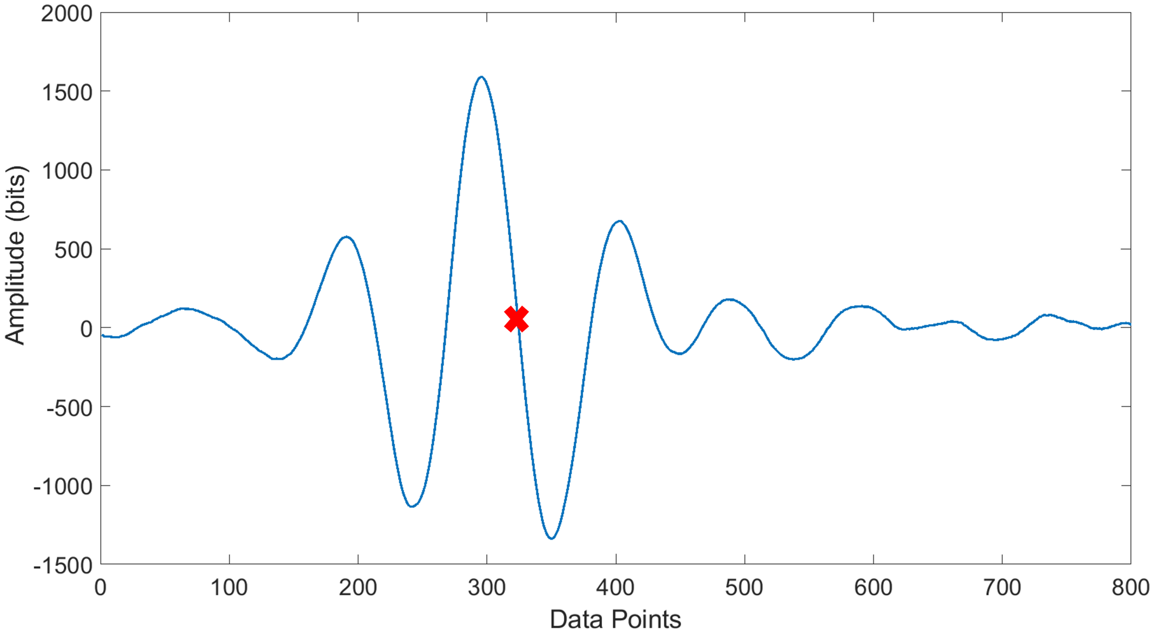

Figure 7.6: Full reflection window for Sensor 1 Configuration 1 100% loading.

The effect of the A-scan window size on the reflection coefficient was studied by defining the central zero crossing point of a reflection (Data Point 320, marked with the red cross in Figure 7.6) and incrementally reducing the window size studied to towards that central point. The reflection is treated as symmetrical about the zero-cross point, due to this the window was initially incrementally reduced from Data Points 1-800 to 1-640 leading to the central zero point being the centre of the reflection window. The reflection coefficient from using a frequency index of 1 MHz at a range of window sizes is shown in Figure 7.7a with a smaller CA range shown in Figure 7.7b.

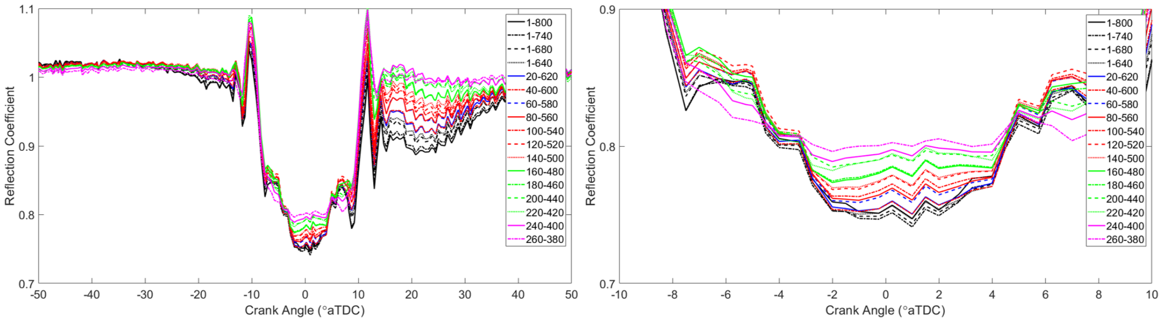

(a) Reflection coefficient variation.

(b) Smaller CA range view of Figure 7.7a.

Figure 7.7: Frequency index reflection coefficient from varying window length.

Figure 7.7 clearly shows that the window size has a major effect on the reflection coefficient on both when the ring was aligned and outside of the alignment zone. A greater window length considered produced a greater reduction in the reflection coefficient as the piston ring moved over the sensor and a greater reduction post ring. Figure 7.7 indicates that selection of the window size has an impact on the reflection coefficient and, therefore, the calculated OFT.

The frequency domain representation of the signal that produced these reflection coefficient variations are shown in Figure 7.8a. One route to define which window size to use is to identify when the maximum amplitude of the signal in the frequency domain and study when that becomes independent of window size. Observation of Figure 7.8a indicates that as the window size was reduced the overall amplitude of the signal reduced (as energy in the reflection was removed) and the peak of the signal in the frequency domain shifts to a lower frequency. The frequency of the maximum amplitude in the frequency domain variation with A-scan window size is shown in Figure 7.8b.

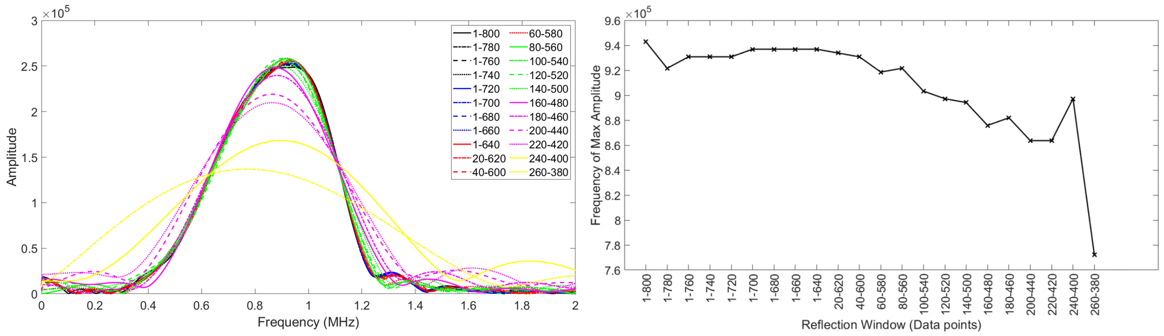

(a) A reflection in the frequency domain from varying window size.

(b) Frequency of the maximum amplitude from the frequency domain view of the signal.

Figure 7.8: The frequency domain view of a signal and isolated frequency of maximum amplitude from varying window sizes.

Figure 7.8b indicates that the frequency of the maximum amplitude is independent of A-scan window size beyond 1-640. Therefore, the window of the reflection could be reduced to 1-640 with minimal effect in the frequency domain. Beneath this window, a progressively increased impact on peak amplitude frequency is seen. The reduced window size has now been used for further data processing as it removes some energy from the considered window with minimal effect in the frequency domain. This method is not to be used as a reliable approach as there is likely to be some energy in the reflection not from the piston ring still included in the reflection from Data points 1-640.

7.2.1 Optimised window spectrograms

The impact the reflection window size has on the spectrogram is shown for a range of window lengths in Figures 7.9a - 7.12a for four window lengths. The case shown is for Sensor 1, Configuration 3 for a high-speed data capture. The case shown is outside of steady-state engine operation as no high-speed captures were recorded at steady-state. Due to this section comparing one test with differing analyses, the need for steady-state operation is deemed to be not an impacting factor on the results. In addition to the spectrograms, reflection coefficient plots are shown for each window considered at a range of frequencies to provide a visualisation of frequency variation in Figures 7.9b-7.12b. Note the data processing for Figure 7.9 is equivalent to the spectrograms shown in Chapter 6.

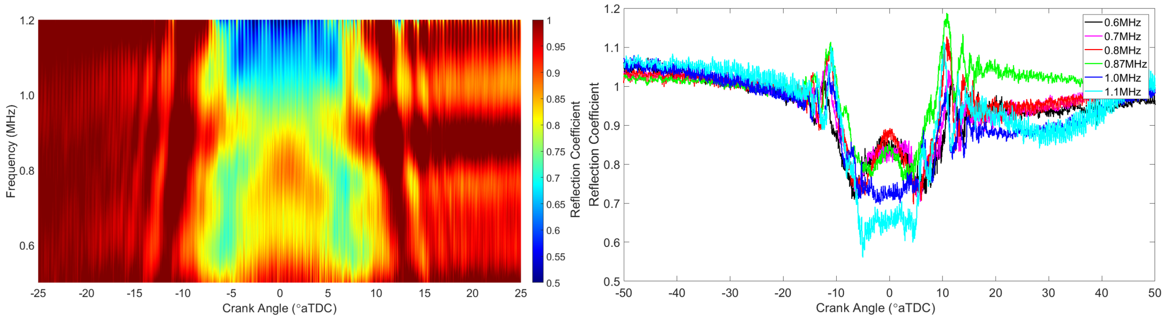

(a) High speed spectrogram.

(b) Reflection coefficient at various frequencies.

Figure 7.9: Spectrogram and frequency variation for window: 1-800.

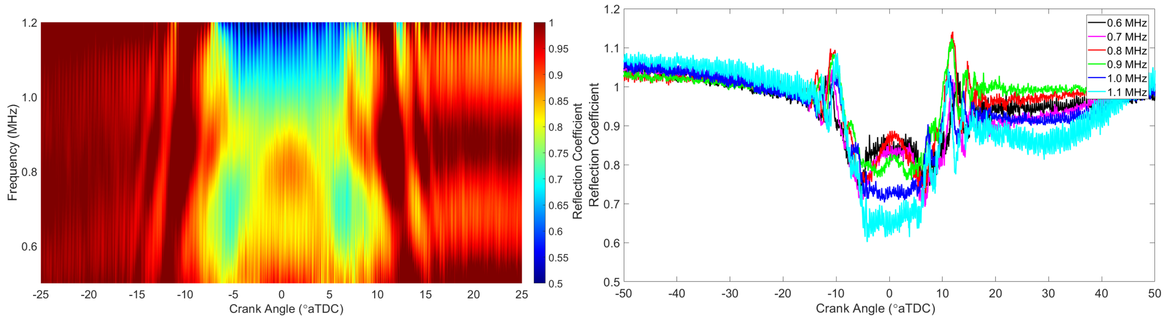

(a) High speed spectrogram.

(b) Reflection coefficient at various frequencies.

Figure 7.10: Spectrogram and frequency variation for window: 1-640.

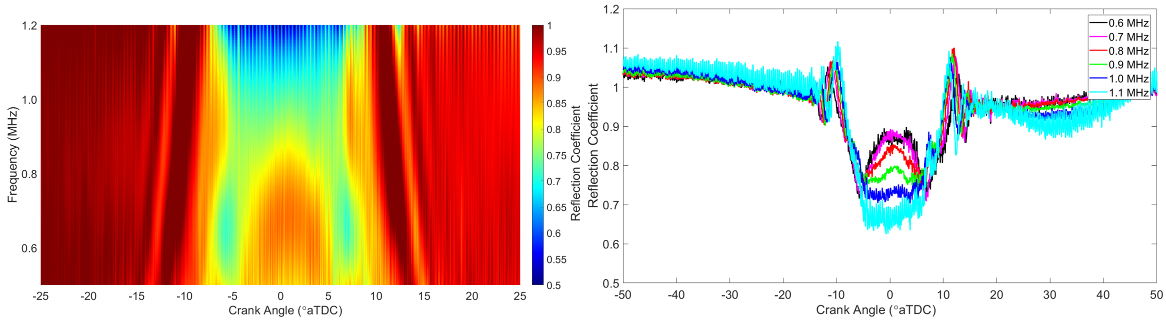

(a) High speed spectrogram. (b) Reflection coefficient at various frequencies.

Figure 7.11: Spectrogram and frequency variation for window: 120-520.

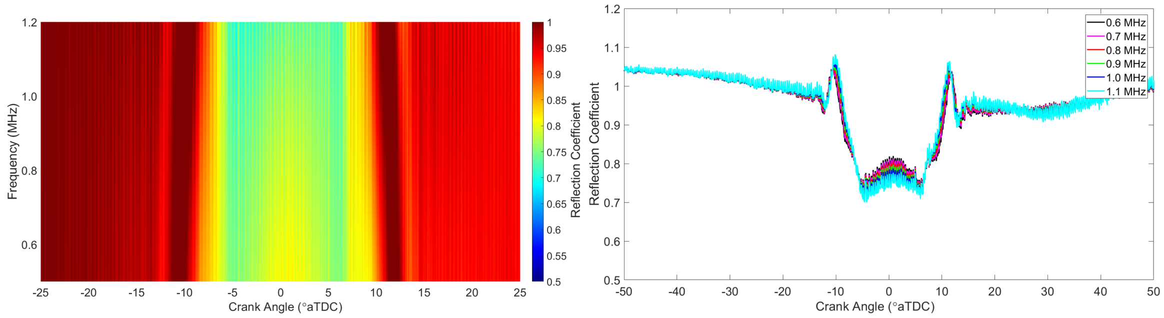

(a) High speed spectrogram. (b) Reflection coefficient at various frequencies.

Figure 7.12: Spectrogram and frequency variation for window: 260-380.

The reduction of the window size modifies several trends that were initially observed in Figure 6.17. The fringe effects initially displayed as an off-vertical pattern whose CA tends towards the TDC at higher frequencies becomes frequency independent at a reduced window size with the multiple bands simplifying to a single peak, such as those in the Hilbert envelope method (see Section 7.5).

The central pattern in the spectrogram (that was previously seen as a double dip at a reflection coefficient of 1 MHz) is even more pronounced at the lower frequencies for the greatest window size (Figure 7.9a). However, it is nearly completely removed at all frequencies by the smallest window size considered here (Figure 7.12a). All frequencies display a marginal increase of roughly 0.05 reflection coefficient shortly after the TDC even for the smallest window in Figure 7.12.

The windowing also completely removes the pattern outside of the piston ring alignment region, initially believed to be a measure of residual oil on the liner. This factor is clearly shown to be in the spectrograms due to the later portion of the signal that is removed from the smaller window sizes.

Frequency variation over the bandwidth of the transducer is shown in Figures 7.9b - 7.12b for six frequencies over the observable bandwidth. These plots clearly show, similar to their respective spectrograms, that as the window size is reduced the frequency variation is reduced until the final window (260-380, Figure 7.12b), the reflection coefficient is frequency independent. Notably, the reflection coefficient at all frequencies tends towards that of the Hilbert envelope for Sensor 1 (see Section 7.5).

The measurable bandwidth of the transducer is also increased with reduced window size, for the full window (1-800) the measurable bandwidth is 0.6-1.2 MHz whilst for a smaller window (260-380) the range increases to 0.1-1.7 MHz (see Figure 7.13).

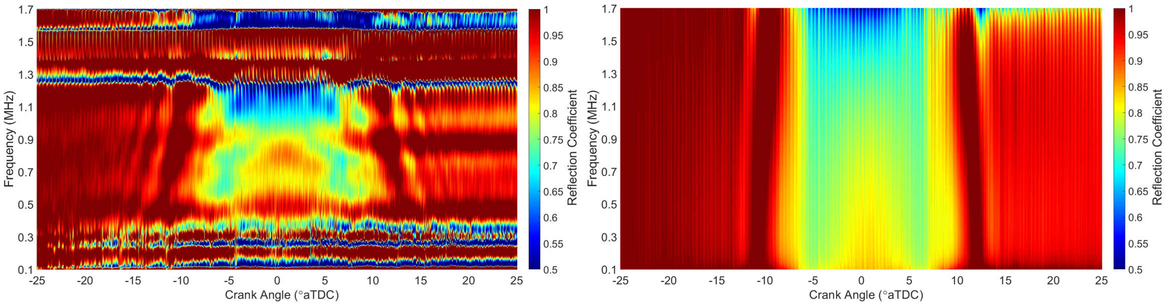

(a) High speed spectrogram 1-800.

(b) High speed spectrogram 260-380.

Figure 7.13: Spectrogram with greater bandwidth for varying A-scan window length.

The spectrograms produced in this work are initially comparable to those in other ultrasonic works, [89, 90], with some similar patterns highlighted, such as the off-vertical fringe effect patterns. Although it is clear that depending on how their reflection was defined, it would have had a significant effect on the spectrogram pattern produced.

This section is not to be used separately from the previous section which studied how the minimum reflection coefficient was affected by the ultrasonic reflection window length but used in conjunction and to visualise its effect on the spectrograms produced. Therefore, although it is not the 'simplest' spectrogram produced, the spectrogram shown in Figure 7.10a is deemed the appropriate spectrogram for this test case due to it having a reduced effect from the extremities of the recorded reflection with an unaffected minimum reflection coefficient.

7.3 Spectrograms

This section advances on single reflection window optimisation (Section 7.2) by using the optimised reflection window length to produce spectrograms at steady-state loading for all engine configurations and engine loading levels.

7.3.1 Configuration variation

The spectrograms for the first engine cycle of Sensor 1 at steady-state 100% engine loading of all three configurations are shown in Figures 7.14a-7.16a. The spectrograms have been limited from 0.9 < R < 1.1 for visualisation of the effect outside of the ring alignment. Whilst the spectrogram for the 5 second capture duration is shown for the three configurations in Figures 7.14b-7.16b respectively.

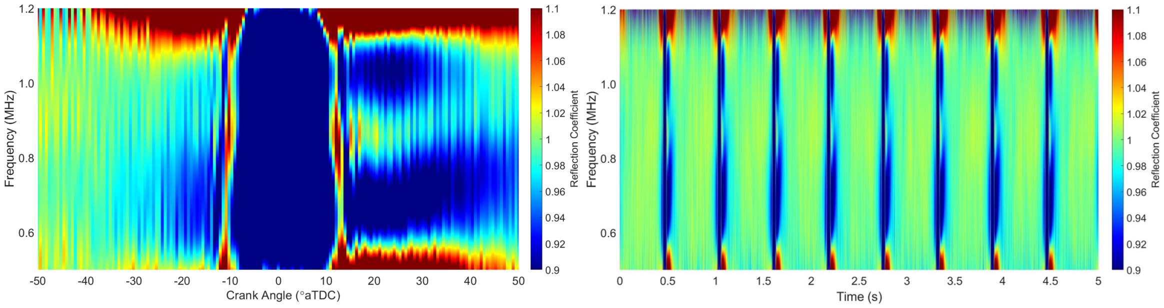

(a) Spectrogram from the first engine cycle. (b) Spectrogram for each cycle in a capture.

Figure 7.14: Optimised spectrograms for Sensor 1 100% loading Configuration 1.

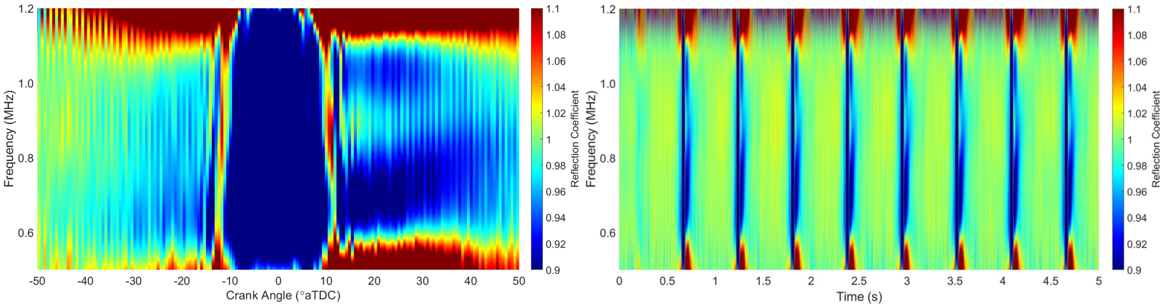

(a) Spectrogram from the first engine cycle. (b) Spectrogram for each cycle in a capture.

Figure 7.15: Optimised spectrograms for Sensor 1 100% loading Configuration 2.

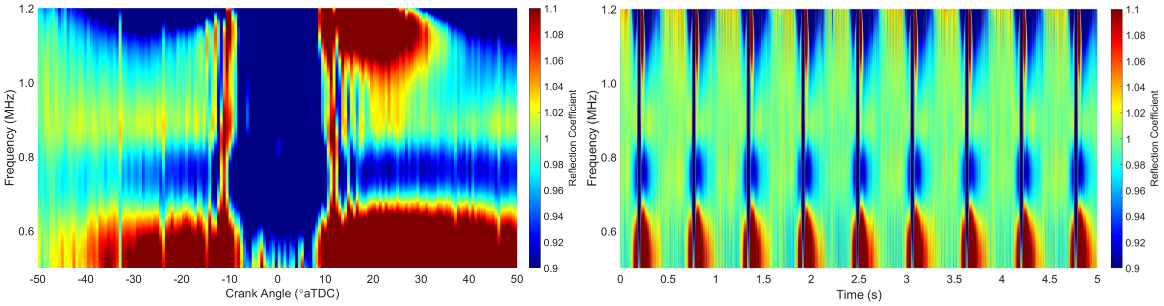

(a) Spectrogram from the first engine cycle. (b) Spectrogram for each cycle in a capture.

Figure 7.16: Optimised spectrograms for Sensor 1 100% loading Configuration 3.

Having optimised the A-scan window length from Figures 6.17, the patterns outside of ring alignment are largely unchanged with the region post ring pack passage leading to a major change in reflection coefficient. In the case of Configurations 1 and 2, two bands of decreased reflection coefficient centring at 0.7 MHz and 1 MHz which tend towards each other as CA increases. Whereas Configuration 3, as often the case, shows differing results with one band of increased and decreased reflection coefficient.

The consistency of these patterns is displayed in Figures 7.14b-7.16b with each configuration having identical patterns produced for at least 8 consecutive cycles at steady-state operation. It is also noted that these patterns are only present on a small CA range immediately before or after the piston rings. No other region differs significantly from a unity reflection coefficient. The horizontal bands on the optimised window spectrograms still are indicative of a residual film in the order of 1500 μm which is observable for a short CA post ring as seen in Section 6.3.2.

The Spring Model (Equation 3.23) can be applied to the ring alignment region (-8.5° to 8.5° CA) of the optimised spectrograms to provide oil film thickness measurements over the complete bandwidth of the transducer. This has been done for the three configurations in Figures 7.17a-7.19a. To aid visualisation, frequency comparison plots of OFT at four specific frequencies are plotted in Figures 7.17b-7.19b with the transducer central frequency in black.

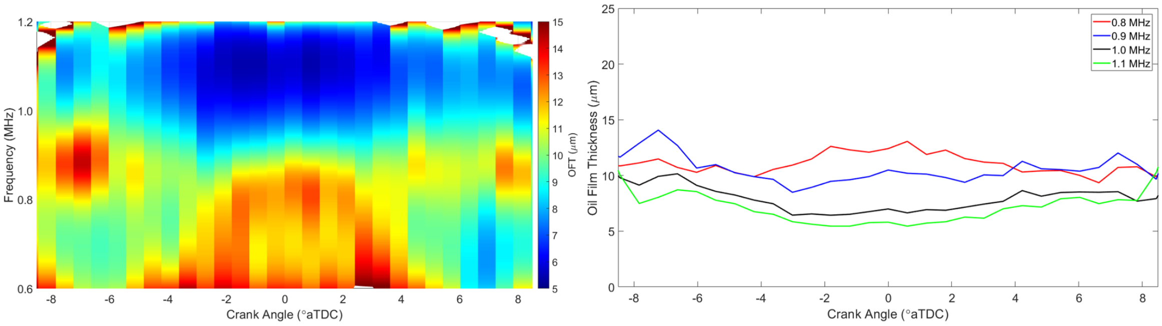

(a) Oil film thickness Spectrogram. (b) OFT from a sample of frequency values.

Figure 7.17: Optimised oil film thickness spectrograms for 100% loading Configuration 1.

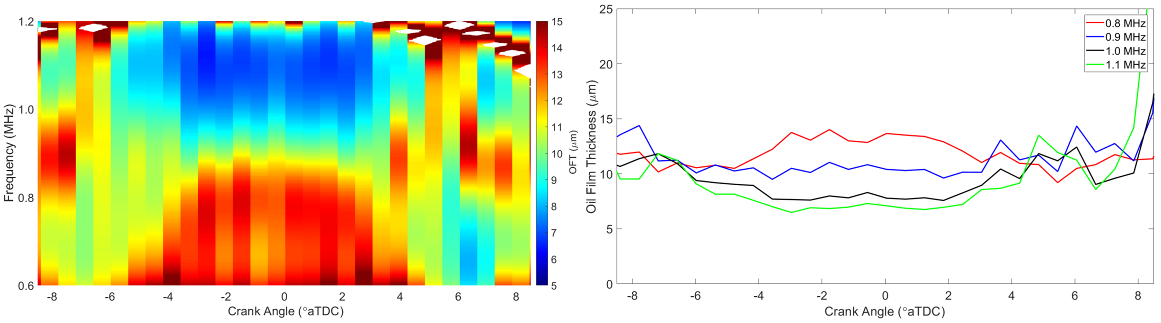

(a) Oil film thickness Spectrogram. (b) OFT from a sample of frequency values.

Figure 7.18: Optimised oil film thickness spectrograms for 100% loading Configuration 2.

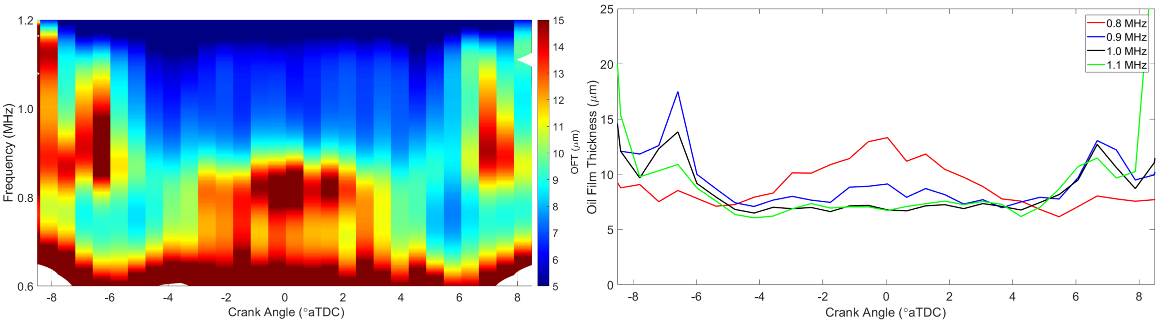

(a) Oil film thickness Spectrogram. (b) OFT from a sample of frequency values.

Figure 7.19: Optimised oil film thickness spectrograms for 100% loading Configuration 3.

The lubricant film thickness is frequency independent, so within the bandwidth of the sensor a uniform film thickness should be observed, see Figure 6.10. This is evidently not the case for Sensor 1 as across all engine configurations the oil film thickness spectrograms display the same peculiar trend as was seen in the reflection coefficient spectrograms (Figures 7.14a -7.16a, that the lower half of the frequency range produces a significantly higher oil film thickness (up to twice at thick) than the higher frequency range half for -3° to 3°

CA. The extent of the frequency variation can be seen in Figures 7.17b-7.19b. The OFT plots display that above the inflexion in the OFT spectrograms (0.85 MHz), near frequency independence is seen for all three configurations above 1 MHz. The cause of this inflexion is unknown and should, therefore, be avoided for any OFT measurements.

7.3.2 Loading variation

Optimised spectrograms have been processed for Sensor 1 Configuration 1 at the three engine loading levels. The first engine cycle of the steady-state recording is shown for 100% to 25% loading in Figures 7.20a-7.22a respectively. Spectrograms for the whole capture duration is shown in Figures 7.20b-7.22b.

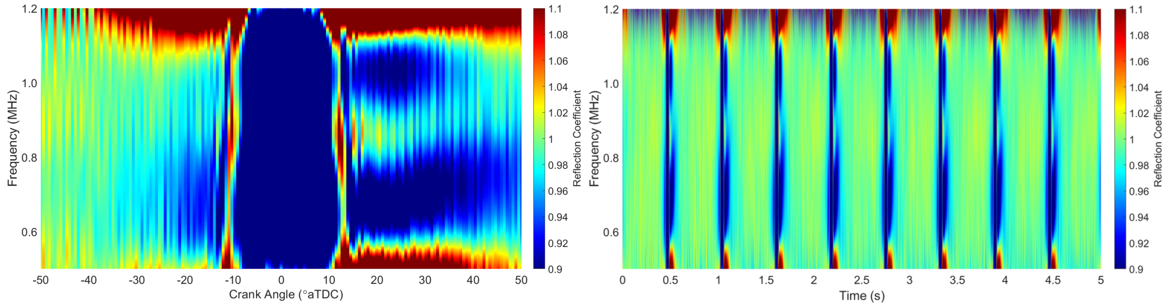

(a) One engine cycle for spectrogram.

(b) Spectrogram for each cycle in a capture.

Figure 7.20: Optimised spectrograms for 100% loading Configuration 1.

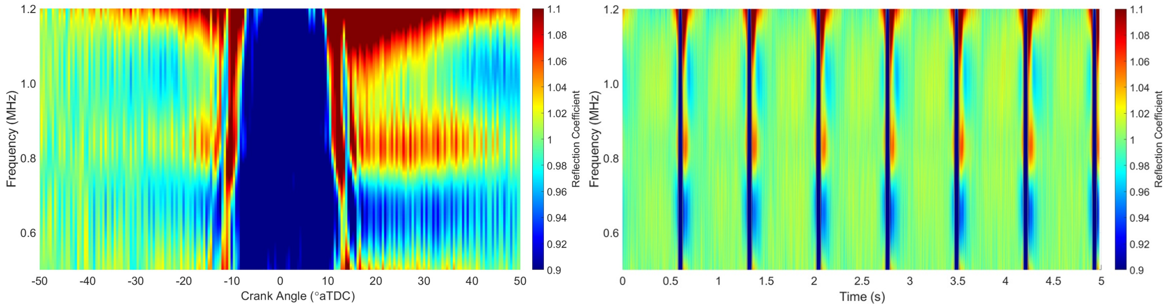

(a) One engine cycle for spectrogram.

(b) Spectrogram for each cycle in a capture.

Figure 7.21: Optimised spectrograms for 50% loading Configuration 1.

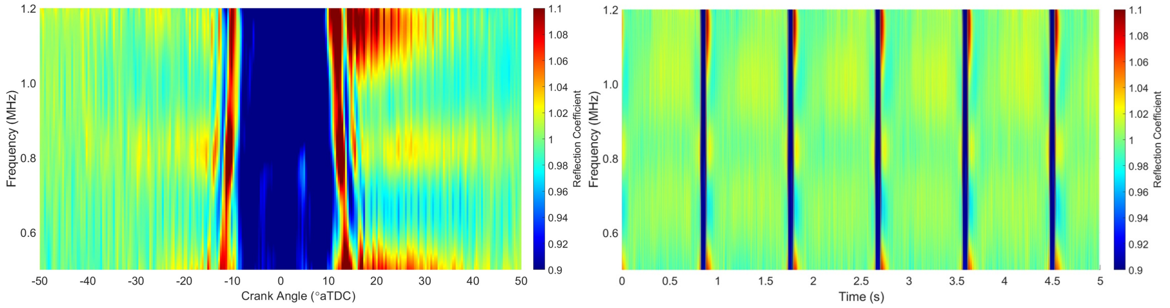

(a) One engine cycle for spectrogram. (b) Specotrogram for each cycle in a capture.

Figure 7.22: Optimised spectrograms for 25% loading Configuration 1.

The extended change in reflection coefficient post piston ring seen for all engine configurations at 100% loading (Figure 7.20a) is nearly completely removed by a reduction to 25% engine loading (Figure 7.22b). This is also consistent for every engine cycle in the data recording as shown in the spectrograms in Figures 7.20b-7.22b. Note a reduced number of engine cycles are seen at lower engine loading levels as the engine speed was also reduced. The reduction in the horizontal bands at lower engine loading, therefore, indicates that these prolonged changes in reflection coefficient are loading dependent. In this RTX-6, the standard oil feed rate in the engine (0.8 g/kWh) is dependent upon engine loading. Therefore, at lower engine load, less oil was sprayed onto the liner which has resulted in less pronounced horizontal bands, therefore, they indeed may be a measure of the residual oil levels.

The fringe effects become more pronounced for the optimised spectrograms at lower engine loading, this is likely due to the reduction in presence of the extended horizontal bands of reflection coefficient variation as opposed to a greater presence of the fringe effects. In Section 7.4, the fringe effects are explored further and the B-scans for differing engine loading levels in Figures 7.29 and 7.32 show a reduction in time delay of the fringes effect at lower loading levels but they remain equally prevalent in the results.

Oil film thickness spectrograms have been produced for the three engine loading levels of Configuration 1 in Figures 7.23a-7.25a for 100% to 25% respectively. To aid in visualisation four frequencies from the oil film thickness spectrograms have been plotted in Figures 7.23b-7.25b with the transducer central frequency in black. OFT values above 25 μm have been removed due to the spring model only being applicable up to 25 microns.

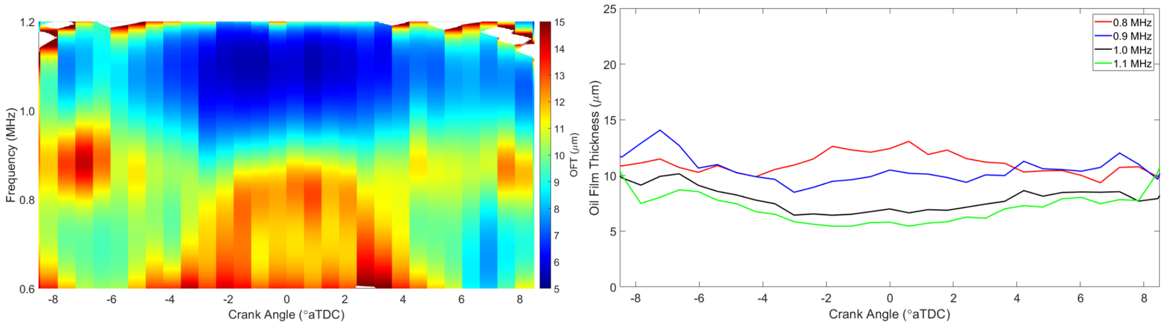

(a) Oil film thickness Spectrogram. (b) OFT from a sample of frequency values.

Figure 7.23: Optimised oil film thickness spectrograms for 100% loading Configuration 1.

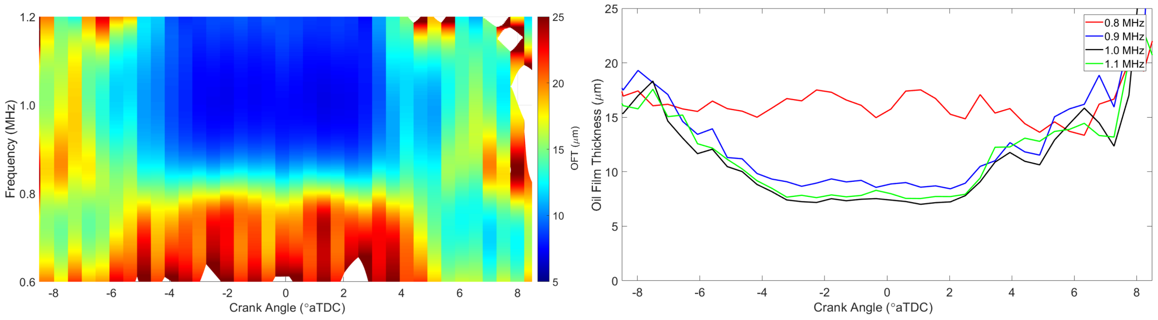

(a) Oil film thickness Spectrogram. (b) OFT from a sample of frequency values.

Figure 7.24: Optimised oil film thickness spectrograms for 50% loading Configuration 1.

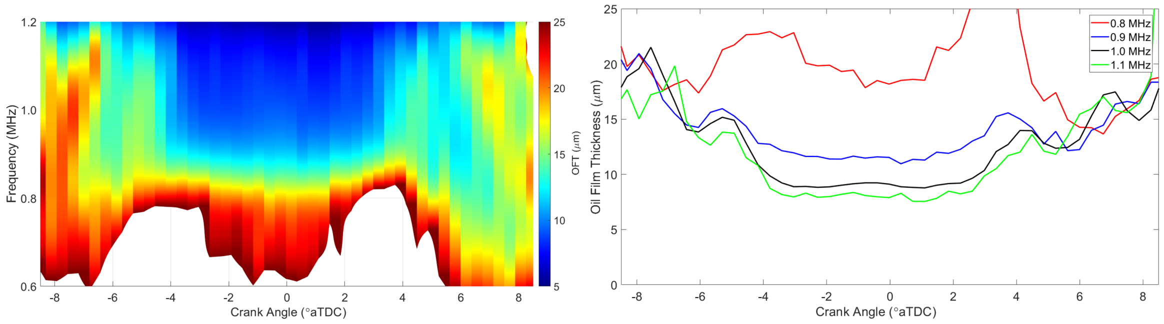

(a) Oil film thickness Spectrogram. (b) OFT from a sample of frequency values.

Figure 7.25: Optimised oil film thickness spectrograms for 25% loading Configuration 1.

The lower engine loading oil film thickness spectrograms in Figure 7.24a and Figure 7.25a overall display the same trend as for the 100% loading case (Figure 7.23a). Whilst the lower loading levels provide a greater OFT, as expected for a reduction in engine loading levels. All loading levels still display the same inflexion in OFT at 0.85 MHz to move from a thicker film to a much thinner film at higher frequencies. The cause of the inflexion requires further research as above this frequency there is near frequency independence of the oil film thickness across all engine configurations and loading levels.

7.3.3 Sensor 2 spectrogram

The spectrograms shown in this section focus on Sensor 1, primarily as it is the simplest transducer with the most discernible trends. An example of a spectrogram from Sensor 2 is shown in Figure 7.26. The increase in complexity of the spectrogram is evident and remains present with an optimised reflection window. Due to Sensor 2 covering two piston rings, this also enables the potential of reflections from adjacent piston rings which are not aligned with the sensor. This is further explored in the section on B-scans (Section 7.4).

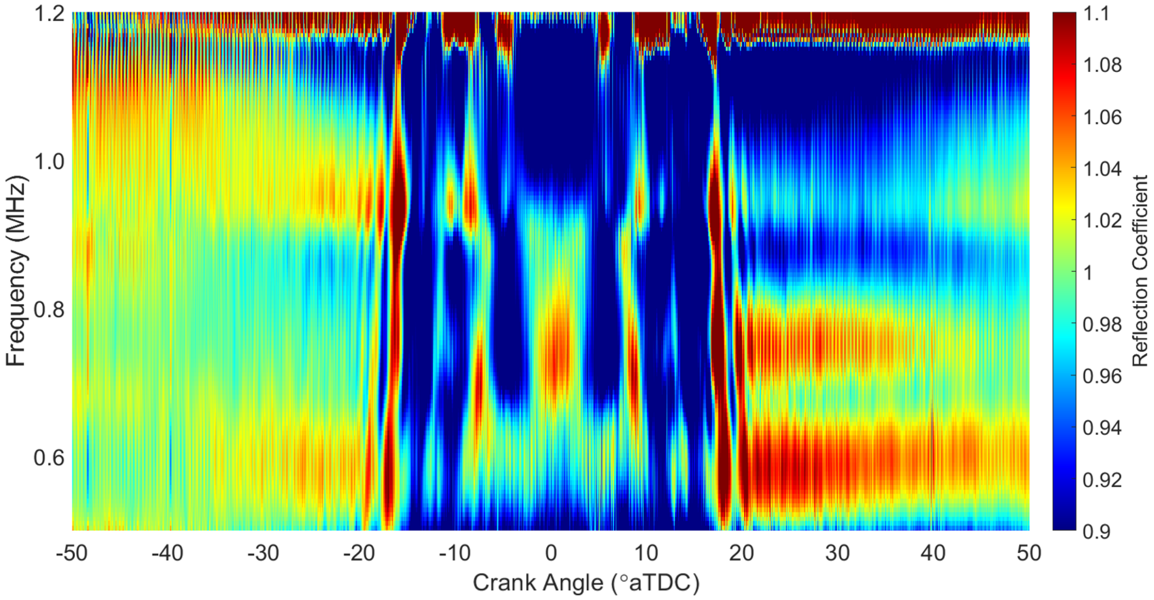

Figure 7.26: Spectrogram for Sensor 2 using Configuration 3 100% loading.

7.4 B-scan analysis

Analysis of the reflection window length and optimised spectrograms indicated that the delayed portions of the reflection (beyond when the reflection is visually observable) have an impact on the overall reflection coefficient. This section studies B-scans in an attempt to visualise these delayed factors impacting the reflection coefficient plots. A B-scan is an alternative viewpoint of the raw data, to stack the raw A-scans together. This has the potential to highlight factors that were previously hidden in the time domain data. A B-scan for a 50° CA range centred around the TDC for Sensor 1 at 100% loading is shown in Figure 7.27.

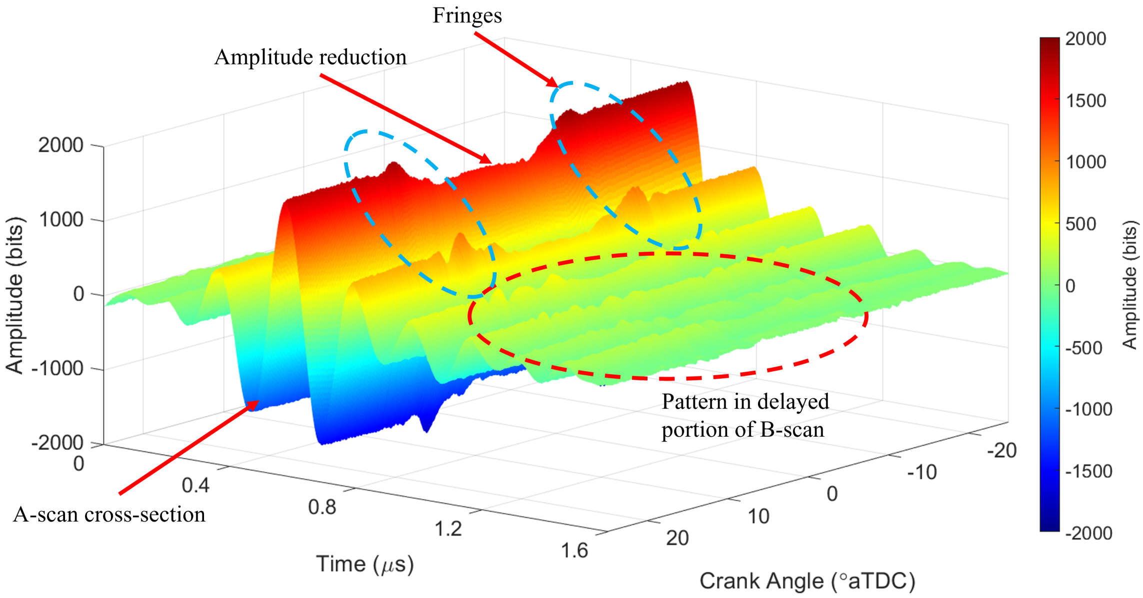

Figure 7.27: B-scan for Sensor 1 high speed testing.

The predominant visual pattern in Figure 7.27 is the decrease in amplitude of the large peaks seen between time 0.4-0.8 μs. With this section of the recorded data being the driving force of the frequency amplitude and Hilbert envelope analysis (see Section 7.5). Following on from the decayed amplitude of successive peaks (after time 0.8 μs) there is also a pattern between the A-scans which was previously unnoticed. This pattern is displayed clearer from a top down view of the B-scan, see Figure 7.28a for the whole time domain length. The trailing portion of the B-scan is shown in Figure 7.28b with a reduced amplitude range to highlight any minor patterns in the results.

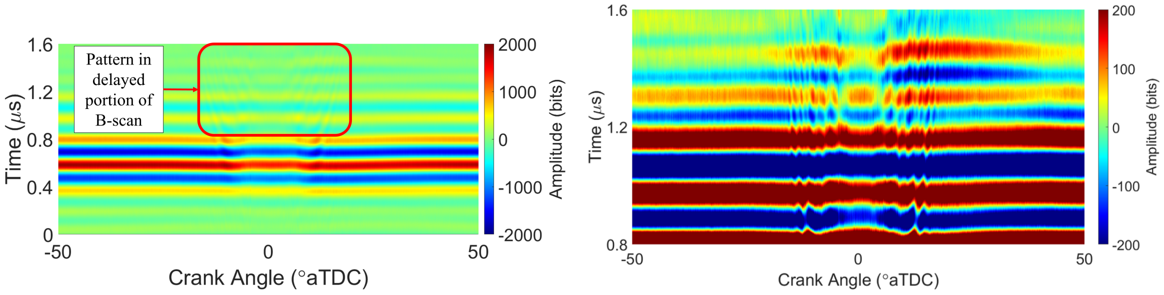

(a) Top view of the B-scan for Sensor 1.

(b) Trailing edge of 7.28a.

Figure 7.28: Top view of the B-scan for Sensor 1.

The trailing edge of the B-scan displayed in Figure 7.28b shows a complex pattern of waves that were previously hidden when analysis studied each time domain reflection individually. This B-scan shows a pattern that extends from -16° to 16° CA. However, geometric analysis on the piston indicated that the first piston ring was aligned with Sensor 1 from -8.5° to 8.5° CA. Therefore, a significant portion of this B-scan pattern is outside of the ring alignment zone.

To aid in the visualisation of this effect the mean reference A-scan has been removed from each reflection ($A(t) - A_{ref}(t)$) so that the B-scan shows the change in amplitude from the reference reflection at each data point, this is shown in Figure 7.29.

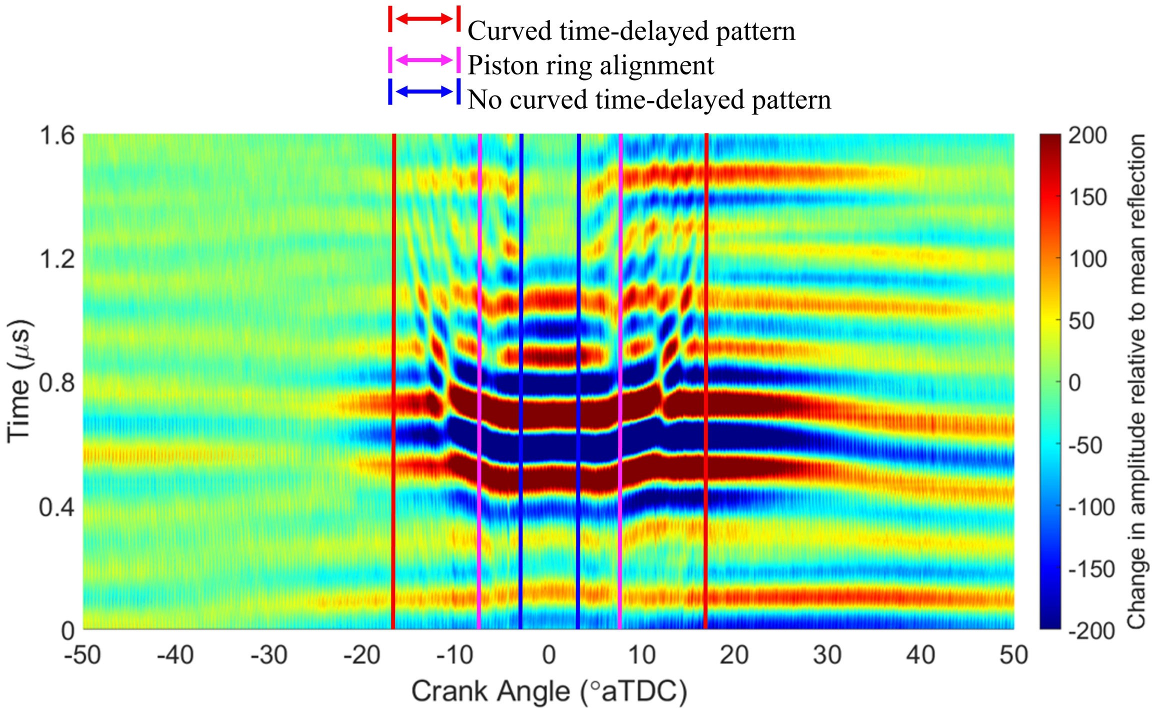

Figure 7.29: B-scan for Sensor 1 having removed the reference A-scan.

The time-domain reflection example in Figure 7.6 indicated the main body of the reflection used in the previous analysis could typically be defined between time 0.3 and 0.9 μs, represented in Figure 7.29 by the large change in amplitude from the reference at these points. In addition to the main body reflection, the true extent of the time-delayed pattern previously hidden in the B-scan is shown.

The prominent pattern in the time-delayed interference is the curved constructive and destructive interference pattern that extends from -16° to 16° CA (indicated via the vertical red lines in Figure 7.29). A significantly greater range than when the ring was aligned with this transducer (-8.5° to 8.5° CA shown via the vertical pink lines). The curved pattern is not present over the whole range from -16° to 16° CA, as from -3° to 3° CA (vertical blue lines) the time-delayed variation is no longer observed. This was when the piston ring was near full alignment (95% alignment) with the sensor, suggesting that outside of this range it may be unsuitable for oil film thickness calculation using the frequency index approach, as other factors are impacting the reflection which would have a significant effect in the frequency domain.

The test case shown is for Configuration 3, which typically has an extensive variation in the reflection coefficient post piston ring, see Figure 7.16a. The same effect is displayed in this B-scan as there is a change in amplitude from the reference reflection for 16° to 50° CA which was not seen before the ring (-50° to -16° CA).

In a preceding section (Section 7.2) on optimising the reflection window length, for this sensor, a length of 1-640 (up to 1.28 μs) was selected due to its minimal effect on the minimum reflection coefficient from a fully aligned piston ring. Observation of the trailing portion of the B-scan (Figure 7.29 post 1.28 μs) does show that a portion of the constructive/destructive interference is removed from window optimisation although a significant portion would remain in the studied reflection using this data processing method. One route to completely remove this factor is seen by applying the Hilbert envelope (Section 7.5).

The analysis in Chapter 6 is based upon the concept that a reflected wave from the piston ring is only detected when the ring was aligned with the transducer. This was indicated to not be the case in Section 7.1 and further shown in Figure 7.29 by the time-delayed change in the reflected wave whose time delay decreases as the piston ring approached the sensor. The pattern is symmetric about the TDC and observed pre and post ring alignment. To add to the theory shown in Section 7.1, this pattern is believed to be due to the time delay from the wavefront spreading and reaching a piston ring outside of the alignment zone that is reflected towards the transducer. When the piston ring is further from the sensor the ultrasonic wave is travelling a greater distance to reflect to the transducer, which causes a greater time delay before being recorded. The time delay reduces as the piston ring approached leading to the curved pattern as seen in Figure 7.29. The pattern is observed until there is no delay, when the ring is suitably aligned. See Figure 7.30 for a visualisation of this.

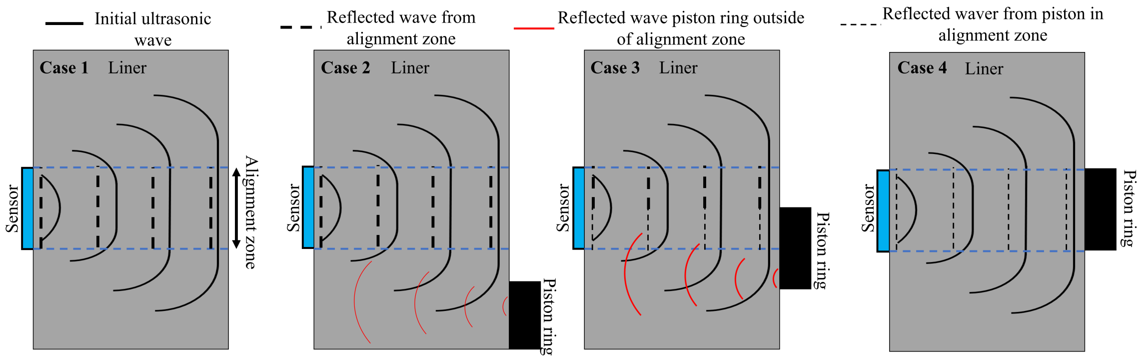

Figure 7.30: Wave propagation through the liner.

The four cases in Figure 7.30 are summarised as follows:

- Case 1: Piston ring not aligned and significantly far away - The only portion of the reflected wave reaching the sensor is from the alignment zone.
- Case 2: Piston ring moves up the liner - The ultrasonic wave outside of the alignment region starts to reflect from the piston ring with a portion being reflected towards the sensor. The reflections from outside the alignment zone are first detected at -16° CA and the time delay reduces as the piston ring approaches. As the piston ring is not aligned with the sensor the constructive/destructive interference from the ring reflections causes fluctuations in the reflection coefficient (fringe effects) centred about unity (R=1).
- Case 3: Partial alignment of the piston ring - The partial alignment causes a drop in reflection coefficient however, there are still reflections from outside the alignment zone being recorded. The combination of constructive/destructive interference and partial alignment causes a drop in reflection coefficient that fluctuates, equivalent to -8.5° to -3° CA and 3° to 8.5° CA.
- Case 4: Full ring alignment - A significant drop in the reflection coefficient as the piston ring is fully aligned. No reflections from outside of the alignment zone are directed to the sensor, therefore, no time delayed factors are seen, equivalent to -3° to 3° CA.

In Chapter 6, Figure 6.13, displayed the reflection coefficient for the three engine configurations at 100% loading. The figure highlighted multiple peaks pre/post rings which were initially theorised to be fringe effects due to a piston ring being marginally outside of the measurement range. The reflection coefficient of these peaks was greater than unity reflection which posed a worrying result, that a greater response was detected than initially propagated into the medium. These peaks were in the frequency index data at -16° to -9° and 9° to 16° CA providing a near-identical alignment with the time-delayed response seen here in the B-scans. Therefore, the B-scans add significant evidence of the measurement of the piston ring outside of the alignment region.

The four cases outlined in Figure 7.30 are overlayed onto the reflection coefficient for Sensor 1 at 100% loading for the three engine configurations in Figure 7.31.

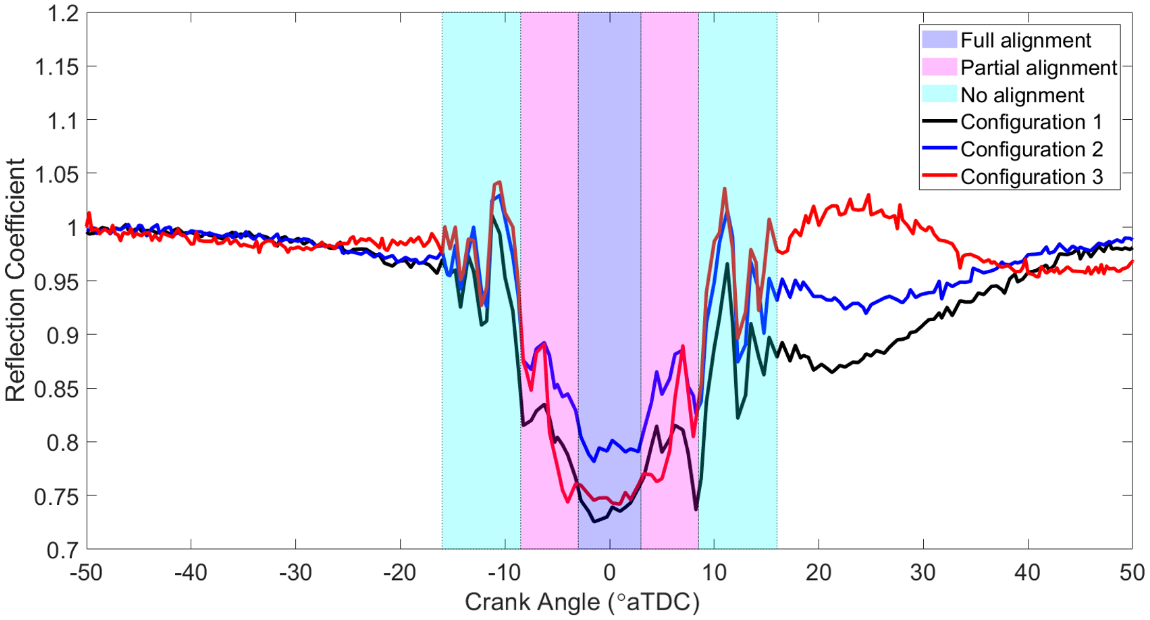

Figure 7.31: Alignment stages overlayed over the reflection coefficient from the frequency index method.

From Figure 7.31 the four cases identified align near perfectly with the trends seen in the reflection coefficient from the frequency index. The reflection coefficient is, therefore, only unhindered from the constructive/destructive interface from -3° to 3° CA. At -3° CA this corresponds to 95% alignment between the piston ring and sensor before the trailing pattern is no longer measurable.

The equivalent B-scans having removed the mean reference reflection for 50% and 25% loading are shown in Figures 7.32a-7.32b respectively. Note these lower loading cases are for Configuration 2 as no high speed 100% test cases were recorded for Configuration 3.

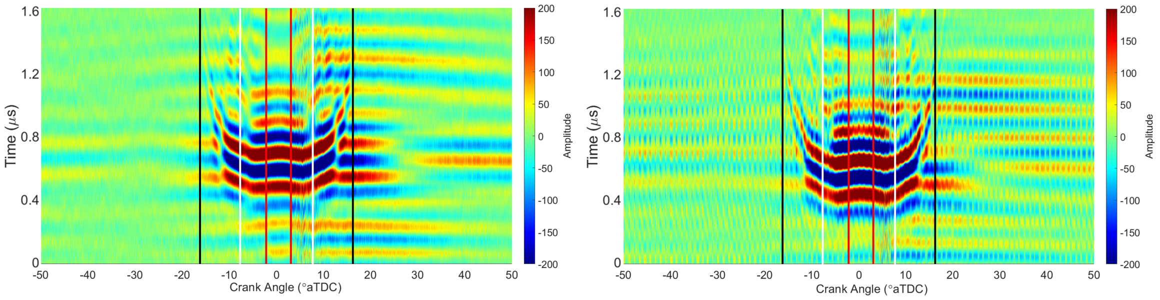

(a) 50% loading.

(b) 25% loading.

Figure 7.32: B-scan of Sensor 1 at 50% and 25% loading.

Comparison of these Figures, relative to the 100% loading case in Figure 7.29 shows that the time-varying response is present at all loading levels. Although by 25% loading there is a smaller time delay as at -16° CA there is no clear constructive/destructive interference post 1.2 μs. Whilst for 100% it is clear for the whole time range recorded. This is theorised to be the case as at lower engine loading the liner temperature is lower, leading to a greater speed of sound of the ultrasonic wave reducing the time delay caused by the greater path length.

A k-Wave model, similar to that outlined in Section 7.1 has been produced to simulate a piston ring fully aligning with a sensor to produce B-scans similar to the experimental B-scans previously shown. The simulated B-scan is plotted in Figure 7.33a and the B-scan with the reference removed in Figure 7.33b. The same system parameters as outlined in Table 7.1 and Figure 7.4 have been applied here.

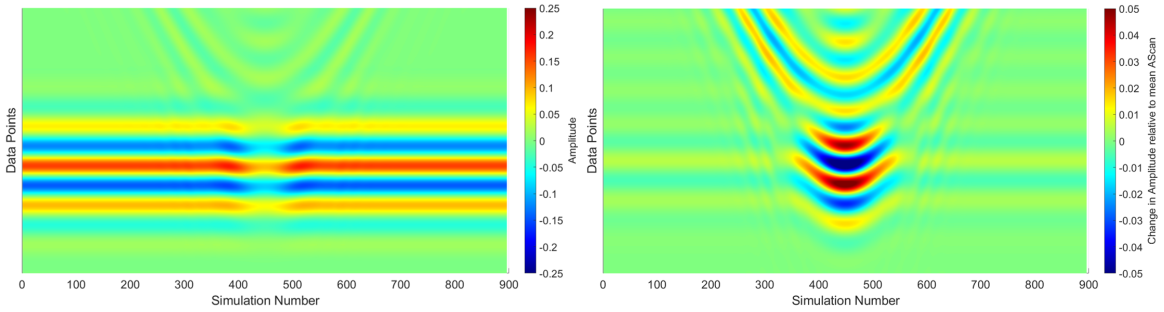

(a) Simulation B-scan

(b) Simulation B-scan with removed reference.

Figure 7.33: B-scans from the k-Wave simulation.

The simulation B-scans further indicate that these delayed reflections are not from an engine parameter such as cylinder pressure as the simulation purely focuses on ultrasonic aspects. The model has resulted in the same delayed curve of reflections as the experimental B-scans. Whilst the extended change in the B-scan post ring (>16° CA) is not present in the simulation which indicates that this may be due to a parameter of the engine. The simulation assumes the liner is fully flooded with oil, representative of an excess residual film, therefore, residual oil film levels are not capable of being simulated with the k-Wave model.

The B-scans indicate that the data analysis method considered needs to be applied to specific CA ranges so that the reflection is purely from when the piston ring was aligned with the sensor. Prior analysis used the range -8.5° to 8.5° CA for Sensor 1 however, B-scan analysis has indicated that the range -3° to 3° CA is appropriate for a more representative view of the oil film. This will also have had an impact on the other longitudinal transducers, whose B-scans are extensively more complex than that of Sensor 1 as the other sensors cover multiple piston rings. An example of the B-scan from Sensor 2 for 100% loading is shown in Figure 7.34.

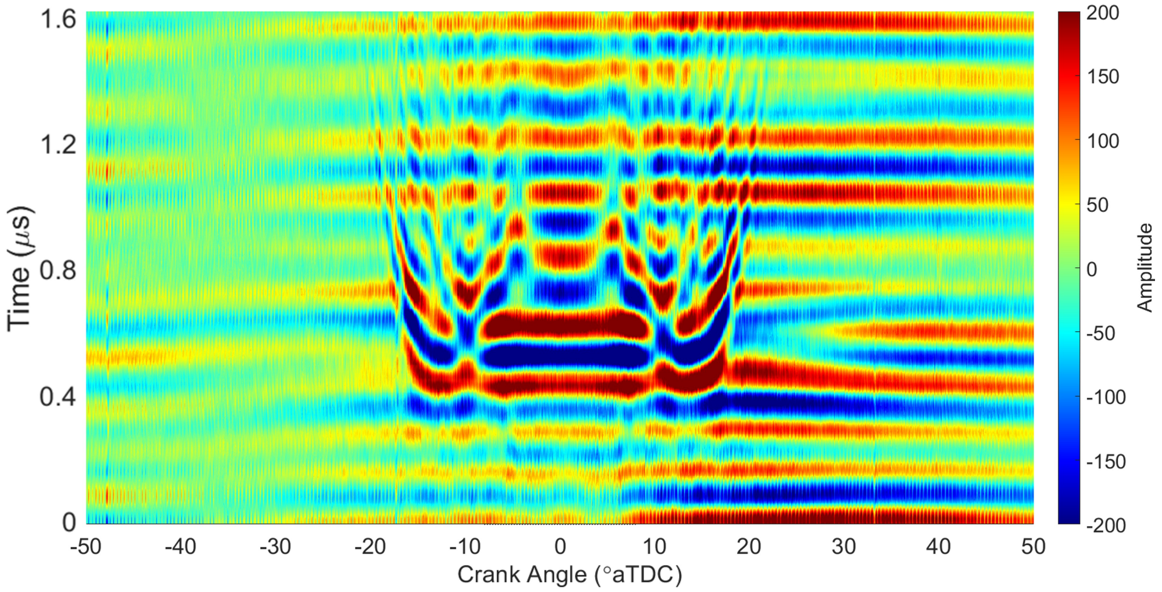

Figure 7.34: B-scan for Sensor 2 having removed the reference reflection.

The B-scan for Sensor 2 has a greater level of complexity than Sensor 1, as it experienced two piston rings, therefore, 3 alignment zones in each revolution of the engine. Some likewise factors can be identified for Sensor 2, such as the curved pattern pre/post ring pack (-22° to -16° and 16° to 22° CA) which lines up with the fringes seen in the frequency index reflection coefficient for Sensor 2 in Figure 6.12. Although this plot shows no identifiable CA range clearly corresponds to each piston ring. As when the first ring was fully aligned with Sensor 2, it will have already being subject to a fringe effect from Ring 2. The ultrasonic instrumentation on the RTX-6 marine engine improved upon previous ultrasonic piston ring research to use transducers of smaller width than the piston rings. However, the B-scans indicate that a smaller ratio between the two is required to provide truly independent recordings from each piston ring. This B-scan also shows a limitation of the frequency indexing approach as for Sensor 2, Ring 1 was detected whilst Ring 2 was aligned and the factors are not discernible in the time or frequency domain.

7.5 Hilbert envelope

The data presented up to this section used a frequency index of the signal in the frequency domain at the central frequency of the transducer. This has been used extensively in ultrasonic tribological research in combination with the Spring Model for analysis on thin oil films (< 20 μm). The thin film allows the reflection from either side of the oil film to be treated as a single reflector. By studying the central frequency in the frequency domain, plots of the reflection coefficient can be defined as shown extensively throughout this work. The frequency domain view produces a measure of the energy distribution at different frequencies, therefore, ensuring that only the desired reflection is studied is of key importance but potentially difficult to practically and scientifically achieve as shown in the section on Reflection Windowing, Section 7.2.

A typical ultrasonic reflection is plotted in Figure 7.35, upon visual inspection of the reflection it is reasonable to conclude that between 0.3 and 0.9 μs the significant amplitude is clearly part of a reflected wave. It is also reasonable to decide that by 1.4 μs the reflection has passed the sensor. However, at what point is the reflection deemed to have started and ended remains troublesome to deduce. One could argue to study the complete recorded timespan (providing no other significant reflections are recorded) to ensure no valuable data is ignored, like previous ultrasonic analysis. Although, reflections from other surfaces may be included in the studied timespan (such as seen in the B-scans), a methodology to study purely the reflection of interest was shown in Section 7.2. Alternatively, this section studies the peak of the reflection in the time domain using the Hilbert envelope, this methodology avoids issues of defining where a reflection starts and ends and focuses on the instant that had the greatest amount of reflected energy. The Hilbert envelope of a typical reflection is shown in Figure 7.35 in red.

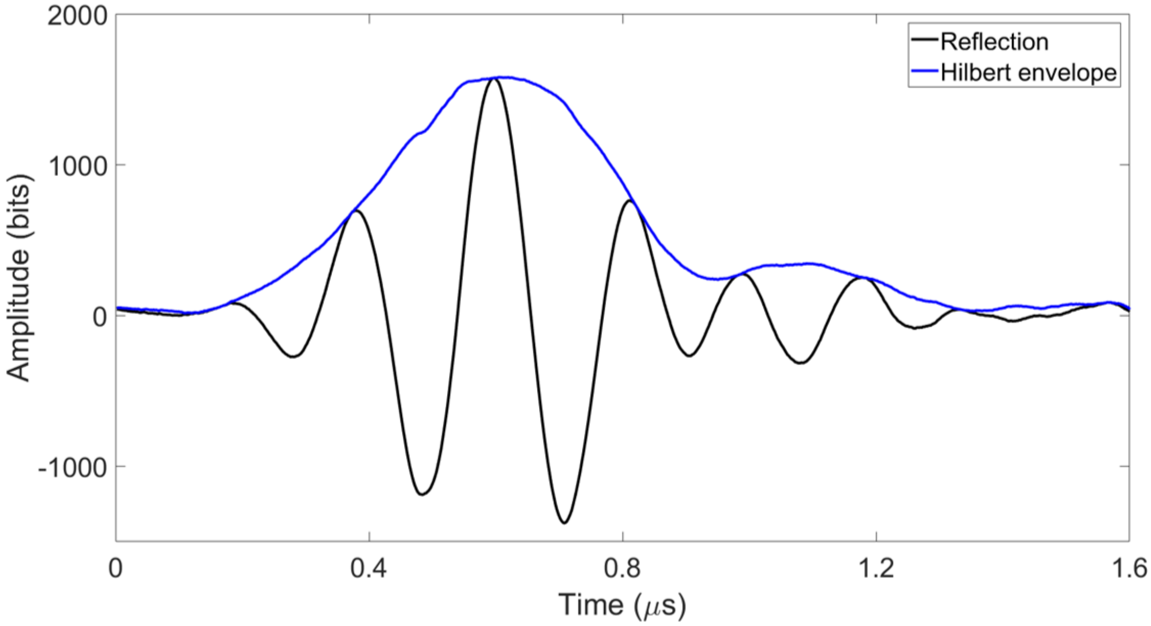

Figure 7.35: Typical ultrasonic reflection with its respective Hilbert envelope.

7.5.1 Frequency index compared to Hilbert envelope

The frequency index and Hilbert envelope provides two different methods to define the reflection coefficient. The reflection coefficient using both methods is plotted in Figures 7.36a - 7.39a for all longitudinal sensors for engine Configuration 1 at steady-state operation, 100% loading. The cylinder pressure is overlayed on these figures. Whilst in Figures 7.36b - 7.39b a comparison of the three engine configurations using the Hilbert envelope peak at 100% loading is shown.

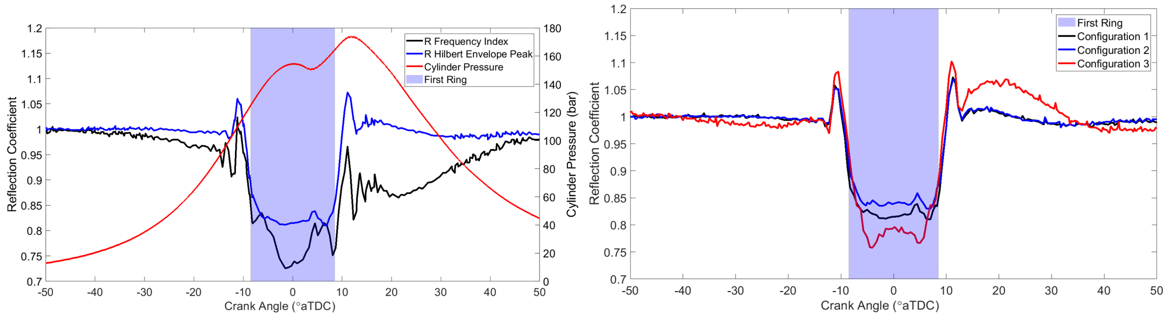

(a) Frequency index vs Hilbert envelope.

(b) Hilbert envelope configuration comparison.

Figure 7.36: Reflection coefficient for Sensor 1 from the frequency index and Hilbert envelope methods.

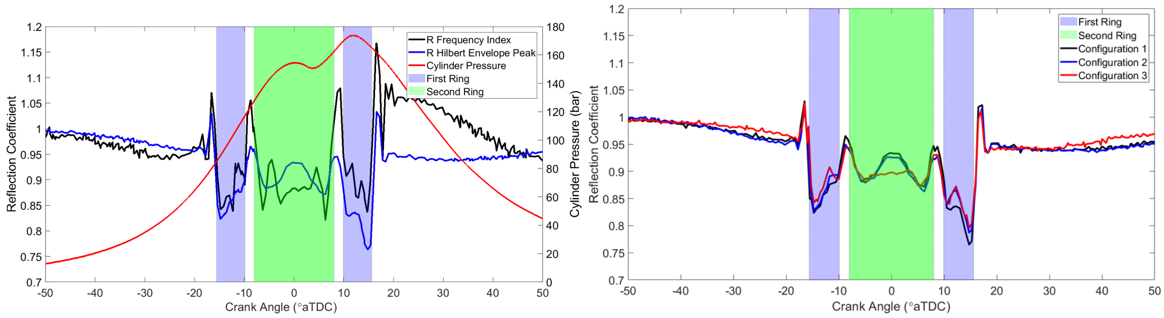

(a) Frequency index vs Hilbert envelope. (b) Hilbert envelope configuration comparison.

Figure 7.37: Reflection coefficient for Sensor 2 from the frequency index and Hilbert envelope methods.

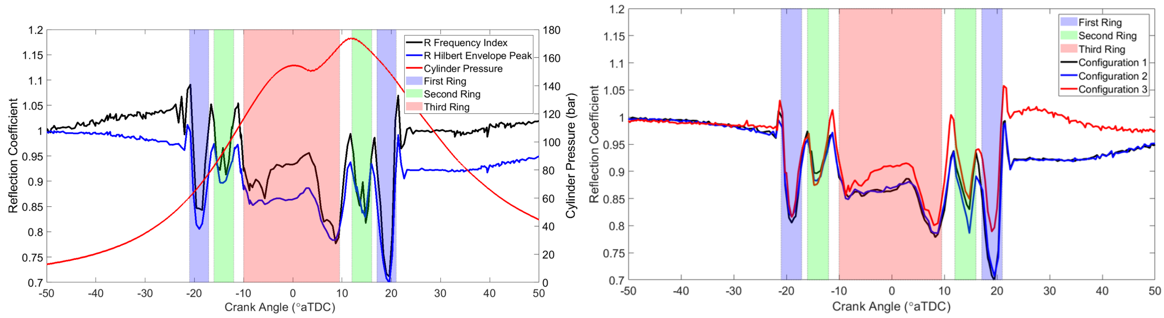

(a) Frequency index vs Hilbert envelope. (b) Hilbert envelope configuration comparison.

Figure 7.38: Reflection coefficient for Sensor 3 from the frequency index and Hilbert envelope methods.

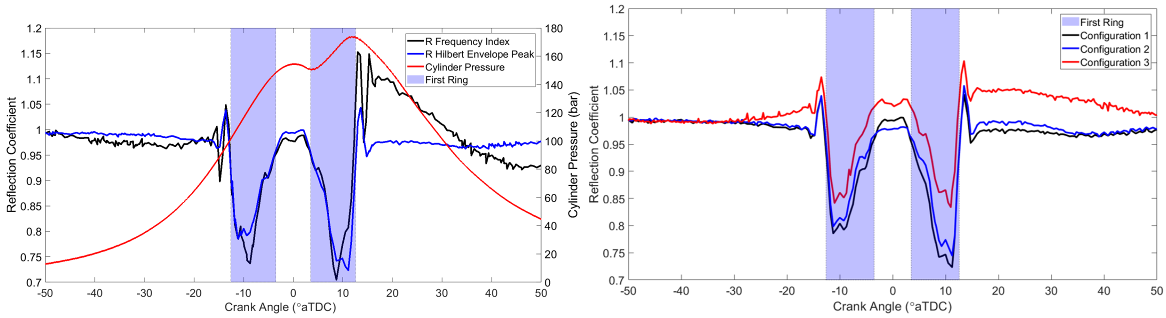

(a) Frequency index vs Hilbert envelope. (b) Hilbert envelope configuration comparison.

Figure 7.39: Reflection coefficient for Sensor 4 from the frequency index and Hilbert envelope methods.

Chapter 6 considered longitudinal Sensors 1-4, and displayed a series of trends in the frequency index data that were shown for all engine configurations. Whilst the Hilbert envelope peak method is not exposed to a number of these, indicating that those trends are merely present due to the data processing method as opposed to a factor from the marine engine itself.

From Figures 7.36a - 7.39a the Hilbert envelope reduces the presence of a prolonged change in reflection coefficient before/after the ring pack for each transducer. Leading to a less unusual result, that the reflection coefficient remains at unity when there is no piston ring over the transducer.

The fringe effects immediately before and after the ring pack that is displayed clearest in Figure 7.36a is reduced by the Hilbert envelope to a single peak, which is also seen to some extent in the other sensors (Figures 7.37a-7.39a). This fringe effect is also no longer seen between piston rings passing for Sensors 2 and 3 in Figure 7.37a and Figure 7.38a respectively.

The 'W' shape that has been seen in numerous ultrasound research of varying applications ([64, 89, 90]) is also minimised and often completely removed from the application of the Hilbert envelope.

The same trends shown from applying the Hilbert envelope to Configuration 1 are displayed for Configurations 2 and 3 in Figures 7.36b - 7.39b. The key variation between the two methods is the timespan they are considering as the frequency index provides a summary of the summation of the whole reflection plus to some extent response from other microvariations due to difficulties identifying the start and end of the reflection. Whilst the Hilbert envelope purely studies the maximum amplitude portion of the reflection. This, therefore, indicates that the factors that lead to; prolonged reflection coefficient variation, fringe effects and the 'W' double-dip are not from the peak of the reflection but factors that arise from the summation of frequencies over a greater time span, as was also seen in the reflection windowing (Section 7.2) and B-scans (Section 7.4). Interestingly, this also affects the dips for Sensor 4 as the frequency index showed a greater dip at the edge closer to the TDC whilst the Hilbert envelope displays a flat dip now, as seen by the other sensors.

The extent of the impact different parts of the ultrasonic reflection has on the reflection coefficient trends can be implied from studying the Hilbert envelope at a series of different points. This has been applied to Sensor 1 for Configuration 1 100% loading at four differing points in the Hilbert envelope.

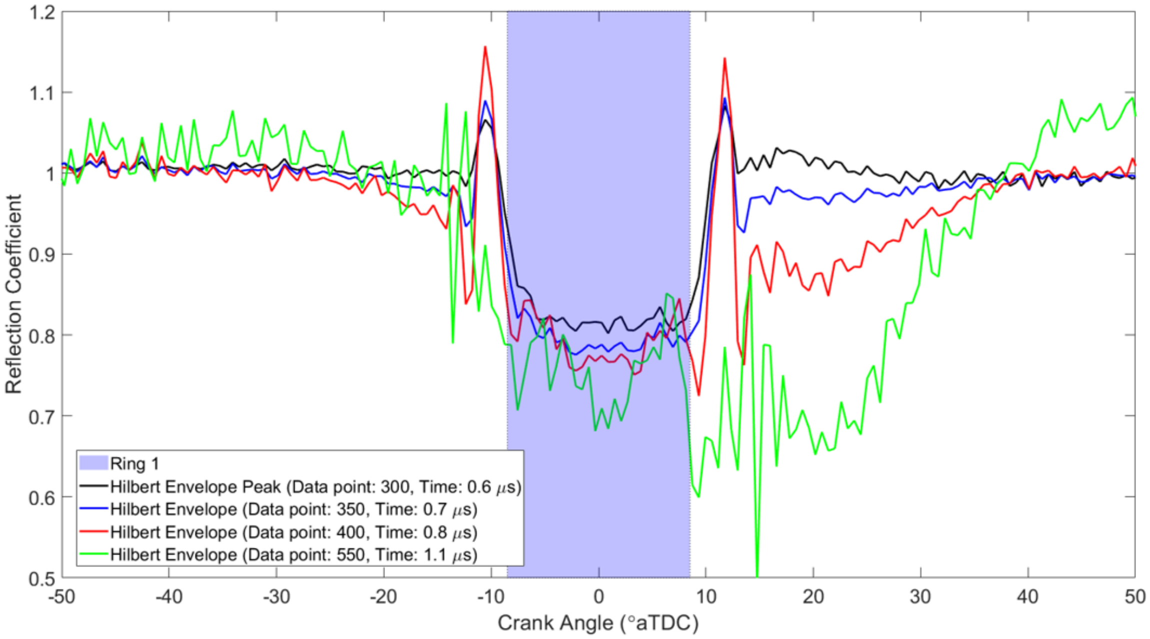

Figure 7.40: The reflection coefficient from the Hilbert envelope using a series of timesteps for Sensor 1 Configuration 1 at 100% loading. The Data points are defined in Figure 7.35.

There are major differences in the reflection coefficient from indexing at differing points of the Hilbert envelope as shown in Figure 7.40. The figure indicates that the trends that were present in the frequency index method, yet not shown via the Hilbert envelope peak are present in the later indexes of the Hilbert envelope. The impact of those trends increase at later points in the Hilbert envelope (shown at times 0.8 and 1.1 μs), as the frequency index studied the complete reflection this, therefore, indicates that the cause of these variations are not from the peak of the reflection, rather the initial or trailing section of the reflection, as was also seen in the B-scans.

The equivalent comparisons between the two processing techniques can be produced for the longitudinal sensor (Sensor 5) above the piston rings in Figure 7.41.

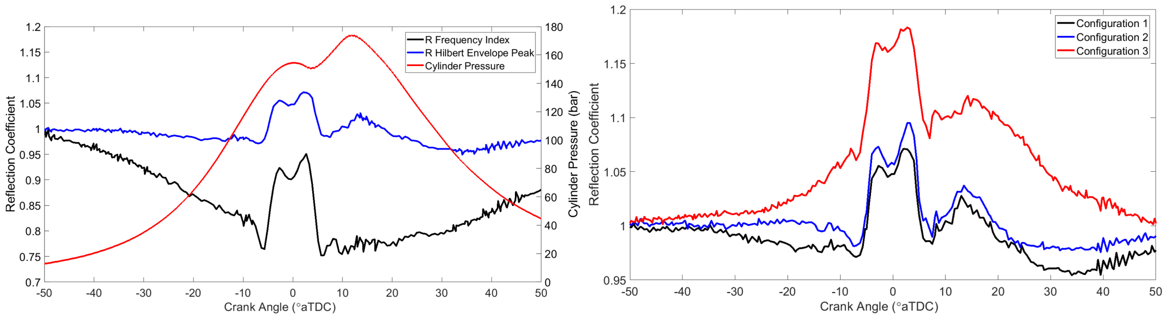

(a) Frequency index vs Hilbert envelope. (b) Hilbert envelope configuration comparison.

Figure 7.41: Reflection coefficient for Sensor 5 from the frequency index and Hilbert envelope methods.

Arguably the most complex reflection coefficient variation is for Sensor 5 and the comparison between the two data processing techniques shows drastically different reflection coefficients in Figure 7.41a. The Hilbert envelope peak method completely removes the major decrease in reflection coefficient pre/post-TDC the cause of which was unknown and seen in Figure 7.2. There is now the emergence of a peak in reflection coefficient at the peak combustion pressure (13° CA). The adjoining fringe effects from -8° to 8° CA are still present in the Hilbert envelope data as this is believed to be caused by a combination of the approaching piston ring in conjunction with heightened cylinder pressure. The Hilbert envelope approach leads to much greater alignment with the k-Wave model seen in Figure 7.5.

The Hilbert envelope peak analysis leads to the same trends in the reflection coefficient for all engine configurations (Figure 7.41b). Configuration 3 experienced a vertical shift in the order of 0.15 reflection coefficient, this is thought to be due to deterioration of the transducer as operation of Configuration 1 and 3 are largely the same. A similar trend was also seen in Figures 7.36b - 7.41b for Configuration 3, this is thought to have arisen due to potential deterioration of the sensors after an exhaustive testing regime and is like that seen in the frequency index analysis in the previous chapter.

The figures in this section indicate that the Hilbert envelope is capable of providing a comparison between the lubricant injection systems. The comparison is achieved whilst removing several trends in the results that arose from the delayed portion of the reflection and highlights other findings that were previously hidden in the frequency index analysis.

The frequency index and Hilbert envelope methods can be compared to the smallest window size considered (central cycle) in Section 7.2, see Figure 7.42.

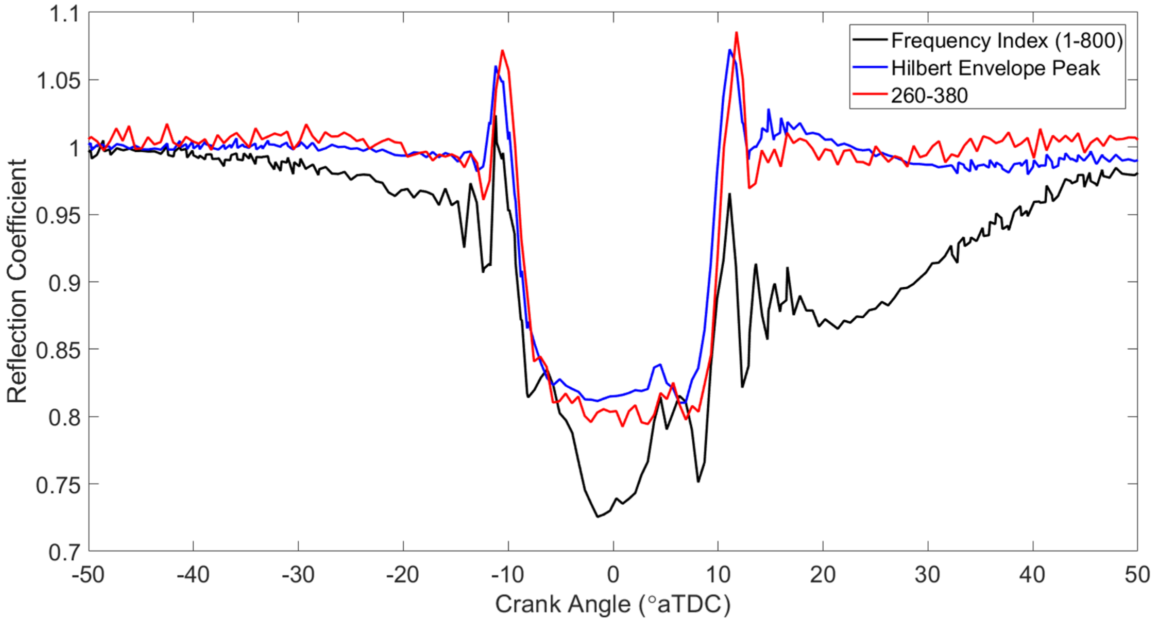

Figure 7.42: Frequency index vs Hilbert envelope vs shortest window size (260-380 data points).

Inspection of the shortest A-scan window considered (260-380) shows that as the window was shortened the frequency index reflection coefficient tends towards that of the Hilbert envelope. Further agreeing with the previous findings that the cause of several trends in the reflection coefficient has arisen from the later portions of the reflection which are potentially not from the piston ring or the piston ring when it is not aligned with the transducer. The independence study to optimise the reflection window size provided one methodology to remove reflected energy from other surfaces being considered although a more consistent result for the various sensors may be achieved in a timely manner from the Hilbert envelope.

7.5.1.1 Oil film thickness comparison

Application of the Spring Model to the reflection coefficient from both data processing techniques provides a comparison between the OFT from the two methods. This has been done for the reflection coefficient of Sensors 1-4 in Figures 7.36-7.39 to show the oil film thickness in Figures 7.43-7.46.

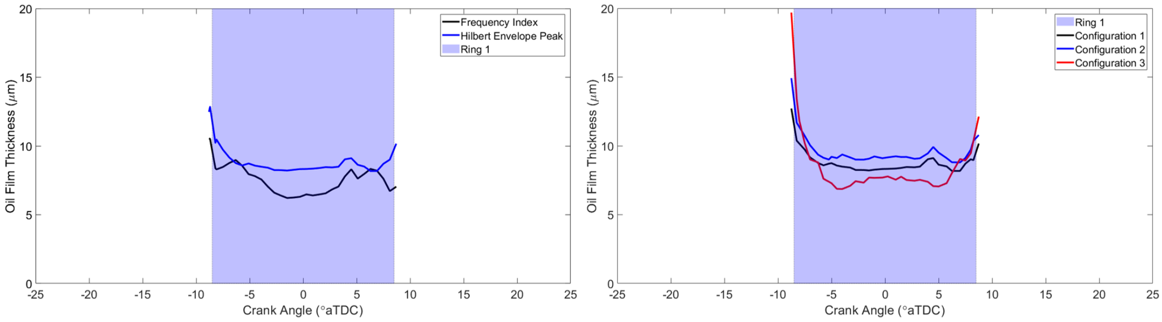

(a) OFT Frequency index vs Hilbert envelope. (b) Hilbert envelope peak method.

Figure 7.43: Oil film thickness over Sensor 1 for all Configurations using both data processing methods.

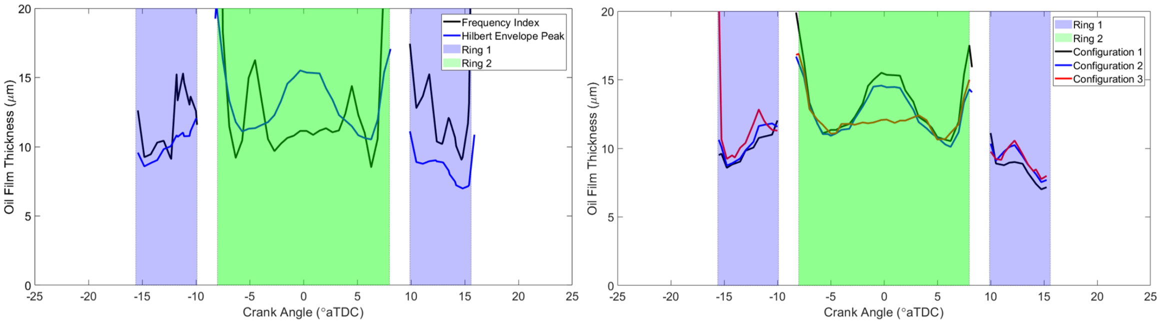

(a) OFT Frequency index vs Hilbert envelope. (b) Hilbert envelope peak method.

Figure 7.44: Oil film thickness over Sensor 2 for all Configurations using both data processing methods.

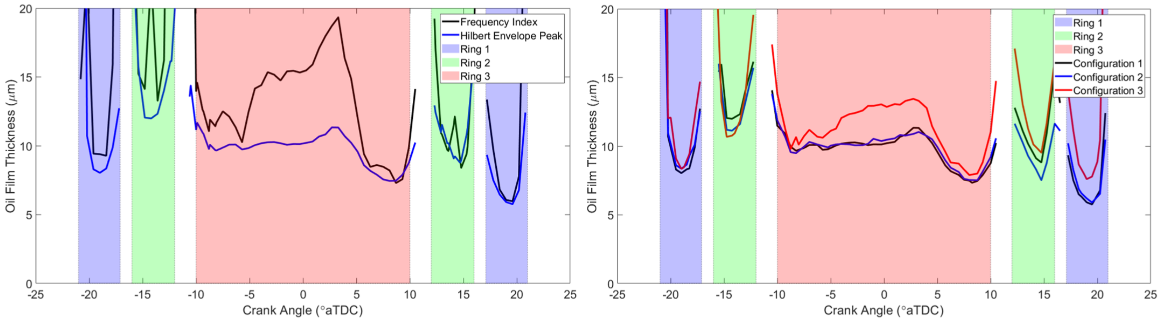

(a) OFT Frequency index vs Hilbert envelope. (b) Hilbert envelope peak method.

Figure 7.45: Oil film thickness over Sensor 3 for all Configurations using both data processing methods.

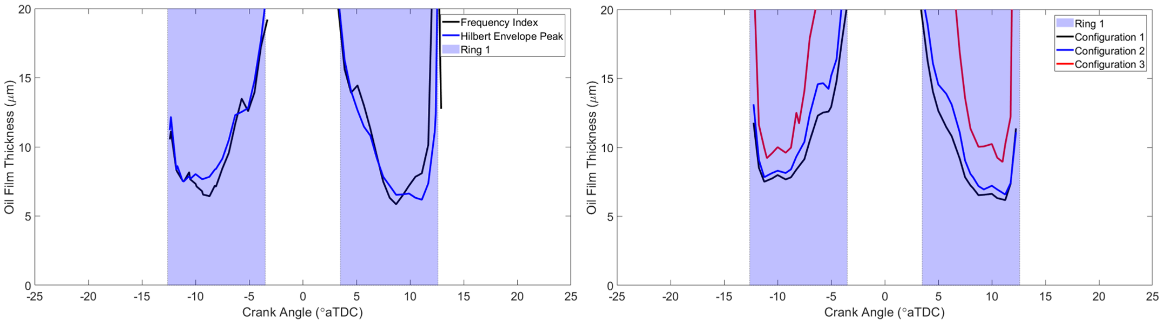

(a) OFT Frequency index vs Hilbert envelope.

(b) Hilbert envelope peak method.

Figure 7.46: Oil film thickness over Sensor 4 for all Configurations using both data processing methods.

Similar to the reflection coefficient figures, the Hilbert envelope OFT is not prone to several factors the frequency index is subject to. There are no double dips in the oil film thickness present for any sensor. Furthermore, the Hilbert envelope produced less anomalous results; Configuration 2 in Figure 7.44 and Configuration 3 in Figure 7.45/Figure 7.46 no longer produce wildly differing trends to the other configurations.

The two processing techniques lead to similar OFT measurements with the clearest difference seen for Sensor 1. In which the Hilbert envelope produced a film 2 μm thicker, equivalent to a 35% increase. The removal of several trends from the Hilbert envelope also leads to a smoother, more consistent variation in the OFT over the alignment regions, indicative of less fluctuation in the piston ring lateral position/greater consistency in engine operation.

It is more difficult to identify which engine configuration led to a greater film thickness from the Hilbert envelope, with Sensor 1 still indicating that Configuration 2 has a greater film thickness although this is not always the case for the other Sensors. In the majority of cases, the thinnest film is caused by either Configuration 1 or Configuration 3 which was anticipated due to the increased rate of lubricant atomisation for these configurations. The key characteristic in film thickness is its minimum value, this is discussed in Section 7.6 to provide a closing comparison between processing techniques considered.

7.5.2 Load variation

The reflection coefficient and oil film thickness can be defined at each steady-state loading level enabling a loading comparison. A typical reflection from the first piston ring at the TDC over Sensor 1 and respective Hilbert envelope from each loading level is shown in Figure 7.47.

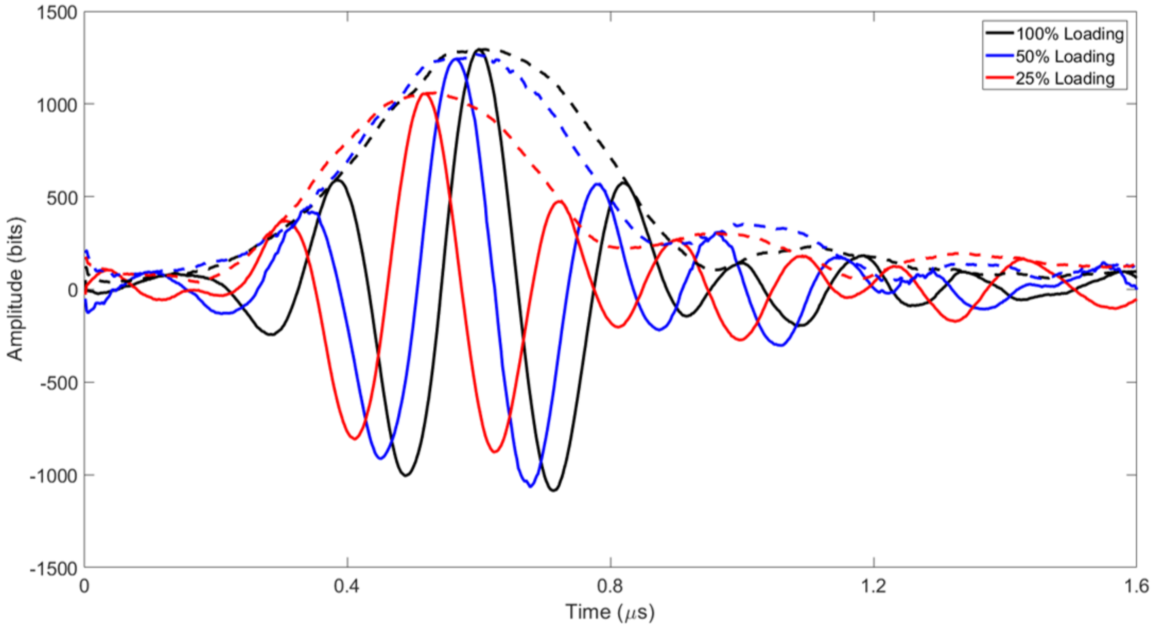

Figure 7.47: Typical loaded ultrasonic reflection using Sensor 1 Engine Configuration 2.

The time-domain reflections in Figure 7.47 show that as the engine loading was decreased this resulted in a timeshift of the reflection. A reduction in loading reduced the time taken for the wave to be reflected to the sensor and the signal had a reduction in amplitude with loading. The reflection shifts to the left as the engine load was reduced, this is due to reduction in oil temperature leading to an increase in the speed of sound and, therefore, the reflection travels back to the sensor in a shorter time.

The reflection coefficient at these loading levels for the 5 sensors is shown using a frequency index at 1 MHz in subplots (a) and the Hilbert envelope peak in subplots (b) in Figures 7.48 - 7.52 respectively.

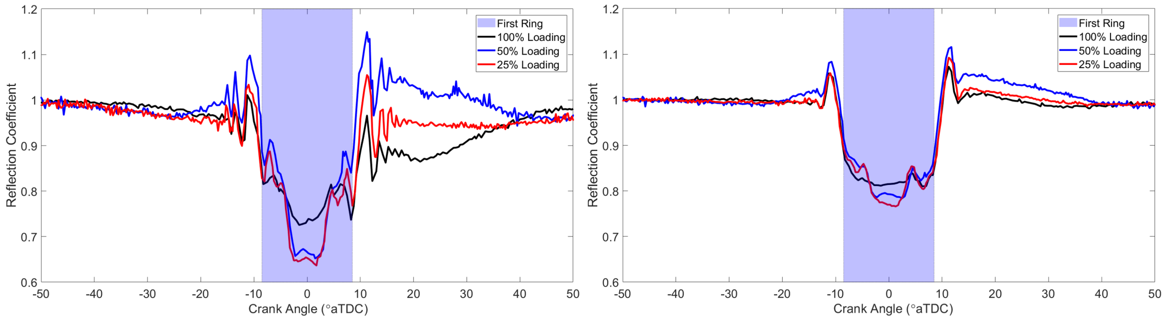

(a) Frequency index.

(b) Hilbert envelope.

Figure 7.48: Reflection coefficient loading comparison for Sensor 1 using both processing methods.

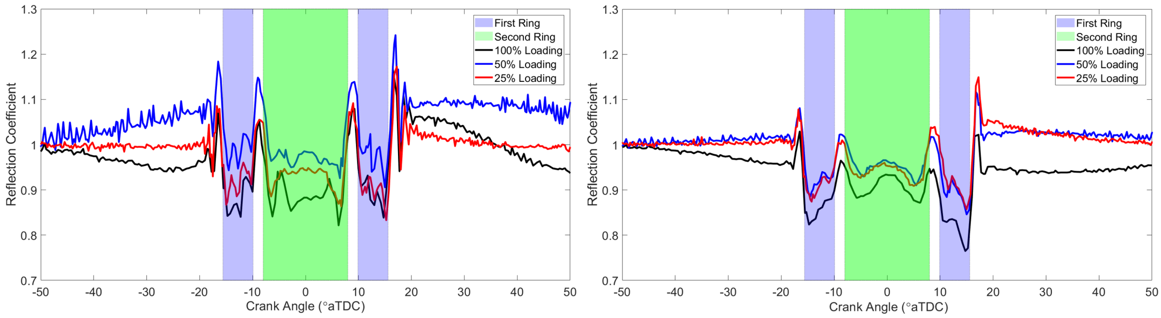

(a) Frequency index.

(b) Hilbert envelope.

Figure 7.49: Reflection coefficient loading comparison for Sensor 2 using both processing methods.

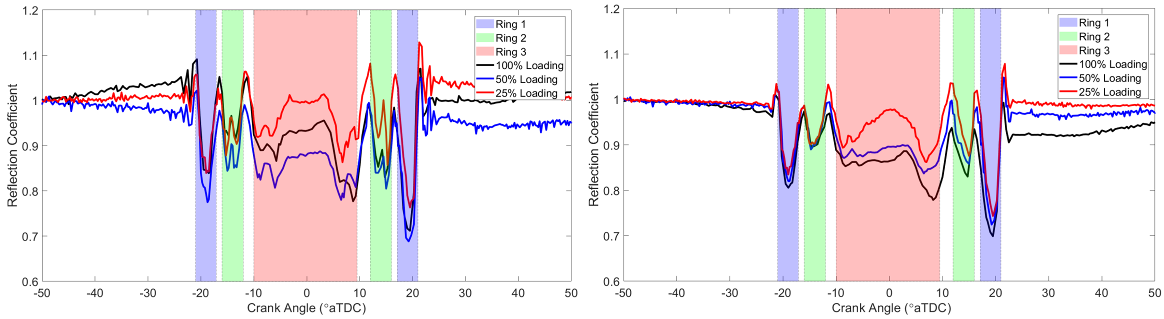

(a) Frequency index.

(b) Hilbert envelope.

Figure 7.50: Reflection coefficient loading comparison for Sensor 3 using both processing methods.

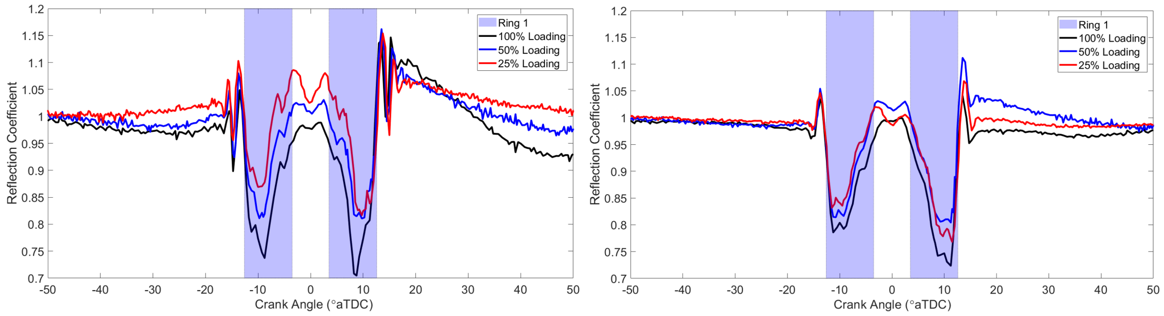

(a) Frequency index.

(b) Hilbert envelope.

Figure 7.51: Reflection coefficient loading comparison for Sensor 4 using both processing methods.

Initial observation upon Figures 7.48a - 7.51a shows an almost a random order of magnitude of dip for the three loading levels. In Sensor 1, Figure 7.48a, the order from smallest to largest dip is: 100%, 50%, 25%. Whereas in Sensor 2, Figure 7.49a, the order is: 50%, 25%, 100%. Whereas for the Hilbert envelope plots in Figures 7.48b - 7.51b, all transducers bar Sensor 1 provide the same magnitude of dip order (25%, 50%, 100%). It is expected that Sensor 1 experienced a different order due to this sensor being exposed to significantly harsher conditions relative to the other sensors. The removal of the 'randomness' from the Hilbert envelope, therefore, enables this method to provide a greater indication of loading variation from this stage of data processing.

The micro-variations detailed in Chapter 6 using the frequency index at 100% loading are shown to occur at all loading levels with typically the same trends occurring. Except for the post ring section of Sensor 1, Figure 7.48a where each loading level has a differing trend. Conversely, the Hilbert envelope removed the bulk of these factors at all loading levels leading to greater consistency. The only variation to remain is the prolonged return to unity reflection coefficient, which is believed to be from a residual oil film that is present for both methods and as the oil injection rate is dependent upon engine load, the residual film levels will vary with engine load.

The equivalent comparison between loading conditions for Sensor 5, which was above all piston rings at the TDC using the two data processing methods is shown in Figure 7.52.

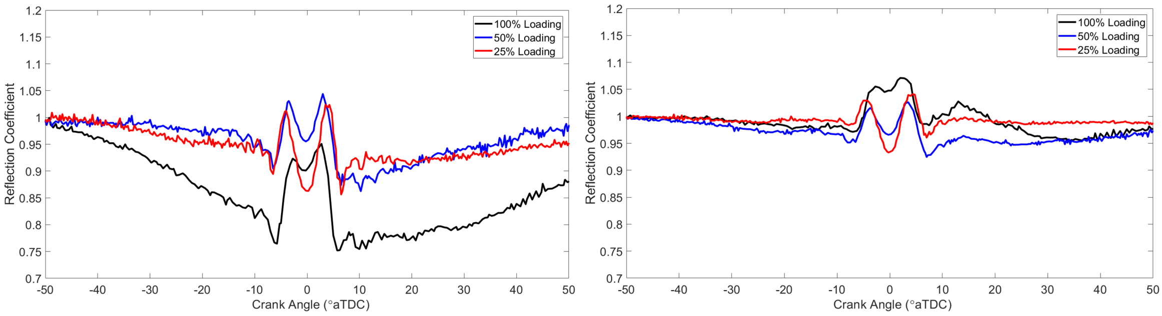

(a) Frequency index.

(b) Hilbert envelope.

Figure 7.52: Reflection coefficient loading comparison for Sensor 5 using both processing methods.

Similar to the other sensors, the Hilbert envelope simplifies the reflection coefficient at all loading levels and produces a more consistent trend between the loading levels. The large reduction in reflection coefficient is completely removed, showing the combustion pressure peak at 13° CA that is also removed at lower engine loading levels. Interestingly, in Figure 7.52b a reduction in engine loading leads to a greater drop in reflection coefficient at the TDC. The cause of which is unknown and requires further study.

7.5.2.1 Oil film thickness loading comparison

The Spring Model has been applied to the reflection coefficient from both data processing techniques from the previous section for varying engine loading levels. The oil film thickness is shown for Sensors 1-4 in Figures 7.53-7.56 respectively. The frequency index oil film thickness is plotted in subplots (a) with the oil film thickness from the Hilbert envelope shown in subplots (b).

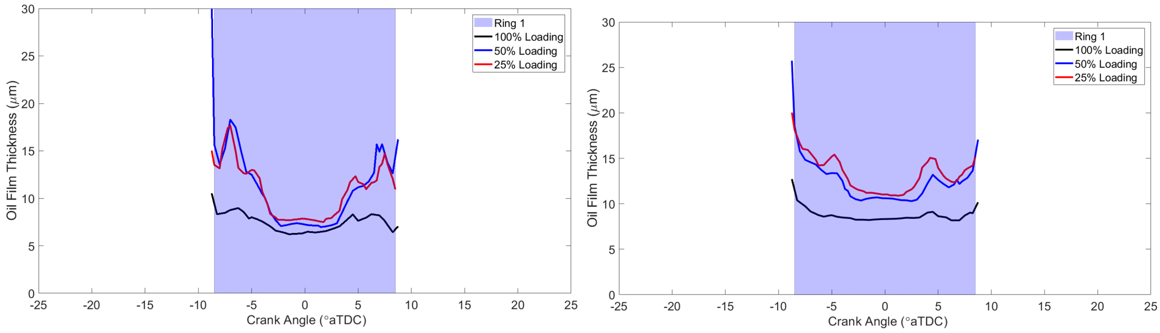

(a) Frequency index.

(b) Hilbert envelope.

Figure 7.53: Oil film thickness loading comparison for Sensor 1 for both data processing methods.

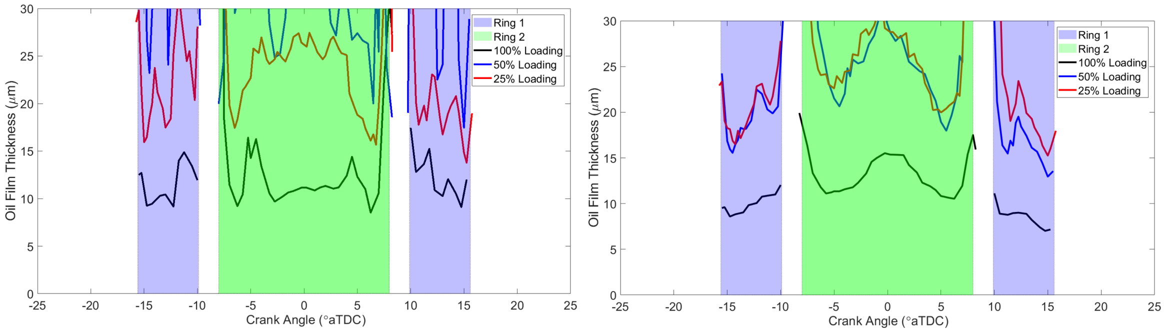

(a) Frequency index.

(b) Hilbert envelope.

Figure 7.54: Oil film thickness loading comparison for Sensor 2 for both data processing methods.

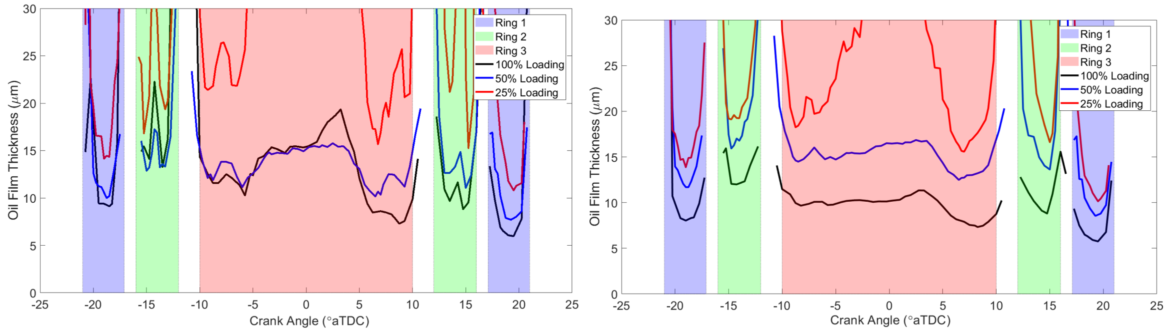

(a) Frequency index.

(b) Hilbert envelope.

Figure 7.55: Oil film thickness loading comparison for Sensor 3 for both data processing methods.

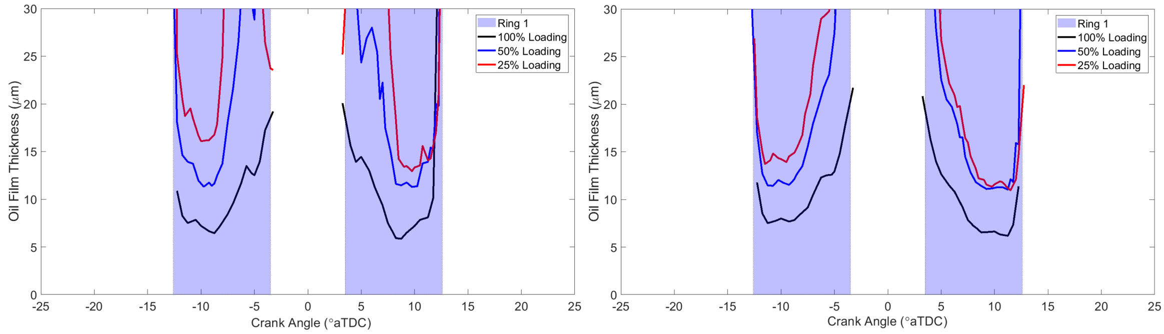

(a) Frequency index.

(b) Hilbert envelope.

Figure 7.56: Oil film thickness loading comparison for Sensor 4 for both data processing methods.

The application of the Spring Model combined with the temperature and pressure measurements at each engine loading remove the almost random order of the reflection coefficient dip magnitude for the frequency index approach in subplots (a). Leading to each plot and subplot, excluding Figure 7.54a, showing 100% loading to have the thinnest oil films and the film thickness increases with reduced engine loading. Whilst the Hilbert envelope oil film thickness results display the same order as their respective reflection coefficient plots and a more consistent result over the CA range. This provides an indication that the Hilbert envelope provides a better insight of the OFT from the reflection coefficient.

The overall trend in the OFT results displays the same trends between loading levels irrelevant to the data analysis method applied. The Hilbert envelope method calculated thicker films, although both techniques provide OFT values in the typical thickness ranges expected for a piston ring contact. However, the application of the Hilbert envelope has the potential to reveal trends, especially at lower engine loadings, that were previously hidden in when using the frequency index method.

7.6 Minimum oil film thickness

The key defining factor of piston ring oil film thickness measurements is the minimum oil film thickness measurement. This chapter has provided additional routes to define the reflection coefficient whilst this closing section provides a final summary between the analyses applied to indicate their effect on the overall steady-state MOFT.

The MOFT has been calculated using the optimised frequency domain index and the Hilbert envelope peak. Although this chapter has shown that this is not a comprehensive comparison. The B-scans have shown that only Sensor 1 appears to have a small CA range unaffected by the time-delayed minor variations that are still present in the optimised A-scan windows. The optimised spectrograms show a near frequency independence for the higher frequency region of the transducer bandwidth however frequency selection remains a factor that affects the oil film thickness value. There are also several additional techniques to define the reflection coefficient such as; phase change [91, 92] or ’exact model - complex’ [93] both have been considered but deemed inappropriate to the thin nature of piston ring film thickness.

The MOFT for each data capture is plotted in Figure 7.57 for Configuration 2. Note the optimised window frequency index MOFT is the same as that from the MOFT data presented in Chapter 6 as the optimised window was defined as having not affected the minimum reflection coefficient, thus no effect on the MOFT. Configuration 2 has been used here as a greater number of data captures were taken over the steady-state loading periods. The mean MOFT across steady-state at all loading levels for each processing method is presented in Table 7.2 in addition to the COV.

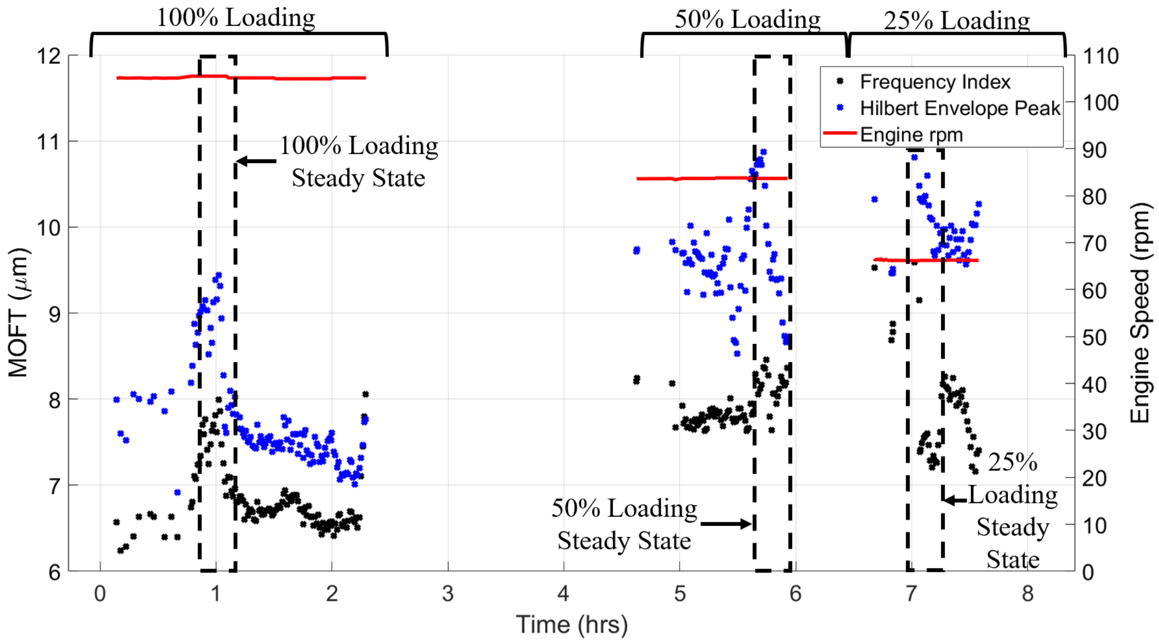

Figure 7.57: MOFT for Sensor 1 Configuration 2 using the Hilbert envelope and the frequency index.

Table 7.2: Steady-state MOFT across all loading levels for engine Configuration 2 for the first piston ring aligned with Sensor 1 from the frequency index and Hilbert envelope analysis.

Engine Loading	**Frequency Index**			**Hilbert Envelope**		
	MOFT (μm)	**Lambda ratio**	**COV (%)**	**MOFT (μm)**	**Lambda ratio**	**COV (%)**
100%	7.4	3.4	4.6	8.9	4.1	3.7
50%	8.1	3.8	2.4	9.8	4.6	7.5
25%	7.9	3.7	10.4	10.4	4.8	1.9

Both data analysis methods presented in Figure 7.57 show the same overall trends in MOFT, with the MOFT increasing as engine load decreased. Although the MOFT ranges are different for each method; the frequency index approach ranged from 6.2-9.1 μm whilst the Hilbert envelope ranges from 7.0-11.0 μm. This represents a typical increase in MOFT of 20% for the Hilbert envelope which is visible for the majority of data captures both within and outside of steady-state testing. The increase in MOFT from the application of the Hilbert envelope method, therefore, also increases the lambda ratio at each engine loading. This moves the ratios closer to indicating a full hydrodynamic film but remains within the mixed regime.

From observation of purely the steady-state engine loading, the same trend in the MOFT is shown as the averaged steady-state data presented in Table 7.2. However, the coefficient of variance over this steady-state period is affected by the data processing technique. The frequency index method has a greater average and peak COV value indicating a greater consistency between captures is shown from the Hilbert envelope method for Configuration 2.

The MOFT for Sensor 1 across all configurations and loading levels from the Hilbert envelope is plotted in Figure 7.58. The MOFT and COV from the first piston ring passing each sensor for each engine configuration presented in Tables 7.3-7.5 for loadings 100% - 25% respectively.

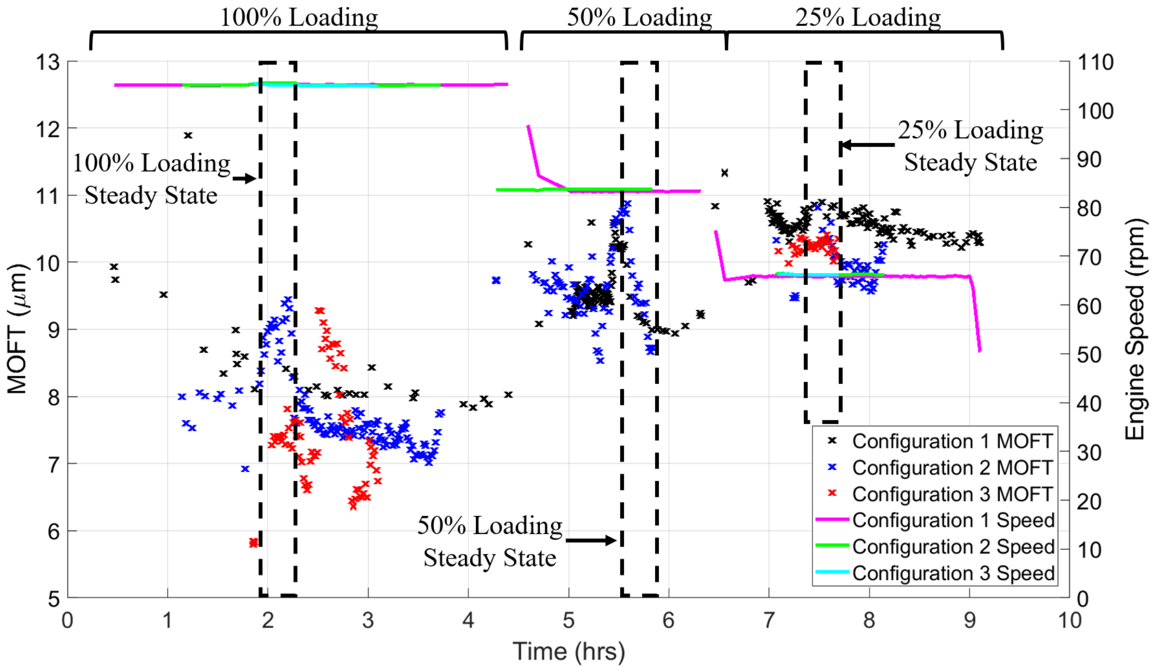

Figure 7.58: MOFT for Sensor 1 at all loading conditions and engine configurations using the Hilbert envelope.

Table 7.3: Steady-state MOFT across 100% loading for all engine configurations for the first piston ring. Note there are no COV values for Configuration 1 as there was only one measurement within this region.

Configuration	**Dist to TDC (mm)**	**-80**	**-40**	**-20**	**0**	**20**	**40**	**80**
	Sensor	**S3**	**S2**	**S4**	**S1**	**S4**	**S2**	**S3**
	Up/Down Stroke	**U**	**U**	**U**	**-**	**D**	**D**	**D**
1	MOFT (μm)	6.0	7.2	6.4	8.4	7.8	8.9	8.3
	COV (%)	-	-	-	-	-	-	-
2	MOFT (μm)	6.2	7.7	8.2	8.9	6.9	8.9	8.4
	COV (%)	1.2	1.1	1.8	3.7	1.6	1.6	0.8
3	MOFT (μm)	9.0	9.7	10.2	7.3	9.5	7.9	7.9
	COV (%)	1.8	1.1	3.0	4.3	2.0	1.1	1.4

Table 7.4: Steady-state MOFT across 50% loading for all engine configurations for the first piston ring.

Configuration	**Dist to TDC (mm)**	**-80**	**-40**	**-20**	**0**	**20**	**40**	**80**
	Sensor	**S3**	**S2**	**S4**	**S1**	**S4**	**S2**	**S3**
	Up/Down Stroke	**U**	**U**	**U**	**-**	**D**	**D**	**D**
1	MOFT (μm)	11.8	15.5	11.1	9.7	10.7	12.7	8.6
	COV (%)	1.3	1.3	1.2	5.4	1.9	1.3	0.8
2	MOFT (μm)	12.4	16.4	12.3	9.8	10.5	13.1	9.4
	COV (%)	0.7	0.9	0.6	7.5	0.7	0.9	0.6

Table 7.5: Steady-state MOFT across 25% loading for all engine configurations for the first piston ring.

Configuration	**Dist to TDC (mm)**	**-80**	**-40**	**-20**	**0**	**20**	**40**	**80**
	Sensor	**S3**	**S2**	**S4**	**S1**	**S4**	**S2**	**S3**
	Up/Down Stroke	**U**	**U**	**U**	**-**	**D**	**D**	**D**
1	MOFT (μm)	14.3	16.5	13.7	10.7	10.8	15.4	10.3
	COV (%)	2.0	0.7	0.7	1.3	0.9	0.8	1.4
2	MOFT (μm)	14.8	16.5	14.2	10.4	11.7	13.3	11.3
	COV (%)	1.3	1.8	2.4	1.9	2.0	1.8	1.8
3	MOFT (μm)	16.3	17.0	14.6	10.3	11.3	12.5	12.2
	COV (%)	1.2	0.9	0.5	0.9	0.9	0.9	1.0

Similar trends to those for the Hilbert envelope peak of Configuration 2 in Figure 7.57 are present for the other two engine configurations in Figure 7.58. Whilst the comparison of the MOFT is not initially clear in the figure, Tables 7.3-7.5 indicate that the MOFT is greater for Configuration 2 at 100% and 50% loading with all configurations having a similar MOFT at 25% loading. The coefficient of variance is significantly lower from the Hilbert envelope method with only four steady-state loading COV values greater than 3.0% whilst the equivalent from the frequency index in Tables 6.4-6.6 had eleven COV values greater than 3.0%. All four of the greatest COV values from the Hilbert envelope also occurred over Sensor 1 from either 100% or 50% loading.

7.7 Conclusions

This chapter has considered several advanced data processing techniques to interpret the ultrasonic data from additional routes on top of those presented in the previous chapter, which were equivalent to previous ultrasonic research in this field. These advancements in this chapter can be summarised in the following conclusions:

- A sensor located above the first piston ring at the TDC should in theory have experienced no discernible change in the reflection coefficient from an approaching piston ring. This is evidently not the case, with a significant change in the reflection coefficient recorded. This sensor has been modelled in k-Wave from an ultrasonic perspective that did not consider any transient engine parameters and it successfully identified similar trends to the experimental results. Observation of a B-scan for Sensor 1 has shown a similar effect of recording a partial reflection from the piston ring outside of the alignment zone which corresponded to the fringe effect seen in some sensors. A likewise effect has, therefore, occurred for this upper transducer with only these fringe effects being experienced.

- The reflection window length has been optimised to reduce the size of the reflection considered for the frequency index method whilst not affecting the minimum reflection coefficient. The optimised windows have been used to produce spectrograms of the reflection coefficient and oil film thickness. The oil film thickness spectrograms show a major variation over the transducer bandwidth. The variation is predominantly in the lower portion of the frequency range, whilst the upper portion of the bandwidth (0.9-1.1 MHz) is near frequency independent.
- The peak of the Hilbert envelope has also been used to define the reflection coefficient with this method removing several minor trends present in the frequency index approach such as; the fringe effect, 'W' double-dip, and prolonged return to unity reflection coefficient. These trends were removed whilst also revealing factors that were hidden in the beforehand analysis such as the pressure effect on the reflection coefficient for Sensor 5.
- The key parameter for piston ring oil film thickness measurements is the MOFT. The optimised frequency index has been evaluated against the Hilbert envelope. The Hilbert envelope provided MOFT values typically 20% thicker than those from the frequency index approach which is arguably a more accurate representation of the oil film as the Hilbert envelope is subject to fewer micro-variations in the reflection. The coefficient of variance across steady-state engine loading is also reduced from the Hilbert envelope method indicating a greater consistency of measurement.
- Overall, from the analyses performed the Hilbert envelope method provides a route to calculate the reflection coefficient and thus OFT in a more accurate and consistent manner. The removal of the impact from reflections of the piston ring outside of the alignment zone and a more consistent steady-state result leads to this method being more appropriate for piston ring OFT measurement in marine diesel engines.

Chapter 8

Fired marine engine shear analysis

Chapter 7 considered several alternative routes to process ultrasonic data from the longitudinal sensors on the RTX-6 marine engine. This chapter applies the additional data processing to the final two sensors instrumented on the RTX-6. The transducers are shear sensors with a 1 MHz central frequency and 14 mm active element diameter that were aligned with the first piston ring at the TDC. These sensors are shown in Figure 8.1 in blue.

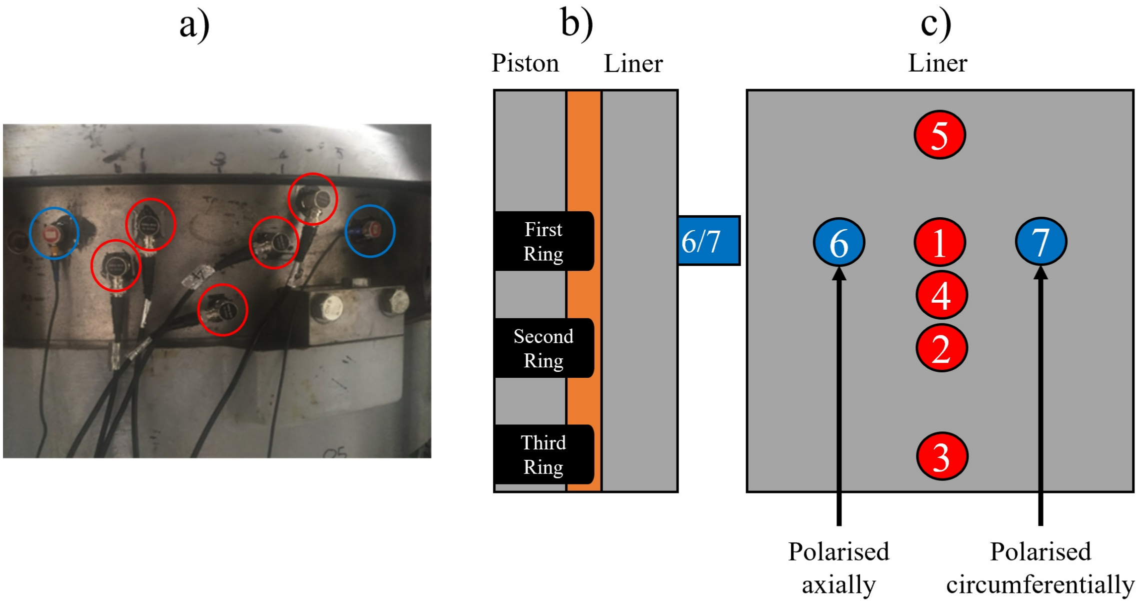

Figure 8.1: Full set of instrumented ultrasonic transducers on the RTX-6 liner. The shear sensors are highlighted in blue. a) Photograph of the sensors. b) Side profile of the shear sensors showing the position relative to the piston rings at their TDC positions. c) The sensor numbering convention of all seven sensors; red were longitudinal sensors covered in Chapters 6 and 7.

Shear sensors operate in the same way as longitudinal sensors, the sensor contains a piezoelectric experiencing material. Although the piezoelectric material is orientated differently than in longitudinal sensors so that the wave oscillation is in a different axis to the wave propagation. Liquids are unable to support shear waves, therefore, shear waves only propagate in solid media. In *theory*, therefore, a fully lubricated piston ring aligned with a shear ultrasonic sensor should see no discernible change in the reflected waves as the piston ring aligns.

8.1 Frequency index method

The traditional frequency index method has been applied to the ultrasonic reflections recorded from the two shear sensors, using the same data processing as outlined in Chapter 6 (Figure 6.10). The reflection coefficient variation for 100% engine loading steady-state engine operation for the three engine configurations is shown in Figure 8.2 for Sensor 6 and Figure 8.3 for Sensor 7, the CA corresponding to the first piston ring being aligned with the sensors has been overlayed. There is no data for Sensor 7 from Configuration 3 as the sensor malfunctioned shortly before the steady-state operation of this configuration. Due to the level of complexity in the experimental setup, the malfunction was unable to be rectified in a timely manner.

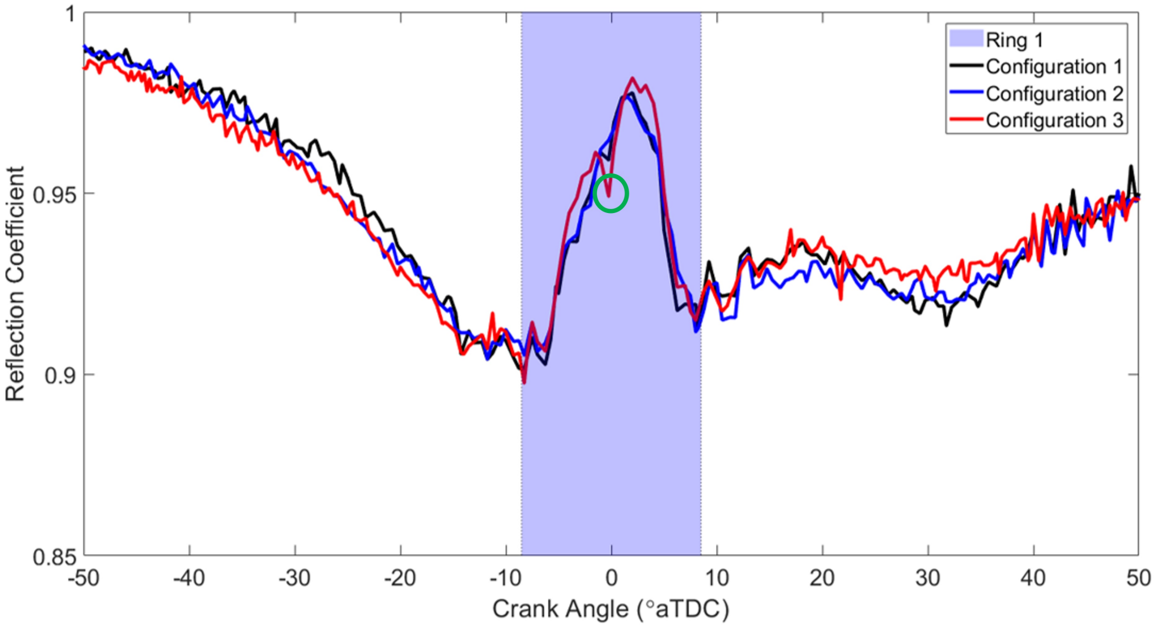

Figure 8.2: Reflection coefficient variation over Sensor 6 at steady-state 100% loading for all engine configurations.

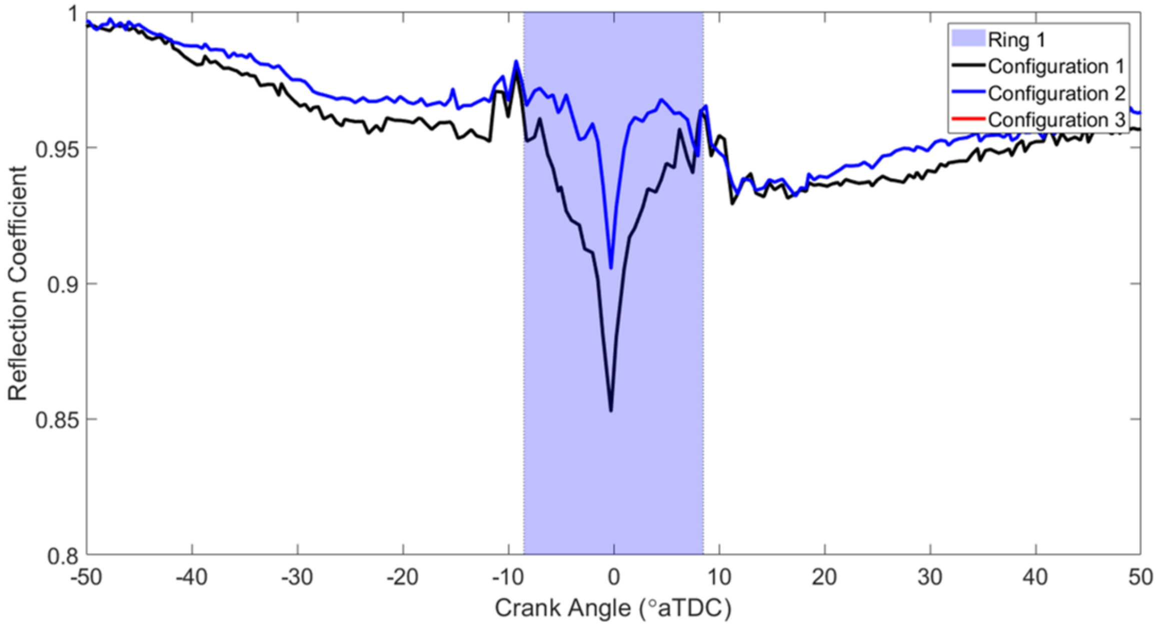

Figure 8.3: Reflection coefficient variation over Sensor 7 at steady-state 100% loading for all engine configurations.

Both Sensors 6 and 7 experience the same extended reduction in reflection coefficient that was present in Sensor 5 (Figure 7.2). The cause of this extended reduction is unknown but was shown to be due to the data processing technique instead of an engine factor as it was removed by the Hilbert envelope in Figure 7.41a. Therefore, it is expected that this factor will have also arisen due to the data processing.

In the piston ring alignment region (-8.5° to 8.5° CA) the two shear sensors show opposing trends. Sensor 6 (Figure 8.2) shows an increase in reflection coefficient as the piston ring becomes more aligned with the sensor, whilst Sensor 7 (Figure 8.3) has a progressive reduction. Two potential causes of this are theorised, the shear sensors are polarised in opposing directions (Sensor 6 polarised axially, Sensor 7 polarised circumferentially) and, therefore, are experiencing differing acoustic elastic effects due to each sensor oscillating in perpendicular directions. This may potentially enable multi-directional stress measurements, expanding on the stress measurements seen during cold rolling in [90]. Alternatively, the lubricating film may be different over the two sensors as the sensors are positioned in slightly different circumferential positions, see Figure 8.1. Over Sensor 6, there may be a fully lubricating film leading to reflection coefficients near R=1 whilst over Sensor 7 there may be a breakdown in the lubricant film, seen via the sharp reduction in reflection coefficient.

Shear waves do not propagate through liquids, therefore, the sharp reduction seen for Sensor 7 (Figure 8.3) for both configurations shortly before the piston TDC is of particular interest. The sharp dip is indicative of either metal-metal contact, a shear wave penetrating through an extremely thin liquid layer, lubricant solidification or piston ring tilt. A minor reduction in the reflection coefficient can also be seen in Figure 8.2 (green circle) for Configuration 3 at 0.25° CA whilst it is not visible identifiable for the two other configurations. In Chapter 6 it was assumed that the region between the piston ring and liner was fully flooded with oil without any metal-metal contact although this may not be the case.

In high-pressure contacts, solidification of the lubricant can lead to shear waves propagating through as the lubricant is no longer fluid. It has been assumed that the lubricant did not solidify on the liner when exposed to the combustion pressure (peaking at less than 200 bar). Therefore, to discern between metal-metal contact and a shear wave penetrating through to the piston ring the shear wave penetration depth is required. This penetration depth is calculated in Section 8.1.1.

Observation of Figure 8.3 shows the second engine configuration provided a significantly smaller reduction in the reflection coefficient. This engine configuration was also the configuration that had the NLT injectors on the upper lubricant rail, which refined how the lubricant was sprayed onto the liner. Ultimately, this configuration reduced the rate of lubricant atomisation and, therefore, led to more oil remaining on the cylinder liner. Under the assumption that the reduction in reflection coefficient is a measure of metal-metal contact, this, therefore, shows Configuration 2 to have led to less metal-metal contact (piston ring scuffing) between the first piston ring and cylinder liner at the TDC. A closer inspection of each engine cycle that comprises the reflection coefficients shown in Figure 8.3 is shown for Configurations 1 and 2 in Figure 8.4a and Figure 8.4b respectively.

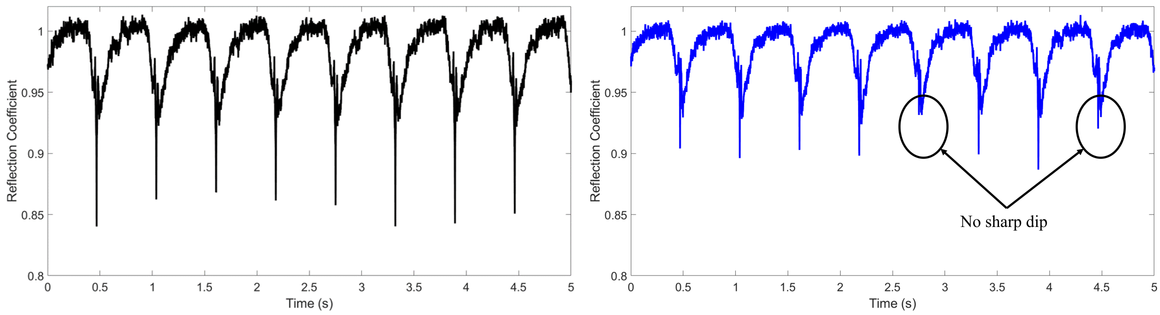

(a) Configuration 1.

(b) Configuration 2.

Figure 8.4: Reflection coefficient variation over the complete recording for Configuration 1 and 2.

The differing rates of lubricant atomisation are directly visible in the raw reflection coefficient data. For Configuration 1 (high atomisation), in Figure 8.4a a sharp reduction in the reflection coefficient is seen every engine cycle with the dips of minimum reflection coefficient varying between 0.84 to 0.88. Whilst for Configuration 2 (low atomisation), in Figure 8.4b the dip minimum varies between 0.89 to 0.91 with two of the engine cycles recorded showing no sharp reduction at all. The sharp reductions in the reflection coefficient, therefore, indicate that either metal-metal contact of ring-liner or a shear wave penetration is occurring in each engine revolution for Configuration 1. Whereas for Configuration 2 it is occurring to a reduced extent with some engine cycles have a significant reduction. Sensor 7 adds more confirmatory evidence to what was shown in Chapter 6, that the second engine configuration led to a more desirable lubrication regime for the first piston ring at the TDC through more lubricant remaining on the liner surface.

8.1.1 Shear wave penetration depth

To discern whether metal-metal contact or a shear wave is penetrating through a very film lubricant film the shear wave penetration depth is required as detailed in Section 3.6. This calculation requires the engine oils viscosity. To provide more applicable measurements for this, oil was scavenged from the RTX-6 engine during 100% loading of Configuration 1. The scavenged oil provides a greater representation of the lubricant in the ring liner contact during the steady-state loading period and the oil will have likely been degraded and contain contaminants such as combustion products. The engine lubricant has been tested in a Brookfield viscometer to provide viscosity measurements at a range of temperatures, a plot of the dynamic viscosity against oil temperature is shown in Figure 8.5.

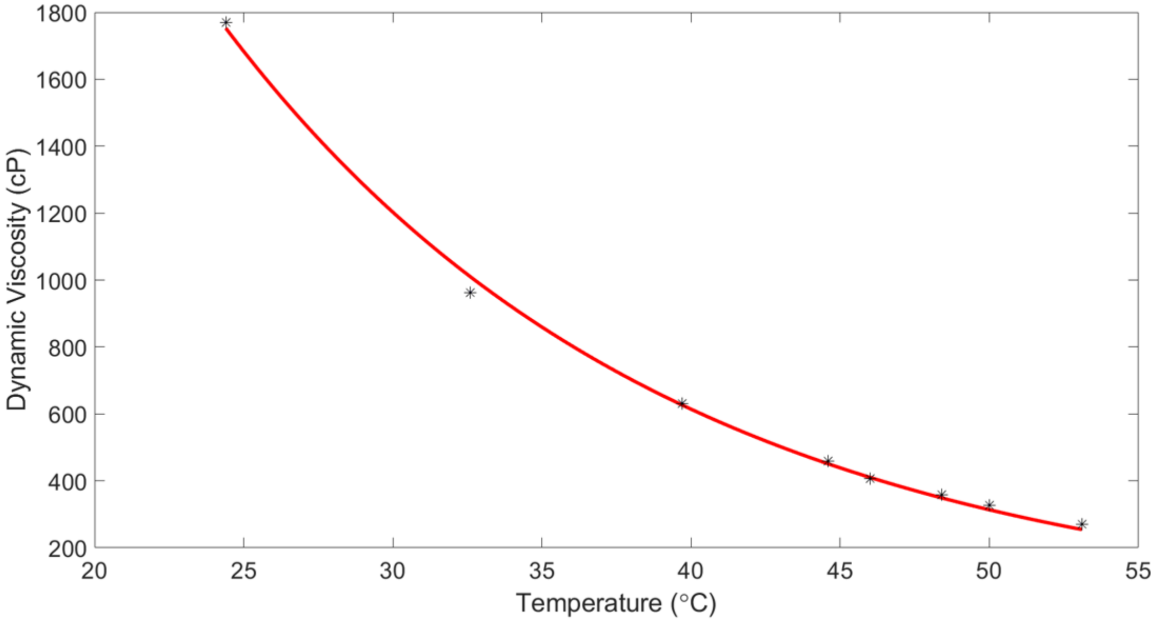

Figure 8.5: Viscosity temperature relation for the scavenged engine oil.

The Vogel Equation (Equation 8.1) has been calculated for the viscosity measurements in Figure 8.5. The equation can be used to provide a value for the engine oil viscosity in the piston-liner contact during engine operation. The calculated Vogel Equation coefficients are shown in Table 8.1.

$$\eta = A \times exp(\frac{B}{T-C}) \tag{8.1}$$

Table 8.1: Vogel equation coefficients.

Coefficient	**Value**
A	5.04×10^{-11}
B	1395.3
C	-423.0

Applying the Vogel Equation with the coefficients in Table 8.1 and the cylinder liner internal surface temperature at 100% loading provides a value for the engine oil viscosity during steady-state operation.

$$\eta = 5.04 \times 10^{-11} \times exp(\frac{1395.3}{216 - -423.0}) = 0.15cP \tag{8.2}$$

The Vogel Equation provides a dynamic viscosity of 0.15 cP. This oil viscosity can be used to calculate the shear wave penetration depth as mentioned in Section 3.6 using Equation 8.3.

$$\delta = \sqrt{\frac{\eta}{\pi f \rho_l}} = \sqrt{\frac{1.5 \times 10^{-4}}{\pi \times 1 \times 10^{6} \times 781}} = 0.25\ \mu m \tag{8.3}$$

The shear wave penetration depth was calculated to be 0.25 μm, more than an order of magnitude lower than the minimum oil film thickness recorded for Sensor 1 of 6.3 μm using the frequency index method (the thinnest MOFT from either data processing technique). As the penetration depth is significantly less than the MOFT, this shows that the shear waves would not have been able to penetrate through a fully formed lubricant film to a parallel piston ring, see Figure 8.6a.

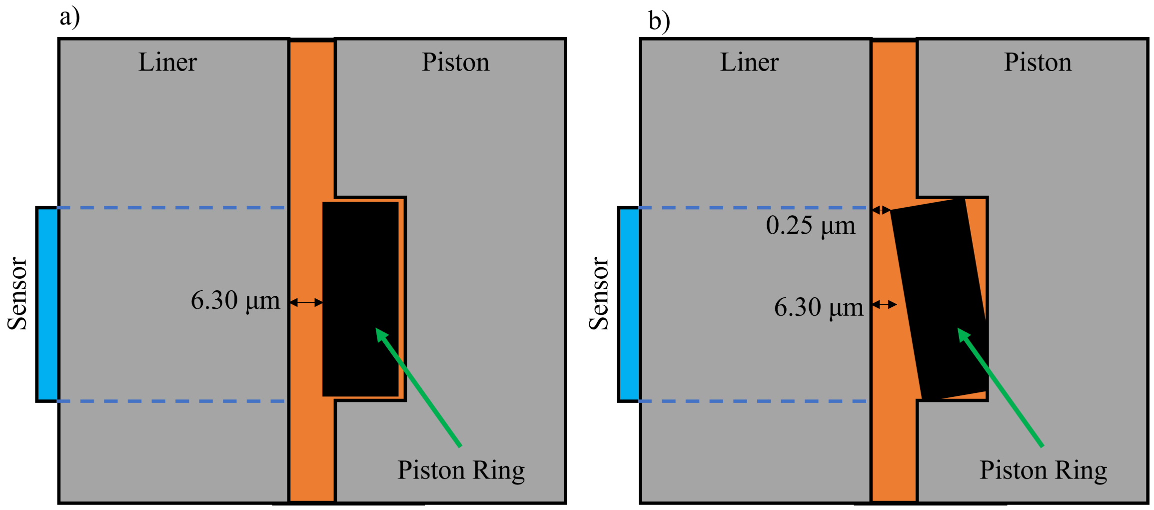

(a) Parallel piston ring film thickness.

(b) Angled piston ring film thickness

Figure 8.6: Piston ring film thickness scenarios.

A significant rotation of the piston and/or ring enables the possibility of a fully formed lubricating film that has a true minimum film thickness of less than 0.25 μm with an average MOFT of 6.3 μm as ultrasonic transducers provide an average over the whole alignment zone. A visualisation of this is shown in Figure 8.6b. However, a film thickness of 0.25 μm is the thickness required for initial penetration of the wave. In Figure 8.3 for example, reflection coefficients of 0.85 were recorded. Therefore, a 15% transmission of the shear ultrasonic wave. For 15% of the sensing area to be below 0.25 μm, whilst the midpoint was 6.3 μm, the true minimum film thickness becomes -2.3 μm, assuming the shape of the barrelled ring is unaltered, see Figure 8.7. This is geometrically unattainable and furthermore, shows that 15% of the shear wave could not have penetrated through a fully formed oil film without metal-metal contact also occurring.

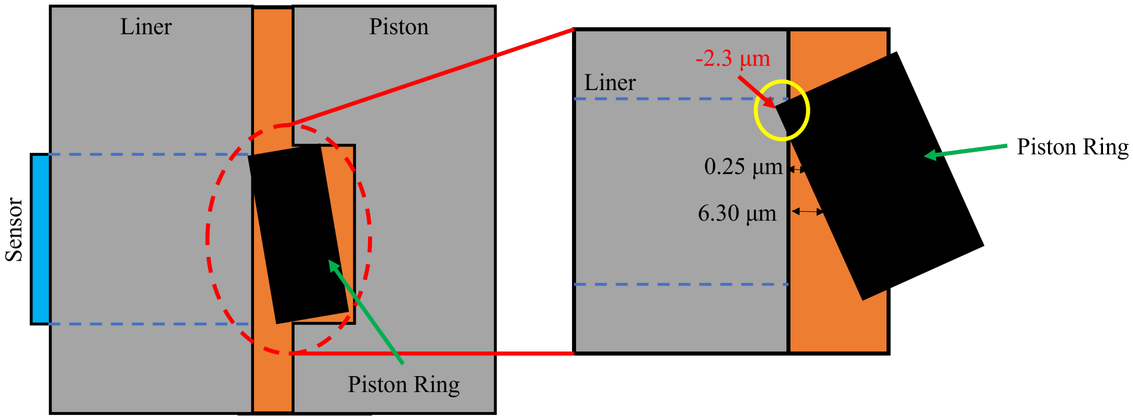

Figure 8.7: Rotation of the piston ring with 15% of the ring face less at 0.25 μm film thickness

It can now be concluded that lubricant solidification or solely penetration of the shear waves through a fully formed oil layer did not occur during the engine testing on the RTX-6. This, therefore, indicates that to achieve the sharp reductions in the reflection coefficient seen in Figure 8.3, metal-metal contact was occurring between the piston ring and liner close to the TDC over Sensor 7.

8.1.2 Pulse rate variation

Ultrasonic data was captured at varying pulse rates (1.05 kHz and 12.4 kHz), this was only achieved for Sensor 6 due to the malfunction of Sensor 7. The reflection coefficient for the two pulse rates is plotted in Figure 8.8 for Sensor 6 at 100% engine loading during the third configuration.

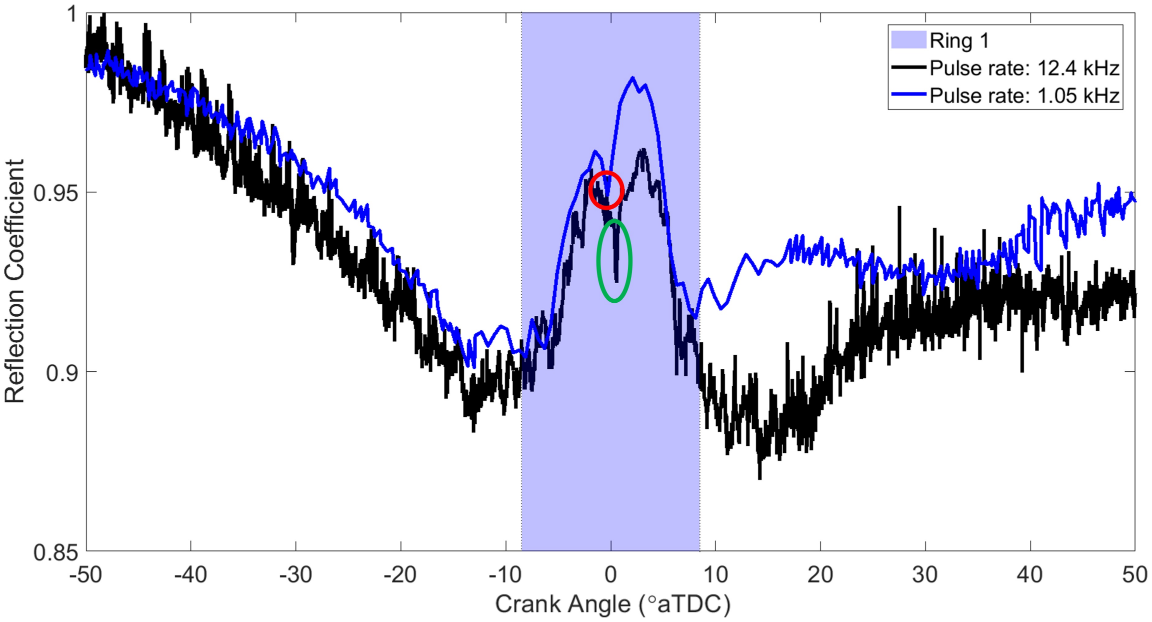

Figure 8.8: Reflection coefficient variation for different levels of pulse rate for Sensor 6. Metal-metal contact for the two pulse rates is highlighted in the red and green circles.

Similar to the pulse rate variations shown for the longitudinal sensors (Section 6.3.1) the two pulse rates show largely similar trends with a large reduction in reflection coefficient pre/post piston ring. The differing reflection coefficients post piston ring is anticipated to have arisen due to the high pulse rate captures being outside of the steady-state operation.

The single data point reduction at 0.25° CA for the 1.05 kHz (red circle) which indicates metal-metal contact is displayed clearer at the higher pulse rate with 10 data points now spanning the sharper reduction in reflection coefficient (green circle). In the slower captures, a data point was recorded every 0.6° CA, whilst in the higher pulse rate it was 0.05° CA and the dip occurred over a 0.5° CA range showing that the slower pulse rates could have completely missed the metal-metal contact. Therefore, the true extent of the ring-liner contact was missed in the lower pulse rate capture due to the metal-metal contact likely to have primarily occurred between two data points. The higher pulse rate capture also shows the dip 2° CA later indicating that the piston ring scuffing may not occur at the same CA each engine cycle. This highlights the requirement to pulse at high pulse rates in complex systems such as internal combustion engines as factors may occur over extremely short timespans, therefore, they may be missed. In this testing, there were no other instances in which pulse rates of 12.4 kHz indicated significant trends that were missed in the 1.05 kHz pulse rate recordings. Although it remains possible that other factors may have occurred over CA ranges smaller than 0.05° CA preventing them from being shown in the high pulse rate plots.

8.1.3 Oil feed rate variation

During each steady-state loading period, the oil feed rate was varied from its nominal rate of 0.8 g/kWh to a high flow (1.2 g/kWh) and low flow (0.6 g/kWh) rate in five-minute intervals. The effect of this change in oil feed rate was previously considered for the longitudinal Sensors 1-4 in Section 6.4.2. Here the same time interval of testing is studied from the shear sensors perspective with a focus on Sensor 7, as Sensor 6 provided no clear change in reflection coefficient indicative of metal-metal contact during steady-state operation at the lower pulse rate. In this case, each individual engine cycle for the central test case for each oil feed rate is considered for Configuration 2 instead of averaging each cycle over the recording interval. This produces Figure 8.9a with an enhanced version for -5° to 5° CA shown in Figure 8.9b.

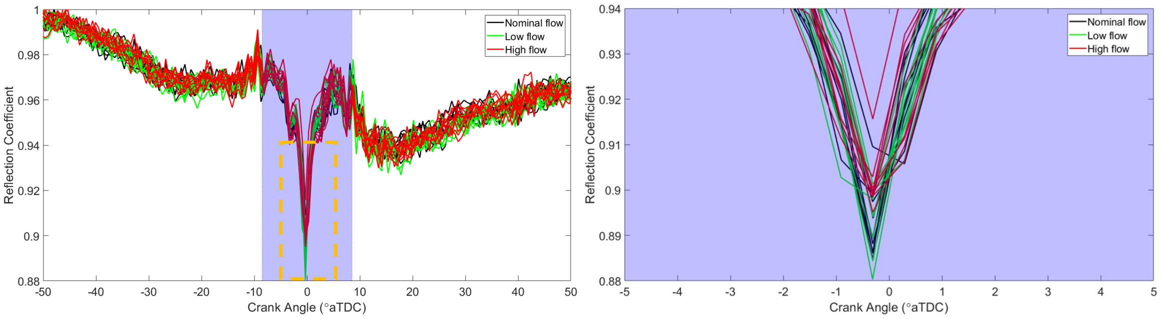

(a) Three oil feed rates.

(b) Enchanced version of Figure 8.9a.

Figure 8.9: Sensor 7 reflection coefficient variation with oil feed rate variation for Configuration 2.

Initial observation for Figure 8.9a shows no clear change in the reflection coefficient at the three differing oil feed rates. Although closer inspection upon the TDC region in Figure 8.9b indicates that the engine cycles with a greater oil feed rate produced a higher reflection coefficient than those of the nominal or low flow rate cases for the majority of engine cycles. This provides an indication that there was less metal-metal contact between the piston ring and cylinder liner when there was more lubricant fed into the contact. Due to the longitudinal transducers providing no such change in reflection coefficient for a change in oil feed rate this suggests that shear transducers are more sensitive to the quantity of lubricant in a contact as shear waves are only supported by solids. It was previously shown in Section 6.4.3 that a greater time interval than 5-minutes was required to often see a change in reflection coefficient as the engine slowed. Therefore, it is likely that a greater duration of each lubricant feed rate would have provided more discernible variations between feed rates.

8.2 Hilbert envelope

The Hilbert envelope method has been evaluated for the shear sensors, the comparison between the two processing techniques is shown in Figure 8.10a and 8.11a for Sensors 6 and 7 respectively. The three engine configurations for Sensors 6 and 7 using the Hilbert envelope are compared in Figures 8.10b and 8.11b.

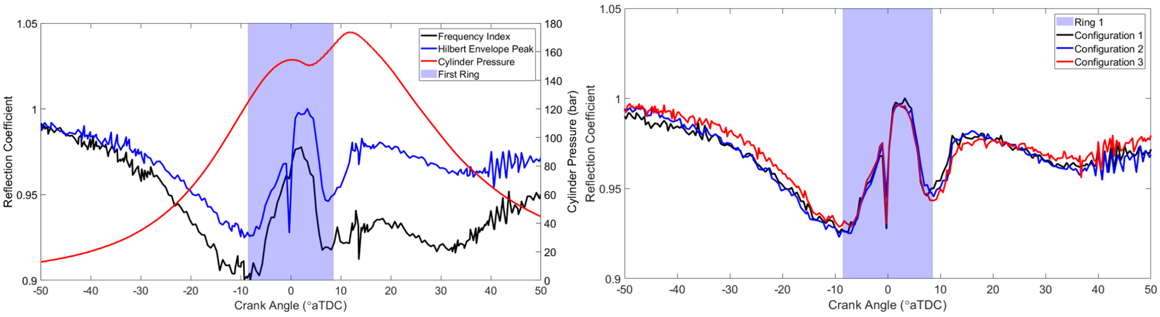

(a) Frequency index vs Hilbert envelope.

(b) Hilbert envelope.

Figure 8.10: Reflection Coefficient for Sensor 6 from the frequency index and Hilbert envelope methods.

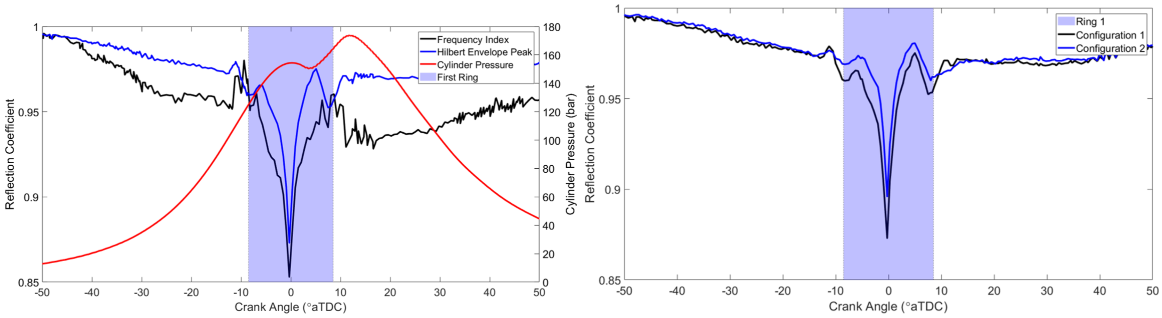

(a) Frequency index vs Hilbert envelope.

(b) Hilbert envelope.

Figure 8.11: Reflection Coefficient for Sensor 7 from the frequency index and Hilbert envelope methods.

Upon initial observation of Figures 8.10a and 8.11a for the shear sensors, a somewhat similar trend to Sensor 5 is observed that the Hilbert envelope method. The processing method removes a large portion of the extended reduction yet it remains present, the cause of which is unknown.

Analysis upon Sensor 6 using the frequency index, shown in Figure 8.2, showed a minor dip at 0.25° CA for Configuration 3 whilst the two other configurations showed no dip. Providing an initial indication that there was no metal-metal contact for Configurations 1 and 2 and marginal contact for Configuration 3. Although this may not be the case, as the Hilbert envelope plotted in 8.10a now displays a sizeable dip that is now likewise seen for Sensor 7. The presence of this dip for all engine configurations gives greater confidence to early analysis on Sensor 7 as Configuration 2 continues to provide a smaller decrease in reflection coefficient than the two other configurations for both sensors. Further indicating that less metal-metal contact occurs from the injection system with a reduced rate of lubricant atomisation.

8.2.1 Loading variation

A loading comparison at the three engine loads for the two data processing techniques is shown in Figures 8.12 and 8.13 for Sensors 6 and 7 respectively.

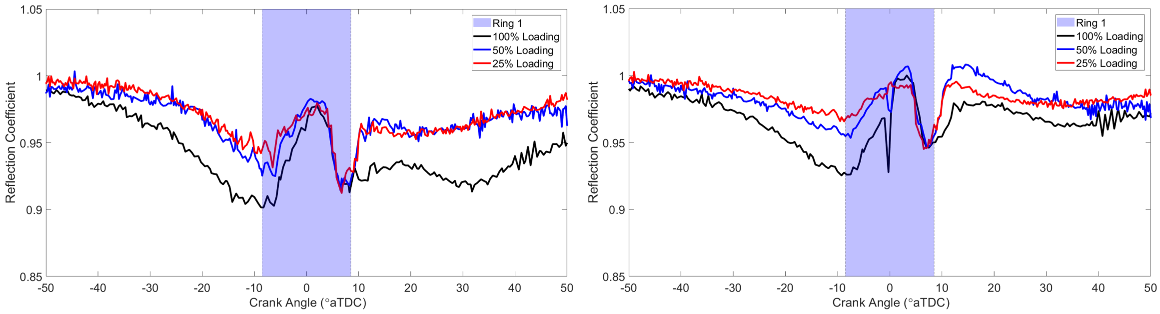

(a) Frequency index.

(b) Hilbert envelope.

Figure 8.12: Reflection Coefficient Loading Comparison for Sensor 6 from the two processing methods.

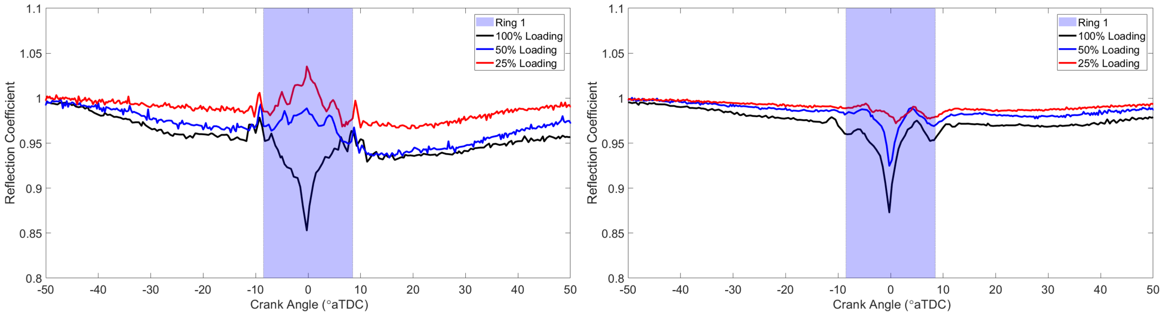

(a) Frequency index.

(b) Hilbert envelope.

Figure 8.13: Reflection Coefficient Loading Comparison for Sensor 7 from the two processing methods.

The frequency index method for Sensor 6 (Figure 8.12a) provides no identifiable change with engine loading and as was previously seen for 100% loading, no identifiable metal-metal contact. Similarly, Sensor 7 (Figure 8.13a) shows metal-metal contact at 100% loading but the two lower loading levels show a peculiar trend of an increased reflection coefficient towards the TDC, the cause of which is unknown. Once again, the Hilbert envelope (Sensor 6 in Figure 8.12b and Sensor 7 in Figure 8.13b) visualises trends hidden via the frequency index. Metal-metal contact can be seen in both sensors at all loading levels and be seen to decrease as the load was reduced. This is an expected result due to a load reduction leading to greater OFT and, therefore, a reduced likelihood of lubricant film breakdown. By 25% loading over both sensors only a minor reduction in reflection coefficient is seen, likely showing only minor levels of metal-metal contact at this point. This, therefore, shows the novelty of this work, as shear ultrasonic transducers have the ability to provide a measurement of metal-metal contact and could be used as a viable tool to minimise wear of the piston rings and liner.

8.2.2 Engine slowdown

There were two engine slow-down periods, from 100% to 50% loading and from 50% to 25%. The reflection coefficient variation for these two time periods for Sensor 7 are shown in Figure 8.14 and Figure 8.15 respectively. The two plots differ in terms of how the data was recorded leading to different visualisation of the plots. From 100% to 50% loading (Figure 8.14) a continuous recording for two minutes was captured, in which the encoder experienced an error. Therefore, no engine speed values are provided.

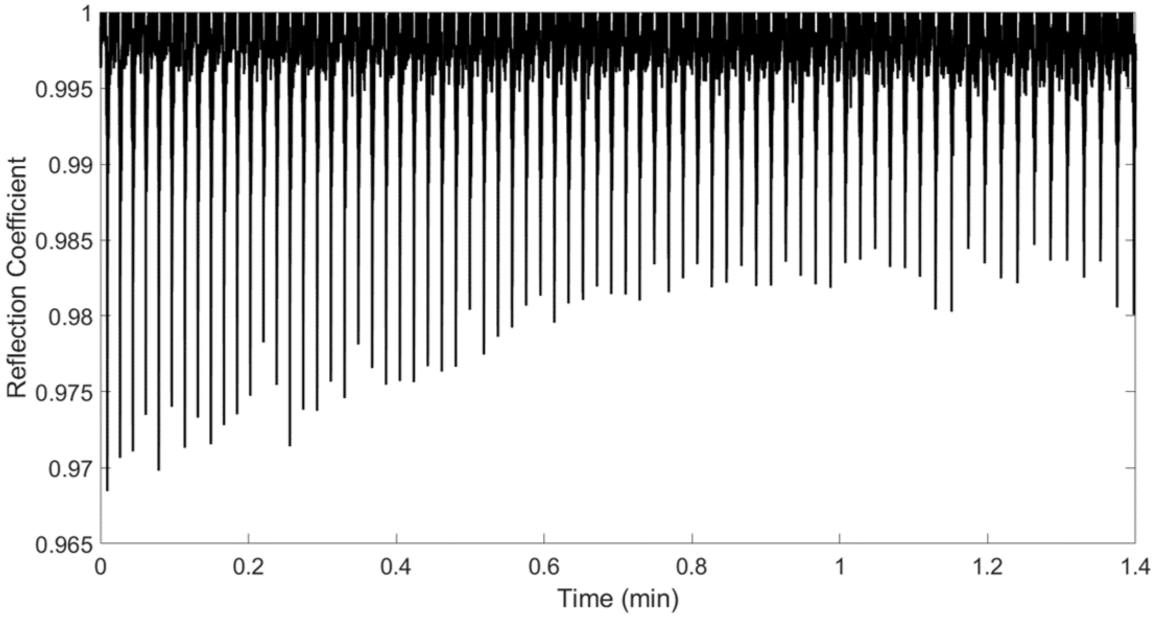

Figure 8.14: Reflection coefficient variation for Sensor 7 as the engine was slowing down from 100% loading to 50% loading testing.

The slowdown from 50% to 25% loading in Figure 8.15 was an interval recording spanning a 44-minute interval in which a 5-second sample was recorded every minute. An example of the first recording interval for the slowdown from 50% to 25% loading is shown in Figure 8.15a with the minimum reflection coefficient from each cycle shown in Figure 8.15b with the engine speed overlayed on the plot.

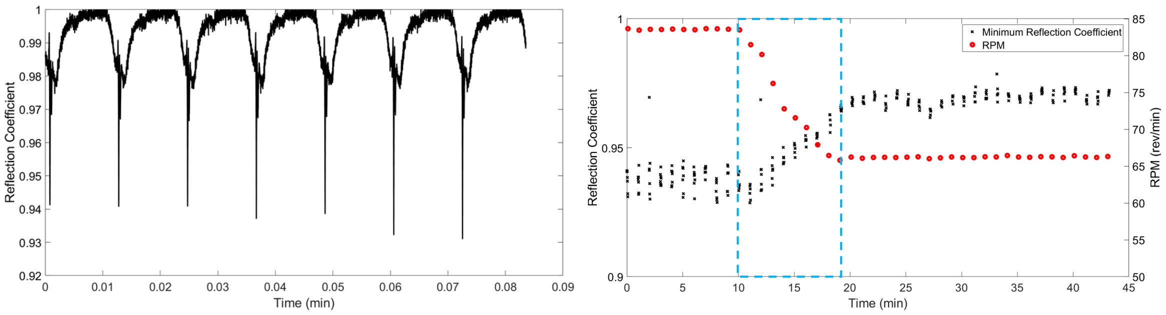

(a) The first interval capture.

(b) All intervals in 44 minute period.

Figure 8.15: Reflection coefficient from engine slowdown from 50% to 25% loading over Sensor 7. The engine slow down interval is highlighted in the blue dashed box.

Comparison between the two engine slow-down plots should be limited to the trend in the reflection coefficient, as engine conditions such as temperature and pressures will have been transient and significantly different between the two slow-down tests, therefore, magnitude of the dip may not be representative. Nevertheless, the variation in engine loading in each figure is shown by a change in magnitude of the dip in the reflection coefficient, that a reduction in each individual figure shows a real-time measure of the reduction in engine load, shown clearest in Figure 8.15b. Towards the end of the 44-minute recording period, the dip magnitude begins to stabilise as the engine approaches steady-state operation at the lower loading level.

Figures 8.14 and 8.15b provide a real-time measure of how metal-metal contact changes over the course of engine loading and speed reduction. In the case of 50% to 25% loading (Figure 8.15b) the halving of engine loading from Minute 10 to Minute 20 is reflected in a near halving of reflection coefficient dip magnitude of typically 0.93 to 0.97.

8.2.3 Engine shut-down

The tests covering the RTX-6 shut-down should be considered separately from those of changing engine loading as the engine will have experienced different variations. Primarily, when the engine moved from 100% to 50% loading, the load on the piston rings and factors such as oil feed rate proportionally reduce but are still operating. Whilst the shut-down tests cover the region where the lubricant system is shutting down leading to less lubricant being injected onto the liner. The reflection coefficient for a shut-down test for Sensor 7 is shown in Figure 8.16 for Configuration 2. For this shut-down test, ultrasonic reflections were recorded for 20 seconds.

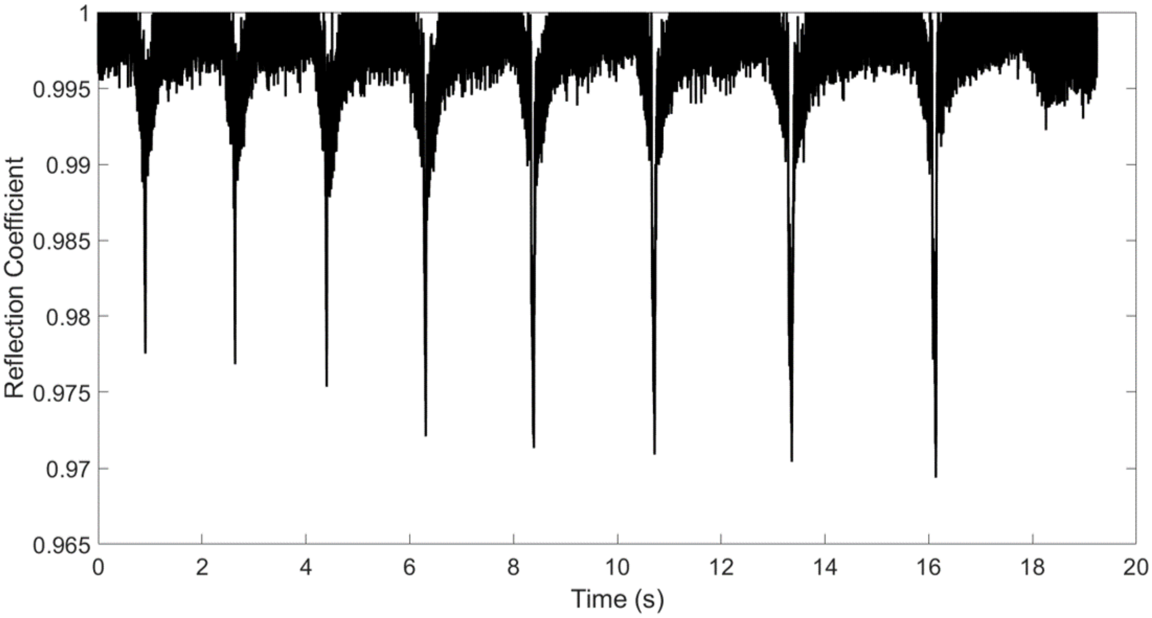

Figure 8.16: Reflection coefficient variation for Sensor 7 as the engine shut-down after 25% loading for Configuration 2.

Throughout the engine shut-down, each cycle leads to a progressively greater reduction in the reflection coefficient than the previous (0.98 to 0.97 over the last 16 seconds of engine operation). This reduction is seen as the lubricant injection system shuts down, therefore, less lubricant is injected onto the liner preventing a fully lubricated oil film between the ring and liner leading to greater amount of metal-metal contact. The reduction in the reflection coefficient in each individual cycle also happens over a greater timespan in each successive engine cycle, reflecting the reduced engine speed.

A combination of the slow-down and shut-down tests in terms of metal-metal contact can be summarised as; A reduction in engine loading reduces metal-metal contact between the piston ring and liner until the lubricant injection system begins to shut off. Following this, the metal-metal contact increases until the engine stops rotating.

8.3 Conclusions

This chapter has detailed the results from the shear ultrasonic sensors instrumented onto the RTX-6 engine. There have been a number of novel findings from these sensors, the key points are summarised as follows:

- Two shear sensors were instrumented onto the external surface of the liner and aligned with the first piston ring at the TDC. Data processing using the frequency index method identified a sharp reduction in reflection coefficient close to the TDC, indicative of either metal-metal contact, shear wave penetration or lubricant solidification. The latter two have been ruled out, indicating this dip was at least partly due to metal-metal contact.

- The piston ring-liner metal-metal contact was present for both Configuration 1 and 2 over Sensor 7. A consistent level of metal-metal contact was seen for Configuration 1, whilst Configuration 2, with a reduced rate of lubricant atomisation, had a lessened amount of metal-metal contact which was significantly less during some engine cycles.

- The frequency index method results of Sensor 6 initially only indicated a single data point reduction in the reflection coefficient for Configuration 3 and was not seen in the other engine configurations. Higher pulse rate captures have shown the dip indicative of metal-metal contact clearer. The higher pulse rates showed the dip to occur over a 0.5° CA range, whilst the lower pulse rates captured data every 0.6°

CA. Therefore, it is likely that the metal-metal contact could have been completely missed in Configurations 1 and 2 at the lower pulse rate.

- Analysis of the longitudinal sensors in Chapter 6 displayed no clear change in reflection coefficient/OFT with oil feed rate. It has been shown for Sensor 7 that the higher flow rate cases led to a smaller reduction in reflection coefficient, implying less metal-metal contact due to a more lubricated piston ring. This implies that shear sensors are more sensitive to the quantity of lubricant present.
- The Hilbert envelope has been evaluated for the shear sensors, this data processing technique has removed a significant portion of the reduction in reflection coefficient pre/post piston ring. In addition, the Hilbert envelope method shows a clear dip due to metal-metal contact in each engine configuration that was previously hidden via the frequency index. Similar findings were seen in a loading comparison between the two methods. The frequency index method displayed no piston ring-liner contact at 50% or 25% loading for either sensor, whilst the Hilbert envelope method does. The magnitude of the reduction in the reflection coefficient also decreases with engine loading. This shows that the metal-metal contact reduced as engine loading was reduced.
- Engine slow-down and shut-down tests have provided a real-time visualisation of how metal-metal contact changed with loading. The findings can be summarised as a reduction in loading leads to less piston ring-liner contact until the lubricant system begins to shut down. Following this, the magnitude of the reflection coefficient dip increases as an insufficient amount of lubricant is present to prevent metal-metal contact which was amplified each cycle until the engine stopped rotating.

Chapter 9

Fired diesel tractor engine

In this Chapter, a fired diesel YTRC2110D engine that is typically used in tractors was considered. The engine features a wet removable liner which enabled a complex array of transducers to be bonded to the liner with minimal modification to the engine. A range of engine speeds and loading levels were tested including studying the start-up and shut-down of the engine.

9.1 Test engine

In the previous three chapters on the RTX-6 engine, a range of advancements have been achieved in the data processing of ultrasonic piston ring film thickness data. These were likely achieved due to the research being performed on a large diesel marine engine. Following these advancements, it was desired to implement the novel data processing techniques onto a smaller fired engine to see if likewise data processing advancements had been achieved and to study engine phases not previously studied with this technology. The smaller engine selected was a YTR engine, specifically a YTRC2110D, a 2-cylinder diesel engine that is typically used in tractor engines. The fired engine connected to a dynamometer is shown in Figure 9.1. The test engine is located at the College of Power and Energy Engineering at Harbin Engineering University. The main engine parameters are summarised in Table 9.1. In the YTR engine there are three piston rings, two barrel rings and a one piece oil control ring.

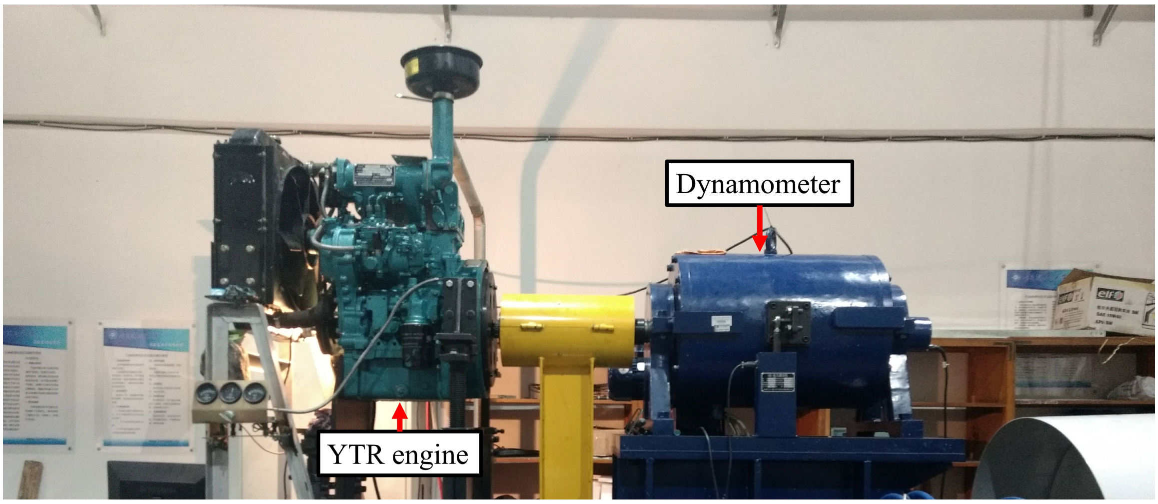

Figure 9.1: YTRC2110D test engine.

Table 9.1: Main engine parameters for the YTRC2110D engine.

Engine parameter	**Value**	**Unit**
Maximum power	21-24	kW
Operating speed range	1000-1500	r/min
Compression ratio	17:1	-
Cylinder bore	110	mm
Piston stroke	125	mm
No. of cylinders	2	-
Cylinder liner roughness	3	μm
No. of rings	3	-
Piston ring roughness	0.8	μm

9.1.1 Lubricant details

The engine was lubricated with a standard 15W/40 mineral engine oil. As shown extensively for the previous chapters, Section 5.1 for the AJ200 and Section 6.1.3 for the RTX-6, the speed of sound in the oil and the density are required for the determination of oil film thickness. Both are functions of temperature and need to be determined.

The acoustic velocity of this oil has previously been measured experimentally in [64] using the time-of-flight of an ultrasonic pulse through a sample of oil in a vessel of known path length in a test rig similar to that shown in Figure 5.1. This experiment was conducted at a range of temperatures in a thermostatically controlled oven. The speed varied approximately linearly with temperature; a curve fit to the data is given in Table 9.2. The lubricant density was also provided by the supplier, see Table 9.2.

Table 9.2: Properties of the YTRC2110D engine oil.

Oil	**Density (kg/m^3)**	**Speed of sound (m/s)**	**Reference**
15W/40	890	-3.328T(°C)+1519	[64]

9.2 Ultrasonic instrumentation

The YTRC2110D engine uses a wet liner, therefore, to enable ultrasonic instrumentation the liner was removed from the engine and a small flat was machined on the external surface of the liner. The machining removed 3 mm of liner material at the central point of the machining. This flat was to locate the transducers and to enable the liner external diameter to remain the same post instrumentation. A total of nineteen high temperature 5 MHz (curie temperature: 350°C) transducer elements (13 longitudinal and 6 shear sensors) were adhesively bonded to the liner. The longitudinal sensors each had a length of 5 mm and width of either 0.8 mm or 1.3 mm, whilst the shear sensors were 3 mm square. For the engine testing, the six best performing transducers of the 19 were used. As the YTR engine has a much thinner liner than the RTX-6 engine, this enabled higher frequency transducers to be instrumented enabling a greater useable bandwidth.

The transducers were bonded to the liner by an industrial adhesive (M-Bond 610) that was curved at elevated temperature in an oven, Figure 9.2a shows the full set of instrumented transducers. Micro coaxial wires were bonded to each sensor and ground onto the liner with a silver epoxy. The sensors were protected by a series of layers of an epoxy potting compound to seal against coolant potentially damaging or shorting the sensors. The instrumented liner post final layer of protective epoxy is shown in Figure 9.2b (under a layer of Kapton tape).

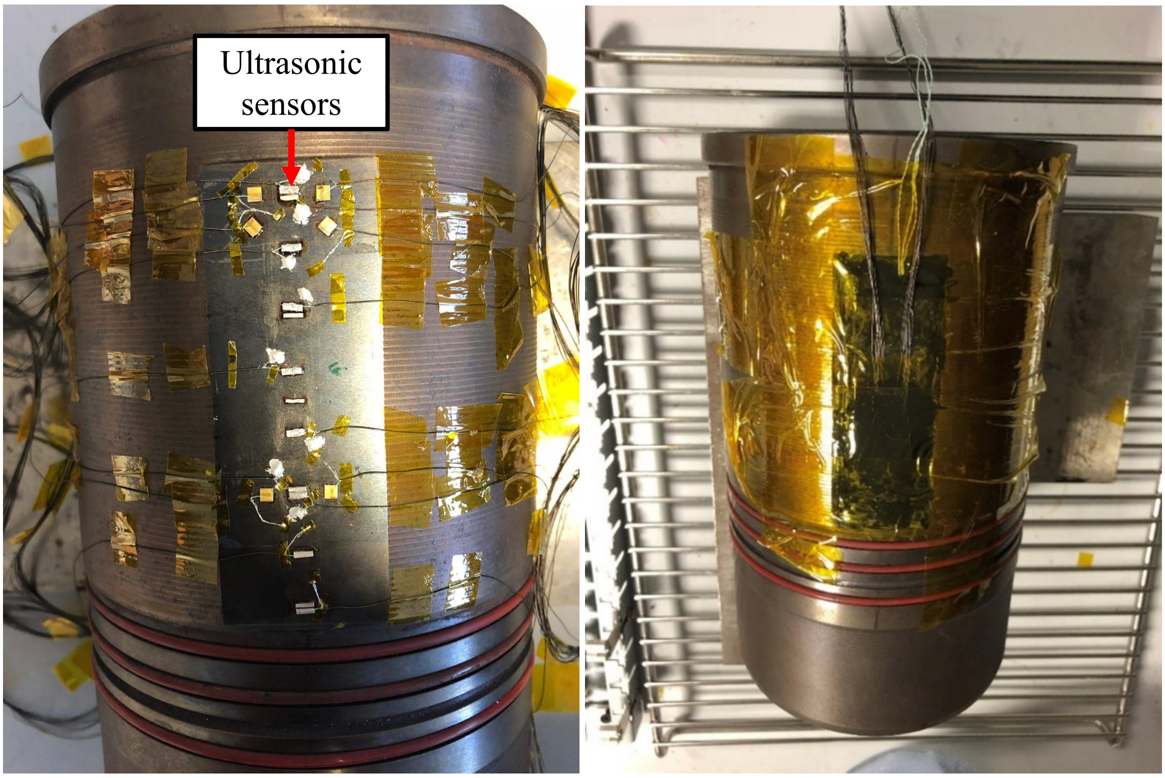

(a) Partial instrumented sensors.

(b) Fully instrumented sensors.

Figure 9.2: Ultrasonic instrumentation on the YTRC2110D liner.

The liner was inserted into the engine block with the sensors on the neutral side of the liner and the wiring loom was fed out through a pre-existing coolant channel that was not in use. Figure 9.3 shows photographs of the liner during the installation process. Once the liner was safely in the engine block, the liner was rotated 90 degrees to position the sensors on the thrust side of the engine. The complete installation process required minimal modification to the engine, the only modification to the engine was the flat machined onto the external surface of the liner, see Figure 9.2a.

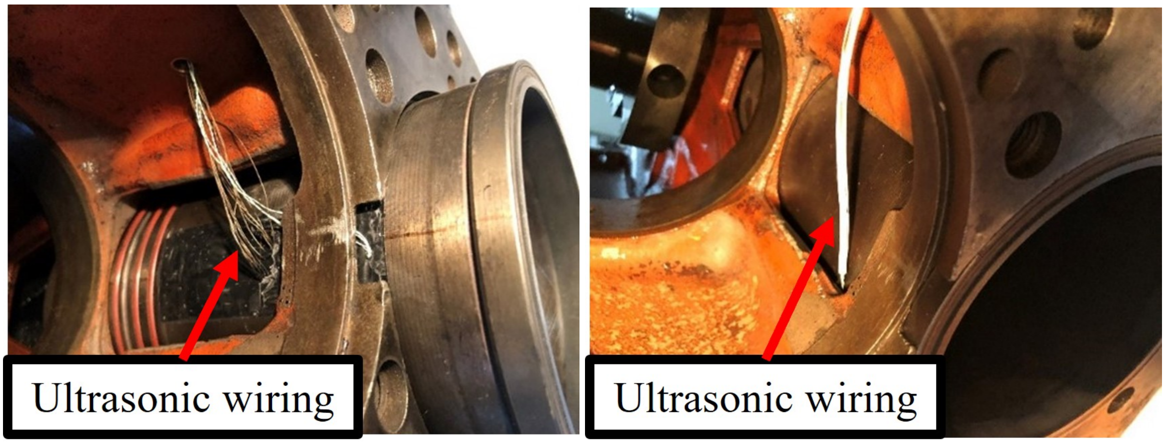

(a) Inserted orientation of the liner (sensors on neutral side).

(b) Final orientation of the liner (sensors on thrust side).

Figure 9.3: Liner installation to the engine.

The location and sensor numbering convention of the six optimal transducers are shown in Figure 9.4. The position of the selected sensors (all longitudinal) and piston ring locations/skirt length relative to the piston crown at the TDC is shown.

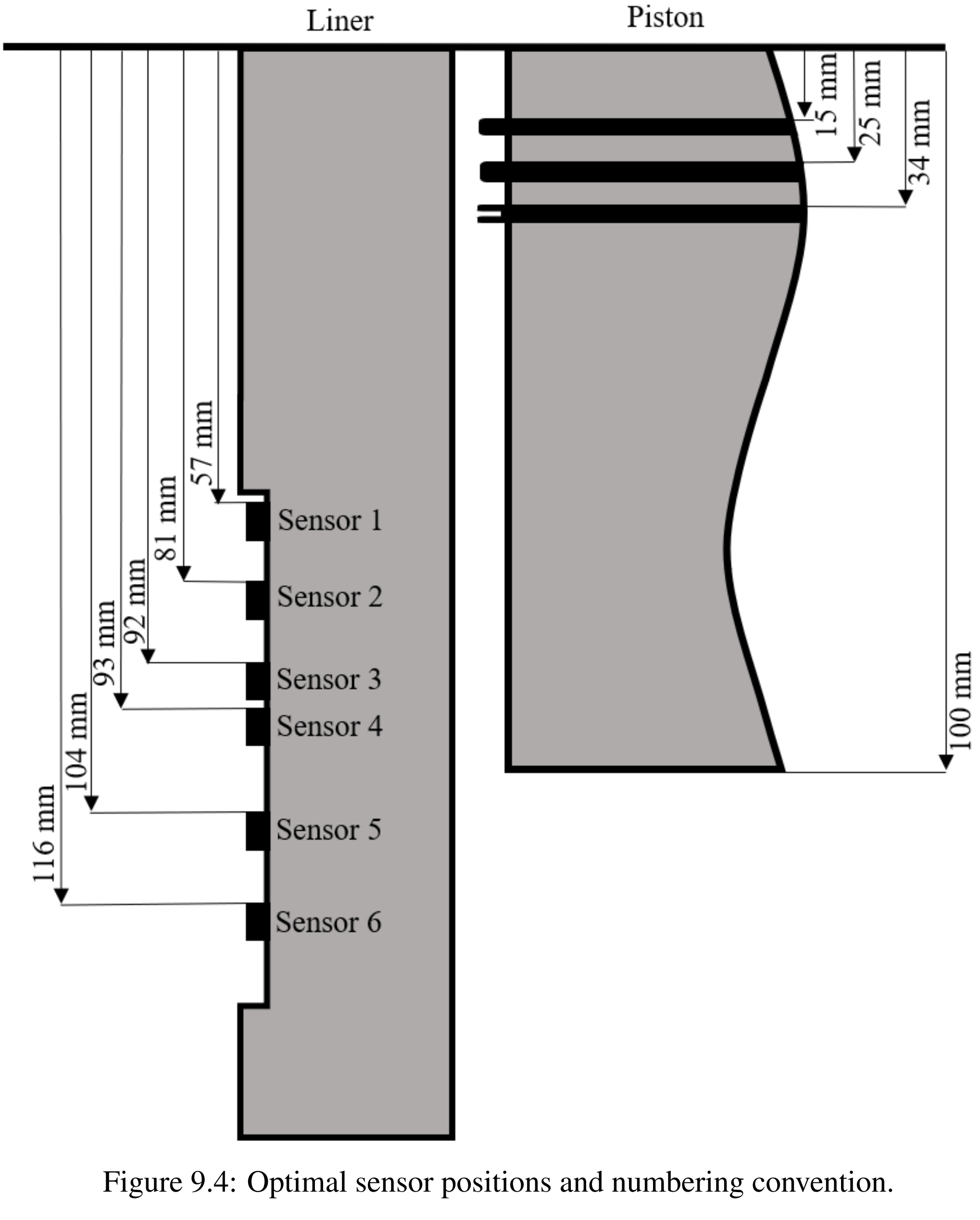

Figure 9.4: Optimal sensor positions and numbering convention.

The same UPR unit as used for the AJ200 and RTX-6 engines was used for the YTRC2110D engine. All recorded parameters (ultrasonic signals, thermocouples, and encoder output) was fed into a in-house produced LabVIEW program to capture the data. A summary of this equipment used is shown in Figure 9.5.

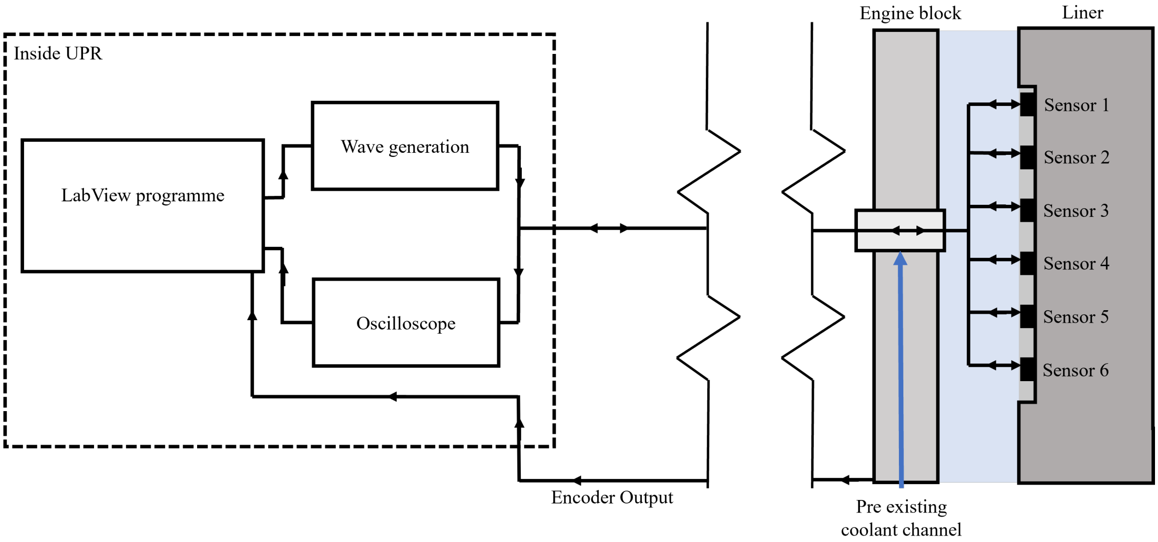

Figure 9.5: Schematic diagram of sensor layout, DAQ, and signal processing equipment.

9.3 Test conditions

The engine was run at a series of loading levels and engine speeds as summarised in Table 9.3. For each engine speed and load combination, the engine was left to reach steady-state operation and then a high-speed data capture was performed lasting 2 seconds on each selected sensor. Steady-state of the engine was defined by a combination of monitoring the thermocouple temperature next to the ultrasonic sensors and from the collaborating partners engine instrumentation. The crankshaft rotational position was captured using a shaft encoder mounted on the end of the crankshaft. In addition to steady-state testing, data were recorded for each start-up and shut-down of the engine with these recordings typically lasting for 10 seconds.

Table 9.3: Test conditions considered on the YTRC2110D engine.

Test type	**Test conditions**	**Units**
Speed variation	1000, 1100, 1300, 1500	rpm
Load variation	0, 343, 765, 1630	Nm
Start-up tests	At each speed/load combination.	
Shut-down tests	At each speed/load combination.	

9.4 Signal processing

The advancements in signal processing developed in Chapter 7 have been applied to this engine such that the peak of the Hilbert envelope was considered instead of a frequency index of the signal in the frequency domain. A typical reflection from the reference and an aligned piston ring is shown in Figure 9.6a with the addition of the Hilbert envelope used for the reflection coefficient. For completeness, the additional steps that are required for the frequency index method are shown in the layer figures in Figure 9.6. This is shown to display the remarkable frequency independence of the oil film thickness in 9.6d indicating the validity of Equation 9.1.

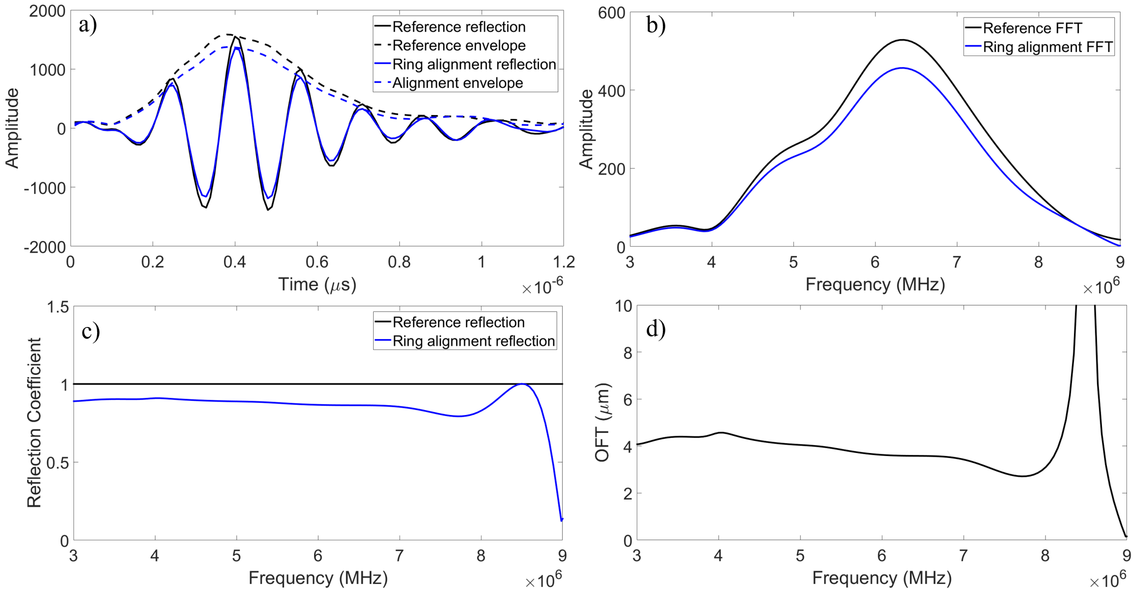

Figure 9.6: (a) Reference and ring aligned reflection; (b) Reference and ring aligned signal in the frequency domain; (c) Reflection coefficient with respect to frequency; (d) Oil film thickness and reflection coefficient with respect to frequency.

$$h = \frac{\rho c^2}{\omega Z_1 Z_2}\sqrt{\frac{|R|^2(Z_2+Z_1)^2-(Z_2-Z_1)^2}{1-|R|^2}} \tag{9.1}$$

Similar to the previous engines, the reference signal was defined when the piston was significantly far from the sensors. This reflection coefficient was input in Equation 9.1 in combination with the speed of sound and density data for the oil to output the oil film thickness between the piston ring and liner.

The engine dynamometer and controller unit provided excessive levels of electrical noise in tests where a load was applied to the engine, an example of which is seen in Figure 9.7. The noise from these components was cyclic with some portions being unaffected by the noise whilst others were rendered unusable. The loaded tests included an additional step of data processing so that only the regions unaffected by excessive noise were used in the data analysis. The unloaded testing providing minor noise levels, like those seen in the 'Normal noise levels' region of Figure 9.7.

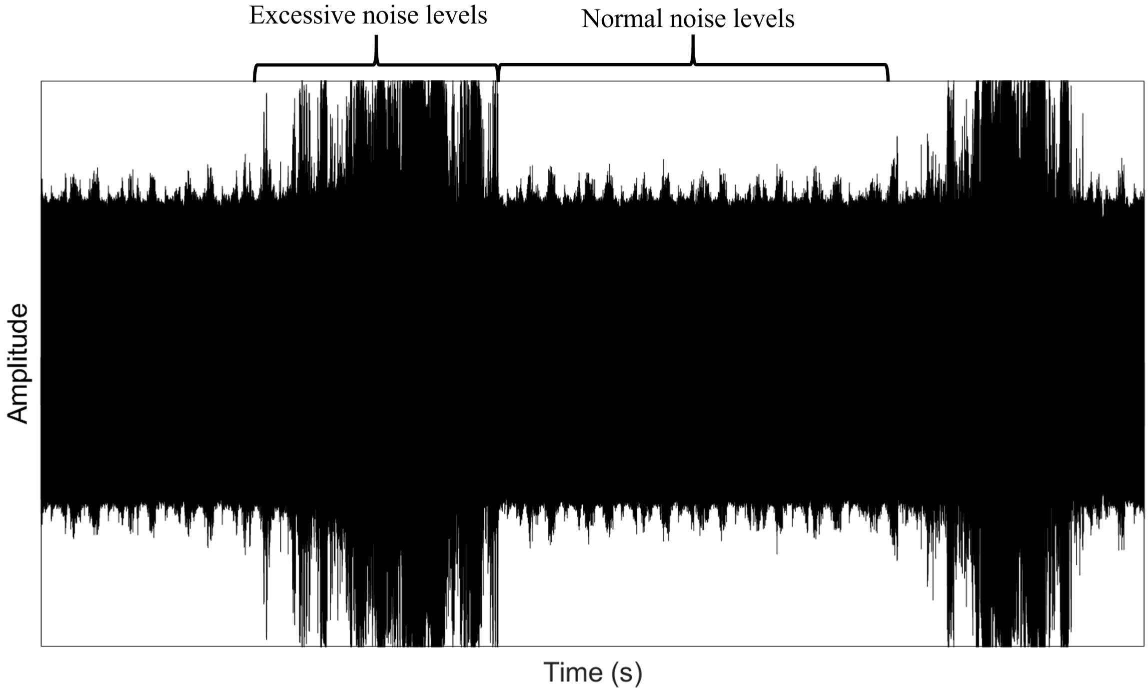

Figure 9.7: Noise from dynamometer during loaded engine captures.

In the data captures, reflected pulses were recorded continuously for 2 seconds, therefore, the four-stroke engine experienced multiple compression and exhaust cycles (0-720° CA) in each capture. Figure 9.8 shows the reflection coefficient over Sensor 1 during part of a compression stroke (270-360° CA) in which the data was averaged from the multiple cycles. The regions where the piston rings and the piston skirt were aligned with a sensor have been highlighted.

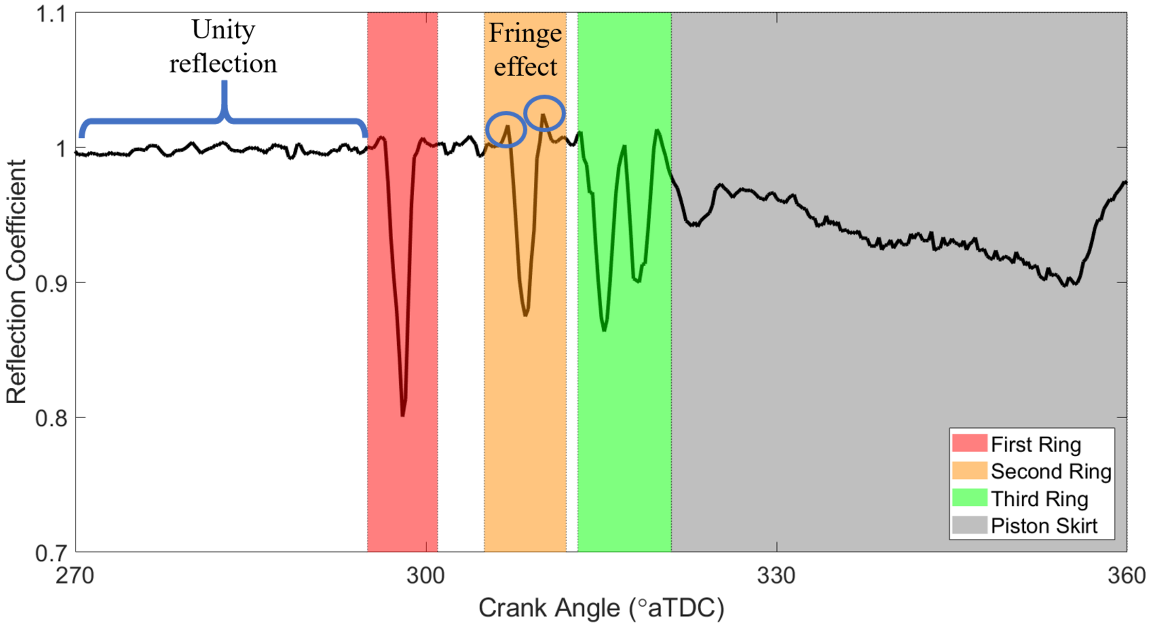

Figure 9.8: Reflection coefficient as the ring pack passes over Sensor 1 during a compression stroke.

Similar to the AJ200 and the RTX-6, when the piston is remote from the sensor, a unity reflection coefficient is maintained (R=1), versus an aligned piston ring reduces the reflection coefficient to 0.8 in some cases. Note that the Hilbert envelope peak is used for this engine, as it was shown in Chapter 7 that this data processing method was not subject to reflections from outside of the alignment zone. The fringe effect for this engine is significantly reduced relative to the previous engines. The RTX-6 fringe effect was typically 1.05 to 1.10 for each piston ring whilst the YTRC2110D the effect is only clearly identifiable for the Second Ring and peaks at 1.02.

The stroke shown in Figure 9.8 is a compression stroke, therefore, the first ring to pass the sensor is the compression ring (First Ring) followed by the scraper ring (Second Ring). Next, the oil control ring (Third Ring) as this ring has two rails each rail passage is detected. Lastly, the skirt of the piston moves over the sensor over an extended CA range leading to a prolonged reduction in the reflection coefficient. This drop in reflection coefficient increases over the course of the stroke suggesting tilting of the piston towards the sensor as it moves up the liner, with a lower value of reflection coefficient indicates a thinner lubricant film so the lower portion of the skirt is in closer proximity to the liner.

The reflection coefficient data was converted into OFT using Equation 9.1. The materials of the ring and liner are steel and cast iron respectively, whilst the piston is made from aluminium. The speed of sound and density are defined in Table 9.2. The resulting oil film thickness variation over the compression stroke of Sensor 1 is shown in Figure 9.9.

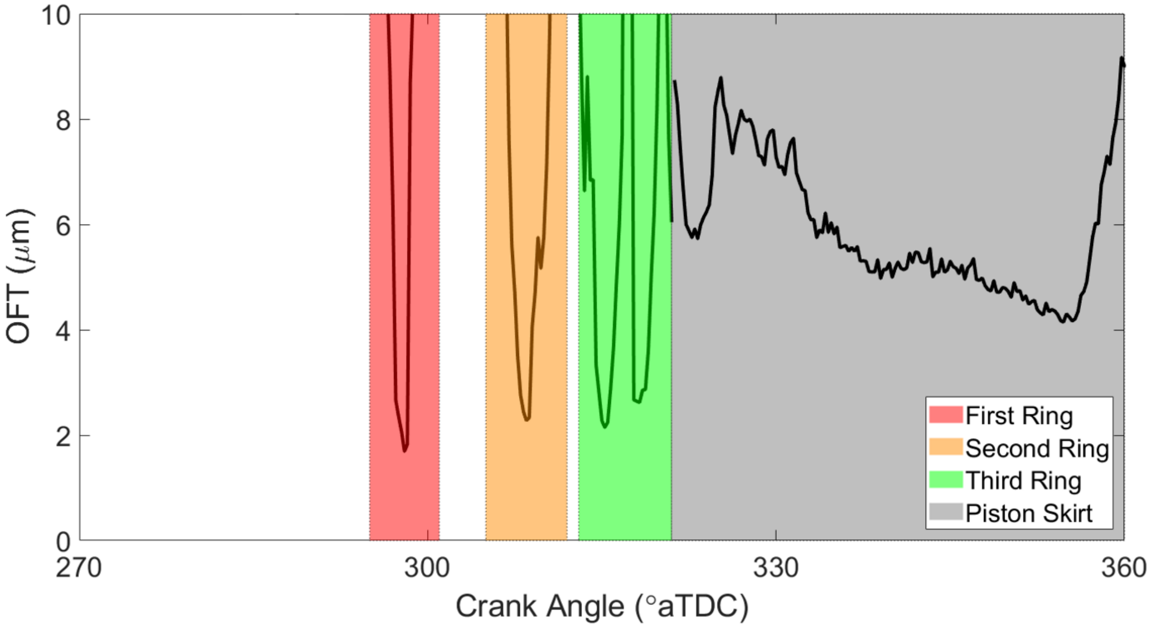

Figure 9.9: Oil film thickness as the ring pack passed over Sensor 1 during a compression stroke.

The oil film thickness of the three rings and piston skirt can clearly be identified for this compression stroke, in Figure 9.9. In this example, the oil film is thinnest for the first compression ring (2 μm) and gets progressively thicker for the scraper ring, oil control ring (2.5 μm) and is thickest for the skirt (4-9 μm). This is the opposite to the peculiar trend of the AJ200, which showed the First ring to have the greatest OFT, although that was thought to be due to the motored operation of the engine. Whereas, in the YTR, the compression ring had the thinnest film as lubricant will not have pooled at the top of the liner and the combustion pressure leads to this ring acting as a buffer between the high and low pressure regions. The ring is expected to be located at the bottom of the ring groove at this point in the stroke, therefore, enabling gases in the combustion chamber behind the ring leading to the ring to conform more to the liner, producing a thinner lubricant film. The thickest film is over the piston skirt and shows a progressive thinning of the film as the piston moves up the liner, this suggests tilting of the piston with the lower edge of the skirt being in closer proximity to the liner. This trend is clear from 330°-350° CA until a sudden increase in the OFT as the piston is nearing its TDC position, suggesting the tilting of the piston may be reversed here.

The anticipated piston ring alignment region for each ring is considerably greater than the OFT measurements indicate. This may be due to the averaging effect of the ultrasonic transducers, as the extremities of these alignment regions cover the instant that a piston ring starts to move over the sensor. In these cases (minor alignment, major misalignment), the averaging effect of ultrasonic sensors will have led to significant over predications of the OFT to the extent that the calculated film is not within the range shown in Figure 9.9. However, the sensors in this work were 0.8 mm or 1.3 mm wide, whilst the piston rings were up to 3.5 mm thick. Therefore, the work will have an improved spatial resolution relative to previous automotive ultrasonic based piston ring work reducing the impact of the averaging effect when the ring and sensor were largely aligned. Although this effect still evidently has an impact on the OFT measurements on the edges of the alignment regions.

Measurements of the reflection coefficient were recorded for all sensors covering the four strokes (0-720° CA) for each of the combinations in the test matrix Table 9.3. Results were processed in the same way to provide oil film thickness.

9.5 Fired testing results

9.5.1 Steady-state operation

The OFT during steady-state operation over each sensor is shown in Figure 9.10 for each stroke of the engine. The regions corresponding to the intake, compression, power, and exhaust strokes are indicated on the plot.

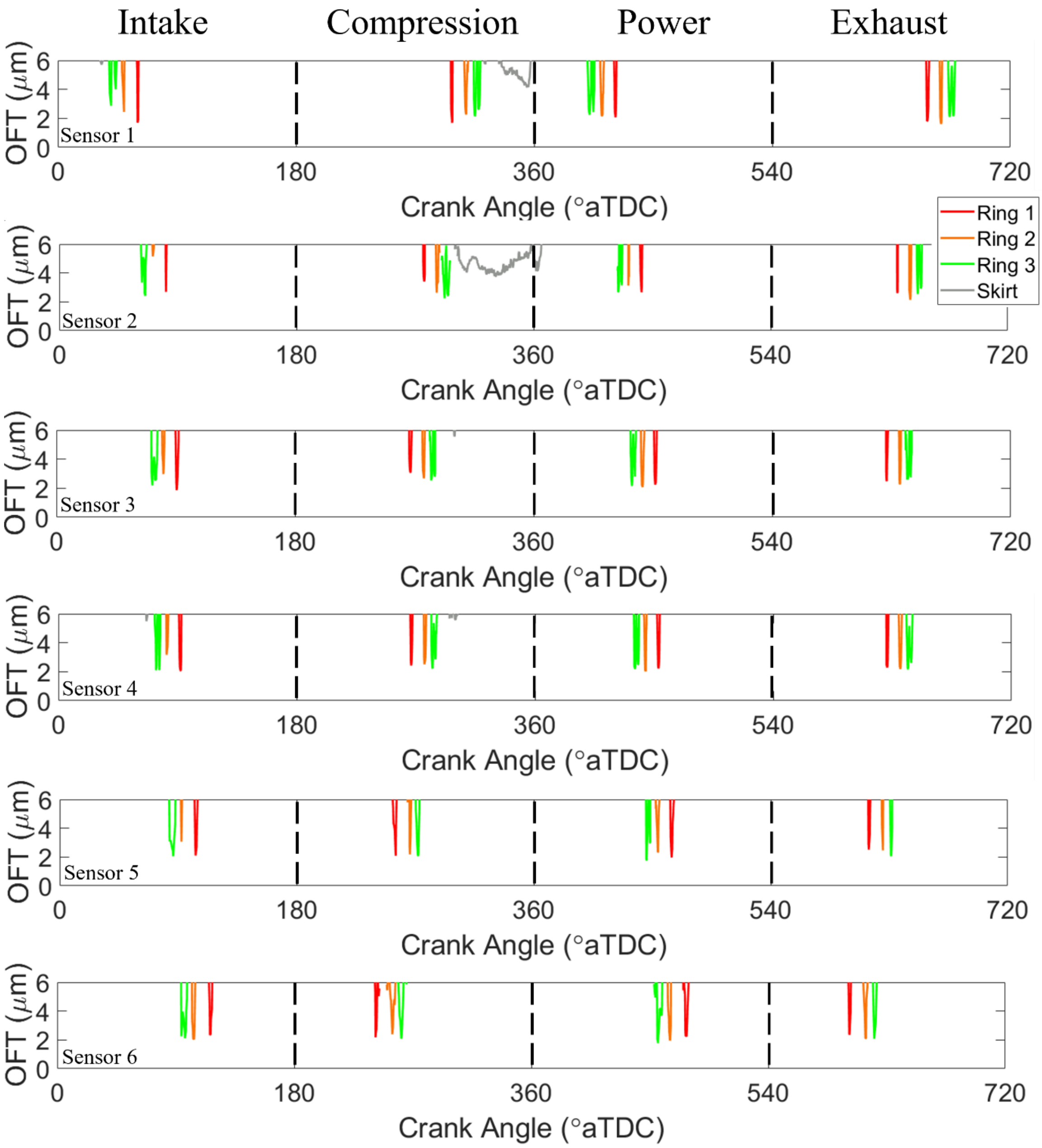

Figure 9.10: Oil film thickness for Sensor 1 (top) to Sensor 6 (bottom) over the four strokes.

In each plot, four sequences of oil film readings can be seen as the ring pack passes over the sensor location for each of the strokes. Sensor 1 is located closest to the TDC, so the CA range between the ring pack passage during the compression and power strokes is the shortest. Whilst for Sensor 6 the CA range between the compression and power strokes is the greatest. Reading the plots from left to right, as the engine rotates also indicates whether the piston is in an up-/down-stroke as in an up-stroke, the first ring to move over the sensing region is the first compression ring, whilst in a down-stroke, it is the oil control ring/piston skirt.

Observation of all sensors indicates the extent to which the cylinder pressure is affecting the first compression ring. For Sensor 1, the sensor closest to the TDC, the first compression ring typically produced a thinner OFT (2 μm ± 0.3 μm) than the oil control ring (3 μm ± 0.4 μm). Whilst for Sensor 6, the sensor closest to the BDC, each piston ring produced a near-identical lubricant film thickness when the pressure in each stroke is relatively negligible (3 μm ± 0.4 μm).

Interestingly, the piston skirt is only measured over a sensor in the compression stroke and for Sensors 1 and 2. This suggests several findings; piston secondary motion is not discernible close to the BDC, as the sensors are on the thrust side any tilting in the early stages of the power stroke is towards the anti-thrust side and during the other up-stroke (exhaust stroke) there is no tilting like that seen during the compression stroke.

9.5.2 Effect of speed on oil film thickness

The MOFT has been extracted by isolating the minimum values each piston ring experienced in each stroke for every engine revolution recorded over the 2 second time interval. These values have been used to define the average MOFT and a standard deviation. The MOFT for the compression ring over each sensor is plotted at each engine speed in the four strokes in Figure 9.11.

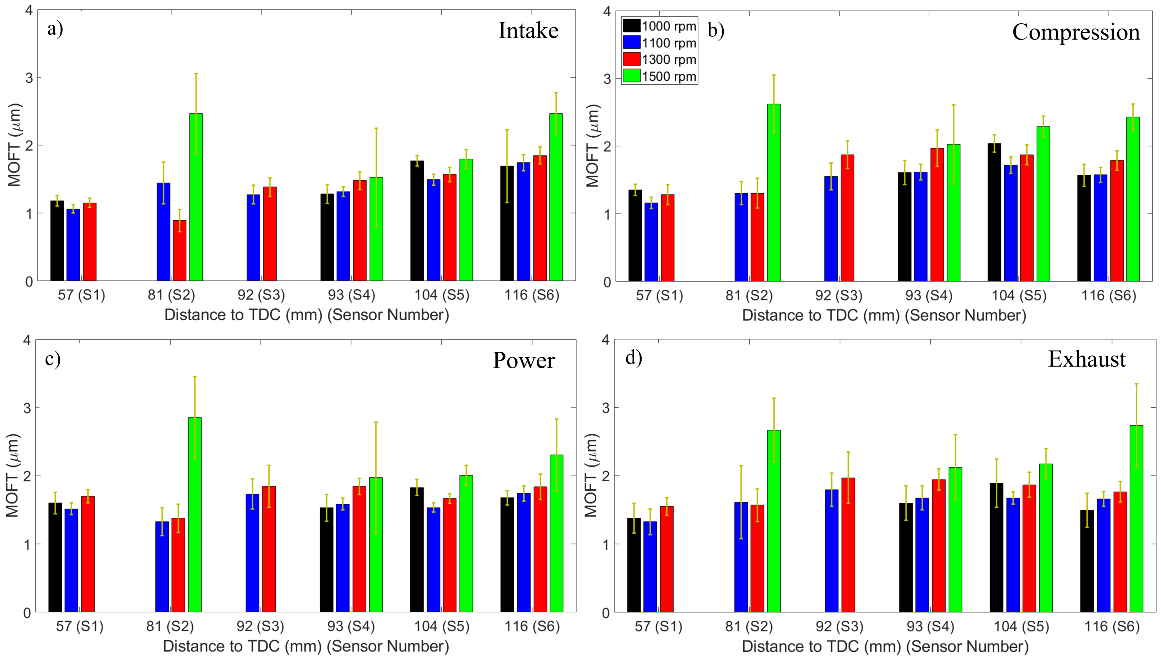

Figure 9.11: Lubricant film thickness for the first compression ring (Ring 1) over multiple strokes. (a) intake, (b) compression, (c) power, (d) exhaust.

The first point to note is that there is not a great deal of difference between the MOFT in either location or with engine speed. Across the first piston ring at all locations, the minimum oil film thickness varies between 1-3 μm with the maximum standard deviation being ± 0.8 μm (at 1000 rpm, 33 engine revolutions were covered in each data capture). The MOFT values provide lambda ratios of up to 1.5, indicating that over the sensors, either boundary or mixed mode lubrication is occurring.

Secondly, there is a general trend for thicker oil films to form at higher engine speeds (1000 rpm: 1 μm $\pm$ 0.3 μm vs 1500 rpm: 2μm $\pm$ 0.5 μm). At higher engine speeds, a greater rate of lubricant entrainment aids to form thicker lubricant films. The standard deviation is generally greatest for the 1500 rpm engine speed, this may be occurring due to the engine having not achieved steady-state operation at this speed, or as 1500 rpm is the maximum speed of the engine this may have led to excessive vibration.

The piston ring oil films are slightly thicker down the engine liner in each engine stroke. Sensor 1 typically had a MOFT of 1 μm whilst for Sensor 6 it was 2 μm. The cylinder pressure will have been a significant contributing factor to this, with the compression ring exposed to greater pressures whilst it is aligned with a transducer further up the liner.

9.5.3 Speed effect for each sensor

A closer inspection of the MOFT for the compression ring over Sensors 4 and 6 is shown in Figure 9.12 to provide a comparison of the MOFT in each stroke at each engine speed.

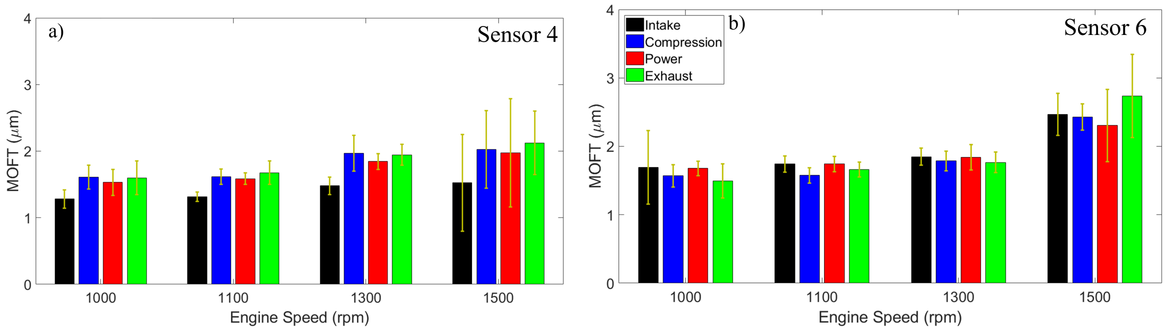

(a) Sensor 4.

(b) Sensor 6.

Figure 9.12: MOFT for the first compression ring (Ring 1) in different engine strokes (a) Sensor 4, (b) Sensor 6.

Figure 9.12 shows the peculiar trend that Sensor 4 consistently led to a marginally thicker lubricant film during the compression and exhaust strokes whilst for Sensor 6, a marginally thicker MOFT is generally present in the intake and power strokes. The compression ring experiences complex motion through each engine stroke and as the sixth sensor is significantly closer to the BDC than Sensor 4 this may have caused the opposing trends as the piston ring motion will have varied by the last sensor. In general an up-stroke at mid-stroke is expected to produce a thicker lubricant film, as during an up-stroke the first ring is the first to pass the sensing region. This may be due to a bow wave of oil or an excessive quantity of lubricant left on the liner. Alternatively, on a downward stroke, the compression ring is the final ring over this sensing area post the oil control ring that will have directed excess oil into the crankcase. These factors indicate the trend like those seen for Sensor 4. Therefore, it is unforeseen why Sensor 6 displays the opposite trends.

This stroke-wise view of the MOFT provides a clearer observation that a greater engine speed leads to a marginally thicker MOFT in each engine stroke with 1500 rpm consistently showing greater engine cycle-to-cycle variation in the lubricant film thickness.

9.5.4 Effect of load on oil film thickness

The engine testing covered a range of engine loading levels at the four rotational speeds, the MOFT for the compression ring in each stroke at each loading level is shown in Figure 9.13.

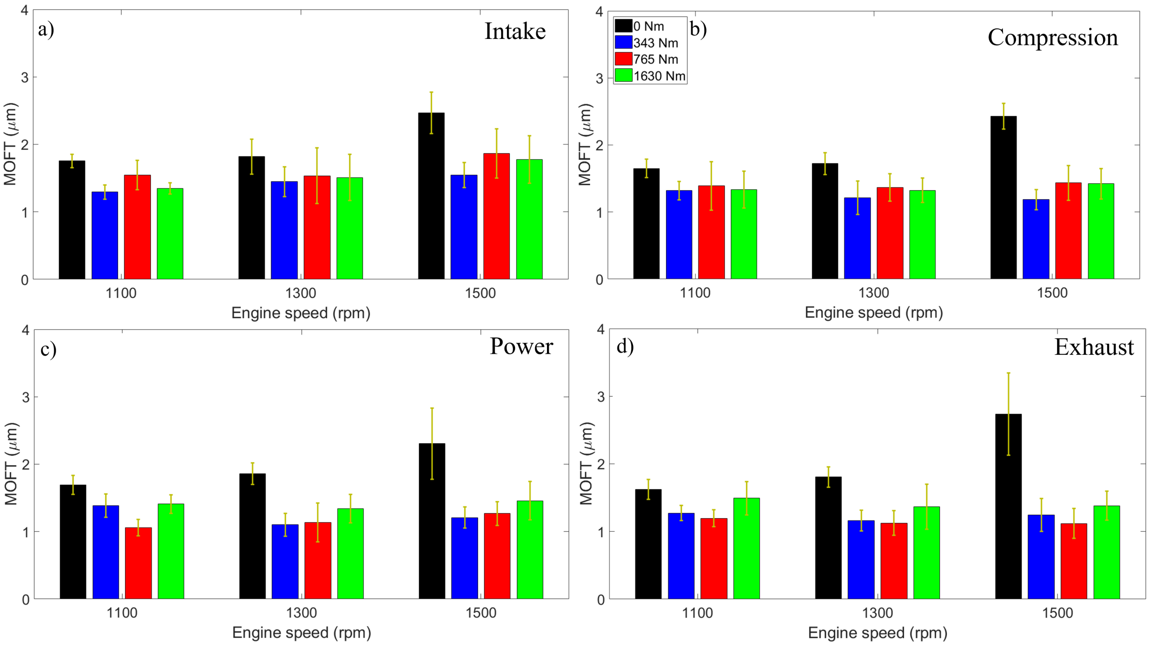

Figure 9.13: MOFT for the first compression ring (Ring 1) in each engine stroke at various engine loading levels over Sensor 6 (a) intake, (b) compression, (c) power, (d) exhaust.

The engine loading comparison in Figure 9.13 shows in each engine stroke zero loading led to a thicker lubricant film (1.75-3 μm), in some cases such as the exhaust stroke at 1500 rpm the MOFT was double the thickness at no loading compared to a loaded value. Whilst the trend in the MOFT as loading continues to increase is less clear for the loaded test cases, with the general trend of full load (1630 Nm) typically having a greater MOFT than that from low load (343 Nm) although the increase is a fraction of a micron (up to 0.4 μm).

A contrast of the MOFT in each stroke at the four loading levels is shown in Figure 9.14 for two engine speeds, 1100 rpm and 1500 rpm.

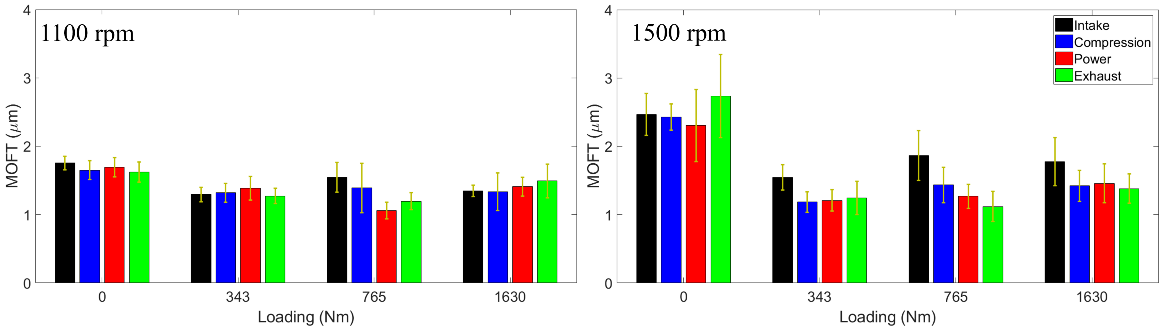

(a) 1100 rpm.

(b) 1500 rpm.

Figure 9.14: MOFT for the first compression (Ring 1) in each engine stroke at various loading levels for Sensor 6 (a) 1100 rpm, (b) 1500 rpm.

It is clear again that the zero loading test cases produced a greater MOFT than at any loading level with the film thickness halving from an increase from 0 Nm to 343 Nm loading at 1500 rpm. Although further increasing of the engine loading has a marginal effect on the MOFT.

The unloaded MOFT in each stroke of Sensor 6, Figure 9.12, showed the down-strokes to have a marginally thicker film, this trend is not maintained at an increased engine loading. For testing at 1100 rpm, no discernible trend is definable between the loading levels, versus at 1500 rpm, during the intake stroke a thicker film was produced with only minor differences between the other strokes.

9.5.5 Film thickness during start-up and shut-down

The engine was shut off between each set of steady-state testing, this enabled start-up and shut-down ultrasonic testing for each speed and load combination. The MOFT was extracted for the compression ring using the same methodology as the previous section. Figure 9.15 shows the MOFT during engine start-up (a) and shut-down (b) for the four different engine strokes with the addition of the engine rotational speed. Note, in the start-up tests the data recording began at time zero and, therefore, there may be a time delay before the first time a piston ring was recorded.

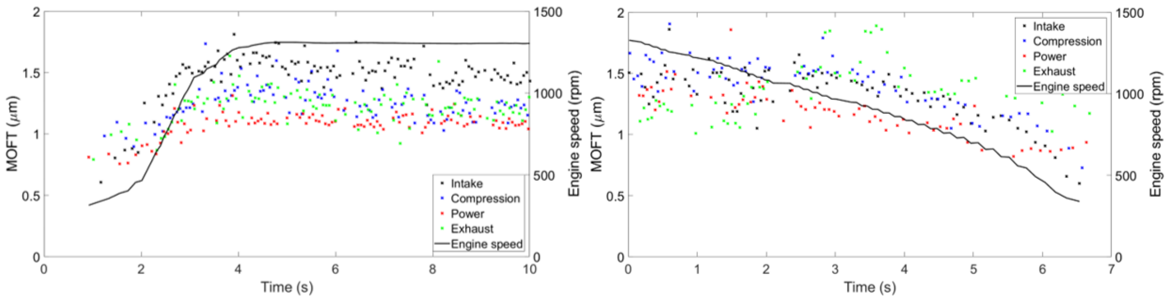

(a) Start-up.

(b) Shut-down.

Figure 9.15: MOFT for the first compression ring (Ring 1) in (a) start-up and (b) shut-down, for Sensor 6 at 1300 rpm and (a) 343 Nm, (b) 765 Nm loading. The four strokes are identified in various colours.

The start-up test case in Figure 9.15 reveals that it took 2 seconds between the first detected ring passage and a consistent MOFT being achieved whilst a consistent engine speed was not achieved for a further 1.5 seconds. A steady build-up of the lubricant film thickness is shown over this period with the four strokes diverging, leading to the intake stroke having the thickest film whilst the thinnest is consistently seen in the power stroke which is similar to the steady-state MOFT for these conditions in Figure 9.13. The absolute minimum MOFT recorded in either the start-up or shut-down was 0.6 μm. This MOFT provides a lambda ratio of 0.3, indicating boundary lubrication is occurring, which increases to 0.7 over the 10-second start-up data recording shown.

The shut-down of the engine over this sensor (Figure 9.15b) produced a less consistent change in the MOFT for the four strokes. Even though each stroke, excluding the exhaust stroke, showed a reduction in the MOFT as the engine shut down. The variation in the MOFT is more pronounced in the start-up of the engine than shut-down, this may be due to only minor levels of oil remaining on the liner before engine start-up, then once the oil pump is engaged a build-up of the MOFT is seen. Whilst for shut-down the oil pump is already engaged with a greater level of oil retained on the liner surface, therefore, the MOFT is less sensitive to engine speed providing a certain threshold of lubricant is maintained as the engine slows.

The MOFT for the compression ring during start-up and shut-down in the power stroke is shown in Figure 9.16 and the intake stroke in Figure 9.17 for a range of engine speeds over Sensor 6.

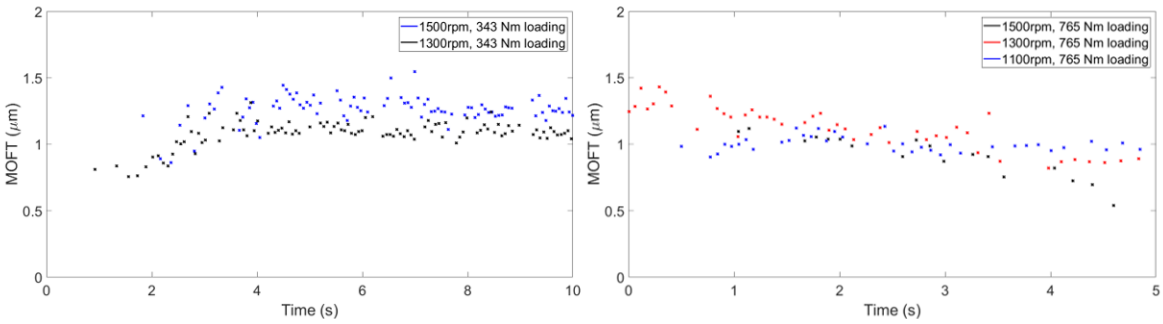

(a) Start-up.

(b) Shut-down.

Figure 9.16: MOFT for the first compression ring (Ring 1) at constant loading for a range of engine speeds during the power stroke. (a) start-up, (b) shut-down.

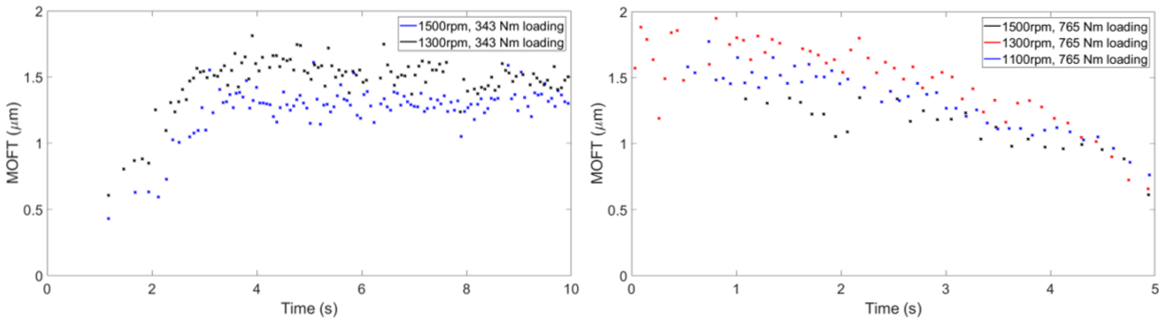

(a) Start-up.

(b) Shut-down.

Figure 9.17: MOFT for the first compression ring (Ring 1) at constant loading for a range of engine speeds during the intake stroke. (a) start-up, (b) shut-down.

The steady-state testing indicated that a greater MOFT was achieved at higher engine speeds in each engine stroke, which is consistent with the engine start-up in Figure 9.16, and somewhat consistent in the shut-down tests in Figure 9.16 and Figure 9.17. However, the opposing trend is observed in the start-up test for the intake stroke in Figure 9.17. Although these increases are all minor was the greatest variation being around 0.75 μm.

The variation in the MOFT is significantly clearer during the intake stroke than the power stroke for both start-up and shut-down with the absolute MOFT in the intake stroke being 0.5 μm ranging up to 2 μm versus 0.75 μm to 1.5 μm in the power stroke. This leads to more defined trends being shown for the intake stroke with a clear build-up and reduction in the lubricant film thickness as the operation of the engine changes. This may be because the combustion pressure causes more piston ring conformity in the power stroke leading to a thinner film. The compression ring is exposed to this for the whole operation of the engine whilst the piston ring has relatively more freedom in the intake stroke to vary with engine operation.

9.6 Additional data processing areas

9.6.1 B-scans

B-scans showing the relative change from the reference for steady-state captures of the YTRC2110D have been produced using the same data processing steps as shown in Section 7.4. A B-scan for Sensor 6 at 1300 rpm is shown in Figure 9.18. The B-scans shown focus on unloaded testing, this is due to the B-scans from loaded test cases presented no additional trends but were hindered by the supplementary noise in the system.

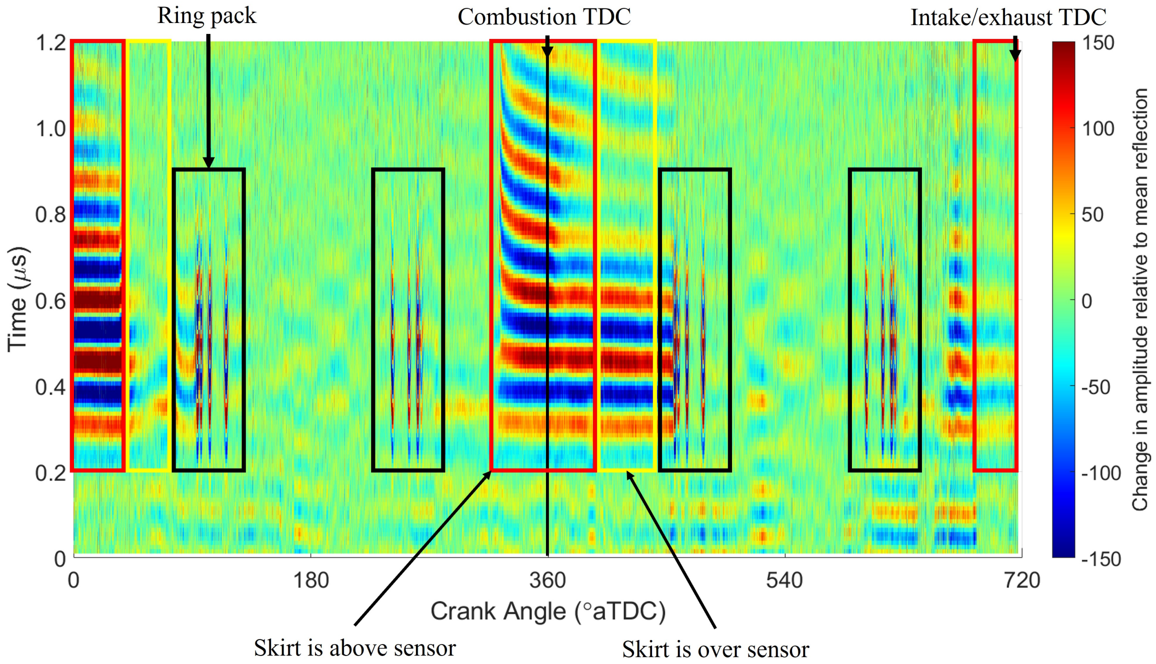

Figure 9.18: B-scan of Sensor 6, unloaded at 1300 rpm having removed the reference reflection.

Upon first inspection, the B-scan for the YTRC2110D is significantly more complex than those previously seen for the RTX-6 (Figure 7.29). This is a combination of the YTRC2110D being a four-stroke engine and the sensor being at a lower relative position down the liner. The ring pack passage in each stroke is highlighted via the black boxes. In addition, there is a large CA range with a prolonged change in the B-scan that occurs close to each TDC (red and yellow boxes, show whether is skirt is over the sensor or not). Whereas when the piston is at the BDC there is no respective B-scan change.

A closer view of the B-scan from the piston rings and the extended pattern close to the combustion TDC is shown in Figure 9.19.

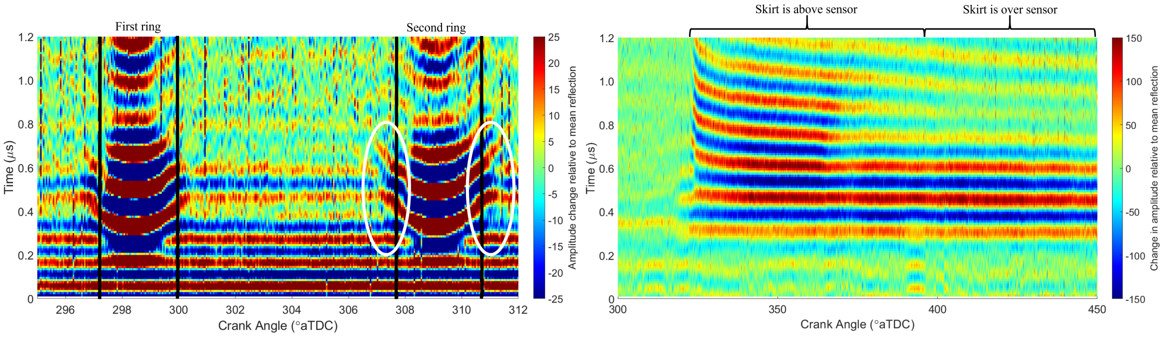

(a) Two piston ring B-scans.

(b) Pattern close to the combustion TDC.

Figure 9.19: Highlighted areas of Figure 9.18.

The two piston rings shown in Figure 9.19a reveal that unlike the RTX-6 (Figure 7.34), the reflections from each piston ring are not impacted by delayed reflections from different piston rings. This, therefore, shows the reflection coefficient for the YTRC2110D is arguably a truer representation of the contact than those that were seen for the sensors on the RTX-6 that covered multiple piston rings. The cause of this is expected to be due to the liner thickness being >100 mm in the RTX-6 whilst in the YTRC2110D the liner is several mm thick. The RTX-6 provided a much greater distance for the ultrasonic waves to spread over, leading to the RTX-6 being able to detect the piston rings at a further distance down the liner from the sensor.

The CA ranges that correspond to the reduction in the reflection coefficient seen in Figure 9.8 are overlayed in Figure 9.19a in black. This shows that the majority of the reflection is seen within the CA range with a relatively minor portion outside of this region, such as in the white ovals. Therefore, the piston ring is only measurement roughly 1° CA before/preceding the piston ring begins to move over the sensor. The minor measurement outside of this window is shown via the minor single peak on either side of the ring passage in Figure 9.8.

The horizontal bands, such as those in Figure 9.19b are partially from when the piston is above the sensor and partially from the piston skirt aligning with the sensor. The pattern starts at 324° CA when the piston moves above the sensor and a minor reduction in the time delay is initially seen. This pattern is likely indicative of an oil film over the sensor in the crankcase as it only occurs when the piston is above the sensor, not below (does not happen when this piston is at the BDC). It also likely indicates that the lubricant film reduces as the CA increases until the skirt moved over the sensor (at 396° CA), the OFT from this is calculated in the following section.

9.6.2 Unloaded spectrograms

The reflection window size was optimised using the route shown in Section 7.2. Unfortunately, the maximum amplitude in the frequency domain did not become frequency independent of the reflection window size, indicating that a greater window size should have been selected for independence. Therefore, the spectrograms for the YTRC2110D should not be considered optimised. To achieve independence a greater window size would have been required which would have limited the ultrasonic pulse rate, reducing the resolution of the ultrasonic data. The lack of independence highlights an additional benefit of the Hilbert envelope as the window size is of less importance when using this method than the frequency index method, providing that the peak of the reflection is recorded, thus enabling a higher pulse rate/resolution of result.

The spectrograms for the YTRC2110D engine, like the B-scans, are more complex than those of the RTX-6 (Figure 6.17), this is due to the sensor location and four-stroke engine operation. A spectrogram for Sensor 6 at 1300 rpm is shown in Figure 9.20. The spectrogram is limited to $0.9 < R < 1.1$ for visualisation purposes.

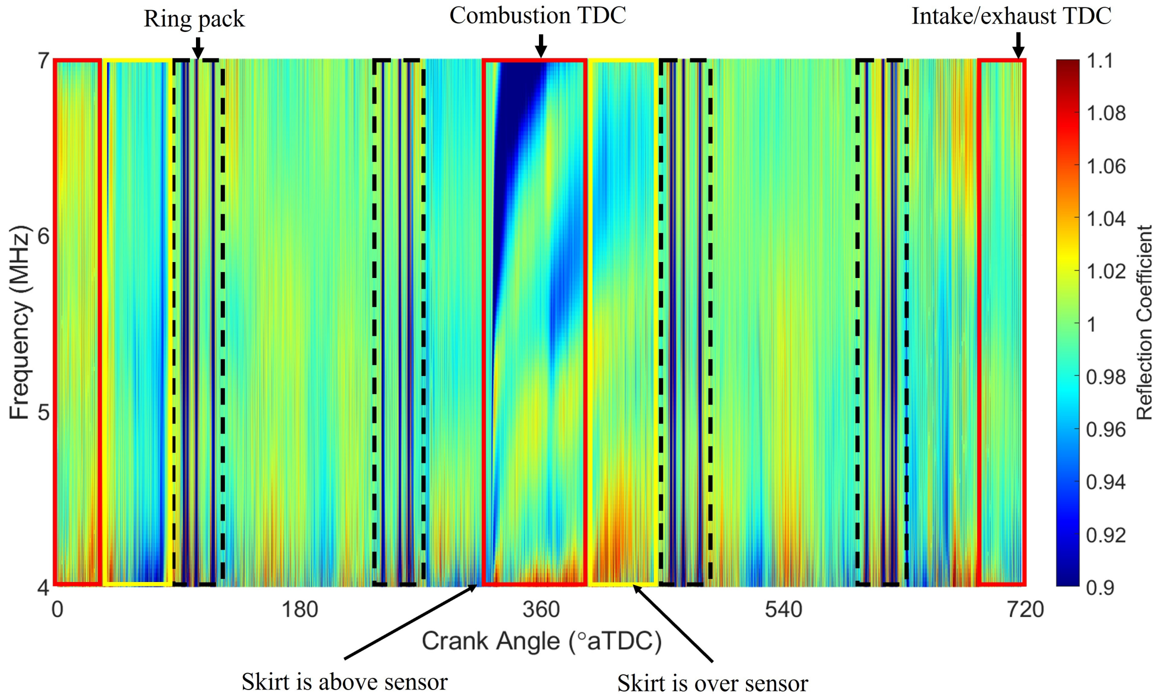

Figure 9.20: Spectrogram for Sensor 6 at 1300 rpm.

Similar to the B-scan, each piston ring pack (black boxes) is visible in the spectrogram with the addition of the pattern close to the combustion TDC (red and yellow box). Interestingly, the pattern is no longer present centred around the intake/exhaust TDC, the cause of which is unknown. The combustion TDC pattern now appears more similar to those from the RTX-6 which were indicative of a 1400 μm residual oil film. The frequency varying resonant dips vary with CA indicating a residual oil film that changes as the crankshaft rotates. A closer inspection of the spectrogram from a ring pack and the pattern covering the combustion TDC from Figure 9.20 are highlighted in Figure 9.21.

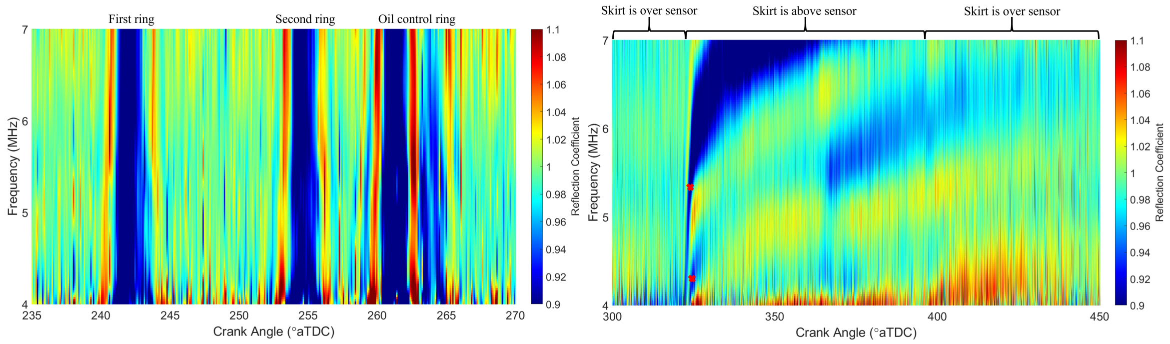

(a) Compression stroke ring pack.

(b) Pattern close to the combustion TDC.

Figure 9.21: Highlighted areas of Figure 9.20.

Figure 9.21a highlights that similar to the B-scans, the spectrogram from each piston ring is unaffected by the other piston rings. Only the two rails of the oil control ring have adjoining patterns, which is not unexpected due to their close proximity. There is minor spreading of the ultrasonic wave as only a single peak of the fringe effect is detected on either side of the ring instead of the multiple cycles like those seen for the RTX-6. This is another factor expected to have been reduced by the reduction in liner thickness relative to the marine engine.

Previously for the marine engine, the extended pattern in the spectrograms was immediately following the first piston ring. Whereas for the YTRC2110D there is no pattern shortly following any piston ring. Whilst a similar pattern begins at 324° CA, immediately following the piston moving completely above the sensor. This shows this factor has not arisen due to piston tilt (the YTRC2110D had nothing aligned and in the RTX-6 the piston is rigidly connected to the piston rod) and further suggests the pattern is a measure of the residual oil film. The size of the engine and location of injectors/lubricant spray dictates when the sensor alignment region becomes exposed to the excess lubricant following a piston ring and, therefore, the resonances in the frequency domain forms at different CAs in the two engines.

The thickness of the residual film can be calculated by the resonant dip technique, see Section 6.3.2. A typical calculation is shown in Equation 9.2 for using the frequency bands at 325° CA, in which the selected frequencies from the resonant bands are marked on Figure 9.21b by the red crosses. The residual OFT at a series of crank angles is shown in Table 9.4.

$$h = \frac{cm}{2\Delta f_m} = \frac{1187}{2(5.4 \times 10^6 - 4.3 \times 10^6)} = 540\ \mu m \tag{9.2}$$

Table 9.4: Residual oil film thickness variation with crank angle.

Crank angle (°)	**Residual OFT (μm)**
325	540
335	310
345	350
355	340
365	290
375	290
385	320
395	340

The unloaded test case shows a thick residual oil film on the liner when it is initially exposed to the crankcase oil that dissipates over time (shown by the diverging nature of the frequency bands). The bands are seen over a large CA range although residual films are calculated up to 395° CA as beyond this the upper band moves out of the usable frequency bandwidth of the transducers, although relatively stable residual OFT measurements are seen for the majority of the range.

9.6.3 Loaded spectrograms

A spectrogram from a 343 Nm loading test case is shown in Figure 9.22. The loaded spectrograms focus on the 343 Nm loading level as some trends in the spectrograms are more pronounced under engine loading however, at higher levels there is a greater impact of system noise on the spectrogram due to the dynamometer producing greater noise levels at higher engine loading.

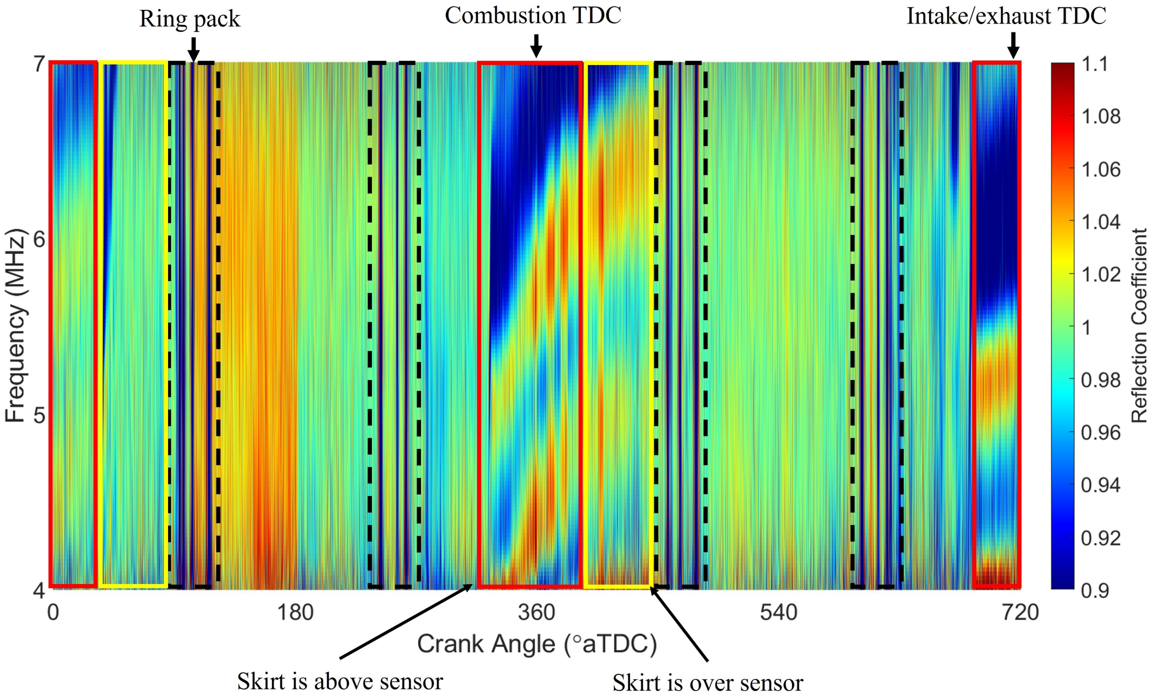

Figure 9.22: Loaded spectrogram Sensor 6 from 1100 rpm 343 Nm loading.

The addition of load on the engine has little impact on the presence of the piston rings (see Figure 9.23a) in the spectrogram as all rings were visible in the unloaded spectrograms. The major difference is seen in the pattern close to the combustion TDC being significantly clearer and the reintroduction of a pattern centred about the intake/exhaust TDC that was only previously seen in the B-scans. Therefore, the residual oil film appears load dependent. The loaded spectrogram from a ring pack and the pattern covering the combustion TDC is shown in Figure 9.23.

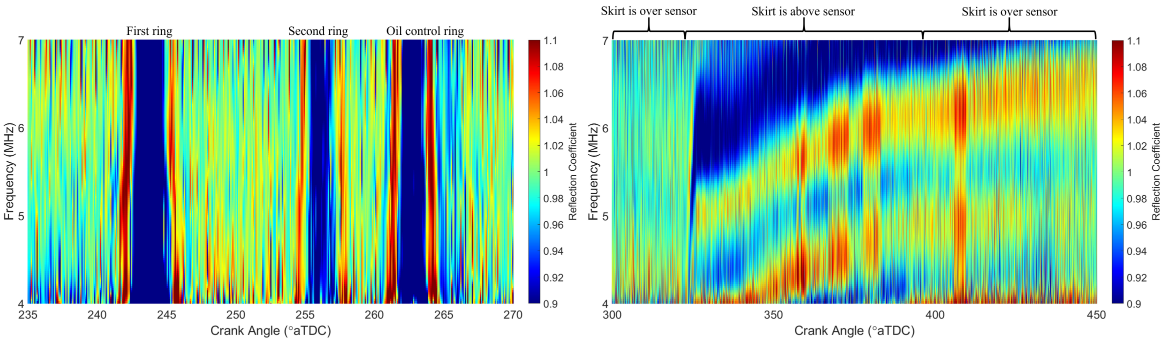

(a) Compression stroke ring pack.

(b) Pattern close to the combustion TDC.

Figure 9.23: Highlighted areas of Figure 9.22.

The true extent of the frequency bands are shown in Figure 9.23b, their respective residual oil film thickness according to the resonant dip method is shown in Table 9.5.

Table 9.5: Residual oil film thickness variation with crank angle from loaded testing at 343 Nm.

Crank angle (°)	**Residual OFT (μm)**
325	440
335	360
345	350
355	360
365	350
375	350
385	340
395	340

Similarly to the unloaded test case, the residual OFT is thicker immediately following the piston moving above the sensor. Following this, the residual OFT is stable over the large CA range even with the frequency bands diverging. The addition of load on the engine leads to a thinner OFT at 325° CA (540 μm unloaded, 440 μm loaded) further indicating that the residual lubricant film may be load-dependent with it decreasing with increased engine load.

9.7 Conclusions

The penultimate chapter has followed the ultrasonic instrumentation and testing upon a fired agricultural engine using the advancements developed in Chapter 7. This has enabled novel measurements such as start-up, shut-down and a more comprehensive study into residual oil levels. The principal findings from this chapter are as follows:

- A series of ultrasonic sensors have been instrumented onto the wet liner of the YTRC2110D at a range of locations down the liner outer surface. The advancements in data processing found on the RTX-6 have been applied to this engine to produce measurements of the oil film thickness.

- The six optimal sensors have shown how the lubricant film thickness changes down the liner surface. The sensors further up the liner were impacted by combustion pressure and experienced piston tilt, whilst all piston rings produce near identical film close to the BDC.

- In each stroke, the MOFT and cyclic variation was found to increase with engine speed. The addition of load on the engine led to a large reduction in the MOFT, although further increases in the load resulted in minor increases in the minimum film thickness.
- The series of start-up tests revealed a 2 second time interval for the build-up of the lubricant film, whilst a further 1.5 seconds was required for a consistent engine speed. The four strokes each began at a similar MOFT value but diverged as the engine speed increased with the power stroke consistently experiencing the thinnest film whilst the thickest was seen in the intake stroke. The shut-down tests provided a less clear decrease in the lubricant film thickness, this is thought to be due to minor levels of oil being retained before engine start-up. Therefore, after the engine is turned on a large build-up of the film thickness is observed, whilst for the shut-down tests, the oil pump is already engaged with lubricant on the liner so a less defined trend is seen.
- The B-scans and spectrograms for the YTRC2110D are significantly more complex than those of the RTX-6 due to the sensors being mid-stroke and the engine being a four-stroke. Both analyses show minor detection of the piston rings outside of the expected region, a large reduction relative to the RTX-6 (leading to a smaller fringe effect). The B-scans and spectrograms both show an extended pattern close to the combustion TDC beginning at 324° CA, immediately following the piston moving above the sensor. Resonant dips in this region indicate a residual oil film in the order of 300-500 μm that is load-dependent, decreasing with an increase in engine loading, that is relatively stable for the remaining CA range while the piston is above the sensor.

Chapter 10

Conclusions

This thesis has presented various routes to quantify the lubricant film thickness between piston rings and the cylinder liner in a range of different sized ICEs. The work has focused on ultrasonic sensors for in-situ oil film thickness measurements and is one of numerous technologies engine manufacturers are using to propel themselves towards meeting emission regulations. In this thesis engines from automotive, marine and agricultural sectors have been considered at a range of engine conditions both in motored and fired operation. This concluding chapter provides a summary of the novelty and main findings of the thesis.

10.1 Aim and objectives review

In the first chapter, the aim and objectives of the thesis were outlined. The overarching aim of the work was to develop a system to quantify piston ring lubricant film thickness in a range of engines, under a range of operating conditions. The aim of the project has been achieved by instrumenting ultrasonic sensors onto three different sized internal combustion engines for motored and fired testing. The testing performed has quantified the film thickness in a broad range of engine conditions with a number of them being quantified for the first time in this work. There were five objectives outlined in the project:

1. Design and production of a motored AJ200 test rig - A test rig has been produced, although due to the impact of the COVID-19 pandemic the research on the AJ200 engine was to a lesser extent than would have been anticipated

2. Refinement of ultrasonic instrumentation capable of withstanding the harsh operational environments close to ICE combustion chambers - The instrumentation technique has been refined to use smaller more robust sensors that have enabled a higher resolution measurement of each piston ring.

3. Instrument ultrasonic transducers on the three engines selected for the project - Three different sized engines have been studied across various engine operating conditions.
4. Refine data processing techniques to improve the oil film thickness calculation - The data processing technique has been refined by applying several novel techniques (Section 10.4).
5. Study the relative similarities and differences in oil film thickness data between the various engines to evaluate the applicability of the technique in each engine - As the RTX-6 is significantly larger than the YTR, the applicability of the ultrasonic technique can be evaluated in different sized engines. In larger engines a higher resolution of measurement can be achieved due to slower engine operation, enabling trends to be identified that are over a narrow CA range. However, the greater liner thickness (and path length of the ultrasonic signal) leads to a greater spreading of the wavefront and, therefore, multiple piston rings may be detected at once. Whilst in the smaller YTR engine, due to the greater engine speed and thinner liner, the opposing trends are seen.

10.2 Measuring lubricant film thickness

A series of techniques have been developed to quantify the lubricant film thickness between piston rings and the cylinder liner in different types of ICEs. Techniques such as; capacitance, laser induced fluorescence, ultrasound and inductance. Each technique is based upon a differing scientific principle but provides relatively similar MOFTs ranging from 0.2 to 20 μm. The key measurement contrast arises from the amount of modification to the engine required to perform the research. Capacitance, inductance and laser induced fluorescence all require replacing the internal surface of the liner with either a sensor or perspex window. This ultimately affects one of the bounding surfaces of the lubricant film and, therefore, may impact the lubricant film formation or thickness. Ultrasound is a favourable technique due to its non-invasive nature as sensors are mounted on the outer surface of the liner enabling the potential of a truer lubricant film thickness measurement.

10.2.1 Ultrasonic lubricant film thickness

Piezoelectric sensors have been used for a range of film thickness measurements in applications, such as; various bearings, cold rolling, piston skirt and piston rings. By studying the amount of an ultrasonic wave reflected relative to a reference reflection and assuming the contact between two surfaces to act like that of a spring within its elastic region, the oil film thickness can be calculated. This can be combined with the acoustic properties of the lubricant and bounding materials to refine the measurement. Previous piston skirt and especially piston ring measurements have been limited by the ultrasonic pulse rates hindering the resolution of the measurements. Through a combination of further developed hardware/software and specifically in the RTX-6 a slower engine operation, a significantly higher resolution of measurement has been achieved.

10.3 Ultrasonic piston ring measurement findings

The project has involved testing three different sized ICEs, each with varying levels of complexity of results produced. The main findings from these engines are summarised as:

- The longitudinal sensors on the RTX-6 showed that a reduction in load/speed led to an increase in the MOFT for all engine configurations and thinner lubricant films were seen closer to the TDC. Within steady-state engine operation, the OFR was varied to three different levels in 5-minute intervals. This produced the unanticipated result, that no variation in the MOFT with OFR was found. Analysis of the engine slowdown captures showed that after the engine load/speed was reduced, often longer than 5 minutes was required before a change was observed in the reflection coefficient. Therefore, it is likely that the 5-minute intervals were not long enough to measure a change in the MOFT with OFR. The application of ultrasonic sensors in the design phase of the RTX-6 enabled the needle-lift type injectors to be identified as consistently producing thicker lubricant films (17% increase relative to the pulse jet injectors) reducing the likelihood of lubricant film breakdown whilst a reduction in engine emissions were seen.

- Previous ultrasonic piston ring analysis was based upon the theory that a piston ring was only detected once it was aligned with the sensor. However, a sensor above the first ring at the TDC has shown a fringe effect, similar to those seen by other sensors. A k-Wave simulation was developed modelling the ultrasonic wave propagation and a likewise trend was observed, displaying that a piston ring was detected outside of the alignment zone. This led to the Hilbert envelope peak being used to define the reflection coefficient as this removed the impact of reflections from an unaligned piston ring. The Hilbert envelope method had a greater deviation from the frequency index approach in the RTX-6 than in the YTR engine, this is expected to be the case due to the significantly greater liner thickness in the RTX-6 providing a greater ultrasonic path length for the wavefront to spread over.

- Spectrograms have shown horizontal diverging resonant bands in the reflection coefficient. At 100% loading in the RTX-6, these bands are indicative of a 1400 μm residual oil film that is reduced at lower engine loading levels. Whereas in the YTR, the thinner liner led to a clearer identification of the resonant bands and calculated residual films that were in the order of 300-500 μm. These residual films were first seen at 324° CA, when the piston skirt moved above the sensor.
- The shear sensors have been shown to measure the lubricant film breakdown over the first piston ring at its TDC position in the RTX-6. A trend that was defined clearer by the Hilbert envelope method. The needle-lift type injectors were shown to reduce the amount of metal-metal contact occurring and it was further reduced by a reduction in engine loading. An increase in the OFR was also found to result in a marginal reduction in metal-metal contact. This indicates that shear sensors may provide a more sensitive measure of the amount of lubricant in the piston ring-liner contact. Engine slow-down and shut-down tests for the shear sensors have visualised the ability of shear sensors to show a real-time measure of metal-metal contact with a reduction in load leading to less piston ring-liner contact. Whereas, when the engine was shutting down an increase in metal-metal contact was seen as the lubricant injection system stopped injecting lubricant.
- The YTR engine showed the MOFT and cyclic variation to increase with engine speed in each stroke of the engine. Furthermore, once the engine was subject to a load, there was a significant reduction in the MOFT. Although further increases in loading resulted in minor increases in the minimum film thickness.
- The YTR engine was shut down after each set of testing parameters, therefore, a series of start-up and shut-down combinations were studied in each of the four strokes. In the case of start-up tests, a 2-second time interval was seen for the lubricant film to build up to a consistent level. Whilst a further 1.5 seconds was required for a consistent engine speed. Each stroke initially provided a similar MOFT but diverged as the engine speed increased, this led to the intake stroke having the thickest film whilst the thinnest was in the power stroke. A less clear trend was seen in the shut-down tests with each stroke showing a minor reduction in film thickness. This is thought to be the case as when the engine was initially turned on, minor levels of oil will have been retained on the liner and the increase in engine speed resulted in a greater quantity of lubricant being delivered to the piston ring zone. Whereas, during the shut-down of the engine the oil pump was already engaged with more oil on the liner, leading to these MOFT measurements being less sensitive to the reduction in engine speed.

10.3.1 Engine comparison

The three ICEs considered in this project each differ in size and complexity of the ultrasonic instrumentation. A summary of the absolute MOFT for each engine is presented in Figure 10.1. The figure uses the MOFT from the first piston ring as it passed each ultrasonic sensor used at each loading level.

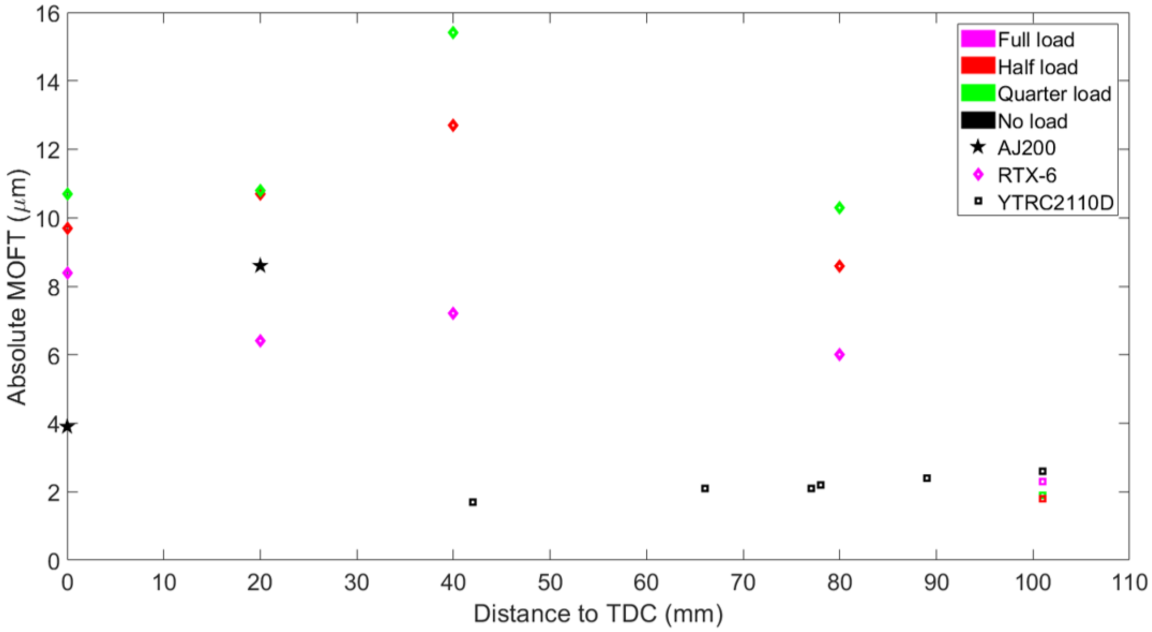

Figure 10.1: A summary of the absolute MOFT from each studied ICE. The figure considers the first piston ring as it passed each sensor. The engine conditions covered are; the AJ200 at 800 rpm, the RTX-6 for Configuration 1 and the YTRC2110D at 1100 rpm. The distances to the TDC are presented in mm for each specific engine, as each engine has a different stroke length, a vertical comparison of the MOFT is not representative.

Figure 10.1 visualises the relative film thickness values from each engine. The AJ200 and YTRC2110D are similar sizes and tested at similar engine speeds. However, the fired YTRC2110D at all conditions produced a thinner MOFT than the AJ200. This was achieved whilst the sensors were at a lower respective position in the YTR engine. This is expected to be due to the motored operation of the AJ200, therefore, a lack of combustion led to significantly thicker films in the AJ200. The thickest films are seen by the RTX-6, the diesel marine engine has a similar peak combustion pressure to the smaller engines. However, the greater lubricant injection rate and power of the engine lead to thicker lubricant films seen at all loading levels.

The B-scans and spectrograms from the RTX-6 and YTRC2110D have shown the thinner liner of the YTRC2110D to reduce the impact of adjacent piston rings on both data processing methods. This led to each piston ring being differentiable in the YTRC2110D and a smaller CA range in which delayed partial reflections were seen. This was seen whilst the B-scans and spectrograms were more complex due to the four strokes of the YTRC2110D engine.

10.4 Thesis novelty

In previous piston ring oil film thickness research from an ultrasonic perspective, the reflection coefficient has been defined by indexing the reflection in the frequency domain at either the sensor central frequency or maximum amplitude of the reflection and comparing it to a reference signal (frequency index method). This has been applied to the motored AJ200 engine block in Chapter 5 and RTX-6 in Chapter 6 producing OFT measurements in the expected order of magnitude and producing similar trends to those from previous works. However, a series of novel data processing routes beyond those of indexing the frequency domain view of the signal have been considered:

- The frequency index method has been refined by optimising the reflection window to improve the definition of the start- and end-point of the reflection. The refinement reduced the reflection window to the point at which a significant impact on the reflection in the frequency domain is seen. This removes a portion of reflected energy that is not from the piston ring. This method has shown minor improvements in the OFT calculated with the clearest changes seen for the spectrograms by the ’smoothening’ of trends.

- By observing the reflection coefficient over the whole bandwidth of the sensor a spectrogram can be produced. The spectrograms have shown the reflection coefficient to decrease due to ring alignment over the complete bandwidth, indicating a range of frequencies may be suitable for OFT measurements. The spectrograms also revealed extended diverging horizontal bands in the frequency domain, indicative of a residual oil film that reduces over time.

- Analysis of stacking the time domain reflections (B-scan) highlighted a pattern in the trailing portion of the reflection. The pattern was found to align with the fringe effects seen in the frequency index reflection coefficient results. In addition, the trend was found to begin when the piston ring was significantly far from the sensor and the time delay reduced as the piston ring approached the sensor. This further indicates the pattern is a measure of the piston ring before it was aligned with the ultrasonic sensor. The time delay of the pattern was reduced by a reduction in engine loading, as at lower loading levels the speed of sound is greater leading to a reduction in the time-of-flight of the ultrasonic reflections. The pattern was present until 95% alignment between sensor and piston ring, indicating the frequency index method is subject to reflections from outside the alignment zone when a sensor is partially aligned, except for a small CA range of near complete alignment.

- The reflection coefficient from the Hilbert envelope peak has also been evaluated, this method considers the peak of the reflection envelope in the time domain. Therefore, it is not subject to the reflections from outside the piston ring alignment zone that is seen in the frequency index method and the B-scans. This data processing method reduced the impact of the fringe effects, the 'W' double-dip, the peak between rings and the prolonged change in reflection coefficient before/after the rings. The Hilbert envelope method was found to reveal trends that were hidden in the frequency index method for both longitudinal and shear sensors, such as piston ring-liner metal-metal contact at various loading levels. The removal of reflections from an unaligned piston ring led to the method typically producing MOFT values 20% thicker than those from the frequency index.

- Experimental ultrasonic piston ring trends have been evaluated against modelling of ultrasonic wave propagation through k-Wave, an open-source toolbox in MATLAB. The modelling of wave propagation has revealed the driving factor behind trends that were observed in the experimental reflection coefficients.

- Ultrasonic sensors have been used outside of the operational phase of an engine for the first time. In the RTX-6, the sensors were used as a design tool to evaluate different lubricant injector designs showing the usefulness of these sensors in the design phase. The piezoelectric sensors showed that a novel lubricant injector design successfully increased the lubricant film thickness, improving the lubrication regime of the piston rings. This was achieved whilst less lubricant was lost to the exhaust manifold and, therefore, a reduction in engine emissions.

- Several novel measurements have been performed using the piezoelectric sensors. The lubricant film thickness has been quantified during previously unexplored operational phases: start-up, shut-down, varying oil feed rates and a measure of residual oil levels on the liner when the piston was above the sensing region. Shear sensors have also been used for the detection of metal-metal contact between the piston ring and liner.

10.5 Future work

This thesis has demonstrated the ability of ultrasonic sensors to monitor the lubricant film between piston rings and the cylinder liner. In addition to being able to provide a quantitative evaluation of the film thickness in different stages of engine operation or different system designs. This has been achieved with minimal modification to the engine highlighting the benefits of this sensing approach. The advancements made have shown several areas for further research that may enhance the findings of this work.

- The piston ring to sensor width ratio has been improved in this work with sensors either being the same width or thinner than the piston rings, increasing the spatial resolution. The B-scans on the RTX-6 highlighted even with this improved ratio only a small portion of the piston ring alignment zone was unaffected by delayed reflections (-3° to 3° CA instead of -8.5° to 8.5° CA). Although this flaw was overcome by using the Hilbert envelope method, further improvements in this ratio would lessen the impact of delayed reflections on the B-scans/spectrograms, this could be combined with a greater complexity in the ultrasonic sensor array increasing the number of sensors. This would lead to a greater representation of how the lubricant film develops/breakdowns as the piston rings approach the TDC. A greater number of sensors may lead to difficulties in maintaining a sufficiently high pulse rate for a high resolution of reflections captured. Therefore, a sequencing table to set the order in which sensors are studied may be required. The continuation of using the Hilbert envelope to define the reflection coefficient may provide a route to maintain high pulse rates. This is because only the peak of the envelope is required for this data processing, therefore, a smaller capture range of the reflection could be used.

- The spectrograms for both the RTX-6 and YTRC2110D have shown resonant bands in the reflection coefficient indicative of a residual oil film on the cylinder liner. A more in-depth study into expected residual films on the liner in ICEs is required as the results presented in this work are orders of magnitudes greater than the piston ring film thickness (partially expected due to the rings themselves limiting the achievable thickness of the lubricant film). However, little current research exists to quantify the amount of oil on the liner outside of piston ring alignment in fired engines.

- The shear sensors on the RTX-6 have shown the lubricant film to break down close to the TDC of the piston. This indicates that the OFT values calculated from the Spring Model in this region are not applicable, due to the condition of a fully formed lubricant film not being met. Therefore, a mixed-mode modification to the calculated

OFT is required to provide a closer measure of the oil film thickness in the pockets of the lubricant film.

- The presented work, and the majority of the historical ultrasonic piston ring research have instrumented sensors on the cylinder liner side. This provides a measure of the lubricant film at discrete points as a piston ring/skirt moves over the sensing region. Research has focused on this side, predominately as less modification to the engine is required. However, the instrumentation of ultrasonic sensors onto the piston side, ideally behind the piston rings, would provide OFT measurements over the whole stroke of the piston. This would provide a significant increase to the quality of results captured as the complete build-up/breakdown of the lubricant film could be quantified.

Appendix A

Associated publications

J. Rooke, X. Li, H. Brunskill, M. Stark, and R. Dwyer-Joyce, "Comparison of Ring-Liner Oil Film Thickness Resulting from Different Injector Designs in a Diesel Marine Engine Using an Ultrasound Measurement Method," SAE Int. J. Engines, vol. 14, no. 6, 2021, doi:10.4271/03-14-06-0053.

J. Rooke, X. Li, and R. Dwyer-Joyce, "Applying the Hilbert Envelope Method to Refine the Ultrasonic Technique for Piston Ring Oil Film Thickness Measurements in a Marine Diesel Engine," SAE Int. J. Engines, vol. 16, no. 2, 2022, doi:10.4271/03-16-02-0011.

J. Rooke, H. Brunskill, X. Li, S. Taghizadeh, A. Hunter, S. He, X. Lu, and R. S. Dwyer-Joyce, "Piston Ring Oil Film Thickness Measurements in a Four-Stroke Diesel Engine during Steady-State, Start-up and Shut-Down." International Journal of Engine Research, 2022. doi:10.1177/14680874221088547.

Appendix B

Density relation derivation

The following section covers the derivation of the density relation seen in Section 6.1.3. The derivation is reproduced from [88].

The bulk modulus of a liquid can be described by the Equation B.1.

$$B = \rho \frac{dp}{d\rho} = \rho c^2 \tag{B.1}$$

When equating the two definitions (Equation B.2) the density term cancels out.

$$\rho \frac{dp}{d\rho} = \rho c^2 \tag{B.2}$$

Both sides of the equation can be integrated:

$$\int 1 \, d\rho = \int \frac{1}{c^2} dp \tag{B.3}$$

In Equation 6.3 the speed of sound under constant pressure was expressed as:

$$c(T = 20, p) = 4.13 \times 10^{-6} p + 1.49 \times 10^{3} \tag{B.4}$$

Substituting Equation B.4 into Equation B.3 gives:

$$\rho(T = 20, p) = \int \frac{1}{(4.13 \times 10^{-6} p + 1.49 \times 10^{3})^2} dP \tag{B.5}$$

$$\rho(T = 20, p) = \frac{-5.88 \times 10^{10}}{p + 3.61 \times 10^{8}} + A \tag{B.6}$$

The constant A can be found be substituting a known value of density for a specific temperature and pressure. At a temperature of 20°C and a pressure of 0 MPa the density is 888 kg/m^3. This shows constant A to be 1050.84.

$$A = \rho(T = 20, p = 0) + \frac{5.88 \times 10^{10}}{p + 3.61 \times 10^{8}} \tag{B.7}$$

$$A = 888 + \frac{5.88 \times 10^{10}}{0 + 3.61 \times 10^{8}} \tag{B.8}$$

$$A = 1050.84 \tag{B.9}$$

Therefore, Equation B.6 becomes:

$$\rho(T = 20, p) = \frac{5.88 \times 10^{10}}{p + 3.61 \times 10^{8}} + 1050.84 \tag{B.10}$$

The relationship between temperature and density is defined in Equation B.11. The values of β and ρ_0 are defined in Equations B.12 and B.13 respectively.

$$\rho_1 = \frac{\rho_0}{1 + \beta(T_1 - T_2)} \tag{B.11}$$

$$\beta = \frac{0.0007m^{\circ}}{m^3} C \tag{B.12}$$

$$\rho_0 = \frac{888kg}{m^3}\ at\ 20^{circ}C,\ 0\ MPa \tag{B.13}$$

Inputting β and ρ_0 into Equation B.11 gives:

$$\rho(T,\ p = 0) = \frac{888}{1 + 0.0007(T - 20)} \tag{B.14}$$

Combining Equation B.10 and B.14 provides:

$$\rho(T,p) = a + \frac{888}{1 + 0.0007(T - 20)} - \frac{5.88 \times 10^{10}}{p + 3.61 \times 10^{8}} \tag{B.15}$$

The constant a can be found be substituting a known value of density for a specific temperature and pressure. This shows constant a to be 162.85.

$$\rho(T = 20,\ p = 0) = a + \frac{888}{1 + 0.0007(T - 20)} - \frac{5.88 \times 10^{10}}{p + 3.61 \times 10^{8}} = 888 \tag{B.16}$$

$$a = \frac{5.88 \times 10^{10}}{p + 3.61 \times 10^{8}} \tag{B.17}$$

$$a = 162.85 \tag{B.18}$$

Substituting *a* into Equation B.15 gives the density relation accounting for temperature and pressure:

$$\rho(T,\, p) \;=\; 162.85 + \frac{888}{1\,+\,0.0007(T-20)} \;-\; \frac{5.88\times 10^{10}}{p\,+\,3.61\times 10^{8}} \tag{B.19}$$

Bibliography

[1] S. C. Tung and M. L. McMillan, “Automotive Tribology Overview of Current Advances and Challenges for the Future,” *Tribology International*, vol. 37, no. 7, pp. 517–536, 2004.

[2] D. E. Richardson, “Review of Power Cylinder Friction for Diesel Engines,” *Journal of Engineering for Gas Turbines and Power*, vol. 122, no. 4, pp. 506–519, oct 2000. [Online]. Available: http://link.aip.org/link/?JETPEZ/122/506/1 https://asmedigitalcollection.asme.org/gasturbinespower/article/122/4/506/463320/Review-of-Power-Cylinder-Friction-for-Diesel

[3] P. Nagar and S. Miers, “Friction between Piston and Cylinder of an IC Engine: a Review,” *SAE Technical Paper 2011-01-14*, 2011. [Online]. Available: http://papers.sae.org/2011-01-1405/

[4] The Society of Motor Manufacturers and Traders (SMMT), “SMMT Motor Industry Facts 2018,” Tech. Rep., 2018. [Online]. Available: http://www.smmt.co.uk/2012/03/motor-industry-facts-2012/

[5] Jaguar Land Rover, “Power Up: Advanced and Efficient New 300PS Petrol Engine for XE, XF and F-Pace Models,” pp. https://media.jaguar.com/news/2017/06/power–advanc, 2017. [Online]. Available: https://media.jaguar.com/news/2017/06/power-advanced-and-efficient-new-300ps-petrol-engine-xe-xf-and-f-pace-models

[6] J. Rooke, X. Li, H. Brunskill, M. Stark, and R. Dwyer-Joyce, “Comparison of Ring-Liner Oil Film Thickness Resulting from Different Injector Designs in a Diesel Marine Engine Using an Ultrasound Measurement Method,” *SAE International Journal of Engines*, vol. 14, no. 6, pp. 885–908, 2021.

[7] D. Sandoval and J. B. Heywood, “An Improved Friction Model for Spark-Ignition Engines,” *SAE Technical Paper 2003-01-07*, 2003. [Online]. Available: http://papers.sae.org/2003-01-0725/

[8] R. A. Mufti and M. Priest, “Effect of Engine Operating Conditions and Lubricant Rheology on the Distribution of Losses in an Internal Combustion Engine,” *Journal of Tribology*, vol. 131, no. 4, 2009.

[9] J. A. McGeehan, “Literature Review of the Effects of Piston Ring Friction and Lubricating Oil Viscosity on Fuel Economy,” *SAE Technical Paper 780673*, vol. 780673, 1978.

[10] C. Sethu, M. Leustek, and S. Bohac, “An Investigation in Measuring Crank Angle Resolved In-Cylinder Engine Friction Using Instantaneous IMEP Method,” *SAE Technical Paper 2007-01-39*, 2007. [Online]. Available: http://papers.sae.org/2007-01-3989

[11] J. Beulshausen, S. Pischinger, and M. Nijs, “Drivetrain Energy Distribution and Losses from Fuel to Wheel,” *SAE International Journal of Passenger Cars - Mechanical Systems*, vol. 6, no. 3, pp. 1528–1537, 2013.

[12] RAC Foundation, “UK Petrol and Diesel Consumption,” 2021. [Online]. Available: https://www.racfoundation.org/data/volume-petrol-diesel-consumed-uk-over-time-by-year

[13] European Commission, “Setting CO2 emission performance Standards for new Passenger Cars and for Light Duty Vehicles,” 2021. [Online]. Available: https://ec.europa.eu/clima/policies/transport/vehicles/regulation_en

[14] Department for Transport UK Government, “CO2 Emission Performance Standards for New Passenger Cars and Light Commercial Vehicles,” 2020. [Online]. Available: https://www.gov.uk/government/consultations/regulating-co2-emission-standards-for-new-cars-and-vans-after-transition/co2-emission-performance-standards-for-new-passenger-cars-and-light-commercial-vehicles#mainchanges

[15] K. Froelund and B. Smith, “Lubricating Oil Consumption Measurements on an EMD 16-645 Locomotive Diesel Engine,” *Springer Technical Conference of ASME Internal Combustion Engine Division*, pp. 361–368, 2003.

[16] K. Froelund and E. Yilmaz, “Impact of Engine Oil Consumption on Particulate Emissions,” in *ICAT International Conference on Automotive Technology*, Istanbul , Turkey, 2004.

[17] Government of the United Kingdom, "Vehicle tax rates," 2021. [Online]. Available: https://www.gov.uk/vehicle-tax-rate-tables

[18] International Maritime Organization, "Resolution MEPC.304(72) - Initial IMO Strategy on Reduction of GHG Emissions from Ships and Existing IMO Activity Related to Reducing GHG Emissions in the Shipping Sector," International Maritime Organization, Tech. Rep., 2018.

[19] K. Hoag, *Vehicular Engine Design*. Wien, Austria: Springer-Verlag, 2006.

[20] HT Howard Engine Specialists, "Honed Cylinder Liner," 2019. [Online]. Available: https://www.hthoward.co.uk/engine-machining-services/cylinder-block-machining/honing/0612em_06_zcylinder_head_honingcrosshatch_angle/

[21] M. Schirru, "Development of an Ultrasonic Sensing Technique to Measure Lubricant Viscosity in Engine Journal Bearing In-Situ," Ph.D. dissertation, University of Sheffield, 2017. [Online]. Available: http://link.springer.com/10.1007/978-3-319-53408-4

[22] SAE International, "Surface Vehicle Standard J300 Engine Oil Viscosity Classification," Tech. Rep., 2021.

[23] BP Castrol, "Safety Data Sheet - Castrol GTX SynBlend 0W-20," 2014. [Online]. Available: http://www.chem.vt.edu/chem-dept/msds/pdf/108-88-3_33.pdf

[24] G. Stachowiak and A. W. Batchelor, *Engineering Tribology*. Oxford, UK: Butterworth Heinemann, 2008. [Online]. Available: http://www.ncbi.nlm.nih.gov/pubmed/22068761

[25] International Maritime Organization, "Resolution MEPC.324(75) Amendments to MARPOL Annex VI," Tech. Rep. November 2020, 2020.

[26] C. Delprete and A. Razavykia, "Piston ring–liner lubrication and tribological performance evaluation: A review," *Proceedings of the Institution of Mechanical Engineers, Part J: Journal of Engineering Tribology*, vol. 232, no. 2, pp. 193–209, 2018.

[27] B. J. Hamrock, S. R. Schmid, and B. O. Jacobson, *Fundamental of Fluid Film Lubrication*, 2nd ed., L. L. Faulkner, Ed. New York: Marcel Dekker, 2004.

[28] R. S. Dwyer-Joyce, D. A. Green, P. Harper, R. Lewis, S. Balakrishnan, P. D. King, H. Rahnejat, and S. Howell-Smith, “The Measurement of Liner - Piston Skirt Oil Film Thickness by an Ultrasonic Means,” *SAE Technical Paper 2006-01-0648*, 2006. [Online]. Available: http://papers.sae.org/2006-01-0648/

[29] R. Mills and R. Dwyer-Joyce, “Ultrasound for the Non-Invasive Measurement of IC Engine Piston Skirt Lubricant Films,” *Proceedings of the Institution of Mechanical Engineers, Part J: Journal of Engineering Tribology*, vol. 228, no. 11, pp. 1330–1340, 2014. [Online]. Available: http://journals.sagepub.com/doi/10.1177/1350650114538616

[30] R. S. Mills, E. Y. Avan, and R. S. Dwyer-Joyce, “Piezoelectric Sensors to Monitor Lubricant Film Thickness at Piston–Cylinder Contacts in a Fired Engine,” *Proceedings of the Institution of Mechanical Engineers, Part J: Journal of Engineering Tribology*, vol. 227, no. 2, pp. 100–111, 2012.

[31] R. Mills, J. Vail, and R. Dwyer-Joyce, “Ultrasound for the Non-Invasive Measurement of Internal Combustion Engine Piston Ring Oil Films,” *Proceedings of the Institution of Mechanical Engineers, Part J: Journal of Engineering Tribology*, vol. 229, no. 2, pp. 207–215, 2015. [Online]. Available: http://pij.sagepub.com/lookup/doi/10.1177/1350650114552538

[32] E. Y. Avan, R. Mills, and R. S. Dwyer-Joyce, “Ultrasonic Imaging of the Piston Ring Oil Film During Operation in a Motored Engine - Towards Oil Film Thickness Measurement,” *SAE International Journal of Fuels and Lubricants*, vol. 3, pp. 786–793, 2010. [Online]. Available: http://papers.sae.org/2010-01-2179/

[33] M. Takiguchi, K. Nakayama, S. Furuhama, and H. Yoshida, “Variation of Piston Ring Oil Film Thickness in an Internal Combustion Engine - Comparison Between Thrust and Anti-Thrust Sides,” *SAE Technical Paper 980563*, 1998. [Online]. Available: http://www.sae.org/technical/papers/980563

[34] T. Seki, K. Nakayama, T. Yamada, A. Yoshida, and M. Takiguchi, “A Study on Variation in Oil Film Thickness of a Piston Ring Package: Variation of Oil Film Thickness in Piston Sliding Direction,” *JSAE Review*, vol. 21, no. 3, pp. 315–320, 2000.

[35] A. Dhar, A. K. Agarwal, and V. Saxena, “Measurement of Dynamic Lubricating Oil Film Thickness Between Piston Ring and Liner in a Motored Engine,” *Sensors and Actuators, A: Physical*, vol. 149, no. 1, pp. 7–15, 2009.

[36] A. Dhar, A. K. Agarwal, and V. Saxen, “Measurement of Lubricating Oil Film Thickness Between Piston Ring-Liner Interface in an Engine Simulator,” *SAE Technical Paper 2008-28-0071*, pp. 494–499, 2008.

[37] S. L. Moore and G. M. Hamilton, “The Starved Lubrication of Piston Rings in a Diesel Engine,” *Journal Mechanical Engineering Science*, vol. 20, no. 6, pp. 345–352, 1978.

[38] J. M. Nouri, I. Vasilakos, and Y. Yan, “Cavitation between cylinder-liner and piston-ring in a new designed optical IC engine,” *International Journal of Engine Research*, pp. 1–15, 2021.

[39] M. Takiguchi, R. Sasaki, and I. Takahashi, “Oil Film Thickness Measurement and Analysis of a Three Ring Pack in an Operating Diesel Engine,” *SAE Technical Paper 2000-01-1787*, 2000.

[40] D. O. Ducu, R. J. Donahue, and J. B. Ghandhi, “Design of Capacitance Probes for Oil Film Thickness Measurements Between the Piston Ring and Liner in Internal Combustion,” *Journal of Engineering for Gas Turbines and Power*, vol. 123, pp. 633–643, 2001.

[41] G. Garcia-Atance Fatjo, E. H. Smith, and I. Sherrington, “Piston-ring film thickness: Theory and experiment compared,” *Proceedings of the Institution of Mechanical Engineers, Part J: Journal of Engineering Tribology*, vol. 232, no. 5, pp. 550–567, 2018.

[42] G. Garcia-Atance Fatjo, E. H. Smith, and I. Sherington, “Mapping Lubricating Film Thickness, Film Extent and Ring Twist for the Compression-Ring in a Firing Internal Combustion Engine,” pp. 112–118, 2014.

[43] S. J. Söchting and I. Sherrington, “The Effect of Load and Viscosity on the Minimum Operating Oil Film Thickness of Piston-Rings in Internal Combustion Engines,” *Proceedings of the Institution of Mechanical Engineers, Part J: Journal of Engineering Tribology*, vol. 223, no. 3, pp. 383–391, 2009.

[44] I. Sherrington and E. H. Smith, “Experimental Methods for Measuring the Oil-Film Thickness Between the Piston-Rings and Cylinder-Wall of Internal Combustion Engines,” *Tribology International*, vol. 18, no. 6, pp. 315–320, 1985.

[45] H. Shinde and A. Bewoor, “Capacitive Sensor for Engine Oil Deterioration Measurement,” in *AIP Conference Proceedings*, vol. 1943, 2018.

[46] M. Kasai, N. Yoshimura, and K. Watanabe, “Evaluation of Engine Oil Deterioration Using a Comb-Shaped Electrode,” *SAE Technical Paper 2016-01-2317*, 2016.

[47] A. Basu, A. Berndorfer, C. Buelna, J. Campbell, K. Ismail, Y. Lin, L. Rodriguez, and S. S. Wang, “"Smart sensing" of Oil Degradation and Oil Level Measurements in Gasoline Engines,” *SAE Technical Paper 2000-01-1366*, 2000.

[48] L. L. Ting, “Development of a Laser Fluorescence Technique For Measuring Piston Ring Oil Film Thickness,” *Journal of Lubrication Technology*, vol. 102, no. 2, pp. 165–170, 1980.

[49] Y. Baba, H. Suzuki, Y. Sakai, D. L. T. Wei, T. Ishima, and T. Obokata, “PIV/LIF Measurements of Oil Film Behavior on the Piston in I.C. Engine,” *SAE Technical Paper 2007-24-0001*, 2007. [Online]. Available: http://www.sae.org/technical/papers/2007-24-0001

[50] R. S. Notay, M. Priest, and M. F. Fox, “The Influence of Lubricant Degradation on Measured Piston Ring Film Thickness in a Fired Gasoline Reciprocating Engine,” *Tribology International*, vol. 129, no. January 2019, pp. 112–123, 2019. [Online]. Available: https://doi.org/10.1016/j.triboint.2018.07.002

[51] R. Taylor and P. Evans, “In-situ Piston Measurements,” *Proceedings of the Institution of Mechanical Engineers, Part J: Journal of Engineering Tribology*, vol. 218, no. 3, pp. 185–200, 2004.

[52] S. R. Nattrass, D. M. Thompson, and H. McCann, “First In-Situ Measurement of Lubricant Degradation in the Ring Pack of a Running Engine,” *SAE Technical Paper 942026*, pp. 153–165, 1994.

[53] S. Kumar, P. S. Mukherjee, and N. M. Mishra, “Online Condition Monitoring of Engine Oil,” *Industrial Lubrication and Tribology*, vol. 57, no. 6, pp. 260–267, 2005.

[54] P. Obert, H. J. Füßer, and D. Bartel, “Oil Distribution and Oil Film Thickness within the Piston Ring-Liner Contact Measured by Laser-Induced Fluorescence in a Reciprocating Model Test Under Starved Lubrication Conditions,” *Tribology International*, vol. 129, no. January 2019, pp. 191–201, 2019. [Online]. Available: https://doi.org/10.1016/j.triboint.2018.07.022

[55] T. A. Dow, C. A. Schiele, and R. D. Stockwell, “Technique for Experimental Evaluation of Piston Ring- Cylinder Film Thickness,” *Journal of Lubrication Technology*, vol. 105, no. 3, pp. 353–360, 1983.

[56] J. Tamminen, C. Sandström, and P. Andersson, “Influence of Load on the Tribological Conditions in Piston Ring and Cylinder Liner Contacts in a Medium-Speed Diesel Engine,” *Tribology International*, vol. 39, no. 12, pp. 1643–1652, 2006.

[57] H. Fujimoto, Y. Yoshihara, T. Goto, and S. Furuhama, “Measurement of Cylinder Bore Deformation During Actual Operating Engines,” *SAE Technical Paper 910042*, 1991.

[58] F. Maassen, F. Koch, M. Schwaderlapp, T. Ortjohann, and J. Dohmen, “Analytical and Empirical Methods for Optimization of Cylinder Liner Bore Distortion,” in *SAE Technical Paper 2001-01-0569*, 2001. [Online]. Available: http://papers.sae.org/2001-01-0569/

[59] F. Koch, E. Fahl, and A. Haas, “A New Technique for Measuring the Deformation of Cylinder Bores During Engine Operation,” *SAE Technical Paper 950540*, 1995.

[60] L. E. Bird and R. M. Gartside, “Measurement of Bore Distortion in a Firing Engine,” in *SAE Technical Paper 2002-01-0485*, 2002.

[61] N. Iijima, T. Sakurai, M. Takiguchi, Y. Harigaya, T. Yamada, and H. Yoshida, “An Experimental Study on Relationship between Lubricating Oil Consumption and Cylinder Bore Deformation in Conventional Gasoline Engine,” *SAE International Journal of Engines*, vol. 2, no. 1, pp. 106–113, 2009.

[62] P. Saad, L. Kamo, M. Mekari, W. Bryzik, V. Wong, N. Dmytrychenko, and R. Mnatsakanov, “Modeling and Measurement of Tribological Parameters Between Piston Rings-Liner in Turbocharged Diesel Engine,” *SAE Technical Paper 2007-01-1440*, 2007. [Online]. Available: http://link.aip.org/link/ASMECP/v2006/i42592a/p551/s1&Agg=doi

[63] M. A. Bulsara, D. V. Bhatt, and K. N. Mistry, “Measurement of Oil Film Thickness Between Piston Ring and Liner using Strain Gauge,” *Industrial Lubrication and Tribology*, vol. 65, no. 5, pp. 297–304, 2013. [Online]. Available: http://www.emeraldinsight.com/doi/10.1108/ILT-02-2011-0013

[64] R. Mills, “Ultrasonic measurement of lubricant films generated at the piston-cylinder interface of internal combustion engines,” Ph.D. dissertation, University of Sheffield, 2012.

[65] R. Mills, E. Y. Avan, and R. S. Dwyer-Joyce, "Measuring Lubricant Films at the Piston-Cylinder Contact: An Overview of Current Technologies with Focus on Ultrasound," *SAE Technical Paper 2013-01-0294*, 2013. [Online]. Available: http://www.sae.org/technical/papers/2013-01-0294

[66] M. Stark and R. Mittler, "Optimization of Tribodynamic Effects to Improve the Reduction Potential of Particulate Matter Concentrations in the Exhaust Gas of Large Two Stroke Marine Diesel Engines," *SAE International Journal of Fuels and Lubricants*, vol. 7, no. 3, pp. 965–978, 2014.

[67] H. J. Pain, *The Physics of Vibrations*, 6th ed. London, UK: John Wiley & Sons, 2005.

[68] J. David and N. Cheeke, *Fundamentals and Applications of Ultrasonic Waves*. Boca Raton, Florida: CRC Press LLC, 2002. [Online]. Available: https://books.google.com/books?id=Lnzb4PeTbeYC&pgis=1

[69] H. Krautkramer and J. Krautkramer, *Ultrasonic Testing of Materials*, 4th ed. Berlin: Springer-Verlag, 1990.

[70] Piezo Technologies, "Ultrasonic contact transducers," 2021. [Online]. Available: https://piezotechnologies.com/contact-transducers/

[71] ASTM Compass, "E1065/E1065M: Standard Practice for Evaluating Characteristics of Ultrasonic Search Units," Tech. Rep., 2014.

[72] NDT Resource Centre, "Radiated Fields of Ultrasonic Transducers," 2019. [Online]. Available: https://www.nde-ed.org/EducationResources/CommunityCollege/Ultrasonics/EquipmentTrans/radiatedfields.htm

[73] M. Schoenberg, "Elastic Wave Behavior Across Linear Slip Interfaces," *Journal of the Acoustical Society of America*, vol. 68, no. 2, pp. 1516–1521, 1980.

[74] R. S. Dwyer-Joyce, P. Harper, and B. W. Drinkwater, "A Method for the Measurement of Hydrodynamic Oil Films using Ultrasonic Reflection," *Tribology Letters*, vol. 17, no. 2, pp. 337–348, 2004.

[75] R. S. Dwyer-Joyce, B. Drinkwater, and C. J. Donohoe, "The measurement of lubricant-film thickness using ultrasound," *The Royal Society*, no. 459, pp. 957–976, 2003.

[76] B. W. Drinkwater, R. S. Dwyer-Joyce, and P. Harper, "On-Line Measurement of Lubricant Film Thickness Using Ultrasonic Reflection Coefficients," vol. 700, no. 2004, 2004, pp. 984–991.

[77] S. Beamish, X. Li, H. Brunskill, A. Hunter, and R. S. Dwyer-Joyce, "Circumferential Film Thickness Measurement in Journal Bearings via the Ultrasonic Technique," *Tribology International*, vol. 148, pp. 1–11, 2020.

[78] A. A. Raimondi and J. Boyd, "A Solution for the Finite Journal Bearing and its Application to Analysis and Design: I," *A S L E Transactions*, vol. 1, no. 1, pp. 159–174, 1958. [Online]. Available: https://doi.org/10.1080/05698195808972328

[79] V. Buckin and E. Kudryashov, "Ultrasonic Shear Wave Rheology of Weak Particle Gels," *Advances in Colloid and Interface Science*, vol. 89-90, pp. 401–422, 2001.

[80] M. Schirru, R. S. Dwyer-Joyce, R. Mills, O. Smith, and M. Sutton, "Development of a Novel Ultrasonic Viscometer for Real Time and In - Situ Applications in Engines," *SAE Technical Paper 2015-01-0679*, 2015.

[81] D. Green, "The Tribological Effects of Soot Contaminated Lubricants on Engine Components," Ph.D. dissertation, University of Sheffield, 2007.

[82] B. Treeby, B. Cox, and J. Jaros, "k-Wave A MATLAB Toolbox for the Time-Domain Simulation of Acoustic Wave Fields," 2021. [Online]. Available: http://www.k-wave.org/

[83] B. E. Treeby, J. Jaros, D. Rohrbach, and B. T. Cox, "Modelling Elastic Wave Propagation using the k-Wave MATLAB Toolbox," *IEEE International Ultrasonics Symposium, IUS*, no. 4, pp. 146–149, 2014.

[84] B. E. Treeby, J. G. Laufer, E. Zhang, F. C. Norris, M. F. Lythgoe, P. C. Beard, and B. T. Cox, "Acoustic Attenuation Compensation in Photoacoustic Tomography: Application to High-Resolution 3D Imaging of Vascular Networks in Mice," *Photons Plus Ultrasound: Imaging and Sensing 2011*, vol. 7899, 2011.

[85] B. T. Cox, S. Kara, S. R. Arridge, and P. C. Beard, "k-space Propagation Models for Acoustically Heterogeneous Media: Application to Biomedical Photoacoustics," *The Journal of the Acoustical Society of America*, vol. 121, no. 6, pp. 3453–3464, 2007.

[86] E. Martin, J. Jaros, and B. E. Treeby, "Experimental Validation of k-Wave: Nonlinear Wave Propagation in Layered, Absorbing Fluid Media," *IEEE Transactions on Ultrasonics, Ferroelectrics, and Frequency Control*, vol. 67, no. 1, pp. 81–91, 2020.

[87] D. Talué, P. Whitwood, G. Page, M. McAllister, F. Borean, and R. Penfold, "Introducing the Ingenium SI Engine: Jaguar Land Rover's New Four-Cylinder Gasoline Engine," in *38th International Vienna Motor Symposium*, Vienna, 2017.

[88] S. Beamish and R. S. Dwyer-Joyce, "Lubricant Characterisation Report," Tech. Rep., 2018.

[89] T. Howard, "Development of a Novel Bearing Concept for Improved Wind Turbine Gearbox Reliability," Ph.D. dissertation, University of Sheffield, 2016.

[90] A. Hunter, "Ultrasonic Measurements of the Strip Thickness, Lubricant Film Thickness, Roll Deflection and Roll Stress in the Roll Bite in the Cold Rolling of Steel," Ph.D. dissertation, University of Sheffield, 2018. [Online]. Available: http://etheses.whiterose.ac.uk/22009/

[91] T. Reddyhoff, S. Kasolang, R. S. Dwyer-Joyce, and B. W. Drinkwater, "The phase shift of an ultrasonic pulse at an oil layer and determination of film thickness," *Proceedings of the Institution of Mechanical Engineers, Part J: Journal of Engineering Tribology*, vol. 219, no. 6, pp. 387–400, 2005.

[92] P. Dou, T. Wu, and Z. Luo, "Wide Range Measurement of Lubricant Film Thickness Based on Ultrasonic Reflection Coefficient Phase Spectrum," *Journal of Tribology*, vol. 141, no. 3, pp. 1–15, 2019. [Online]. Available: https://doi.org/10.1115/1.4041511

[93] M. Yu, L. Shen, T. Mutasa, P. Dou, T. Wu, and T. Reddyhoff, "Exact analytical solution to ultrasonic interfacial reflection enabling optimal oil film thickness measurement," *Tribology International*, vol. 151, nov 2020. [Online]. Available: https://doi.org/10.1016/j.triboint.2020.106522